Spring 1-1-2011

Modeling Earth's Outer Radiation Belt Electron Dynamics --- Radial Diffusion, Heating, and Loss

Weichao Tu
University of Colorado at Boulder, tuweichao@gmail.com

Modeling Earth's Outer Radiation Belt Electron Dynamics — Radial Diffusion, Heating, and Loss

by

Weichao Tu

B.S., Peking University, 2006

M.S., University of Colorado, 2008

A thesis submitted to the

Faculty of the Graduate School of the

University of Colorado in partial fulfillment

of the requirement for the degree of

Doctor of Philosophy

Department of Aerospace Engineering Sciences

2011

This Thesis entitled:
Modeling Earth's Outer Radiation Belt Electron Dynamics
— Radial Diffusion, Heating, and Loss
written by Weichao Tu
has been approved for the Department of Aerospace Engineering and Sciences

_____
Prof. Xinlin Li

_____
Prof. Dan Baker

_____
Dr. Jack Gosling

_____
Prof. Scott Palo

_____
Dr. Howard Singer

Date _____

The final copy of this proposal has been examined by the signatories, and we find that both the content and the form meet acceptable presentation standards of scholarly work in the above mentioned discipline.

Tu, Weichao (Ph.D., Aerospace Engineering Sciences)

Modeling Earth's Outer Radiation Belt Electron Dynamics

— Radial Diffusion, Heating, and Loss

Thesis directed by Prof. Xinlin Li

Earth's outer radiation belt is a relativistic electron environment that is hazardous to space systems. It is characterized by large variations in the electron flux, which are controlled by the competition between source, transport, and loss processes. One of the central questions in outer radiation belt research is to resolve the relative contribution of radial diffusion, wave heating, and loss to the enhancement and decay of the radiation belt electrons. This thesis studies them together and separately. Firstly, we develop an empirical Fokker-Planck model that includes radial diffusion, an internal source, and finite electron lifetimes parameterized as functions of geomagnetic indices. By simulating the observed electron variations, the model suggests that the required magnitudes of radial diffusion and internal heating for the enhancement of energetic electrons in the outer radiation belt vary from storm to storm, and generally internal heating contributes more to the enhancements of MeV energy electrons at L=4 (L is approximately the radial distance in Earth radii at the equator). However, since the source, transport, and loss terms in the model are empirical, the model results have uncertainties.

To eliminate the uncertainty in the loss rate, both the precipitation and the adiabatic loss of radiation belt electrons are quantitatively studied. Based on the observations from Solar Anomalous and Magnetospheric Particle Explorer (SAMPEX), a Drift-Diffusion model is applied to quantify electron precipitation loss, which is the dominant non-adiabatic loss mechanism for electrons in the heart of the outer radiation belt. Model results for a small storm, a moderate storm, and an intense

storm indicate that fast precipitation losses of relativistic electrons, on the time scale of hours, persistently occur in the storm main phases and with more efficient losses at higher energies over wide range of L regions. Additionally, calculations of adiabatic effects on radiation belt electrons at low altitudes demonstrate that the adiabatic flux drop of electrons during the storm main phase is both altitude and storm dependent. During the main phase of a moderate geomagnetic storm, due solely to adiabatic effects a satellite at low altitude sees either zero electron flux or a fractional flux drop depending on its altitude.

To physically quantify the radial diffusion rate, we use power spectral density and global mode structure of the Ultra-Low-Frequency (ULF) waves, which are derived from the Lyon-Fedder-Mobarry (LFM) MHD simulation and validated by field data from real satellites. The calculated total diffusion rate is shown to be dominated by the contribution from magnetic field perturbations, and much less from the electric field. Fast diffusion generally occurs when solar wind dynamic pressure is high or nightside geomagnetic activity is strong and with higher diffusion rates at higher L regions.

Work performed in this thesis provides realistic loss rate and radial diffusion rate of radiation belt electrons, as well as a comprehensive Fokker-Planck model that can take the loss and radial diffusion rates as inputs and then determine the internal heating rate with less uncertainty. By this approach, we will be able to quantitatively understand the relative contribution of radial diffusion, wave heating, and loss to the variations of radiation belt electrons.

Dedication

To my parents, who always offer me unconditional love, support, and encouragement.

Acknowledgements

First and foremost, I would like to express my deepest gratitude to my advisor, Prof. Xinlin Li, who has been an ideal advisor in offering me excellent guidance in coursework, research, and career goal setting. Without his sound advice and encouragement, I would not have been able to complete all the course requirements in two years and keep a straight A's record. During my research, Xinlin always provided me with knowledgeable guidance and patient encouragement, which inspired all of my work and make this thesis possible. I am also heartily thankful for his invaluable advice on my career goal setting, especially the guidance from his personal experience as a foreign student. There is an old Chinese saying, 'He who teaches me once is my father-figure for life', which I would refer to as my sincere gratitude to Xinlin. Next I would like to thank all my thesis committee members for their efforts and helpful career advice throughout the course of this thesis. Their encouragement makes me feel more confident about my future career. I also want to express my gratitude to Doctors Mike Temerin, Richard Selesnick, and Scot Elkington, who I have had delightful and fruitful collaborations with for various projects in this thesis, for our many meaningful discussions and their insightful comments. I am very thankful to Aerospace Engineering Sciences Department and Laboratory for Atmospheric and Space Physics (LASP) for their excellent facilities and generous support. I have been extremely lucky to be able to work in LASP, one of the top institutions in space physics, and with so many enthusiastic researchers who are experts in various fields. There are so many colleagues in LASP I want to thank individually: thank you so much my colleague and friend, Drew Turner, for the inspiration and motivation I gained from our discussions together, and for

bringing me to all kinds of fun American and Canadian style parties; special thanks to Wenlong Liu for providing me great help with THEMIS data and being the person whom I can ask silly research questions and 'gossip' some Chinese with; I am also grateful to Theodore Sarris, from whom I saw the real joy of research, and I would always remember the many times in your office when we were totally into each other's research and losing track of time in our discussions; also, thank you to Lauren Blum, for letting me appreciate the 'gentle' part of space physics and for patiently answering my English grammar questions; and I want to thank Quintin Schiller for the enthusiasm he brought to our group and his questions about space physics fundamentals that help to refresh and strengthen my knowledge. Last, but surely not least, I owe an immense debt of gratitude to my boyfriend and family, Qiang, who is always there to half my sadness and double my happiness, and who provides me solid and warm support in life and in work.

Contents

Chapter

Tables

Table

Figures

Figure

Chapter 1

Introduction

Earth's outer radiation belt is a relativistic electron environment resident in the magnetosphere, where electrons with energies from a few hundreds keV to several MeV are trapped on stable orbits. The energetic electron flux in the outer radiation belt is detected to be highly variable. Since the outer radiation belt is the environment where a great number of satellites are located, particularly those for communication and navigation, these relativistic electrons under great variations can pose a significant threat to satellite electronics and astronauts. Thus, there is an increasing need to extensively explore and fully understand outer radiation belt dynamics. An unprecedented number of spacecraft missions have been launched in the modern era to provide observations of the outer radiation belt, tracking the relativistic electron variations in various orbits. An important mission designed specifically to explore the Earth's radiation belt environment is to be launched in 2012, named Radiation Belt Storm Probes (RBSP) mission by NASA.

After decades of observations and research, we understand that the large electron flux variations in the outer radiation belt are controlled by the competition between various source, transport, and loss processes. However, there are still several outstanding questions regarding the true nature of outer radiation belt variations, a central one of which is to resolve the relative contribution of radial diffusion, wave heating, and loss to the enhancement and decay of the outer radiation belt electrons. This question cannot be answered by data analysis only, since the observed electron variation is a mix of all the simultaneous processes. Therefore, in order to achieve quantitative results of the relative importance of radial diffusion, wave heating, and loss, physics-based models of radiation belt electrons are required. Inspired by this, sophisticated physical models are developed in

this thesis, simulating the various competing mechanisms acting on outer radiation belt electrons both together and separately.

I begin with a chapter providing the background knowledge for our radiation belt study. Earth's radiation belts are introduced in the context of Earth's magnetosphere. Charged-particle motions in the radiation belts and the physical quantity, phase space density, are described in preparation for the discussion of radiation belt electron dynamics, with a detailed description of the calculation procedure for phase space density. A review of the current understanding of radiation belt electron dynamics follows, covering the various transport, source, and loss mechanisms. Especially, the difficulties in distinguishing between radial diffusion and internal heating and in resolving the relative contributions of different mechanisms to the observed electron variations are discussed. This leads into the importance of radiation belt modeling, with a brief review of the important radiation belt models finishing up Chapter 2.

In Chapter 3, I introduce an empirical Fokker-Planck model that includes all the factors of radial diffusion, internal heating, and loss to simulate the observed electron variations. The model can test the relative importance and timing of these processes against data, but since the source, transport, and loss rates used in the model are empirical, the model results have uncertainties. On one hand, to eliminate the uncertainty in electron loss rate, both the non-adiabatic precipitation loss and the adiabatic loss of radiation belt electrons are quantified. In Chapter 4, a Drift-Diffusion model is applied to quantify electron precipitation loss observed by the Solar Anomalous and Magnetospheric Particle Explorer (SAMPEX). The model can provide electron lifetimes during different geomagnetic storms for electrons at different energies and for various space locations. Calculations of the adiabatic flux drop of radiation belt electrons during the storm main phase are performed in Chapter 5, which for the first time focuses on electrons mirroring at low altitude. The variations of the adiabatic flux drop at different altitudes are also investigated. On the other hand, to physically quantify the radial diffusion rate, in Chapter 6 we use the power spectral density and global mode structure of the

Ultra-Low-Frequency (ULF) waves, which are derived from the Lyon-Fedder-Mobarry (LFM) MHD simulation and validated by field data from real satellites. The method provides physical radial diffusion rates of radiation belt electrons as a function of electron energy, space, and time.

In the last chapter, our conclusions are summarized together with discussions about the proposed future work, one of which is to use the physically quantified electron lifetime and radial diffusion rate as inputs for the comprehensive Fokker-Planck model to determine the internal heating rate with less uncertainty, then finally achieving the quantification of the relative contribution of radial diffusion, wave heating, and loss to the radiation belt electron dynamics. I then finish with discussions about how our work in this thesis is closely tied to the upcoming NASA RBSP mission and some lessons learned during my research. The appendices cover some detailed derivations and some trial-and-error and troubleshooting procedures that come up during the work.

Chapter 2

Relevant Background

2.1 The Contextual Setting of Earth's Electron Radiation Belt

2.1.1 Earth's Magnetosphere

The magnetosphere is a tear-shaped cavity surrounding the Earth and containing the Earth's magnetic field, formed by the interaction between the solar wind and the Earth's own magnetic field (see Figure 2.1 for illustration). Its boundary, magnetopause, is at a geocentric distance of about 10 Earth radii (R_E) on the dayside; while on the night side, the magnetosphere extends into a long magnetic tail (well past 200 R_E). The magnetosphere is a complex system, with various currents throughout and different populations of charged particles trapped inside, as illustrated in Figure 2.1 [Kivelson and Russell, 1995]. Among all the current systems, the ring current is an important one because its growth is a characteristic of a geomagnetic storm.

A geomagnetic storm is a temporary disturbance of the Earth's magnetosphere caused by a disturbance in space weather. The disturbance is measured by the Disturbance Storm Time (Dst) index, essentially based on the average value of the horizontal component of the Earth's magnetic field measured hourly at four near-equatorial geomagnetic observatories. A classic magnetic storm can be divided into three phases: storm sudden commencement when Dst shows a sudden rise, storm main phase when Dst drops and reaches negative values, and storm recovery phase when Dst gradually returns to the normal level. During the storm main phase, charged particles in the near-Earth plasma sheet are energized and injected deeper into the inner magnetosphere, producing the storm-time ring current; while during the storm recovery phase the ring current begins to recover.

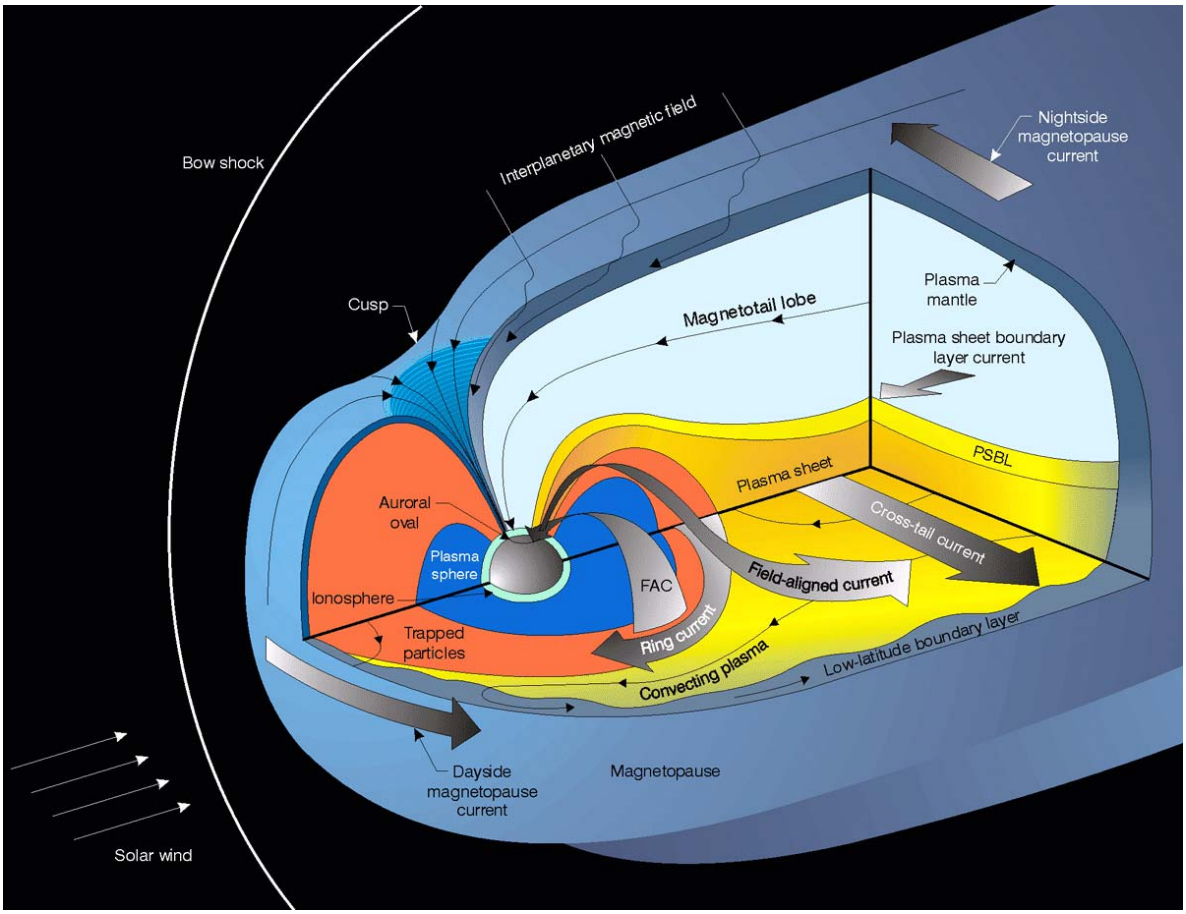

Figure 2.1: Configurations of Earth's magnetosphere (reproduced from Kivelson and Russell, 1995).

Using Dst as an index of storm strength is possible because the strength of the surface magnetic field at low latitudes is inversely proportional to the energy content of the ring current, which increases during geomagnetic storms.

Geomagnetic storms have two main interplanetary origins: the southward-oriented magnetic field of the high-pressure regions formed in the interplanetary medium by the interaction of low- and high-speed solar wind streams co-rotating with the Sun, and the interplanetary disturbances driven by fast coronal mass ejections (CMEs) [e.g., Gonzalez et al., 1999]. The former is recurrent with the Sun's rotation period (~27 days), most frequent in the declining phase of the solar cycle. The latter, on the other hand, is most frequent near solar maximum, and typically involves an encounter with both an interplanetary shock wave and the CME that drives it [e.g., Gosling et al., 1990, 1991].

A magnetospheric substorm is a brief disturbance in the Earth's magnetosphere that causes energy to be released in the magnetotail. It is characterized by specific large scale auroral intensifications and corresponding magnetic perturbations at high latitudes typically close to magnetic midnight [Kivelson and Russell, 1995]. A substorm is also accompanied with fast flows in the magnetotail, plasma ejection in the tailward direction, energetic particle injections at geosynchronous distances, strong intensifications of field-aligned current systems, etc.

2.1.2 Earth's Radiation Belt

Earth's radiation belts reside in the magnetosphere. Back in early 1958, a torus of energetic charged particles about the Earth was discovered by the Explorer 1 mission under Dr. James Van Allen at the University of Iowa. This belt was named Radiation Belt, or Van Allen Radiation Belt. The radiation belt consists of energetic protons and electrons trapped on fairly stable orbits within the Earth's global magnetic field, with energies from a few hundreds keV to several MeV and beyond. Energetic electron radiation belts are distributed in two distinct regions separated by a broad region of depleted flux referred to as the slot region, while protons normally form a single belt. Figure 2.2

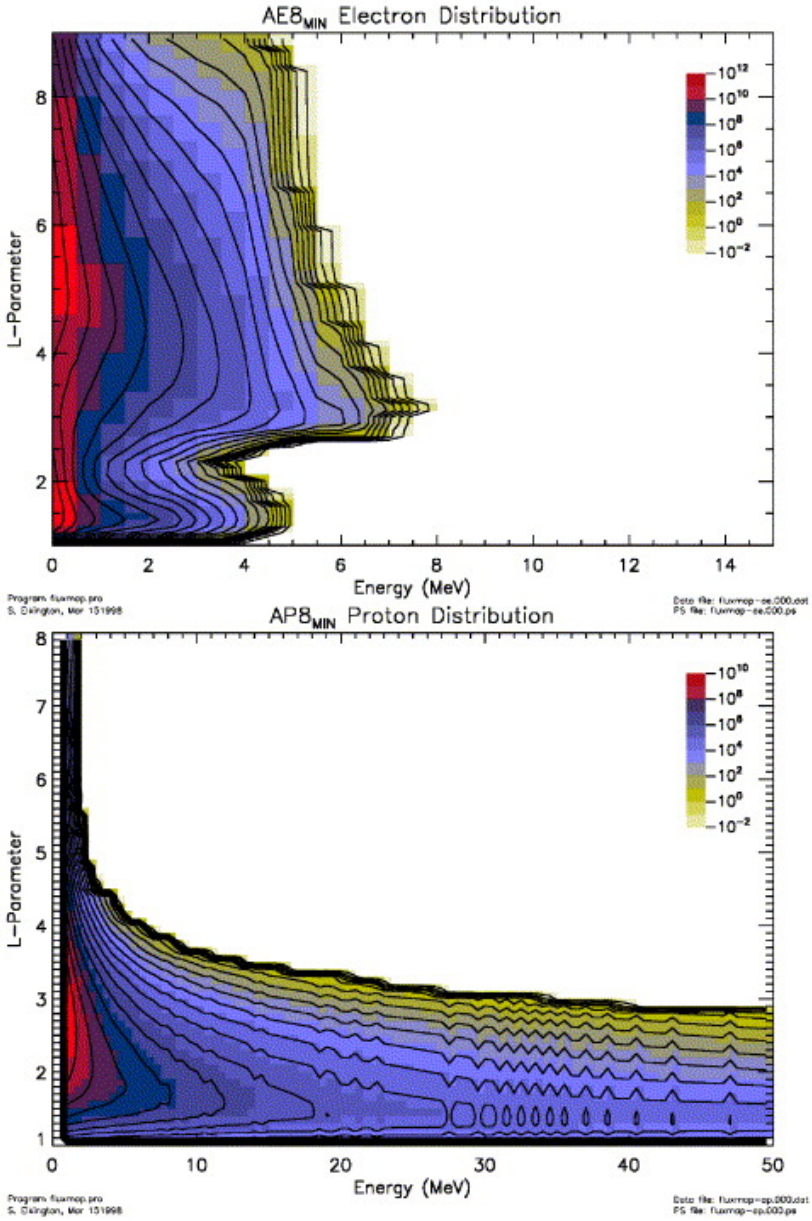

Figure 2.2: NASA AE-8 and AP-8 model results for solar minimum, showing integral electron and proton fluxes on a relative scale (reproduced from Elkington et al., 2004, Copyright Elsevier Ltd 2004).

shows the spatial distribution and energy range of protons and electrons from the NASA AE/AP empirical model (a static model based on data from more than 20 satellites from the early sixties to the mid-seventies). The fluxes are binned as functions of energy and L-value (L is approximately the radial distance in Earth radii (R_E) at the equator from the center of the Earth, which will be discussed in detail later). Since this thesis is about radiation belt electron dynamics, here and after I will focus on introducing the electron radiation belts. Figure 2.2 shows that for 1-2 MeV electrons the inner electron radiation belt centres near 1.5 R_E from the center of the Earth in the equatorial plane, and the outer electron belt is most intense between 4 and 5 R_E.

The above description may give a false impression that the electron radiation belt is quite static. However, although the structure of the inner electron belt tends to be relatively stable, the outer electron belt is highly dynamic, exhibiting electron flux variations over orders of magnitude on time scales ranging from a few minutes to several years. Figure 2.3 (observations from Solar Anomalous and Magnetospheric Particle Explorer (SAMPEX)) shows the variations of the outer electron belt on different time scales, including geomagnetic storms (days), solar rotation, semiannual and even solar cycle. In addition, the locations of the peak flux and outer zone boundaries are also highly variable. The radiation belt is the environment where major space weather activity occurs and many spacecraft operate. Since the energetic electrons in the radiation belt can damage spacecraft electronics, such as leading to satellite failure via deep dielectric charging of spacecraft components [e.g., Baker et al., 1998a, 2001; Fennell et al., 2001], as well as the bodies of astronauts, there is a clear need to effectively model the dynamics of radiation belt electrons.

The complex role of geomagnetic disturbances, including geomagnetic storms and substorms, in the variations of energetic electrons in the outer radiation belt has received considerable attention in radiation belt studies. Reeves et al. [2003] performed a statistical study on 276 moderate and intense geomagnetic storms and found that about half of magnetic storms increase the flux of

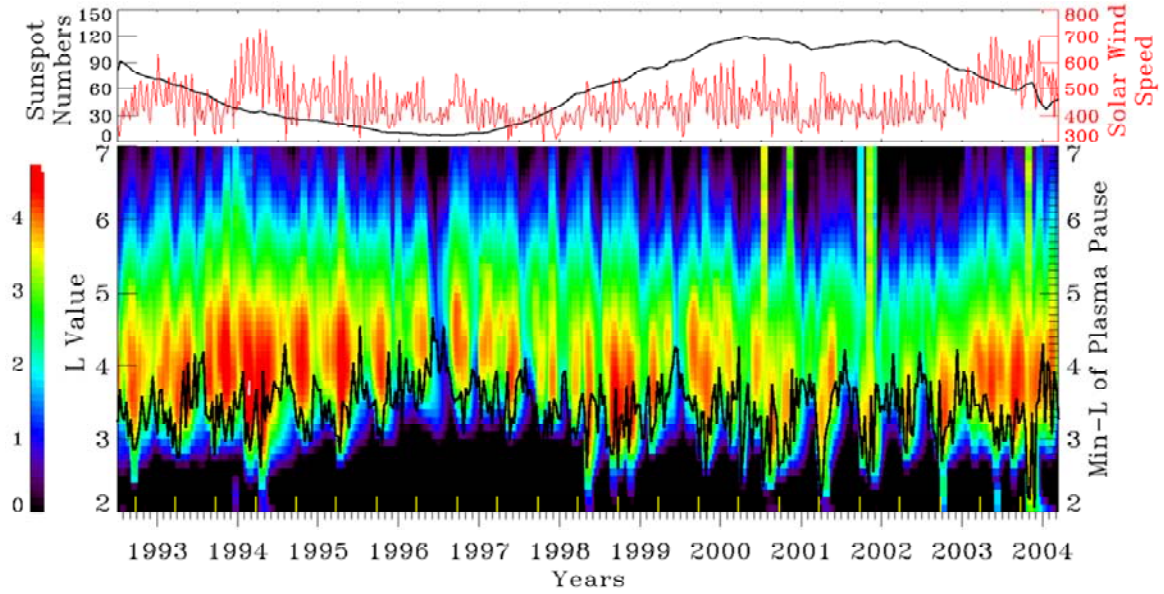

Figure 2.3: (top) Variations of yearly window-averaged sunspot numbers (black curve) and weekly window-averaged solar wind speed (km/s, red curve). (bottom) Monthly window-averaged, color-coded in logarithm, and sorted in L (L bin: 0.1) electron fluxes of 2–6 MeV (#/cm2-s-sr) by SAMPEX since its launch (July 3, 1992) into a low-altitude (550 × 600 km) and highly inclined (82°) orbit. The superimposed black curve represents every 10-day's minimum Lpp based on an empirical model [O'Brien and Moldwin, 2003]. The yellow vertical bars on the horizontal axis are marks of equinoxes. (Reproduced from Li et al., 2006, Copyright 2006 American Geophysical Union.)

relativistic electrons at geosynchronous orbit, while one quarter decrease the flux, and one quarter show little or no change in the flux. It seems that for any given storm 'strength' (minimum Dst), a wide range of relativistic electron responses is possible. Meredith et al. [2002] presented three case studies to investigate the outer zone relativistic electron acceleration, including a strong geomagnetic storm case that contains prolonged substorm activity during its recovery phase, a strong geomagnetic storm case that contains very little substorm activity during its recovery phase, and a case with a period of prolonged substorm activity in the absence of a significant storm signature. Their results suggest that the relativistic electron enhancements are associated with prolonged substorm activity. However, since the overall structure of the radiation belts and their variability are controlled by the competition between source, loss, and transport processes, to understand such dynamics requires knowledge of the transport, acceleration, and loss mechanisms of the energetic electrons in the radiation belt, which will be discussed extensively in Section 2.4 of this chapter.

2.2 Charged-Particle Motion in the Radiation Belt

In order to understand the dynamics of radiation belt electrons, we need to be prepared with the knowledge of charged-particle motion in Earth's magnetosphere. Under the principles of electromagnetism, charged particles can be trapped by Earth's magnetic fields, undergoing three distinctive motions: gyromotion, bounce motion, and drift motion (see Figure 2.4 for illustration). Electrons drift eastward around the Earth as they bounce between the mirror points (with stronger magnetic fields) in the northern and southern hemispheres and gyrate around the local magnetic field. More energetic particles bounce and drift faster. These three motions usually have well-separated time scales. For example, for a 1 MeV electron with an equatorial pitch angle of 60^{o} at a radial distance around 6 R_E (R_E is the Earth's radius), the gyration, bounce, and drift periods are about 10^{-3}, 10^{0}, and 10^{3} seconds, respectively.

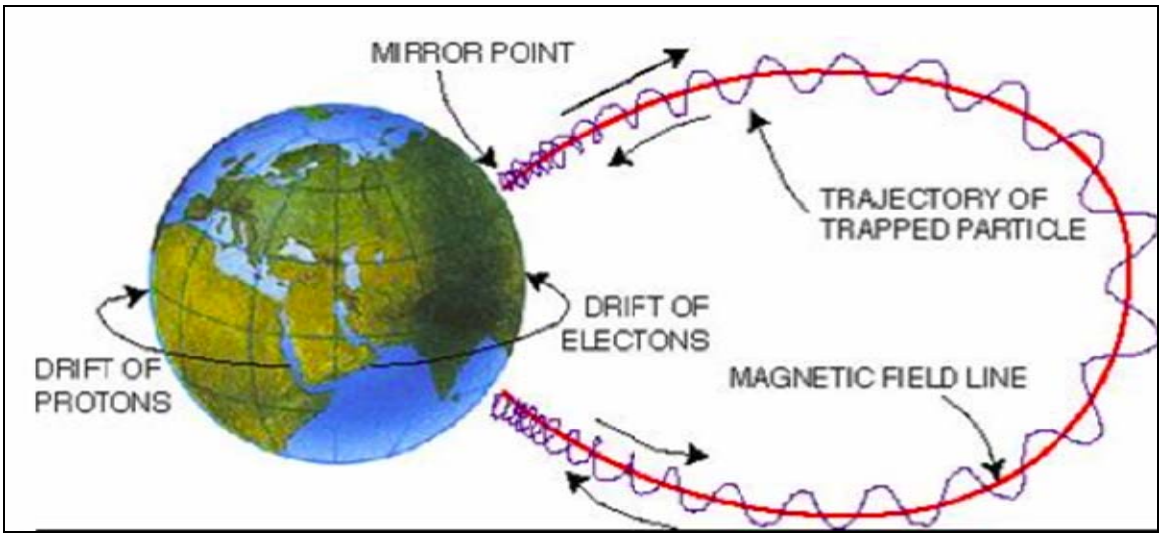

Figure 2.4: Trajectories of particles trapped on closed field lines.

Based on the Hamiltonian action integral, there is an adiabatic invariant associated with each type of motion, a quantity which is conserved if the fields vary slowly as compared to the oscillation frequency associated with that motion [Northrop, 1963]. The conservation and violation of these invariants is critical to study the energization and loss of radiation belt electrons. The first adiabatic invariant is defined as $\mu = p_\perp^2 / 2m_0 B$ (where $p_\perp$ is the relativistic momentum perpendicular to the local magnetic field (B) and m_0 is electron rest mass). The particle's magnetic moment, μ, is conserved if the fields vary slowly in time relative to the gyroperiod and in space compared to the gyroradius. The second adiabatic invariant corresponding to bounce motion is given by $J = \oint p_\parallel ds$, where $p_\parallel$ is the parallel relativistic momentum and ds is an element of the guiding center path and the integral is taken over a full oscillation between the mirror points. J is zero for equatorially mirroring particles. To avoid the dependence on electron momentum, often the derived quantity, $K = \frac{J}{2\sqrt{2m_0\mu}} = \int_{S_m}^{S_m'} \sqrt{B_m - B(s)}\, ds$, is used instead (here the subscript m denotes the mirror point, and B_m and $B(s)$ are the field strengths at the mirror point and the point s respectively). Here K is a purely field-geometric integral. J (and K) is conserved if the field varies much slower than the bounce period, and there are no forces acting parallel to the magnetic field. The third invariant, Φ, is the magnetic flux through the electron's drift shell, given by $\Phi = \iint_S \vec{B} \cdot d\vec{S}$, where $\vec{B}$ is the magnetic vector, and S is the cross section of the drift shell. The quantity L^*, Roederer L parameter, is associated with the third invariant in the form of $L^* = 2\pi k / (\Phi R_E)$, where k is Earth's magnetic moment and R_E is the Earth radius [Roederer, 1970]. L^* (and Φ) is conserved if the field varies much slower than the particle drift period. There are two other commonly used L parameters, dipole L and McIlwain L. Dipole L is defined in a dipole field and is simply the radial distance of a particle

in R_E at the equator. McIlwain L (or L_m) is calculated from (B_m, K) coordinates by applying the functional relation between L_m, B_m, and K, derived for a dipole field. In a dipole field, L^*=Dipole L=L_m, but among the three L parameters L^* is the most physical label to identify particle's drift shell under non-dipole fields.

2.3 Phase Space Density: A Quantity to Describe the Radiation Belt

After introducing the three adiabatic invariants associated with three periodic motions of charged particles, we are now ready to introduce a very important quantity in the description of radiation belt dynamics: the phase space density (PSD). The radiation belt could be completely characterized at a time point by its distribution function in six-dimension phase space, $f(x, y, z, p_x, p_y, p_z)$, which is also called the phase space density. For a conserved system, Liouville's theorem demands a constant PSD along the path in phase space. The PSD may be equivalently written in terms of the three invariants and corresponding phases: $f(x, y, z, p_x, p_y, p_z) = f(\mu, K, L^*, \phi_1, \phi_2, \phi_3)$. Since the conditions of observation typically preclude the distinction of particle phases, for essentially most practical purposes radiation-belt observations are phase-averaged. Then PSD can be taken as the function of only the three invariants, $f = f(\mu, K, L^*)$.

Although a physical understanding of the dynamics requires an investigation of PSD, the real-life measurements of radiation belt electrons are the electron flux. One measured quantity is the differential flux, j, which is a function of position, pitch angle and energy, defined as the number of particles at energy E within dE which cross a unit area dA perpendicular to the specified look direction within a unit solid angle $d\Omega$ per unit time dt, in the form of: $j(E_{ch}, \alpha, \vec{r}) = \frac{dN}{dA d\Omega dE dt}$.

We could calculate the PSD based on the flux measurement using the relation: $f = j / p^2$, where f is the PSD and p is the momentum of the electron.

However, converting the differential flux, $j(E_{ch}, \alpha, \vec{r})$, to PSD, $f(\mu, K, L^*)$, is not as simple as it appears. Chen et al. [2006] developed a methodology for PSD calculation using the flux data from geosynchronous satellites with the general procedure shown in the flow diagram in Figure 2.5. The calculation of PSD distribution consists of two steps: the first is to compute the corresponding three adiabatic invariants and the second is to transform the flux to PSD values. Chen et al. [2006] use arrays of (μ, α) as input. After selecting an appropriate magnetic field model (Tsyganenko 2001 storm model for their calculation), for given (μ_0, α_0), first, they can compute K_0 and L_0^* based on the given local pitch angle α_0 according to the definitions: $K = \int_{s_m}^{s_m'} \sqrt{B_m - B(s)}\, ds$, and $L^* = \frac{2\pi K}{|\phi| R_E}$. Then, using equation $\mu = \frac{P_\perp^2}{2 m_0 B}$ they can calculate the corresponding energy E_0 for the given (μ_0, α_0). Interpolating the flux data over a full pitch angle distribution could provide them with the flux $j(E_{ch}, \alpha_0, \vec{r})$ for all the energy channels. Then, based on the following relation [Hilmer et al., 2000], they generate the PSD for all energy channels:

$$f_{ch} = \left\{ \frac{j_{ch}}{\left\langle p^2 c^2 \right\rangle_{ch}} \left[1.66 \times 10^{-10} \right] \right\} \times 200.3, \; j_{ch} \; [cm^{-2} sr^{-1} keV^{-1} s^{-1}], f_{ch} \; [c^3 / (MeV \cdot cm)^3] \qquad (2.1)$$

where c is the light speed and $\left\langle p^2 c^2 \right\rangle_{ch}$ is defined as:

$$\left\langle p^2 c^2 \right\rangle_{ch} = \frac{1}{2} [K_{\min}^{ch} (K_{\min}^{ch} + 2 m_0 c^2) + K_{\max}^{ch} (K_{\max}^{ch} + 2 m_0 c^2)] \qquad (2.2)$$

where $K_{\min}^{ch}$ and $K_{\max}^{ch}$ are the lower and upper limit of each energy channel in MeV, and $m_0 c^2$ is the rest energy of an electron. Additionally, they define the energy for each channel as

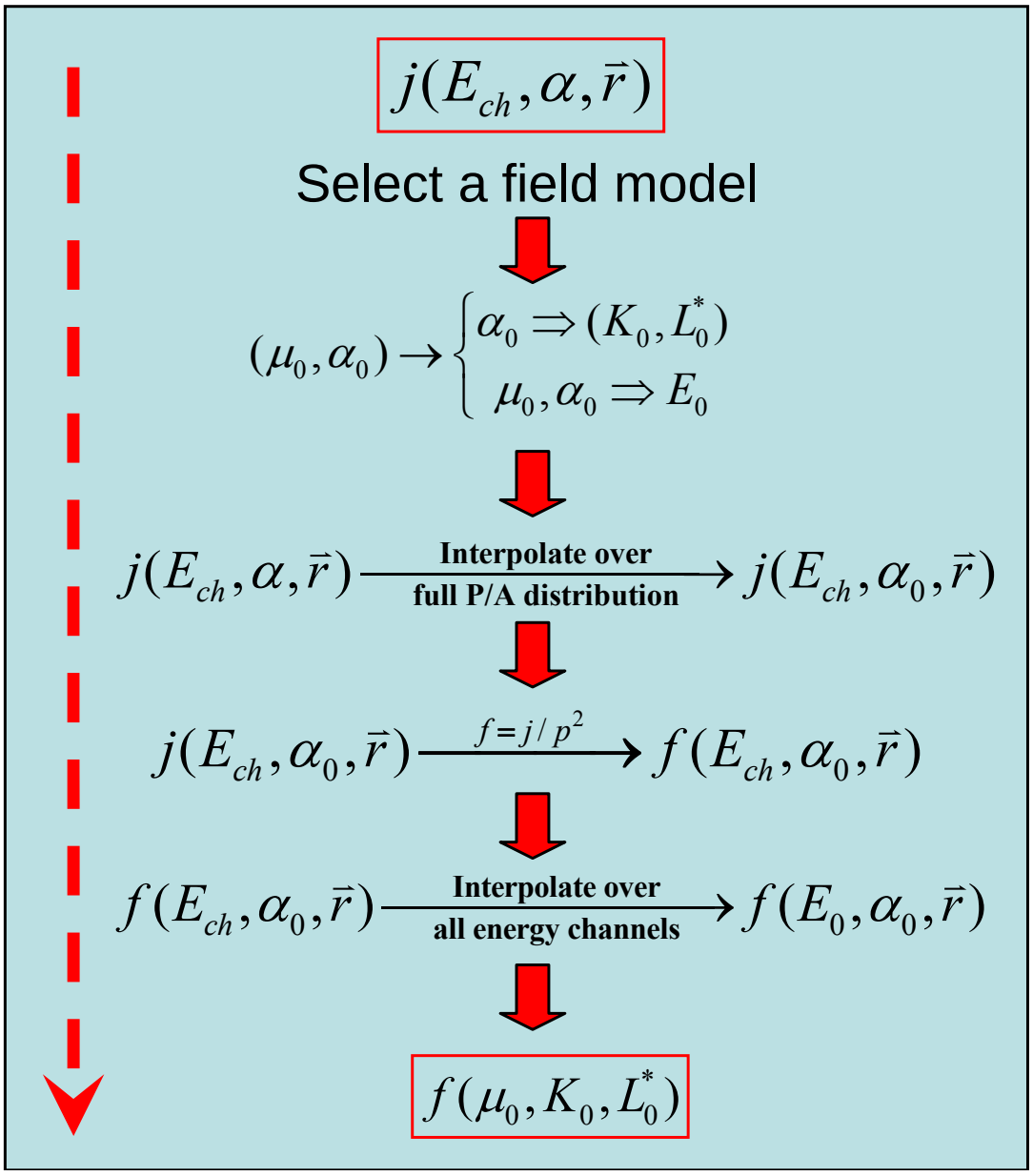

Figure 2.5: Flow diagram showing the calculation of phase space density from flux.

$E_{ch} = \sqrt{K_{\min}^{ch} \cdot K_{\max}^{ch}}$ considering a falling electron energy spectrum. Finally, after another interpolation for $f(E_{ch}, \alpha_0, \vec{r})$ over all the energy channels, they create the PSD for E_0, $f(E_0, \alpha_0, \vec{r})$, which is just $f(\mu_0, K_0, L_0^*)$ combining previous results. Then performing this calculation for other pairs of (μ_0, α_0), they could obtain the PSD distribution with respect to the three adiabatic invariants.

Here I have introduced the PSD calculation methodology by Chen et al. [2006] in great detail because it is the method used in our work. The calculation of PSD is not a trivial procedure, not only due to the complicated logic as introduced, but also because the calculation depends on the performance of the magnetic field models, none of which are perfect. Furthermore, errors would be introduced from the poor data fits. The significance of these error sources are discussed in detail in Green and Kivelson [2004].

2.4 Relativistic Electron Dynamics in the Radiation Belt

The dynamics of relativistic electrons in the Earth's outer radiation belt is a delicate balance of transport, acceleration, and loss processes. In the following subsections, I will discuss the transport, acceleration, and loss mechanisms acting on outer radiation belt electrons.

2.4.1 Transport and the Fokker-Planck Equation

As introduced in Section 2.3, an essentially complete physical description of radiation belt electrons is provided by the phase space density (PSD) in terms of the three adiabatic invariants and time. Under certain circumstances, the adiabatic invariants can be violated, resulting in the transport of electrons in electron pitch angle, energy, and L^*. If the force field responsible for violating any of the adiabatic invariants exhibits sufficient spatial and temporal coherence and phase randomness, the

transport of electrons can be represented by diffusion of the phase-averaged electron PSD with respect to the violated invariants. The diffusion process is given by the Fokker-Planck equation

$$\frac{\partial f}{\partial t}+\sum_i \frac{\partial}{\partial J_i}\left[(\frac{dJ_i}{dt})_\nu f\right]=\sum_{ij}\frac{\partial}{\partial J_i}\left[D_{ij}\frac{\partial f}{\partial J_j}\right]-\frac{f}{\tau}+S \tag{2.3}$$

in which f is PSD, J_i (i=1,2,3) are the action integrals, or equivalently, the three adiabatic invariants, the subscript ν refers to frictional (non-stochastic) processes, D_{ij} is the tensorial diffusion coefficient, τ is the particle lifetime and S is the source rate. The second term on the left hand side of the above equation stands for the coherent terms, such as friction; the first term on the right hand side represents stochastic processes, which are referred to as diffusion; f/τ is the loss term and S is the source term [Schulz and Lanzerotti, 1974].

Due to the special properties of radiation belt electrons, high energies and low densities, the stochastic processes are the most important operative dynamics on these particles, which lead to the diffusion of particle distributions with respect to the adiabatic invariants as described above. Diffusion, in any coordinate, will act to smooth out gradients in that variable (see Figure 2.6 for illustration). The net 'current' G of particles diffusing across a position in one dimension is given by Fick's law: $G=-D\frac{\partial f}{\partial x}$. The main diffusive processes in the radiation belt include: radial diffusion (which only violates the third adiabatic invariant, L^*), pitch angle diffusion and energy diffusion (which violate μ or K, usually both, as well as L^*). These forms of diffusion are closely related to the acceleration and loss of radiation belt electrons. For example, radial diffusion transports charged particles inwards from an external source or rearranges particles injected by an internal source, which is accompanied by particle acceleration or deceleration; while pitch-angle diffusion moves particle mirror points along field lines, causing particle loss to an atmospheric sink. I will leave the discussion

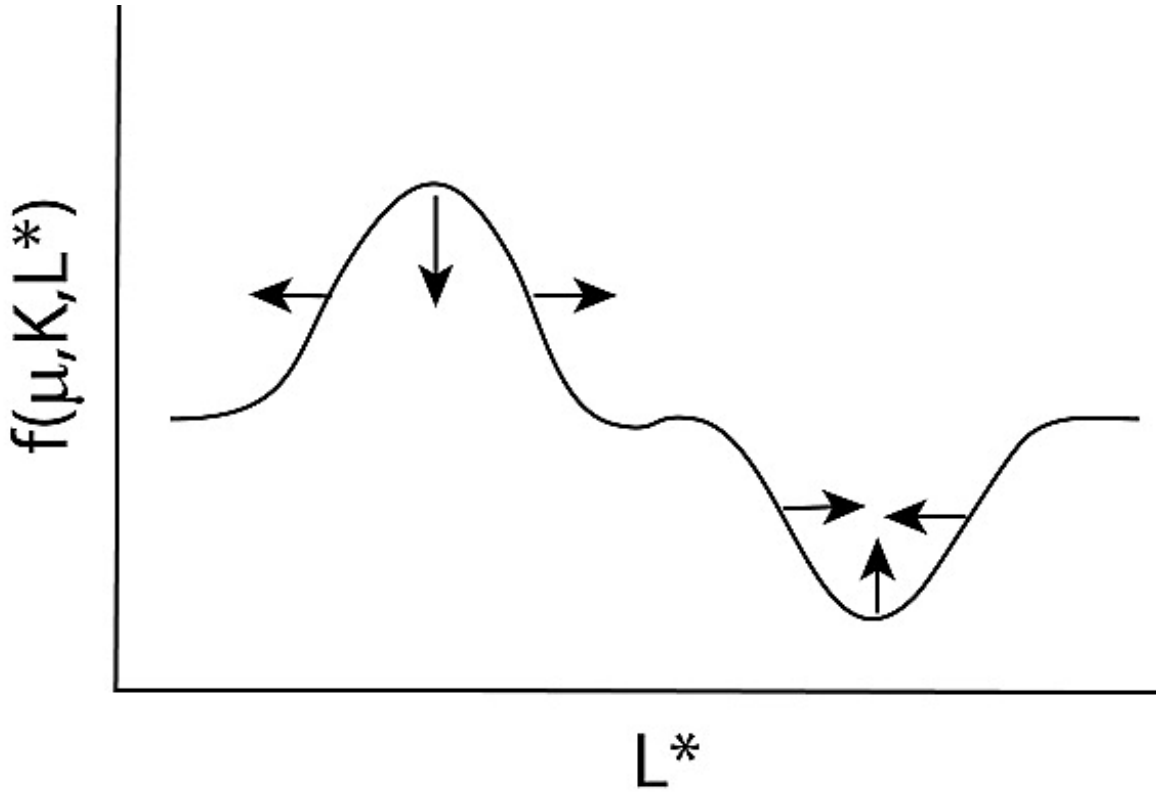

Figure 2.6: Schematic showing how radial diffusion smoothes out PSD gradient. (Reproduced from Green and Kivelson, 2004, Copyright 2004 American Geophysical Union.)

about the distinctive acceleration and loss mechanisms for radiation belt electrons to the following two subsections.

2.4.2 Acceleration Mechanisms

Outer radiation belt MeV electron fluxes vary greatly during geomagnetic storms and substorms. How such electrons are accelerated is not only interesting scientifically but also practically, since these killer electrons can cause damage to spacecraft electronics. There are several acceleration mechanisms that are responsible for the enhancement of outer radiation belt electrons.

Adiabatic energization. The adiabatic effect (or Dst effect) is simply an adiabatic reversible process in which all three adiabatic invariants are conserved. Strictly speaking, because the adiabatic effect does not involve a net energy gain or loss, it is not a real acceleration mechanism. But since very often a satellite observes particle intensity changes due to this effect, it is still necessary to introduce it here. In the following, I discuss the adiabatic effect for equatorially mirroring electrons. During the course of a magnetic storm, a ring current enhancement decreases the local magnetic field inside of the current, and to conserve the third adiabatic invariant, or the magnetic flux, a drift shell expands radially. Since the electrons move out to a lower magnetic field region, their energy drops to conserve μ. The steep negative slope of the particle energy spectrum as well as a possible outward pointing PSD gradient will cause a detector at a fixed energy range to observe a decrease in particle flux at its given position following the Dst dropout during storm main phase [Kim and Chan, 1997]. In other words, the spacecraft measures the flux of electrons previously at smaller radial distance and shifted to lower energy resulting in a flux decrease (see Figure 2.7 for illustration). On the other hand, during the subsequent decay of the ring current, the energetic electrons recover to their original distribution and get re-energized. The flux should be restored to what it was before the storm if the adiabatic effect is dominant (spacecraft observes the return of flux). But usually this is not the case, since other non-adiabatic acceleration and loss mechanisms may take effect simultaneously.

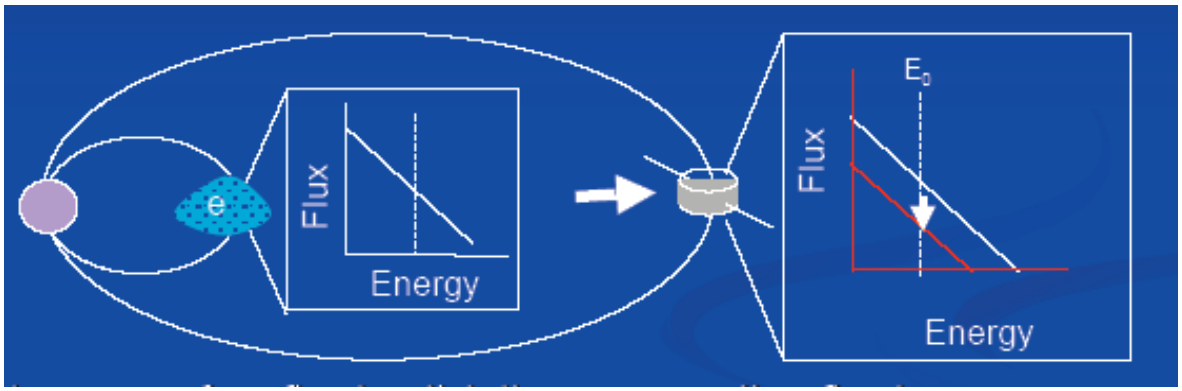

Figure 2.7: Schematic showing adiabatic effect for electrons on the equator (courtesy of Elkington, S.R.).

To conclude, the magnitude of the adiabatic flux variations due to the adiabatic effect depends on the steepness of the energy spectrum, radial gradients, the magnitude of the disturbance in the field, and the background magnetic field. Nevertheless, in order to reveal the true dynamics of outer radiation belt electrons during storms, the adiabatic effect has to be taken into account and removed. This could be done by using the calculated PSD instead of using the directly observed electron flux data.

Inward radial transport. Inward radial transport, conserving the first and second adiabatic invariants, μ and K, energizes electrons by bringing less-energetic electrons inward from larger L-shells. Since $\mu = p_{\perp}^2 / 2m_0 B$ is conserved, the enhancement of B strength as electrons are transported inward leads to the electron energization. The transport process can be enhanced in two ways, one is interplanetary shock-associated transport and acceleration, the other is inward radial diffusion.

When a strong interplanetary shock impacts the magnetosphere, an enhanced inductive electric field will be generated and drive the electrons inward. The whole energization process occurs on a time scale of less than the electron drift period. A dramatic example is the CRRES event of a shock injection during the March 24, 1991 storm. In this event an intense flux of electrons and protons with

energies of tens of MeV were formed at L~2.5 in 90 s [Vampola and Korth, 1992; Blake et al., 1992]. This event has been well modeled [Li et al., 1993; Hudson et al., 1995], but this type of event is comparatively rare.

One of the classic acceleration mechanisms for outer radiation belt electrons is inward radial diffusion [Fälthammar, 1965; Schultz and Lanzerotti, 1974; Brautigam and Albert, 2000; Li et al., 2001a; Barker et al., 2005], which is due to large-scale fluctuations in the magnetosphere's magnetic and electric fields with frequencies comparable to the electrons' drift frequencies (in mHz range) acting on a pre-existing outward positive radial gradient in the PSD. This so-called drift-resonant acceleration could occur in the particle interaction with Ultra-Low-Frequency (ULF) waves, whose frequencies are also in mHz range. The observed association of ULF waves with relativistic electron enhancement [Baker et al., 1998b, c; Rostoker et al., 1998] and the MHD/particle simulations by Hudson et al. [1999, 2000] led to the proposal of the role of ULF waves in relativistic electron enhancements. Elkington et al. [1999] quantitatively investigated the nature of such drift-resonant acceleration, by tracking particle trajectories in a simplified field model consisting of a compressed dipole and global, toroidal-mode Pc5 range (2-7 mHz [Kivelson and Russell, 1995]) ULF waves. They found that a particle with drift frequency ω_d will gain energy through drift-resonant interaction with toroidal-mode waves of frequency ω and global mode number m if satisfying the resonance condition:

$$\omega = (m \pm 1)\omega_d \tag{2.4}$$

To quantify the effect of radial diffusion, we need to solve the simplified version of the Fokker-Planck equation introduced in subsection 2.4.1, which ignores friction and with only diffusion in L^*:

$$\frac{\partial f}{\partial t} = L^2 \frac{\partial}{\partial L}\left(\frac{D_{LL}}{L^2}\frac{\partial f}{\partial L}\right) - \frac{f}{\tau} + S \tag{2.5}$$

A representation of the diffusion coefficient, D_{LL}, is required for solving the above equation. Theoretical analysis of the diffusion coefficient, started in the early years of the space era

[Fälthammar, 1965; Schulz and Lanzerotti, 1974], relates the diffusion rate to the power spectral density of the stochastic fluctuating field at the electrons' drift frequency and its harmonics. However, the difficulty of determining the global mode structure and spectra of ULF waves in the magnetosphere has guided researchers towards specifying an empirical form of the diffusion coefficient. For example, Li et al. [2001a] specified their diffusion coefficient as a function of solar wind parameters and Brautigam and Albert [2000] used the well-known empirical form of D_{LL} as a function of the Kp index, $D_{LL} = 10^{(0.506Kp-9.325)} L^{10}$.

Here I want to discuss more about the Li et al. [2001a] model, in which they predict MeV electrons at geosynchronous orbit based on solar wind measurements. Paulikas and Blake [1979] showed that there is a very good correlation between the solar wind velocity and the MeV electron flux at geosynchronous orbit. Baker et al. [1990] first tried using solar wind velocity to predict MeV electrons at geosynchronous orbit. Then Li et al. [2001a] further modeled the diffusion coefficient as directly linked to solar wind parameters, including: the solar wind velocity, the southward component of the interplanetary magnetic field, and solar wind velocity fluctuations.

In situ acceleration. Another important acceleration mechanism for energetic electrons in the radiation belt is in situ acceleration (or local heating, wave heating). Data have shown that PSD can peak as a function of radius inside geosynchronous orbit [Selesnick and Blake, 2000; Green and Kivelson, 2004; Iles et al., 2006; Chen et al., 2007]. Since some such peaks cannot be explained by radial diffusion, a greater emphasis has been placed on the in situ acceleration of electrons by wave-particle interactions, which violates the first adiabatic invariant [Horne and Thorne, 1998; Summers et al., 1998; Meredith et al., 2002; Horne et al., 2005a, b], as a mechanism responsible for the energization of outer radiation belt electrons.

Although wave-particle interactions are thought to be important in precipitating electrons from the radiation belts by pitch angle diffusion (invoked as a loss mechanism and will be discussed later),

they can also involve energy diffusion. It was originally suggested that the resonant interactions between the relativistic electrons and the chorus whistler waves outside the plasmasphere could lead to energy diffusion and heat radiation belt electrons [Temerin et al., 1994; Li et al., 1997]. In the kinetic theory of wave-particle interaction in relativistic plasma, the general cyclotron resonance condition is:

$$\omega - k_{\|} v_{\|} = n\Omega / \gamma \tag{2.6}$$

where ω is the wave frequency, k is the wave number, v is the electron velocity, parallel subscript means parallel to the magnetic field, Ω is the electron gyrofrequency, γ is the Lorentz relativistic factor and n is an integer. Horne and Thorne [1998] identified potential wave modes that are capable of resonating with electrons over the important energy range from 100 keV to a few MeV. Based on these concepts, Summers et al. [1998] calculated the resonant diffusion curves for electron cyclotron resonance with field-aligned electromagnetic waves and proved that significant electron energy diffusion can occur during resonant interactions with whistler mode waves and the potential for energization is most pronounced in regions of relatively low plasma density. The whistler wave related processes are based on the substorm injections of "seed" electrons (10-100 keV), which can be subsequently accelerated and also lead to a growth in whistler wave intensity.

In more recent work, Horne et al. [2007] suggested that, in addition to whistler mode chorus waves, another type of wave, known as fast magnetosonic waves, can also be very effective in accelerating electrons up to relativistic energies in the outer radiation belt. Acceleration occurs via electron Landau resonance (n=0 in Eq. 2.6). And since magnetosonic waves are generated by unstable proton ring current distributions, this acceleration process is an important mechanism for energy transfer from the ring current to the Van Allen radiation belts. Acceleration of the low energy component is most effective inside the high density plasmapause, but higher energies will be achieved outside. And a seed population of low energy electrons, such as injected by substorms, is still required for this wave heating to occur.

Difficulties in distinguishing the acceleration mechanisms. Now we are familiar with different types of acceleration mechanisms for the outer radiation belt. A fundamental question in radiation belt dynamics research is the relative contributions from these acceleration mechanisms in the enhancement of outer radiation belt electrons. In order to answer this question, we first need to distinguish between these different acceleration mechanisms.

Interplanetary shock induced acceleration is distinguishable from other acceleration mechanisms because of its fast time scale. However, it has been difficult to distinguish between radial diffusion and in situ acceleration. In both cases, there is a source of less-energetic electrons with substantially larger phase space density that can be energized and thus, less-energetic electrons at either larger L-shells or on the same L-shell are a feasible source of electrons. Since inward radial diffusion is driven by magnetic and electric field fluctuations on a time scale of the drift period of the radiation belt electrons and the observed field fluctuations almost always have more power at lower frequencies, less energetic electrons diffuse inward faster than more-energetic electrons [Schulz and Lanzerotti, 1974; Li et al., 2005; Turner and Li, 2008], leading to a longer delay for the enhancement of the more energetic electrons. However, this longer delay of the more-energetic electrons can also be explained by in-situ heating of electrons by VLF waves on the same L-shell, since it would also take a longer time to energize the local low electrons to larger energies on the same L-shell.

However, based on the introduction of these two mechanisms, radial diffusion and in situ acceleration, it seems that differentiating between them is just a simple task of identifying peaks in the PSD versus L. If the radial gradient of PSD is clearly positive, it suggests that inward radial diffusion could be operating. If the phase space density has a peak in its radial profile while the overall phase space density is increasing, this suggests that the peak is due to in situ acceleration (as illustrated by Figure 2.8). Some attempts have been made along this line of reasoning [Selesnick and Blake, 1997; Li et al., 1999; Selesnick and Blake, 2000; Brautigam and Albert, 2000; Hilmer et al., 2000; Green

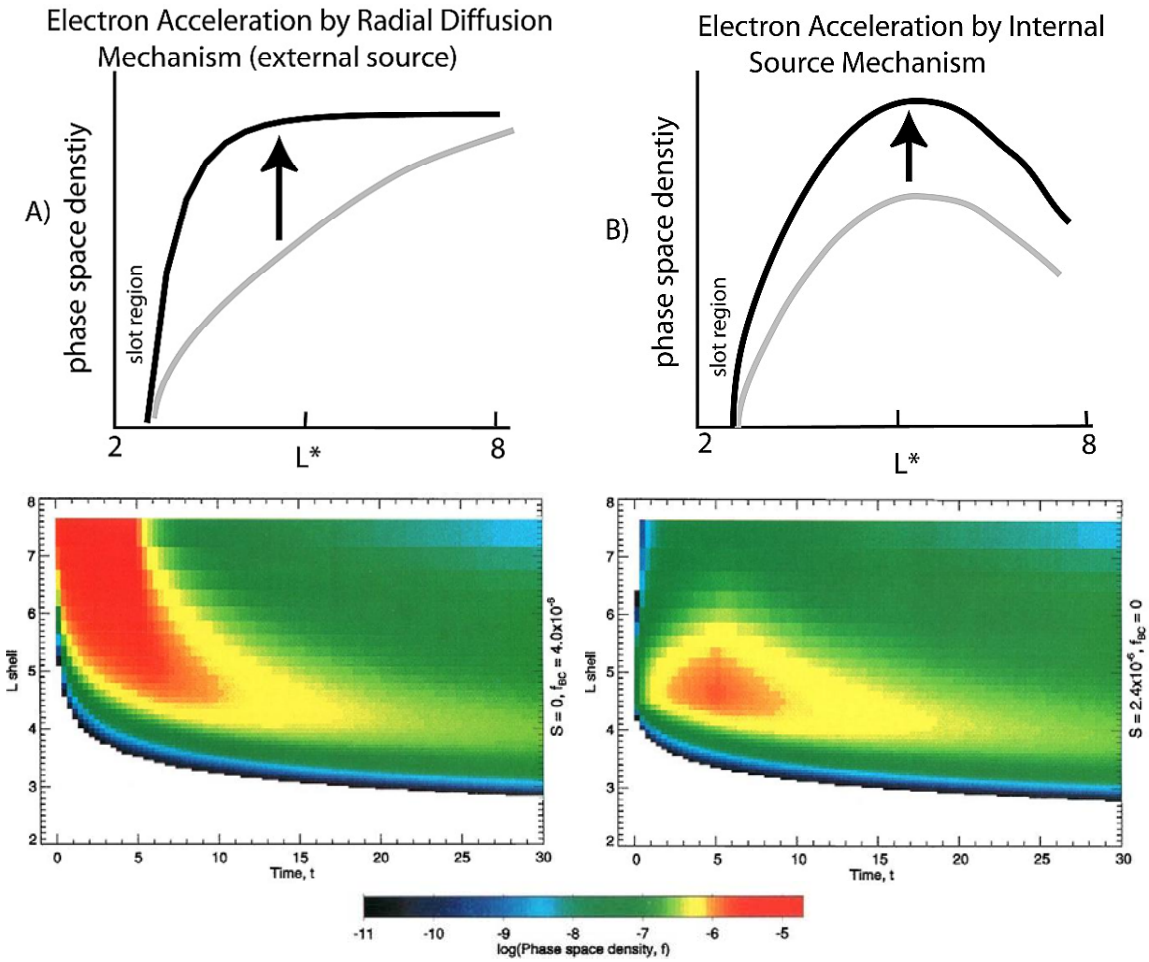

Figure 2.8: Schematic comparing the type of PSD increases produced by radial diffusion from an external source and by local acceleration of an internal electron source. Top panels: the shaded traces in both panels represent PSD at the start of an acceleration event. (left) A PSD increase caused by radial diffusion from an external source, with the black trace showing the PSD once equilibrium is achieved; (right) PSD increases predicted by local internal source acceleration mechanisms, with the black trace showing the PSD after the electron acceleration (Reproduced from Green and Kivelson, 2004, Copyright 2004 American Geophysical Union.). Bottom panels are simulated phase space densities based on the radial diffusion model: (left) a boundary condition source at L=9 and $0 < t < 5$ day; (right) an internal source S at $4.5 < L < 5$ and $0 < t < 5$ day (Reproduced from Selesnick and Blake, 2000, Copyright 2000 American Geophysical Union.).

and Kivelson, 2004; Taylor et al., 2004; Chen et al., 2006; Chen et al., 2007; Tu et al., 2009]. For example, Brautigam and Albert [2000] analyzed the enhancement of outer belt electrons measured by CRRES during one storm on October 9, 1990. They found that the electron PSD gradient was positive for lower μ (<1000MeV/G) and became negative for higher μ. Their radial diffusion model could reproduce the enhancement of the lower energy electrons but not the higher energy electrons. They did not have a heating term in their model, but they suggested that in situ heating should be responsible for the enhancement of higher energy electrons. Chen et al. [2007], based on two years of PSD data for μ ranging from 500 to 2000 MeV/G, found that electron PSD peaks near L =5-6 are common and suggested that in situ heating is likely the dominant acceleration mechanism for outer belt electrons.

Actually, to distinguish one electron acceleration mechanism from the other is not as simple as it seems, due to the lack of PSD data with appropriate temporal and spatial coverage, and the simultaneous occurrence of energization and loss. For example, a local peak of PSD does not always indicate internal acceleration. Acceleration by radial diffusion from an external source combined with a changing source population or faster loss at large L can also produce local PSD peaks (illustrated in Figure 2.9 as an example). Since the observed electron enhancement is the net result of a delicate balance among energization, transport, and loss, to quantitatively distinguish the relative contributions from different acceleration mechanisms, physical models are needed.

2.4.3 Loss Mechanisms

For the study of outer radiation belt dynamics, the understanding of electron loss processes is as important as that of the acceleration mechanisms.

Adiabatic loss. As we discussed in the previous section, observed decreases in the trapped flux with a build-up of the ring current can be caused by adiabatic effects.

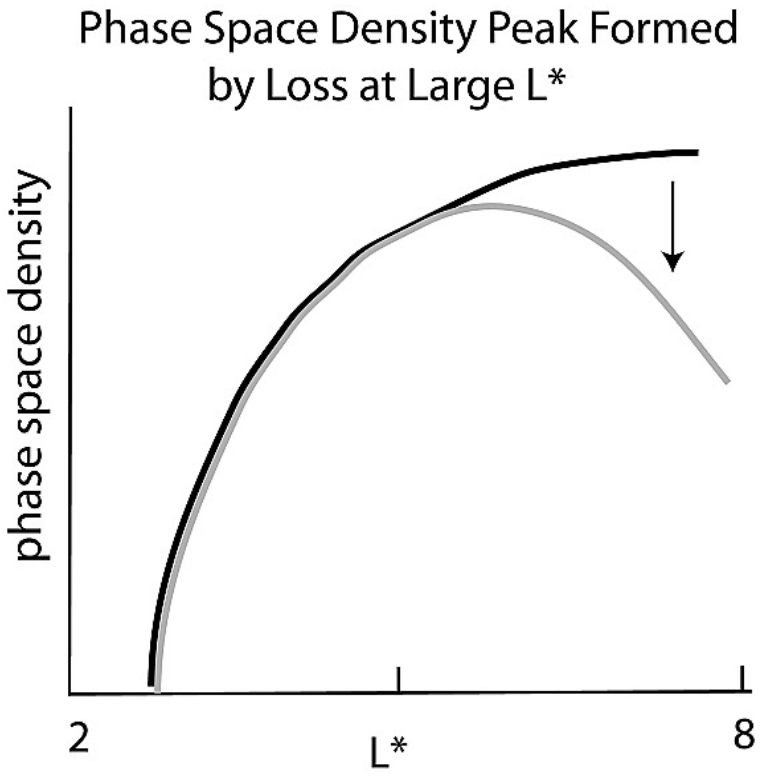

Figure 2.9: Schematic showing how losses at large L^* cause a peak in the phase space density versus L^* profile. (Reproduced from Green and Kivelson, 2004, Copyright 2004 American Geophysical Union.)

Magnetopause shadowing. Adiabatic motion can cause real (non-adiabatic) loss if electrons move out far enough to encounter the magnetopause. Kim and Chan [1997] studied the November 2-5, 1993 storm in detail and suggested that the observed flux decrease before the storm main phase was probably due to the non-adiabatic loss when the drift shell of the synchronous orbit electrons intersected the magnetopause. For electron loss due to magnetopause shadowing, the drift trajectories of electrons are open. However, if the PSD data as a function of (μ, K, L^*) exist with finite L^* value, it means the drift orbit for these electrons is closed. Therefore, for radial diffusion model given

by Eq. 2.5, an explicit loss term due to electron drift to the magnetopause is unnecessary if the PSD at the outer boundary is well defined [Tu et al., 2009].

Outward radial diffusion. Just as inward radial diffusion can lead to the energization of radiation belt electrons, outward radial diffusion can produce loss [e.g., Reeves et al., 1998; Shprits et al., 2006a; Loto'aniu et al., 2010]. The same mechanism works here. Since radial diffusion acts to reduce the radial gradient of PSD, a negative slope produced by, e.g., losses to the magnetopause or a decreased source in the plasma sheet can cause outward diffusion (see the diffusion around the right half of the first bump in Figure 2.6). Then the conservation of μ and the decreasing of magnetic field strength will decelerate the electrons. For a radial diffusion model represented by Eq. 2.5, adopting realistic variable outer boundary conditions will have the outer radial diffusion process automatically incorporated [Shprits et al., 2006a; Tu et al., 2008].

Precipitation to atmosphere. The most important and complicated non-adiabatic loss mechanism for outer radiation belt electrons is believed to be wave-particle interactions precipitating electrons into the upper atmosphere. As mentioned in the in situ acceleration part in subsection 2.4.2, wave-particle interactions can induce pitch angle diffusion which violates the first two adiabatic invariants. Resonant wave-particle interactions occur when the Doppler-shifted cyclotron resonance condition Eq. 2.6 is satisfied. Timescales associated with the wave loss can be specified by means of pitch angle diffusion coefficients, which is directly related to the power spectral density and spatial distribution of the resonant plasma waves. Several key waves are suggested to be capable of resonant interaction with radiation belt energetic electrons and inducing rapid pitch angle diffusion, including EMIC (electromagnetic ion cyclotron) [Summers and Thorne, 2003; Meredith et al., 2003a], chorus [O'Brien et al., 2004; Thorne et al., 2005; Shprits et al., 2007] and plasmaspheric hiss [Abel and Thorne, 1998; Meredith et al., 2006, 2007] waves, whose distribution with respect to the plasmasphere is shown schematically in Figure 2.10. Some of these waves have been introduced in

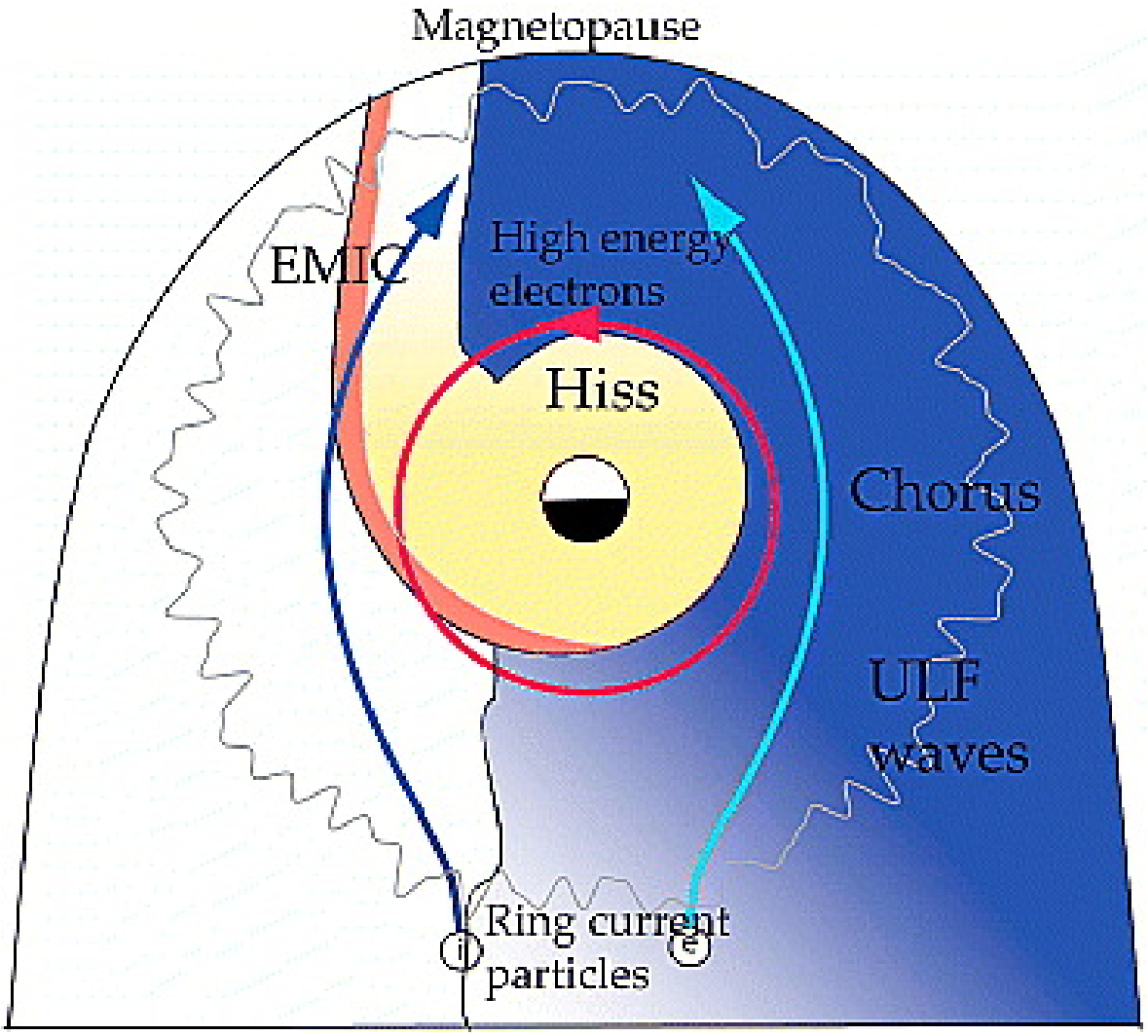

Figure 2.10: Schematic diagram showing the distribution of plasma waves capable of resonant interactions with relativistic electrons. Light and dark blue arrowed lines show the convective injection trajectories of ring current particles. Ring current electrons excite whistler mode chorus waves (blue). Whistler mode hiss waves (yellow) are confined to the plasmasphere. Interaction of ring current ions with high-density cold plasmasphere and regions of plumes excite EMIC waves (red). The wavy line denotes ULF waves. Red arrowed line shows the circular trajectory of the relativistic electrons in the radiation belt. (Reproduced from Shprits et al., 2006, Copyright 2006 American Geophysical Union.)

the in situ acceleration part as efficient for particle heating, but they are also active in wave induced precipitation.

Plasmaspheric hiss is a broadband ELF (100 Hz-few kHz) whistler-mode emission primarily confined to high density regions such as the plasmasphere and dayside drainage plumes [Hayakawa and Sazhin, 1992]. Generally, the hiss wave amplitude increases with magnetic activity [Meredith et al., 2004] and is more intense in the dawn to evening sector. The pitch angle diffusion by plasmaspheric hiss is believed to be a primary mechanism for the formation of the slot region [Lyons et al., 1972; Lyons and Thorne, 1973]. But the generation mechanism of plasmaspheric hiss is not fully understood yet.

Chorus consists of discrete whistler-mode emissions observed outside the plasmasphere in the frequency range ~100 Hz–5 kHz [Hayakawa and Sazhin, 1992]. It has been recognized as a source for wave heating by inducing energy diffusion in the previous section, but it will be discussed here as a loss mechanism by pitch angle diffusion. The chorus wave intensity peaks near dawn [Meredith et al., 2001, 2003a]. Due to the similarity in the local time distributions of chorus wave and microburst precipitation of 10–100 keV electrons, the microburst precipitation has long been associated with pitch-angle scattering by VLF chorus [Imhof et al., 1992; Lorentzen et al., 2001]. Chorus is considered to be generated by the electron-cyclotron instability [Kennel and Petschek, 1966] near the equator associated with freshly injected electrons from the plasma sheet. Its intensity increases during enhanced substorm activity [Meredith et al., 2001] and also during the recovery phase of storms.

Electromagnetic ion cyclotron (EMIC) waves propagate at frequencies below the proton gyrofrequency, the waves are thought to be driven by a ring current anisotropy associated with protons injected during storms and substorms [Jordanova et al., 2001a, b]. Theoretically, EMIC wave could only serve for pitch angle diffusion loss for relativistic electrons, and it is ineffective for stochastic acceleration [Summers et al., 1998]. It may cause rapid dropouts of relativistic electrons on

timescale of hours during storms [Meredith et al., 2003a; Albert, 2003] and may be preferentially generated near the plasmapause or the plasmaspheric plume region near dusk where the ring current overlaps the cold dense plasmasphere [Fraser et al., 2001]. Engebretson et al. [2007] noted that there is yet little ground-based evidence for the occurrence of EMIC waves during the storm main phase. Although this could perhaps be explained by the failure of EMIC waves to propagate from space to the ground, it remains controversial whether EMIC waves are the dominant loss process for the outer radiation belt electrons during magnetic storms.

Even though the wave populations described above have long been recognized as responsible for the non-adiabatic precipitation loss of outer radiation belt electrons, and the theoretical wave-particle interactions have been well studied, the electron precipitation processes and the associated loss rates are still not well-understood. This is because in reality we have a lack of wave observations and a clear picture of electron pitch angle distribution around the loss cone.

2.5 Outer Radiation Belt Models

One of the central questions in outer radiation belt studies is to distinguish among the relative contributions of different acceleration and loss mechanisms to the relativistic electron enhancement and decay in the outer radiation belt. However, since the observed electron variation is a delicate balance among energization, transport, and loss, without physical models we cannot quantitatively evaluate the relative contributions from different processes. In addition, models are complementary to data in that often data lack temporal and spatial coverage and are limited in distinguishing temporal and spatial variations. This section is a brief review of different types of models that are commonly used for studying the outer radiation belt dynamics.

The first type of model to simulate the variations of outer radiation belt electrons is the diffusion model solving for the evolution of phase-averaged PSD using Eq. 2.3. For fixed first and

second invariants, μ and K, and without friction, the Fokker-Planck Eq. 2.3 may be simplified as a one-dimensional radial diffusion equation as shown in Eq. 2.5 [e.g., Schulz and Lanzerotti, 1974; Tu et al., 2009]. Or for fixed L and electron energy, Eq. 2.3 can be written in the form of a pitch angle diffusion equation for electron PSD [e.g., Schulz and Lanzerotti, 1974; Shprits et al., 2006b]. Recently, a code solving the three-dimensional Fokker-Planck equation that includes radial diffusion, pitch angle diffusion, and energy diffusion was developed by Subbotin and Shprits [2009]. Based on that model, Subbotin et al. [2010] further included the mixed-diffusion terms which were ignored in the previous diffusion models, for the purpose of evaluating the importance of mixed diffusion in the Fokker-Planck diffusion equation for radiation belts simulations.

While the diffusion model solves for phase-averaged PSD of electrons, another type of model further resolves the phase-dependence of PSD, such as electron bounce phase and drift phase, which is called convection-diffusion model. For comparison with the drift loss cone electrons observed by SAMPEX, Selesnick et al. [2003] developed a drift-diffusion model that includes the effects of azimuthal drift as well as pitch angle diffusion into the atmosphere, with some results shown in Figure 2.11. Further comparison with the bounce loss cone electron data requires a model with a dependence on the bounce phase, which was developed by Selesnick [2004]. However, the drift speed in Selesnick et al. [2003] and Selesnick [2004] is approximated as in a dipole magnetic field. To include more realistic drifts of electrons in the radiation belt, Fok et al. [2008] developed a kinetic model that calculates the temporal evolution of PSD by solving a bounce-averaged Boltzmann transport equation, called the Radiation Belt Environment (RBE) model. The bounce-averaged drift velocities in RBE model are calculated kinetically under more realistic magnetic and electric field models. The RBE model is also coupled with a plasma sheet model, plasmasphere model, and wave-diffusion model.

Test-particle simulations, another useful approach for studying radiation belt dynamics, use the charged-particle equations of motion to directly track the particle trajectory under the model electric

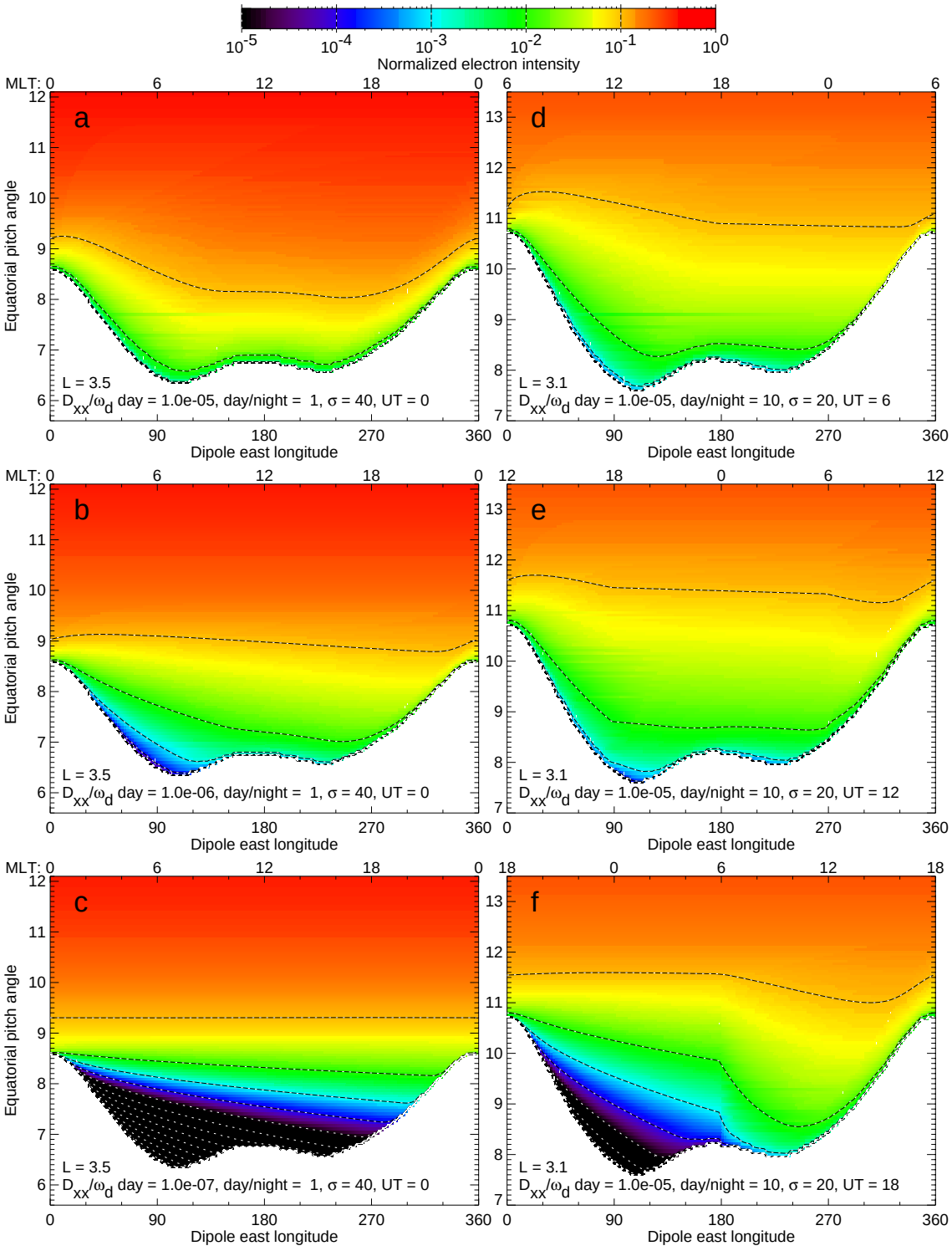

Figure 2.11: Color-coded solutions of the drift-diffusion model with selected values of the model parameters. They are normalized to electron intensity f=1 at 90 degree equatorial pitch angle. The lower boundary where f = 0 is the bounce loss cone angle. Contours are shown every decade in f. (Reproduced from Selesnick et al., 2003, Copyright 2003 American Geophysical Union.)

and magnetic fields. They are useful in simulating the formation of the outer electron belt. For example, assuming a relatively simple analytic field model, Li et al. [1993] performed guiding center simulations of the March 24, 1991 storm sudden commencement that was induced by an interplanetary shock. Their model results remarkably reproduced the rapid formation of a 'new' electron belt at L~2.5 observed by satellite. Test-particle simulations can also be used to elucidate specific physical processes which affect charged particles in the radiation belt. For example, Elkington et al. [1999] quantitatively investigated the nature of the drift-resonant acceleration, by tracking particle trajectories in a simplified field model consisting of a compressed dipole and global toroidal-mode Pc5 ULF waves. Elkington et al. [2003] used a similar approach but further included the poloidal-mode ULF waves in the field model to examine their effects on energetic electrons. Also for the study of the relativistic electron transport by ULF waves, a more realistic field model, the Lyon-Fedder-Mobarry (LFM) MHD model which took the actual solar wind measurements as input, was used in the test-particle simulations by Fei et al. [2006]. They compared the MHD/particle simulation results with a purely diffusion model to study the extent to which radial transport may be treated as a diffusive process.

Data-assimilative models have become increasingly popular in the modeling of radiation belts. They smoothly combine models and measurements to produce the optimal estimates of current and future states. The techniques of data assimilation have been widely used for other fields, e.g., spacecraft orbit determination, meteorology, and oceanography [see references in Kondrashov et al., 2007], and have only recently been applied to the study of radiation belts. The advantages of data-assimilative techniques include that they take both the uncertainties in data and model into consideration, and they can fill the spatial and temporal gaps in data. Koller et al. [2007] used data assimilation to blend incomplete PSD data from POLAR, three LANL Geosynchronous satellites, and one GPS satellite (shown in the top panel of Figure 2.12), with a simple radial diffusion model. Even though multiple satellites are involved, the data coverage in space and time is still incomplete.

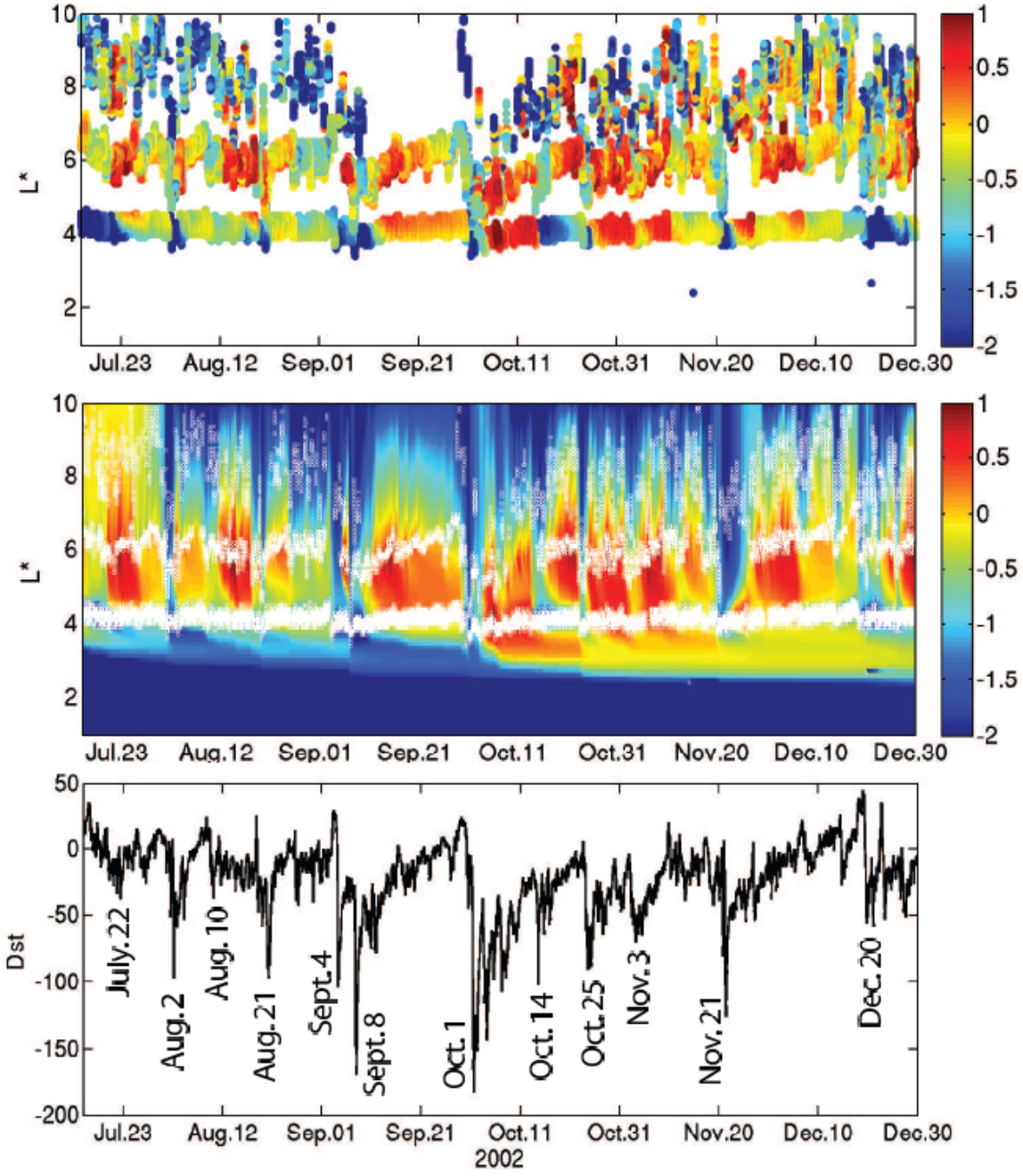

Figure 2.12: Observations (top), reanalysis results (middle), and Dst (bottom) from July 15 to December 30, 2002. (courtesy of Josef Koller)

The data assimilation results are shown in the middle panel of Figure 2.12, with white circles marking the locations of the data shown in the top panel. Based on the assimilation results, they were able to identify the regions in the radiation belts where simple radial diffusion is inadequate to capture the variations of the data, indicating missing physics in the model such as local acceleration and loss mechanisms. Data-assimilative models can not only be used to estimate the evolutions of electron PSD, but also be used to estimate the values of parameters included in the physical models for radiation belt dynamics, e.g., electron loss lifetime [Kondrashov et al., 2007] and electron local heating rate (code being developed by Quintin Schiller in LASP by private communication).

Chapter 3

An Empirical Fokker-Planck Model: Storm-Dependent Radiation Belt Electron Dynamics

This chapter is based on the paper titled *"Storm-dependent radiation belt electron dynamics"* by Tu, W., X. Li, Y. Chen, G. D. Reeves, and M. Temerin, published in *J. Geophys. Res.* in 2009.

3.1 Introduction

In subsection 2.4.2 of last chapter, I have discussed that the relative contribution from radial diffusion and local acceleration to the enhancement of relativistic electrons in the outer radiation belt has not been clear, due to the lack of PSD data with appropriate temporal and spatial coverage, and the simultaneous occurrence of energization and loss. Some recent modeling work has included both radial diffusion and local acceleration. For example, Varotsou et al. [2005] and Fok et al. [2008] simulated electron dynamics in the outer radiation belt by combining radial diffusion and wave acceleration due to whistler mode chorus waves. They concluded that in situ acceleration by whistler mode chorus followed by inward and outward radial diffusion can populate the entire outer radiation belt at high energies. However, uncertainties still exist in the quantification of the radial diffusion coefficient and the bounce-averaged pitch angle and energy diffusion coefficients.

For the first time, a well-calibrated electron PSD dataset at fixed first and second adiabatic invariants (μ and K) was published by Chen et al. [2006, 2007], using flux and field measurements from multiple satellites. Panel (a) in Figure 3.1 is an example showing the PSD as a function of L^* and time. By tracing the temporal evolution of the PSD radial distribution for the storm starting on Oct. 16th 2002, Chen et al. [2007] concluded that the radial peak in the PSD at geosynchronous orbit was caused by in situ acceleration. However, since the outer radiation belt dynamics are caused by a

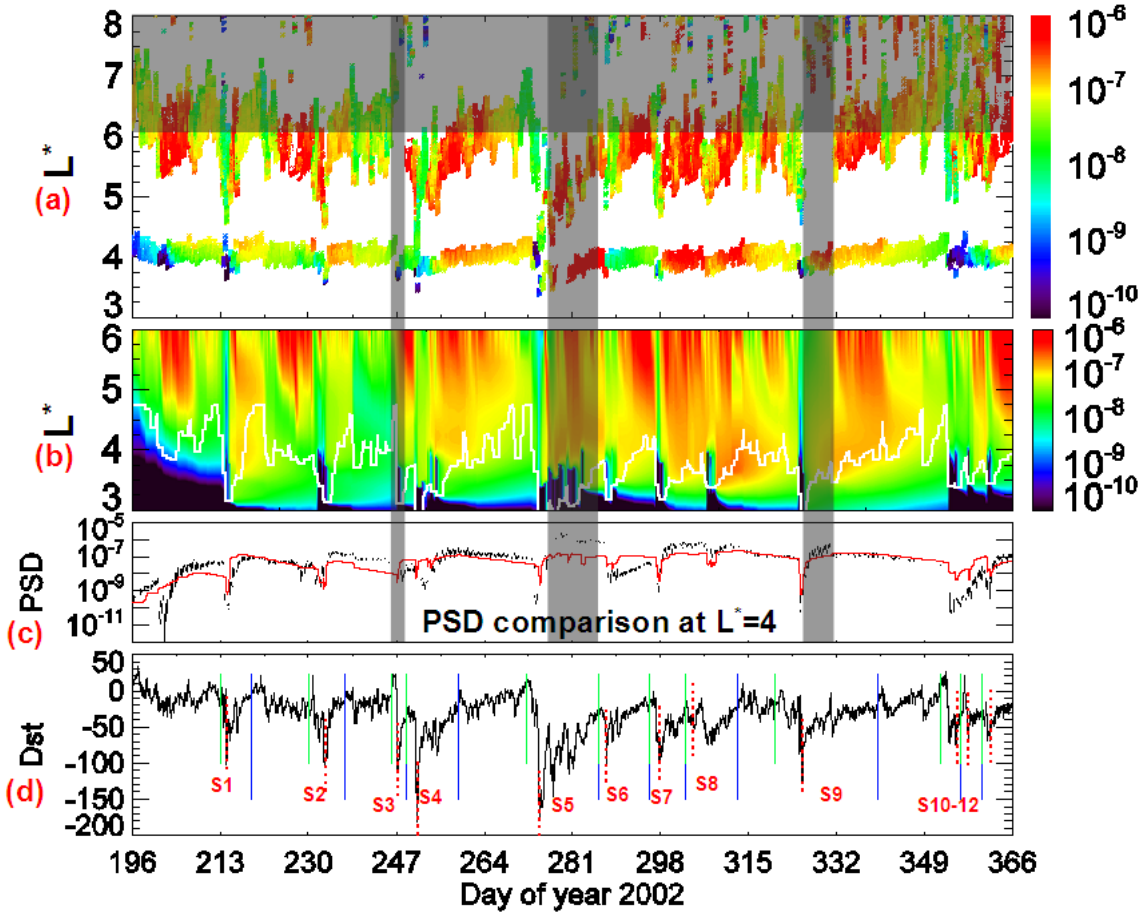

Figure 3.1: Panel (a) shows the PSD data for μ=2083 MeV/G and $K = 0.03G^{1/2}R_E$ from day 196 to 365 of 2002 (DOY). PSD is in units of $(\mathrm{c/MeV/cm})^3$. The data between L^*=6 and 8 are shaded for better comparison with panels (b) and (c). Gray areas correspond to data gaps in the PSD at L^*=6 (outer boundary of the model). Panel (b): model results with radial diffusion, internal heating and losses. The white curve shows the plasmapause location. Panel (c) shows the PSD comparison between data (black curve) and model results (from panel (b), red curve) at L^*=4±0.2. Panel (d): the Dst data with all 12 storms marked (green vertical line: the storm start; blue vertical line: the storm end; red dotted line: the turned-on time for internal heating).

combination of the simultaneous acceleration, transport and loss processes, to determine the relative contributions of radial diffusion, wave heating and loss to the formation and decay of electron radiation belt requires a model that incorporate all these factors and tests the relative importance and timing of these processes against data. This modeling work is performed here. In this chapter, we compare electron PSD data from Chen et al. [2007] with a Fokker-Planck model of radiation belt electrons that includes empirical radial diffusion, internal heating, and finite electron lifetimes, to study electron acceleration mechanisms and loss processes both on average and during individual storms.

3.2 Model Description

Our model uses the Fokker-Planck equation [Schulz and Lanzerotti, 1974]:

$$\frac{\partial f}{\partial t} = L^2 \frac{\partial}{\partial L}\left(\frac{D_{LL}}{L^2}\frac{\partial f}{\partial L}\right) - \frac{f}{\tau} + S \tag{3.1}$$

where L is L^* but we drop the (*) here and in the rest of the equations in this chapter, $f(L,t)$ is the gyro, bounce and drift phase-averaged PSD at fixed μ and K, D_{LL}, the radial diffusion coefficient, τ, the electron lifetime, and S, the heating rate. For given D_{LL}, τ and S, this equation can be solved numerically for $f(L,t)$ using, for example, the Crank-Nicolson method as is done here. In our model, we introduce simplified functional descriptions of acceleration, transport and loss with free parameters in those functions. Then we perform a least squares fit to these free parameters using the geosynchronous satellite data near L^*=6 as a boundary condition to optimize the fit of the GPS PSD data near L^*=4. Based on the comparison of the numerical magnitude of different terms and the quality of fit, we find which processes dominate during different events.

For the diffusion coefficient, in order to compare with other colleagues' work, we adopt the widely used empirical form [Shprits et al., 2005 and 2006; Kondrashov, et al., 2007**]:**

$D_{LL}(Kp) = 10^{(0.506Kp-9.325)} L^{10}$ (Kp is an index, measuring magnetic activity) from Brautigam and Albert's [2000] magnetic diffusion coefficient D_{LL}^{M}, since the magnetic diffusion coefficient is substantially larger than the electric diffusion coefficient. Their application of $D_{LL}(Kp)$ to model relatively low-energy electrons (E<1 MeV) agreed well with the data. However, for higher-energy electrons (E>1MeV), their model under-produced the PSD throughout the recovery phase, indicative of an internal source or possible errors in $D_{LL}(Kp)$. Since the diffusion coefficient is, in principle, related to the global mode structure and power spectral density of the stochastic fluctuating field at electron drift frequencies and harmonics [e.g., Fälthammar, 1965; Fei et al., 2006], which are difficult to determine, the form $D_{LL}(Kp)$ is only approximate. Until better information exists, the strength of radial diffusion is therefore adjusted by using a free parameter, A:

$$D_{LL} = A \times 10^{(0.506Kp-9.325)} L^{10} \quad (3.2)$$

where A and D_{LL} are in units of $(R_E)^2 day^{-1}$.

The electron lifetime, τ, varies with magnetic activity and location and also requires careful consideration. An explicit loss term due to electron drift to the magnetopause is unnecessary in our model since the PSD at L^*=6, our outer boundary, was well defined by the PSD data. The variation of Roederer L (L^*) with respect to the actual radial distance already incorporates or rather removes the Dst effect [Li et al., 1997; Kim and Chan, 1997] from the PSD data, allowing us to focus on non-adiabatic losses due to wave-particle interactions. Summers et al. [2007] derived the loss timescale for the radiation belt electrons due to the combined loss effect from chorus, plasmaspheric hiss, and EMIC waves. And for calculating the pitch angle diffusion coefficient, they made some detailed assumptions on the related wave and background plasma properties. However, this report is the first attempt to empirically parameterize the electron lifetime incorporating the expected loss effects from three different waves that interact with electrons in different regions of the

magnetosphere: outside the plasmasphere, inside the plasmasphere, and near the plasmapause. We calculate loss rates separately for these regions and the plasmapause is taken to be a dynamic boundary given by the empirical model of O'Brien and Moldwin [2003]:

$$L_{PP} = -1.57 \log_{10} \left| Dst^* \right| + 6.3 \tag{3.3}$$

where L_{PP} is the plasmapause location from the center of the Earth in earth radii and Dst^* is the minimum value of Dst during the previous 24 hours. Then the three regions are defined as: $L \geq L_{PP} + \Delta L_1$, outside the plasmasphere, $L_{PP} - \Delta L_1 < L < L_{PP} + \Delta L_1$, near the plasmapause and $L \leq L_{PP}$, inside the plasmasphere, where ΔL_1 provides a finite width of the effective region for the wave population acting close to the plasmapause.

Outside the plasmasphere ($L \geq L_{PP} + \Delta L_1$) we consider chorus waves. Shprits et al. [2007] has parameterized the loss timescale of radiation belt electrons due to chorus waves as a function of the geomagnetic index, AE:

$$\tau\_Chorus = 4.8 \times 10^4 B_w^{-2} L^{-1} E^2 \tag{3.4}$$

with

$$B_w^2 = 2 \times 10^{1.7 + 2.3 \times 10^{-3} AE^*} \, pT^2 \tag{3.5}$$

where τ_Chorus is the electron lifetime in days, B_w, the total wave amplitude in pT, E, the kinetic energy of the electrons in MeV, and AE^*, the maximum value of the AE index during the previous three hours. For electrons mirroring near the equator and for a given μ in MeV/G, energy, E, can be expressed as a function of dipole L, which is approximated as L^* in our model, and then the loss timescale is approximated as:

$$\tau\_Chorus = C \times 2.4 \times 10^{2.3 - 2.3 \times 10^{-3} AE^*} \times L^{-1} \times (\sqrt{0.512^2 + 0.307 \mu L^{-3}} - 0.512)^2 \text{ day} \tag{3.6}$$

C is introduced as a free parameter to adjust the lifetime outside the plasmasphere and compensate for the uncertainties in Eq. 3.4. For C=1, AE^*=900 nT, μ=2083 MeV/G (as in our case), $\tau\_Chorus \approx 1.1$ day at L^*=6 and ≈ 7.4 day at L^*=4.

Losses inside the plasmasphere are mainly caused by resonance with plasmaspheric hiss on timescales on the order of 10 days, and scale with geomagnetic activity [Abel and Thorne, 1998; Meredith et al., 2004]. Since there is no well-parameterized form of electron loss timescale due to plasmaspheric hiss and since the electron lifetime inside the plasmasphere is not critical for our current model because the PSD data we use are for electrons at $L^* \geq 4$, which stay mostly outside the plasmasphere, we set the electron lifetime, for simplicity, inside the plasmasphere uniformly as:

$$\tau\_hiss = 10 \text{ days.} \tag{3.7}$$

EMIC waves may cause rapid dropouts of relativistic electrons on a timescale of hours during storms [Meredith et al., 2003a; Albert, 2003] and may be preferentially generated near the plasmapause where the ring current overlaps the cold dense plasmasphere [Fraser et al., 2001]. Therefore we assume that the EMIC-active region is close to the plasmapause. Recently, Engebretson et al. [2008] noted that there is little ground-based evidence for the occurrence of EMIC waves during the storm main phase. Although this could perhaps be explained by the failure of EMIC waves to propagate from space to the ground, it remains controversial whether EMIC waves are the dominant loss process for the outer radiation belt electrons during magnetic storms. However, fast electron precipitation during the storm main phase is observed [Iles et al., 2002; Selesnick, 2006], indicating that some intense wave activity must be present to account for the strong pitch angle diffusion of electrons. This is consistent with the often observed sudden dropouts of PSD data at L^*=4 at specific times when Dst falls below a certain value (see the black curve in Figure 3.1c and the black sporadic data curve in Figure 3.2 panel A1). Since this work is not aiming to identify the role of specific loss mechanisms, we simply simulate the observed fast loss to the first order approximation with a free parameter. We also introduce the critical Dst parameter, $\mathrm{Dst}_{\mathrm{cri}}$, which effectively determines when significant losses take effect. This is an important

assumption in our model. Then, when Dst< Dst_{cri} , we parameterize the electron lifetime close to the plasmapause separately, scaling with the storm index, Dst:

$$\tau\_fastLoss = \tau_0/(\frac{Dst}{-50nT}) \tag{3.8}$$

where τ_0 is a free parameter to adjust for this fast loss during the storm main phase and to compensate for the uncertainty introduced by this simplified loss term.

Thus, the final form for the electron lifetime in our model is:

$$\begin{cases} L \geq L_{PP}: \ \tau = C \times 2.4 \times 10^{2.3-2.3\times10^{-3}AE^*} \times L^{-1} \times (\sqrt{0.512^2 + 0.307\mu L^{-3}} - 0.512)^2 \ \text{day} \\ L < L_{PP}: \ \tau = 10 \ \text{day} \end{cases} \tag{3.9}$$

when Dst<Dst_{cri}, $\tau = \tau_0 /(\frac{Dst}{-50nT})$ at L_{PP}-ΔL_1<$L < L_{PP} + \Delta L_1$

Now we specify the heating term. Meredith et al. [2002] suggested that electron acceleration occurs in the presence of enhanced chorus waves, mostly during storm recovery phases containing prolonged substorm activity. Since acceleration is most efficient just outside the plasmapause [Horne et al., 2005b], we add a heating term during the storm recovery phase (from four hours after the minimum of Dst until the end of a storm) just outside the plasmapause. (A storm is identified when Dst falls below -50 nT. After acquiring the local minimum Dst point, the storm interval for our modeling purposes is defined as: starting point: one day before the first zero Dst point before the local minimum Dst; end point: the recovery of Dst to zero. Dst dips more than three days apart during one storm interval are counted as separate storms, with the end of one storm defined as the next Dst peak, which is also the start of the next storm.) According to the model results of Shprits et al. [2007], chorus wave amplitudes can be parameterized as a function of AE^* as in Eq. 3.5, which can be used to specify our internal source term. But the parameterization for the chorus amplitudes in Eq. 3.5 is based on the wave observation of day-side chorus (06-15 MLT) at latitudes between 20 and 30 degrees, that was specifically constructed to estimate loss rates [Shprits et al., 2007], and

local heating is expected to be more efficiently excited by equatorial nightside chorus [Li et al., 2007]. However, Meredith et al. [2003c] suggested that the intensity of off-equator chorus waves in the pre-dawn sector is qualitatively comparable to that of near-equator chorus in the morning sector based on spacecraft measurements. Meredith et al. [2003c] also showed that relativistic electron flux enhancements were correlated with increased magnetic activity as monitored by the AE index. So far, the parameterization of the wave responsible for electron local heating is still uncertain due to inadequate wave observations with decent spatial and temporal coverage and resolution, and current unavailability of the parameterization for nightside chorus intensity. Because of this and the fact that our model simulated the gyro, bounce and drift phase-averaged PSD (the wave heating by chorus both on the dayside and nightside needs to be drift-phase (or MLT) averaged), we still define our source term as proportional to the wave amplitude in Eq. 3.5 and as a function of AE index:

$$S=\begin{cases} S_0 \times B_w^2 = S_0 \times 2 \times 10^{1.7+2.3\times10^{-3}\,AE^*} & (L_{PP}<L<L_{PP}+\Delta L_2) \\ 0 & \text{(other L regions)} \end{cases} \tag{3.10}$$

where S_0 is the scaling factor of the magnitude of the internal source, which is also used to compensate for the uncertainties in the source term, and ΔL_2 defines a finite region of local heating.

To summarize, the free parameters in our model are: A, the scaling factor for the diffusion rate; Dst_{cri}, the Dst based critical parameter; C, the chorus scaling factor; τ_0, the EMIC scaling factor; ΔL_1, the effective width for the EMIC wave region measured in Earth radii; S_0, the internal source rate scaling factor in $(c/MeV/cm)^3 day^{-1}$ since PSD is in $(c/MeV/cm)^3$ and ΔL_2, the width of internal heating region in Earth radii.

Using this model we simulate the PSD variation between L^*=2.5 and L^*=6. We compare the logarithm of the model results and the PSD data around L^*=4. The model performance is measured

by the prediction efficiency (PE) [Li et al., 2001a] and the linear correlation coefficient (LC) (alternatively, the covariance of the two vectors) over the defined interval. Specifically, PE is defined as: $\mathrm{PE} = 1 - \frac{\text{mean square residual}}{\text{variance of data}} = 1 - \frac{\sum_{i=1}^{n}(d_i - p_i)^2}{\sum_{i=1}^{n}(d_i - \bar{d})^2}$, where d_i and p_i are the data and model results, respectively, and $\bar{d}$ is the mean of all d_i (PE=0: model results are as good as the averaged data, $p_i = \bar{d}$; PE>0: the model is better than reproducing the average and PE=1: perfect modeling). Since we actually compare with the PSD data over $L^*=4 \pm 0.2$ (and assume they are at $L^*=4$) to include enough statistics without being too wide, our model results are also averaged over $L^*=4 \pm 0.2$.

One thing we would like to clarify is that our model approach is different from the wave study approach which uses energy and pitch angle diffusion to study the outer radiation belt dynamics [e.g., Shprits et al., 2007; Li et al., 2007]. First, these two approaches are complementary, both of which have to assume parameters. For example, to calculate the energy and pitch angle diffusion rates, the Li et al. [2007] work assumes the spectral distribution of the wave power, the ratio of plasma frequency to electron gyrofrequency (f_{pe} / f_{ce}), the distribution of wave normal angles, local time content etc, while our model has its assumed free parameters in the lumped source and loss terms. The difference is the wave study approach uses the full Fokker-Planck solution, but our model, based on a 1-D Fokker-Planck equation and parameter fitting, approximates the effects of energy and pitch angle diffusion without explicitly using these diffusion coefficients. An advantage, however, is that our model can estimate the effects of many simultaneous processes as shown below in the model results.

3.3 Model Results for Half a Year

Table 3.1: The optimum parameter values and corresponding prediction efficiency (PE) and linear correlation coefficient (LC) for the half-year run. Numbers in italic type indicate fixed parameters.

Half Year	**A**	Dst_{cri} **(nT)**	**C**	τ_0 **(day)**	ΔL_1 **(Re)**	τ_{hiss} **(day)**	$S_0 \times 10^{10}$	ΔL_2 **(Re)**	**PE**	**LC**
Values	0.668	-66.8	0.1089	0.0011	0.6087	***10***	0.242	2.7504	**0.477**	**0.693**

The model is run between L^*=2.5 and L^*=6, with μ=2083 MeV/G (corresponding to E~1.3 MeV at L^*=6 and 2.7 MeV at L^*=4) and $K = 0.03G^{1/2}R_E$ (equatorial pitch angle near 90 degree) from July 15, 2002 to Dec. 31, 2002. The PSD at the inner boundary is fixed at $f(L=2.5)=10^{-15}$ $(\text{c/MeV/cm})^3$ to denote the low flux in the slot region. The outer boundary is set to the PSD data averaged over 5.5 < L^* < 6.5 with a time resolution of 10 minutes (Here the PSD gradient over L^* is less steep than near L^*=4 based on the data in Figure 3.1a and so we can average over a wider L^*.). We interpolate across data gaps. For the initial condition we interpolate across L^* using the available PSD data at L^*=6 (from LANL satellites) and L^*=4 (from GPS satellites).

We first run the model for the second half of 2002. There are twelve storms during this period based on the storm definition in the previous section, which are marked in Figure 3.1d (Dst profile, green vertical line denotes the start of a storm; blue vertical line denotes the end). The heating turn-on time for each storm (four hours after the minimum Dst) is indicated by the vertical red dotted line. The heating lasts until the end of the storm. After adjusting all the parameters, the maximum PE for the long-term run is 0.477. The corresponding parameter values are shown in Table 3.1. The model results are illustrated in Figure 3.1b and the comparison between the model results and the PSD data at L^*=4 is depicted in Figure 3.1c. The vertical gray areas in Figure 3.1 are gaps in the PSD data at L^*=6 (the outer boundary of our model) where I interpolate to get the boundary values. The model results are not valid in and just following those regions. Worth

mentioning is that ΔL_2, the width of the local heating region, is 2.75 Re (see Table 3.1), indicating local heating is needed almost across the entire region from the plasmapause (illustrated by the white curve in Figure 3.1b) to the outer boundary (L^*=6). Overall, the model fairly well captures the general PSD variations, but with over-prediction and under-prediction at different times.

From Figure 3.1c it is clear that the model does not simulate correctly some of the PSD dropouts at L^*=4 (e.g., the PSD dropout in storm #5, around DOY 274). One possibility is that the Dst effect is not totally removed from the PSD data for such times. Although, the variation of L^* for the PSD data should have incorporated the Dst effect, possible errors from imperfect magnetic field models or poor assumptions of particle pitch angle distributions could still have created some Dst effect, especially near L^*=4 where the PSD has a steep gradient. Another possibility lies in an error in L_{PP} (Eq. 3.3), the plasmapause location from the center of the Earth. This dynamic boundary defines the three loss regions. However, our model uses the Roederer L coordinate and we take L_{PP} to be Roederer L. This approximation may lead to incorrect losses in our model and may degrade the model performance. The most important influence of L_{PP} is on the EMIC-loss region ($L_{PP} - \Delta L_1 < L < L_{PP} + \Delta L_1$), which creates the fast loss of electrons. Due to the possible errors of L_{PP}, the turn-on of fast EMIC loss near the plasmapause with the same value of ΔL_1 can locally lead to a poorer performance of our model. In individual storm studies we can compensate for the offset of the estimated L_{PP} since for each storm we can use a different ΔL_1 value.

The model sometimes also under-predicts the PSD at L^*=4. For example, during the recovery phases of storm #7 (around DOY 298), the modeled PSD is less than the PSD data with the internal heating turned on, which means the modeled internal source was not strong enough. The simulation can be improved by increasing S_0, the internal source scaling factor, during such storms. On the other hand, for example during the interval between storm #4 and storm #5, when there is no

internal heating, the model under-predicts the PSD at L^*=4 possibly because the model radial diffusion is not strong enough during that time. By increasing A, the diffusion rate scaling factor, the results can be improved. Thus, the same set of parameters couldn't be applied to all storms and the relative contribution of radial diffusion and internal heating seemed to vary from storm to storm.

3.4 Model Results for Individual Storms

Based on the above analysis of the long-term run, we realize that a simulation of individual storms would be interesting. Therefore we simulate individually four storms in the second half of 2002: S1, S2, S4 and S7. We choose these storms because they lasted long enough ($\geq$6 days) to include sufficient data; there are no large data gaps at the outer boundary; and the PSD is enhanced after the storm. First, in order to investigate the relative contribution from radial diffusion, internal heating, and loss, we model each storm without the heating term (S_0=0). Such a model shows the behavior of the electron population at L^*<6 from just radial diffusion and loss. Two such runs are done. For the first run, A, the diffusion scaling factor, is set to one in Eq. 3.2 and the other parameters are adjusted. For the second run, A is made adjustable. The results of these two runs indicate how well these storms can be simulated by only radial diffusion and losses. Then the heating term is included to investigate the significance of internal heating. Finally we reduce radial diffusion to zero (A=0) and simulate the storms with only an internal source plus loss.

For each run all adjustable parameters are determined by maximizing the PE. The optimum values are shown in Tables 3.2 to 3.5. The corresponding PEs and LCs are also shown together with S_{ave} (unit: $(\mathrm{c/MeV/cm})^3\mathrm{day}^{-1}$), the average heating rate outside the plasmapause over the heating period (between the red dotted line and blue solid line of corresponding storm in Figure 3.1d) since the internal source S varies as a function of AE^*. Comparing the parameters across all the runs, we find that the chorus loss scaling parameter, C, is sometimes 1000, indicating an

Table 3.2: The optimum parameter values and corresponding PE and LC for each run of storm #1. Numbers in italic type are nonadjustable parameters; underscored numbers indicate calculated values and the rest are free parameter values. (RD=radial diffusion with A=1; RD_{enh} =enhanced radial diffusion with A>1; SRC=internal source, with S_{ave} in unit: $(c/MeV/cm)^3 day^{-1}$)

Storm #1		A	Dst_{cri} (nT)	C	τ_0 (day)	ΔL_1 (Re)	τ_{hiss} *(day)*	$S_0 \times 10^{10}$	$S_{ave} \times 10^7$	ΔL_2 (Re)	PE	LC
R1	**RD+Loss**	***1.0***	-95.4	1000	0.0113	1.0698	***10***	*0*	\	\	**0.025**	**0.364**
R2	RD_{enh} **+Loss**	8.933	-46.4	0.0498	0.0049	0.5922	***10***	*0*	\	\	**0.856**	**0.960**
R3	RD_{enh} **+SRC+Loss**	10.583	-46.4	0.1456	0.0048	0.9549	***10***	1.789	**3.418**	0.4612	**0.948**	**0.974**
R4	**SRC +Loss**	***0***	-48.9	1000	0.0115	0.6679	***10***	1.078	**2.060**	0.6717	**0.910**	**0.958**

essentially infinite lifetime, which implies no loss from chorus. Now we discuss the model results for storm #1 and #2 in detail.

First, we run our model for storm #1 without internal heating ($S_0 = 0$). The best modeled PSD at L^*=4 for A=1 (the red dotted line in Figure 3.2 panel A1) has a PE of only 0.025. A comparison with the PSD data at L^*=4 (the sporadic black curve) shows that radial diffusion with A=1 is not strong enough to explain the enhanced PSD, especially during the storm recovery phase. Increasing radial diffusion (i.e., increasing A) gives the results shown as the blue solid line in Figure 3.2 panel A1, better reproducing the PSD data (PE=0.856). The losses for this run are larger than the "A=1" run as indicated by the smaller C and τ_0 values in the second row of Table 3.2. Increasing "A" greatly improves the simulation, indicating that a sufficient source existed at the outer boundary and that the dynamics of electrons in the inner magnetosphere (L^*=4) could be explained from variations at the outer boundary (L^*=6) propagating inward through radial diffusion. Thus radial diffusion could be the main acceleration mechanism for this storm. This is also consistent with the radial gradient of the PSD at $L^* \approx 4$, indicated by the '$\vee$' shape of the PSD data (zoomed-in region in Figure 3.2 panel B1) inferred from the passage of GPS satellites near their minimum L^*. Since the PSD data are actually covering $L^* = 4 \pm 0.2$, considering the schematic geometry shown in Figure 3.3, the '$\vee$' shape implies that the PSD increases with L^*, in agreement

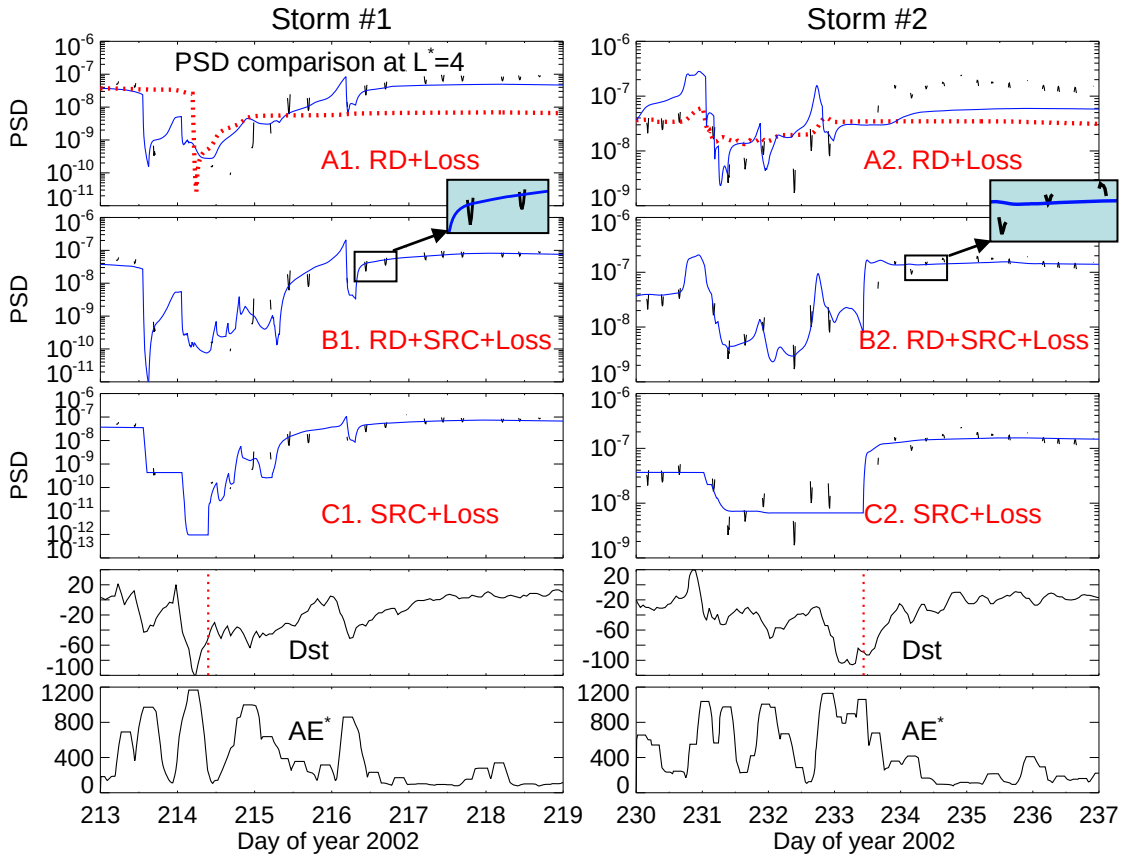

Figure 3.2: Comparison between PSD data and model results at $L^*=4\pm0.2$ for two storms: S1 from DOY 213/2002 to DOY 219/2002 in the left panels, and S2 from DOY 230/2002 to DOY 237/2002 in the right panels. In the top six panels, black curves are PSD data, solid blue and dotted red curves are model results, including: RD(A=1)+Loss (red curves in panels A1 and A2), RD_{enh} (A>1)+Loss (blue curves in panels A1 and A2), RD_{enh} +Source+Loss (panels B1 and B2), Source only+Loss (panels C1 and C2). Bottom two panels are the Dst and AE^* time profiles. The '$\vee$' and '$\wedge$' marks (explicit in squared zoom-in regions in panels B1 and B2) indicate the radial gradient of the PSD ('$\vee$': positive gradient; '$\wedge$': negative gradient).

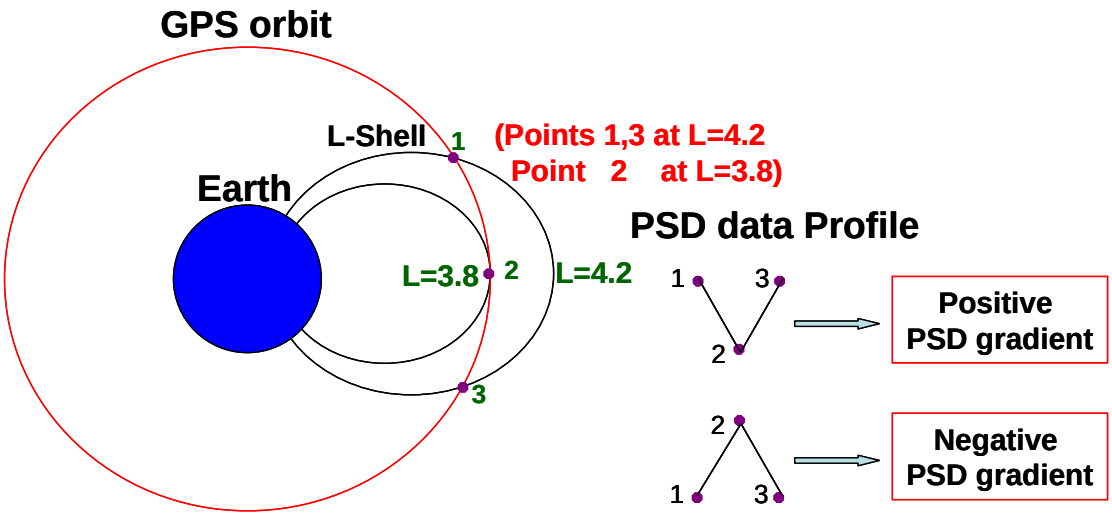

Figure 3.3: The correspondence between the shape of the PSD data at $L^{*}\approx4$ and the local PSD gradient. '∨': positive gradient; '∧': negative gradient.

with the positive PSD gradient required for inward radial diffusion to be effective in increasing the PSD.

Although this case could be well simulated by only enhanced radial diffusion and losses, we cannot exclude the possibility of significant local heating inside L^*=6 partly compensated by larger losses, since the positive PSD gradient at L^*=4 could also be explained by a local peak in the PSD at larger L^* but inside L^*=6, given that peaks in the PSD in the region 5< L^*<6 are common [Chen et al., 2007]. Therefore, we include an internal source (the turn-on time of the source is indicated by the red vertical line in the Dst profile of Storm #1, 4 hr after minimum Dst) and readjust the radial diffusion and losses to obtain the best PE. The results are shown as the blue line in Figure 3.2 panel B1 with a PE=0.948. A comparison of "RD_{enh}+Loss" and "RD_{enh}+Source+Loss" runs of this storm based on Row 2 and Row 3 of Table 3.2 shows that the other loss parameters are almost comparable except that the fast EMIC loss region is wider in the "RD_{enh}+Source+Loss" run. Larger losses then require increased radial diffusion (A $\approx$8.9 in Row 2 to A $\approx$10.6 in Row 3) to best simulate the PSD variations even though internal heating is included. Internal heating seems to help only a little in reproducing the PSD enhancement for this case given the enhanced radial diffusion.

It is also interesting to investigate how well the PSD can be simulated using only internal heating and losses. Figure 3.2 panel C1 (PE=0.910) shows the best result with A=0 (no radial diffusion). Though one might have expected this run, "Source+Loss", to have a larger internal source than "RD_{enh}+Source+Loss", according to the last row in Table 3.2 it has both smaller internal sources and losses (C and τ_0 are bigger than those in row 3). One explanation is that strong radial diffusion removes electrons from a heating region close to L^*=4, thus requiring a stronger source. Also worth mentioning is the parameter C. For the first run PE is larger when C is larger

Table 3.3: The same as Table 3.2 but for storm #2.

Storm #2		A	Dst_{cri} (nT)	C	τ_0 (day)	ΔL_1 (Re)	τ_{hiss} (day)	$S_0 \times 10^{10}$	$S_{ave} \times 10^7$	ΔL_2 (Re)	PE	LC
R1	RD+Loss	*1.0*	-33.9	1000	0.0503	0.4597	*10*	*0*	\	\	0.172	0.757
R2	RD_{enh}+Loss	23.218	-45.3	1000	0.0063	0.5664	*10*	*0*	\	\	0.430	0.688
R3	RD_{enh}+SRC+Loss	11.910	-42.9	0.0437	0.0417	0.6631	*10*	1.563	1.420	2.35	0.945	0.972
R4	SRC +Loss	*0*	-41.1	1000	0.0886	0.4579	*10*	0.549	0.499	1.05	0.906	0.952

(that's why we set C=1000 or effectively infinite), and even better with C negative. This indicates that there is probably some in-situ heating farther outside the plasmapause for this case. In the last run (Row 4 in Table 3.2), PE is very insensitive to C, staying at 0.910 for C between10 and 10000. Since this storm can be well reproduced either by "RD_{enh}+Loss", "RD_{enh}+Source+Loss" or "Source +Loss", we cannot conclude which mechanism is dominant. Although either enhanced radial diffusion (with A>1) or internal heating can account for the PSD at L^*=4, the results are better when both mechanisms work together.

The second example is storm #2. Again, in Figure 3.2 panel A2 the dotted red line is the model results at L^*=4 without any in situ source and A=1. The sporadic black line shows the PSD data. Even with a significantly larger radial diffusion (A =23.218) (the blue line in Figure 3.2 panel A2) the model still under-predicts the PSD data during the storm recovery phase (PE=0.430, Table 3.3), indicating that there is not a sufficient source at the outer boundary and thus an internal source is required. With the source turned on at the time of the red vertical line in the Dst profile, and with a different set of parameters (Row 3 in Table 3.3), the results fit the PSD data at L^*=4 well as shown by the blue line in Figure 3.2 panel B2. For this run PE increases as ΔL_2, the width of internal heating, becomes wider and only stops increasing when ΔL_2 reaches 2.35 (probably the outer boundary), indicating that a wide internal source is needed for this storm. During this storm's recovery phase the PSD profile had '∧' shapes, implying a PSD peak inside L^*=4. One can even see a change of the wedge-shapes from '∨' to '∧' (zoomed-in region in Figure 3.2 panel B2)

Table 3.4. The same as Table 3.2 but for storm #4.

Storm #4		A	Dst_{cri} (nT)	C	τ_0 (day)	ΔL_1 (Re)	τ_{hiss} *(day)*	$S_0 \times 10^{10}$	$S_{ave} \times 10^7$	ΔL_2 (Re)	PE	LC
R1	RD+Loss	*1.0*	-90.2	1000	0.0648	1.3358	*10*	*0*	\	\	**0.500**	**0.867**
R2	RD_{enh}+Loss	3.275	-127.4	1000	0.1527	2.7200	*10*	*0*	\	\	**0.780**	**0.885**
R3	RD_{enh}+SRC+Loss	0.143	-93.7	0.3925	0.7131	2.6002	*10*	1.702	**4.713**	0.3609	**0.904**	**0.951**
R4	SRC +Loss	*0*	-148.1	1000	0.4580	1.4100	*10*	1.056	**2.924**	0.4232	**0.851**	**0.923**

Table 3.5. The same as Table 3.2 but for storm #7.

Storm #7		A	Dst_{cri} (nT)	C	τ_0 (day)	ΔL_1 (Re)	τ_{hiss} *(day)*	$S_0 \times 10^{10}$	$S_{ave} \times 10^7$	ΔL_2 (Re)	PE	LC
R1	RD+Loss	*1.0*	No Loss					*0*	\	\	**0.242**	**0.712**
R2	RD_{enh}+Loss	7.594	-66.0	1000	0.0008	0.6604	*10*	*0*	\	\	**0.876**	**0.941**
R3	RD_{enh}+SRC+Loss	7.614	-69.9	0.0258	0.0013	0.8104	*10*	2.265	**5.936**	2.0154	**0.930**	**0.966**
R4	SRC +Loss	*0*	-61.7	1000	0.2364	0.7533	*10*	0.863	**2.262**	0.8459	**0.881**	**0.939**

indicating a temporal evolution of the direction of PSD radial gradient from positive to negative during the storm (see Figure 3.3 for illustration).

Results of internal heating only plus losses are shown in Figure 3.2 panel C2 (PE=0.906). Again without radial diffusion a smaller rather than a larger internal source with smaller losses gives the optimum results. Again, a wide internal source is needed for this run. PE increases as ΔL_2 increases until ΔL_2 reached 1.05. There is a simple explanation for this based on the consideration that without radial diffusion different L shells act independently. Similar to 'RD+Loss' case of Storm #1, PE is larger for larger C, and is even better for negative C, meaning that some internal heating extended well outside the plasmapause. For the "RD_{enh}+Source+Loss" and "Source +Loss" cases, PE is insensitive to the value of C.

The parameter values and results for storm S4 and S7 are shown in Table 3.4 and 3.5 and Figure 3.4. Both these two storms can be well reproduced by enhanced radial diffusion only plus some losses (the blue curves in Figure 3.4 panels A1 and A2 with PE=0.780 and 0.876 respectively),

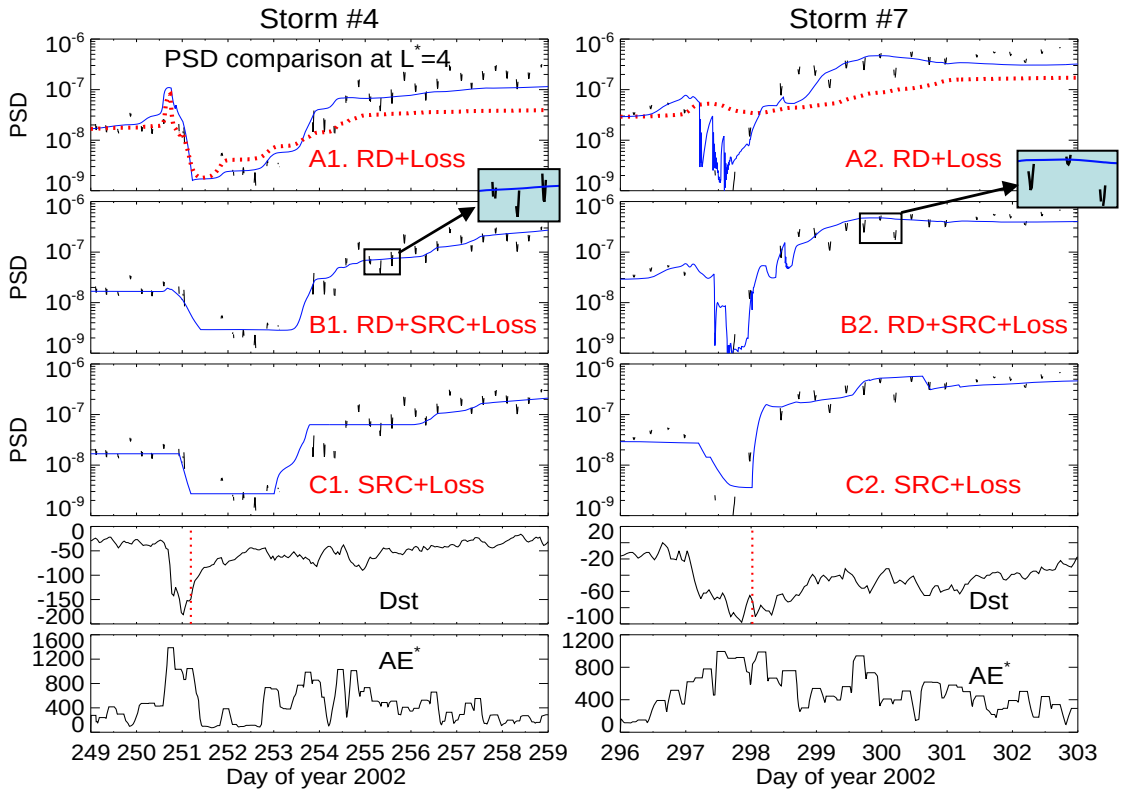

Figure 3.4: Comparison between PSD data and model results at L^*=4±0.2 for the other two storms: S4 and S7. The configuration is the same with Figure 3.2.

which agree with the successive '$\vee$' shapes shown in the PSD profile during the time when PSD is increasing (zoomed-in boxes in Figure 3.4 panels B1 and B2). With internal sources, both cases are better simulated. For S4 radial diffusion decreases (A from 3.275 to 0.143 in Table 3.4) but for S7 it increases because of faster losses (comparing Row 2 and Row 3 of Table 3.5) in order to obtain the highest PE. Since S4 is a big storm with a sharp narrow Dst dip (minimum Dst reached ~-190 nT), its optimum Dst_{cri} value is smaller than that for the other storm; the L_{PP} value is smaller; and the width of fast EMIC loss region is bigger (see Table 3.4). Also the "Source+Loss" runs could reproduce the PSD variations in these two storms. Again, both cases are best simulated with both radial diffusion and internal heating acting together ("RD_{enh} +Source+Loss"). However, a comparison of A, the diffusion rate scaling factor, and S_{ave}, the average heating rate, (Row 3 in Tables 3.4 and 3.5) shows that the relative contribution from the two acceleration mechanisms is very different. Although the loss parameters differ, with a comparable average internal source S7 requires much stronger radial diffusion than S4.

In summary, of the four storms, three could be well reproduced either by acceleration from radial diffusion or from internal heating only, though the best results are achieved using both. The other storm clearly requires additional local heating to account for the enhancement of the PSD. Different storms require different relative magnitudes of radial diffusion and internal heating. Therefore, one conclusion is that the relative contributions of radial diffusion and internal heating responsible for the enhancement of radiation belt electrons vary from storm to storm.

3.5 Discussion

In individual storm studies we have simulated each storm using four different runs. In one storm (storm #2) the source term is definitely dominant but in the other three storms both "RD_{enh} +Loss" and "Source+Loss" give fairly reasonable results, although the PE for

"Source+Loss" is bigger than the PE from "RD_{enh}+Loss" for all four storms. That means that both "RD_{enh}+Loss" and "Source+Loss" can account for the increase in the electrons. Thus, the study of outer radiation belt dynamics only based on PSD data interpretation is accompanied with some uncertainties, which further proves the benefit of modeling efforts. And as I discussed, the most physical case is when both radial diffusion and internal heating are acting together, or the "RD_{enh}+Source+Loss" run. But how to decide which acceleration mechanism contributes more? For this we need to compare the "RD_{enh}+Source+Loss" run with the other two runs, "Source+Loss" and "RD_{enh}+Loss". The results (Tables 3.2-3.5) show that from the run "Source+Loss" to the run "RD_{enh}+Source+Loss", the source term increases; while from the run "RD_{enh}+Loss" to the run "RD_{enh}+Source+Loss", the radial diffusion term generally decreases or stays the same (except for storm #1 and that's only a small increase in A). If we consider the value of source in the "Source+Loss" run as the necessary amount of source to reproduce the electron enhancement and the radial diffusion strength in the "RD_{enh}+Loss" run as the necessary strength of radial diffusion, the results mean that in the "RD_{enh}+Source+Loss" run there is even more source than necessary to account for the increase in the electrons while there is often less radial diffusion than necessary to account for the electron enhancement. Based on these, we conclude that internal source term contributes more.

Comparing results from all four storms, we find that radial diffusion with A=1 is never enough to reproduce the PSD enhancement during the storm recovery phase. The A values in "RD_{enh}+Loss" runs are 8.9, 23.2, 3.3, and 7.6 for four storms and in the "RD_{enh}+Source+Loss" runs ≈ 10.6, 11.9, 0.143, and 7.6, that is, averaging around 10, substantially larger than one would have expected from the results of Brautigam and Albert [2000]. This is interesting, since if

$D_{LL}(Kp)$ with A=1 worked well in Brautigam and Albert's model for lower energy electrons, for higher-energy electrons the diffusion coefficient should be even smaller (A<1) since electrons with higher energies have higher drift frequencies and resonate with ULF waves at higher frequencies which have less power. So how to reconcile the large values of the radial diffusion coefficients? Radial diffusion makes a connection between the boundary conditions at L^*=6 and the PSD at L^*=4. But there is more than one way to make this connection other than radial diffusion at constant first and second adiabatic invariants. We know that low and high energy electrons at L^*=6 are well correlated (with high energy electrons delayed with respect to the low energy [Li et al., 2005; Turner and Li, 2008]), and the lower energy electrons at L^*=6 can be transported to L^*=4 faster, either by direct convection or by faster diffusion. Such lower energy electrons at L^*=4 can act as source for local heating. Putting these points together gives us a model for the connection of higher energy electrons between L^*=6 and L^*=4 that mimics radial diffusion but is much faster. (Of course assuming that the real radial diffusion is smaller makes the source term even more dominant.) This gives a possible explanation for the large values of radial diffusion coefficient.

Now we discuss the parameter sensitivity of our model. We vary each of the loss-term tunable parameters (Dst_{cri}, C, τ_0, ΔL_1 and τ_{quiet}) by $\pm 20\%$ for 'RD_{enh}+Loss' run of storm #1. The PEs changes within ± 0.01 with respect to changes of all the loss-related parameters except for ΔL_1 (PE decreases to 0.67 when ΔL_1 changes to 0.8) and Dst_{cri} (PE=0.68 when Dst_{cri}=-38.0). ΔL_1 is a sensitive parameter since it defines the finite region of EMIC-wave loss whose time scale is much shorter than of the other losses (See Table 3.2). The model is also sensitive to Dst_{cri} because it is critical to turning on the fast storm-time losses. For the same run, we also check the sensitivity of our model to the electron lifetime due to plasmaspheric hiss, τ_{hiss}, which is assumed to be 10 days. PE is very insensitive to τ_{hiss}, which varies within ± 0.03 when

τ_1 changes from 1 day to 100 days, ensuring the validity of our assumption. This is because the plasmapause is mostly inside L^*=4 during storms, where the PE is calculated. To consider the effect of the delay time (four hours) to turn on the internal source after the Dst minimum, we select the 'RD_{enh}+Source+Loss' run for storm #1. The PE varies within ± 0.001 as the delay time varies from 0 to 6 hr with the highest PE for four hours.

Next we discuss the possible sources of error involved in our modeling efforts. The first is from our database: the PSD data from Chen et al. [2007]. Possible error sources in the PSD calculation, such as the imperfect magnetic field model and poor assumption of particle pitch angle distribution, can lead to some uncertainties in our conclusions. Chen et al. [2007] chose the T01s model for PSD calculations because its statistical performance is best during the storm times and they took efforts to construct instrument inter-calibration to constrain all these errors.

Another error source is in the auxiliary empirical models and in our simplified assumptions. First, there are errors associated with the empirical form of the diffusion coefficient from Brautigam and Albert [2000], which was derived from fitting only two D_{LL} values at each Kp value. Second, uncertainties also lie in the estimated plasmapause location from O'Brien and Moldwin [2003]. Third, we simplify the electrons losses by dividing them into three regions, because there are likely three different wave populations that interact with electrons depending on the region. It is assumed that chorus waves are most effective outside the plasmasphere, EMIC waves dominant close to the plasmapause and plasmaspheric hiss inside the plasmasphere. The parameterized electron lifetime due to chorus wave from Shprits et al. [2007] may have inaccuracies. Since the properties of EMIC waves are not yet well-known, the empirical electron lifetime (Eq. 3.8) from EMIC waves or whatever waves leading to loss of electrons near the plasmapause may also be unrealistic. The form of plasmaspheric hiss loss is over-simplified in the model, even though it doesn't play a significant role in our model performance because of its relatively slow loss rate. Finally, the internal source

term in our model is accompanied with uncertainties. It is assumed time and region limited in the model, while it can also happen sporadically during the storm main phase and over extended L^* regions. Additionally, the source term is parameterized proportional to the intensities of chorus waves. Actually the magnitude of local heating depends not only on the wave power available to heat the electrons but also on the number of electrons available to be accelerated, which is related to the electron distribution function.

Overall, all the radial diffusion, source, and loss terms in this model are empirical, but with some free parameters to be tuned against data. Uncertainties from these empirical terms lead to uncertainties in our model results for the relative contributions of individual acceleration and loss mechanisms to the variation of outer radiation belt electrons. For example, without a realistic loss rate, we cannot accurately include the source to compensate the loss. Or specifically, during the storm main phase the state of no internal source could also be a compromise of the added internal source and enhanced losses. Therefore, it is highly necessary to incorporate more realistic quantification of the loss, radial diffusion, and source rates into the current Fokker-Planck model, which brings out the works described in the following chapters of this thesis.

In spite of the uncertainties associated with the empirical radial diffusion, source, and loss terms, the model results can quite well capture the temporal features in the PSD data decreases and increases. The good simulation results for the individual storms with very high PE (Figures 3.2 and 3.3, Tables 3.2-3.5) self-justify that the forms of wave loss and heating terms used in our model are appropriate, though with uncertainties. In addition, compared to previous empirical Fokker-Planck models, our model has its merits. First, instead of using a lumped electron lifetime we tried to approximate the expected losses of electrons from three different wave populations that interact with the electrons in different regions. Secondly, local heating is included in our model by adding an internal source term to the radial diffusion equation.

3.6 Conclusions

In this chapter we combined newly available PSD data and our newly developed empirical Fokker-Planck model to study the acceleration of relativistic electrons in the outer radiation belt. In our model, we parameterized the loss term by the different wave-particle interactions dominant in different L^* regions. We added an internal source as a function of the AE index to the radial diffusion equation to represent local heating.

We considered PSD data at given μ and K, corresponding to 2.7 MeV electrons at L^*=4 mirroring near the earth's equator. The model results for the long-term run from 07/15/2002 to 12/31/2002 reproduced the average variations of radiation belt electrons between L^*=2.5 and L^*=6 but with over-prediction and under-prediction at different times, suggesting that the same set of parameters cannot be applied to all twelve storms in the second half of 2002. After detailed study of four individual storms, we found that three storms could be reproduced either by radial diffusion only with losses or by internal heating only with losses, but including both led to the best results; while the other storm clearly requires significant local heating during the storm recovery phase.

Based on our model results, we conclude the required magnitudes of radial diffusion and internal heating and the relative contributions of these two acceleration mechanisms responsible for the enhancement of energetic electrons in the outer radiation belt vary from storm to storm. However, the reason for these differences needs further study. After comparing the results from different runs for four storms and analyzing the radial diffusion coefficients, we suggested that internal heating contributes more to the enhancements of the fairly high energy electrons at L^*=4.

Chapter 4

Drift-Diffusion Model: Quantification of the Precipitation Loss of Radiation Belt Electrons Observed by SAMPEX

This chapter is based on the paper titled *"Quantification of the precipitation loss of radiation belt electrons observed by SAMPEX"* by Tu, W., R. Selesnick, X. Li, and M. Looper, published in *J. Geophys. Res.* in 2010.

4.1 Introduction

As emphasized in previous chapters, since the overall structure of the radiation belts, and their variability, are controlled by the competition between source and loss processes [Selesnick and Blake, 2000; Reeves et al., 2003; Li, 2004], a detailed understanding of the loss is a required step towards developing comprehensive models for radiation belt electron dynamics, because only when the loss rate is accurately determined will it be possible to appropriately include acceleration and transport processes at the level necessary to compensate for the losses and model the observed enhancements [Tu et al., 2009 or Chapter 3].

In Chapter 2 I have introduced different types of non-adiabatic loss mechanisms for electrons in the outer radiation belt, including magnetopause shadowing, outward radial diffusion, and precipitation to the atmosphere. Electron precipitation losses into the atmosphere are dominant in the heart of the outer radiation belt (L~4), which are due to wave-particle interactions that induce pitch angle diffusion. The quantification of the total electron loss rate should be addressed, not only for the quantification of the acceleration mechanisms in the comprehensive radiation belt dynamics model discussed before, but also for particle tracing and radial diffusion codes [e.g., Elkington et al., 2003; Ukhorskiy et al., 2005; Shprits and Thorne, 2004; Barker et al., 2005]. However,

uncertainties in the theoretical precipitation loss calculations lead to inconsistent electron lifetimes used in radiation belt codes. Although theoretical calculations of pitch angle diffusion based on scattering by different types of plasma waves have been carried out since the 1960s [e.g., Kennel and Petschek, 1966; Thorne and Kennel, 1971; Summers et al., 1998; Shprits et al., 2007], due to the lack of adequate observation of the waves [e.g., Engebretson et al., 2008] and a clear picture of the pitch angle distribution of electrons around the loss cone, electron precipitation processes and the associated loss rates are still not well understood [e.g., Friedel et al., 2002; Millan and Thorne, 2007; Tu et al., 2009]. The electron loss rates or lifetimes used in current papers are inconsistent and can diverge by an order of magnitude. For example, Shprits et al. [2005] set the electron lifetime as a constant of 10 days inside plasmapause and empirically as a function of the Kp index (3/Kp) outside the plasmapause, which varied from 0.7~4 days in their study events; Barker et al. [2005] made the lifetime a function of L and limited it to 3 days at L=6 and 29 days at L=4 in their model; and Thorne et al. [2005] concluded that the effective lifetimes of relativistic electron in the outer radiation belt are comparable to a day based on an analysis on microburst observations. This demonstrates that so far we have an unclear understanding of the actual total loss rates.

Selesnick et al. [2003, 2004] and Selesnick [2006] introduced a Drift-Diffusion model to directly simulate the radiation belt electron data from a low-altitude satellite, SAMPEX, and to estimate the electron loss rate. Low altitude measurements are most useful in determining the electron precipitation loss rate into the atmosphere, since the electron bounce loss cone opens up at low altitude, and SAMPEX data are ideally suited not only because of its low altitude orbit, but also its large geometric factors and the fast time resolution of its detector. Selesnick et al. [2003] developed a prototype of the Drift-Diffusion model to represent the low-altitude electron distribution, as a balance between azimuthal drift and pitch angle diffusion. The steady decay solution of the model was calculated numerically to fit various data sets during quiet times (when electrons decay steadily) and thus a source mechanism was not included in the model. In Selesnick

et al. [2004], bounce phase dependence was added in the model to simulate the bounce loss cone electrons and detailed physical models for pitch angle diffusion coefficients and electron atmospheric backscattering were used. Then Selesnick [2006] reverted to the bounce-averaged model in Selesnick et al. [2003] but with a newly added source term and to determine the electron loss rates during geomagnetic active periods. The two storm events well-simulated in Selesnick [2006] demonstrated that the Drift-Diffusion model can reasonably represent the low-altitude electron distribution, and the temporal variations of electron loss rate during the two storms indicated that the loss rates typically increase and are highest during the storm main phase.

In this chapter, we apply the Drift-Diffusion model method from Selesnick [2006] in order to quantify the electron loss rate for various storm events and a much wider L region. In Selesnick [2006], the rates and variations of electron loss into the atmosphere were only studied for two intense storms (Dst<-100 nT) and only at L=3.5; here we further explore the temporal variations of electron loss rates for different types of storms, including another intense storm (Dst<-100 nT), a moderate storm (Dst<-50 nT), and a small storm (Dst<- 30nT), from which we will investigate, for instance, whether the loss is always faster during the storm main phase, and whether and how the losses vary with different types of storms. Furthermore, since the outer radiation belt exhibits strong electron flux variations in both time and space, fundamental questions about the spatial variations of electron loss rate into the atmosphere are also important. The spatial variations of the loss rate include both radial dependence and local time dependence. In this chapter, we extend the investigation of the temporal variations of electron loss rate over wider L regions, and we can also obtain some knowledge of the local time variations of electron loss rate. The quantified electron lifetimes from this chapter can be used as input for the Fokker-Planck model discussed in Chapter 3 to replace the empirical lifetime.

4.2 Data Description

The main data sets used in this work are the energetic electron measurements taken by the PET (the Proton/Electron Telescope) instrument [Cook et al., 1993] on SAMPEX. SAMPEX was launched on 3 July 1992 into a nearly polar orbit with altitude of ~600 km and an 82^{o} inclination [Baker et al., 1993]. It orbits the Earth 15 times each day and has been continuously providing measurements of radiation belt electrons since its launch, covering many different radiation belt conditions. The SAMPEX/PET instrument includes three electron rate counters, measuring electrons with energies from low to high, providing the electron counts every six seconds. They are labeled as P1, counting electrons with E>0.5 MeV, ELO with 1.5<E<6 MeV, and EHI with 2.5<E<14 MeV, respectively. P1, unlike the other two counters, is a single detector measurement [Cook et al., 1993]. Note that these energy ranges are only approximate and for reference use. The detailed energy response of each counter is given by the response function [Selesnick et al., 2003], used later in our work. After comparing with PET/PLO proton event data, we have confirmed that there is no significant proton contamination in P1 electron data for the events studied here. Necessary corrections for instrumental deadtime and detector background counts have been performed on the entire PET count rate data used in this work. Additional correction for chance coincidences of the ELO data has also been made (for details please see Appendix A in Selesnick et al. [2003]).

4.2.1 SAMPEX Data Geometry

In order to apply the Drift-Diffusion model to the SAMPEX measurements, some basics about the SAMPEX data geometry need to be understood, for which illustrative cartoons are drawn in Figure 4.1. On the right side of panel (b), the green sphere in the center is the Earth, with the dipole magnet (red square) off the Earth center as in the real case; the yellow circle represents the SAMPEX low-altitude polar orbit around the Earth and the two blue circles (with the left one partly covered by a red curve) illustrate two conjugate magnetic field lines for the same L shell (e.g.,

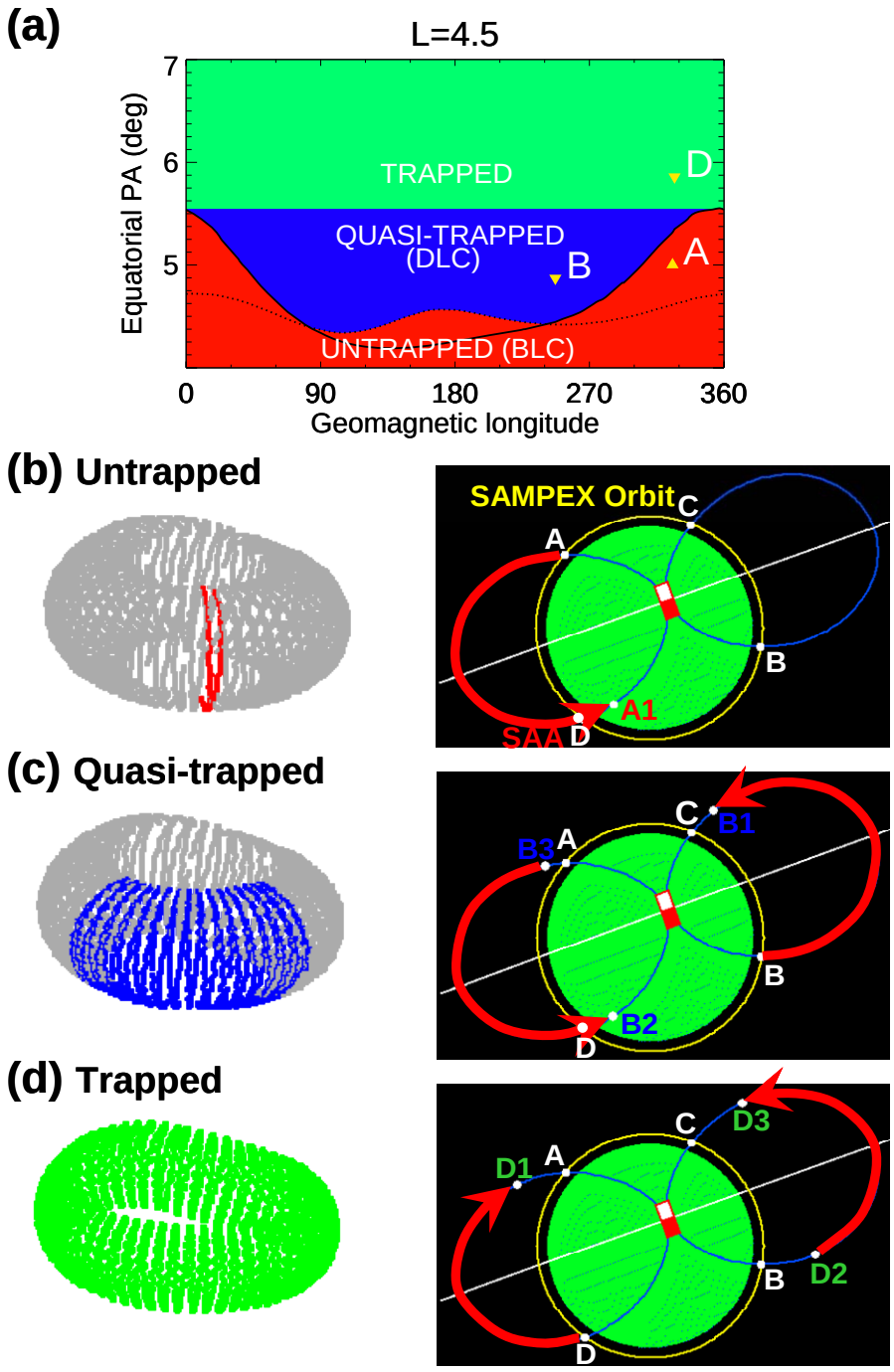

Figure 4.1: Cartoons illustrating SAMPEX data geometry. SAMPEX measures three electron populations: trapped, quasi-trapped and untrapped, with their equatorial pitch angle ranges at L=4.5 shown in panel (a). Within each electron population area, a representative point is marked: point A, B, and D respectively. The three points together with another point C are the four detecting positions by SAMPEX at a given L shell within one orbit, shown in panels (b), (c), and (d), which respectively illustrate how the points A, B, and D detected by SAMPEX can be untrapped, quasi-trapped and trapped. The L shell is shown on the left of each panel with the electron trajectories shown in color.

L=4.5). Therefore, within one orbit period SAMPEX crosses a given L shell four times, labeled as A, B, C and D in white.

For each magnetic field line around the Earth, or each magnetic longitude, there is a bounce loss cone (BLC), the range of equatorial pitch angles (PA) where electrons will precipitate into the atmosphere within one bounce period. For our model, we define the BLC specifically as the range of equatorial PA with electrons mirror points below 100 km in either hemisphere. The nondipolar nature of the Earth's magnetic field results in nonuniform magnetic field strength at both 100 km and the magnetic equator, hence a longitude-dependent BLC, as shown in the two black curves in panel (a). The solid curve is the 100km BLC angle at L=4.5 in the southern hemisphere and the dotted curve is for the northern hemisphere. So the final 100km BLC at each longitude is the maximum of these two, with the range of equatorial PA inside the BLC filled by red color in panel (a). The peak location of the BLC angle is at ~0^o or 360^o longitude, where the 100 km magnetic field is the weakest for the fixed L value, and this region is called the South Atlantic Anomaly (SAA). The electrons inside the BLC are classified as 'untrapped', since they will be lost within one bounce as illustrated in panel (b). Taking point A from panel (a) inside the BLC as an example, it is detected by SAMPEX in the northern hemisphere near the SAA longitudes. But when it bounces to the southern hemisphere (the SAA region), the electron mirrors below 100 km (at point A1) and is lost into the atmosphere.

The drift loss cone (DLC) is defined as the range of equatorial PA between the local BLC at one specific longitude and the maximum BLC over all the longitudes, shown in the blue region in panel (a). Note this definition of DLC is simplified for the International Geomagnetic Reference Field (IGRF) model (for details see: http://www.ngdc.noaa.gov/IAGA/vmod/igrf.html) used in this work, under which and if without pitch angle diffusion, the electron equatorial PA does not change when it drifts around the Earth. The particles inside the DLC are called 'quasi-trapped', such as

point B. These particles can stay trapped at some longitudes (B to B1 in panel (c)), but when they drift to the SAA region, they will get lost (at B2). Therefore, the particles inside the DLC cannot stay longer than a drift period. However, for particles outside the DLC, the green area in panel (a), they will stay trapped at all longitudes (assuming no pitch angle scattering). We take point D in panel (a) as an example and show the geometry in panel (d): detected by SAMPEX near the SAA region at point D, then bounce to D1, and then D2 to D3 after drift.

4.2.2 PA-Longitude Plot

As I described, points A, B, C and D are the four measuring locations of SAMPEX at a given L shell within one orbit. And from panels (a)-(d) in Figure 4.1 we understand that SAMPEX can observe all three different electron populations: trapped, quasi-trapped and untrapped. In panel (a) of Figure 4.2 I plot out the maximum equatorial PA of electrons measured by SAMPEX at a given L shell within one day, versus geomagnetic longitude. It uses the pattern in panel (a) of Figure 4.1 as the background. The maximum equatorial PA corresponds to detected electrons with local PA equal to 90^{o} or mirroring at SAMPEX locations. The yellow triangles represent the data points detected by SAMPEX at L=4.5 within the day 2009/02/13. Note that the geomagnetic longitude is calculated under the Corrected GeoMagnetic coordinates (CGM) using the IGRF model [Gustafsson et al., 1992] and the L shell value used is the McIlwain L [McIlwain, 1961] obtained by using the IGRF model. Since the Earth is rotating underneath SAMPEX's orbit, the data can reach full-longitude coverage after at least half a day. And since SAMPEX orbits the Earth 15 times per day, within one day it crosses a given L shell ~60 times, resulting in ~60 data points in the figure. Upward triangles indicate crossings in the northern hemisphere and downward triangles are in the southern hemisphere. Based on the maximum observed PA, the detected electrons can be approximately classified as trapped (in the green area), quasi-trapped (in the blue area) and untrapped (in the red area).

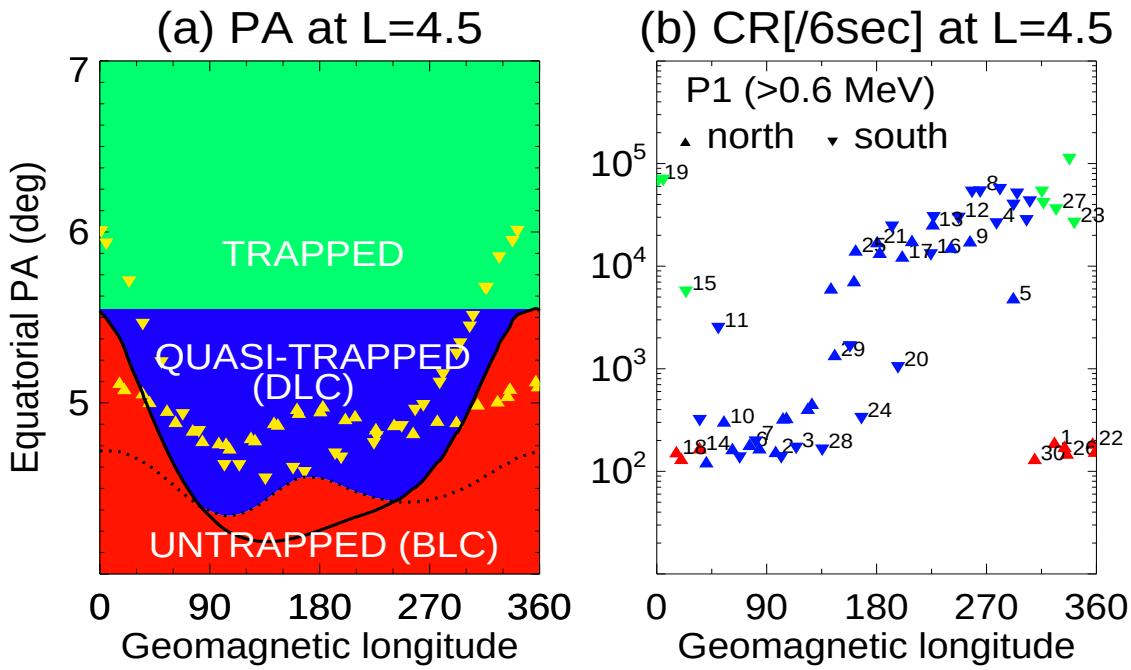

Figure 4.2: Panel (a) shows the maximum equatorial pitch angle distribution of electrons measured by SAMPEX at L=4.5 within the day 2009/02/13, versus geomagnetic longitude. The maximum observed pitch angle data are in yellow, which fall into three categories in the colors same with panel (a) of Figure 4.1. The upward triangles were detected in the northern hemisphere and the downward ones were in the southern hemisphere. Panel (b) illustrates the count rate distribution of the same data points in panel (a), where the first 30 crossings at L=4.5 within that day are numbered in chronological order, with the trapped electrons in green, the quasi-trapped ones in blue and the untrapped ones are in red.

There will be certain errors from the approximate electron classification based on the maximum observed PA, since not all the measured electrons will have local PA equal to 90^o. However, it is virtually unachievable for SAMPEX to provide the exact local PA of measuring electrons, given the wide look angle of its detector. So the possible scenarios are: some so-called 'trapped' electrons in panel (a) of Figure 4.2 can be actually quasi-trapped (due to local PA$<90^o$) or some 'quasi-trapped' electrons are actually untrapped. But the classified as 'untrapped' electrons will be truly untrapped, and there are no trapped electrons falling into the 'DLC' region. In this work, we only use this approximate classification as an intuitive reference when we want to qualitatively discuss the physical behavior of electrons in the three populations. In the quantitative model, the approximation is not really used, which will be clearer later.

4.2.3 Count Rate-Longitude Plot

We know the approximate PA versus longitude distribution of data as shown in panel (a) of Figure 4.2. The corresponding count rate (CR) distribution for the same data is shown in panel (b). It illustrates the logarithm of the electron counts per 6 seconds detected by P1 within the same day at L=4.5, plotted over geomagnetic longitude. Each CR data point in panel (b) corresponds to one PA data point in panel (a) at the same geomagnetic longitude. So there are also 60 data points. Again, upward triangles are for northern hemisphere crossings and downward triangles are in the south. Note that the ~60 points within one day are aligned according to their longitudes, not in time sequence. For time reference, the first 30 crossings on 2009/02/13 are numbered in chronological order in panel (b). Two consecutive crossings at L=4.5 are either ~15 minutes or ~30 minutes apart in time, depending on their hemispheres.

After categorization by PA distribution in panel (a) the trapped electrons are plotted in green for consistency; similarly, untrapped data points are in red and data inside the DLC are in blue. From the CR distribution plot, notice that high CR detected in the southern hemisphere (green

downward triangles) near the SAA longitudes are stably trapped electrons. Low fluxes in the same longitude range but in the northern hemisphere (red upward triangles) are electrons in the BLC. They generally have the lowest data rates. And the low CR to the east of SAA in the DLC, from both north and south, gradually increase with longitude as the DLC filled in by pitch angle diffusion along with the eastward electron drift. The generally reasonable count rate distributions of the three different electron populations over longitude demonstrate that the approximate classification of electrons is qualitatively acceptable. Since the DLC electrons cannot survive a drift period, the relative trapped and quasi-trapped intensities can be used to indicate the electron loss rate. Still, we simulate these data with the Drift-Diffusion model in order to quantify the electron loss rate.

4.3 Model Description

Since the observed electron flux variation is a complicated balance between loss and energization, for any quantitative study, a physical model is needed. Here we adapt the Drift-Diffusion model in Selesnick [2006] to simulate the low-altitude electron distribution from SAMPEX. The model is governed by the equation:

$$\frac{\partial f}{\partial t} + \omega_d \frac{\partial f}{\partial \phi} = \frac{\omega_b}{x} \frac{\partial}{\partial x} \left(\frac{x}{\omega_b} D_{xx} \frac{\partial f}{\partial x} \right) + S \qquad (4.1)$$

where $f(x, \phi, t)$ is the bounce-averaged electron distribution function at a given L shell and kinetic energy E, as a function of $x = \cos\alpha_0$, where α_0 is the equatorial pitch angle, drift phase ϕ, and time t; ω_d is the bounce-averaged drift frequency (assumed α_0-independent for numerical simplicity since the variations from α_0 are within a factor of 1.5); ω_b is the bounce frequency; D_{xx} is the bounce-averaged pitch angle diffusion coefficient; and S is the source rate. In the model, there are 90 grid points in ϕ and 135 grid points in $x = \cos\alpha_0$, covering from α_0=90° to DLC until BLC. The left hand side of Eq. 4.1 is an advective time derivative including

the effects of azimuthal drift, and the first part of the right hand side represents pitch angle diffusion. The diffusion coefficient is

$$D_{xx} = D_{dawn/dusk}\widetilde{E}^{-\alpha}\frac{1}{10^{-4}+x^{30}} \tag{4.2}$$

where $\widetilde{E} = E/(1\text{ MeV})$. The constant 10^{-4} is included for numerical stability at low x values (or high equatorial pitch angles). In this case, the x-dependence in D_{xx} will be distorted to some extent from the exponential x^{-30} for low x values, but remain x^{-30} for high x values. The power index 30 on x is chosen as a typical value by fitting both the high altitude data from the Polar satellite and the low altitude data from SAMPEX in [Selesnick et al., 2003]. Hence the pitch angle diffusion is faster for electrons with larger equatorial pitch angles, consistent with the essentially flat pitch angle distributions at equatorial pitch angles around 90°. Even though the model results in Selesnick et al. [2003] showed some variations of the power index on x, ranging from 20-60, and since the model solution is insensitive to this index when it exceeds 20, especially in the low α_0 regime, fixing it at 30 is reasonable. D_{dawn} and D_{dusk} are independent parameters, which are separated for the purpose of investigating the possible magnetic local time (MLT) dependence of the diffusion rate, taking advantage of the geometry that the SAMPEX orbital plane is basically in the dawn-dusk sector during the three events described in the next section. D_{dawn} is for 0 to 12 hours MLT with D_{dusk} for the other half. The source rate function is

$$S = S_0\widetilde{E}^{-\nu}\bar{g}_1(x)/p^2 \tag{4.3}$$

where $\bar{g}_1$ is the lowest-order eigenfunction of the drift-averaged pitch angle diffusion operator, p is the electron momentum for a given E, and S_0 is always positive. Here the source mechanism is unspecified which could be either radial diffusion or local heating. Overall, the free parameters in the model are D_{dawn}, D_{dusk}, α, ν and S_0. As represented by the model

equation, the observed low-altitude energetic electron distribution is a balance of azimuthal drift, pitch angle diffusion into the upper atmosphere, and possible concurrent sources.

Given the free parameter values, appropriate initial conditions and boundary conditions for $f(x,\phi,t)$, Eq. 4.1 can be solved numerically combining operator splitting, Crank-Nicolson and upwind differencing methods. The sample solutions for the electron distribution f as a function of longitude and equatorial pitch angle at two different L shells with different sets of parameter values are shown in Figure 1 in Selesnick et al. [2003] (Figure 2.11 in Chapter 2). The three model solutions on the left-hand side (panels (a)-(c)) show that for high values of the ratio D_{xx}/ω_d, diffusion is dominant over drift and losses occur over all longitudes; as the ratio D_{xx}/ω_d decreases, the drift becomes more significant over diffusion and losses start to occur over a smaller longitude range to the west of SAA. And the other three solutions on the right-hand side (panels (d)-(f)) demonstrate how different values of D_{day} and D_{night} work in the model (in our case it would be $D_{dawn/dusk}$, which works in a similar way).

Boundary conditions. The boundary conditions used in the model include: first, $f = 0$ at the edge of the BLC. So the BLC distribution versus geomagnetic longitude forms the longitude-dependent lower boundary of the simulations. In other words, the model requires the BLC to be relatively empty, which will be true under the slow diffusion (or weak diffusion) assumption. If the strong diffusion limit is approached, when the electrons scatter into the loss cone even faster than the atmosphere can remove, the assumed boundary condition will break down [Schulz and Lanzerotti, 1974]. More discussions about this assumption will be included in Section 4.5 combined with the event study results. The second boundary condition at the high equatorial PA end is: $\partial f/\partial x = 0$ at $x = 0$ (or $\alpha_0 = 90^o$) for each ϕ, or the PA distribution at 90° is flat. The initial model energy spectrum for a specific storm event is obtained by best-fitting the stably trapped

electron flux from the PET/Pulse-Height Analysis (PHA) data from ELO and EHI along with the count rate data from P1 for the first time interval before the storm (Please refer to [Mewaldt et al., 2005] for a description of similar PHA spectrum calculation but for solar electrons). The PET/PHA events data is a subset of the ELO and EHI data being pulse-height analyzed, which provides a measure of the energy deposit in each detector from individual electrons [Cook et al 1993, Mabry et al., 1993]. Besides, the initial model pitch angle distribution is considered the same shape with $\bar{g}_1(x)$ in Eq. 4.3 but normalized by the initial energy spectrum, and assumed uniform over all the longitudes.

Energy spectrum. The model is run at eight logarithmically spaced energies from 0.5 to 5.66 MeV. The model results at other energies are obtained by exponential interpolation or extrapolation. Now we have the modeled phase space density, f, as a function of x, ϕ and E at each time step. Model flux, j, is calculated based on the equation $j = p^2 f$. However, in order to generate the model count rates to directly compare with the observations from P1, ELO, and EHI, the counter response function R, as a function of energy and polar angle from the telescope axis of a incoming particle, is needed to integrate the modeled flux over both local pitch angles and energies for a measured electron count rate from a given counter, at specific time and location and with corresponding satellite orientation. The details about the PET response functions and the count rate simulation are introduced in the appendix of Selesnick et al. [2003].

Parameter tuning. Now we understand how the Drift-Diffusion model works to simulate the count rates from different counters at different locations and times, but how to constrain the five free parameters in the model? As I discussed in the 'Data Description' section, the count rate data show considerable variations over geomagnetic longitudes, indicating a delicate balance of azimuthal drift and pitch angle diffusion. Therefore, to fully constrain the model free parameters, primarily in the pitch angle diffusion rate and source rate, the model requires data with

full-longitude coverage, such as the count rate data shown in panel (b) of Figure 4.2. Since SAMPEX takes a half day to cover all longitudes, the model is not capable of resolving the parameter variations on timescales less than 12 hours. Thus, when simulating one storm event, the data and the model are processed basically on a daily basis; except for during the main phase, when the data may change rapidly, the data and simulation interval is switched to half a day. Then within one data interval (one day or half a day), the parameters are iteratively tuned to achieve the least mean square difference between the logarithms of the modeled electron rates (p_i) and the data (d_i), defined

$$\mathrm{K}^2 = \frac{\sum_{i=1}^{n} (\lg d_i - \lg p_i)^2}{n} \tag{4.4}$$

where n is the total number of data points within the interval. The quasi-Newton method is used in the parameter iteration [Tarantola, 2005]. The model results $f(x,\phi,E)$ from the end of last interval are passed as the initial condition into the current interval within which another parameter tuning initiates.

Electron lifetime. Electron lifetime, τ , is the e-folding timescale defined for a steady-decay state, which represents the loss rate only if the parameters are unchanged for a period much longer than $1/(\lambda_2 \overline{D})$ (see explanations of $\overline{D}$ and λ_2 below). After obtaining the optimum set of parameters for each time interval in our model solutions, the actual pitch angle diffusion rates at different energies can be determined using Eq. 4.2. Then the electron lifetime for a specific energy can be approximately inferred as

$$\tau = 1/(\lambda_1 \overline{D}) \tag{4.5}$$

where $\overline{D}$ is the longitude-averaged model diffusion coefficient defined as $\overline{D} = (D_{dawn} + D_{dusk})\widetilde{E}^{-\mu}/2$, and $\lambda_1 \approx 100$ is the lowest order eigenvalue of the normalized diffusion operator (the first terms on the RHS of Eq. 4.1 involving $\partial/\partial x$, divided by $-\overline{D}$). λ_2 above is the 2nd order eigenvalue. Eq. 4.5 is analytically derived from solving the drift-averaged

pitch angle diffusion equation (Eq. 4.1 without the drift and source terms and with $D_{xx} = \overline{D}\frac{1}{10^{-4} + x^{30}}$) and λ_1 is calculated numerically for L values from 3.5 to 6.5 (see Appendix A for detailed derivations). Based on this, the electron lifetimes at different energies for each time interval can be easily estimated from the determined diffusion coefficients.

One thing I would like to clarify is that our model approach in estimating the electron pitch angle diffusion rate is different from the wave study approach using quasi-linear theories [e.g., Summers et al., 2007; Li et al., 2007]. They are complementary approaches, both of which have to assume parameters. For example, Li et al. [2007] made certain assumptions on the spectral distribution of the wave power, the ratio of plasma frequency to electron gyrofrequency (f_{pe} / f_{ce}), the distribution of wave normal angles, local time content etc. But our model assumes the form of D_{xx} in Eq. 4.2 with free parameters, and estimates the pitch angle diffusion rate based on parameter fitting to real data, without explicitly using the wave and plasma properties. An advantage is that we can estimate the electron precipitation loss rate of many simultaneous processes as shown in Section 4.4.

4.4 Model Results from Event Study

In this work we select three different types of storms for detailed study, one is a small storm in February 2009; the other is a moderate storm in March 2008 and the third is an intense storm in September 2002. The first two are during the current deep solar minimum and the last one is right after the last sunspot maximum. For each event we run the Drift-Diffusion model for four different L regions (L=3.5, 4.5, 5.5 and 6.5), hence for four different data sets, one at each L. Then each data set is divided into several daily or half a day intervals to achieve full-longitude coverage within each interval. Here I first discuss the simulation results for the February 2009 storm in detail.

4.4.1 February 2009 Event: A Small Storm

The overall electron count rate variations over the February 2009 storm are shown in Figure 4.3 as a function of L shell (Y-axis) and time (X-axis). The logarithm of daily-averaged count rates are color coded according to the color bar shown on the right side of the plot, one panel for each rate counter with the energy range shown on the left. Electron rates are binned in bins of 0.1 L on the Y-axis. The white curve on top of the color spectrum plot shows the plasmapause location calculated using an empirical model in O'Brien and Moldwin [2003]. Although the storm is small with Dst only reaching ~-40 nT (see the Dst profile in the bottom panel of Figure 4.3), it causes a very dynamic radiation belt responses: the electron count rates drop significantly during the storm main phase, recover during the early recovery phase, and increase above the pre-storm levels later in the recovery phase.

Count rate simulations. The Drift-Diffusion model is used to simulate this event, with the count rate data and the simulation results at L=4.5 shown in Figure 4.4. The count rates from three different rate counters are plotted as a function of geomagnetic longitude within each interval, with corresponding time period specified on the top of each panel. According to the bottom Dst profile in Figure 4.3, panel (a) is during a quiet day prior to the storm; panel (b) immediately follows panel (a) in time and includes the storm main phase (lasting about half a day); panel (c) is during the early recovery phase and panels (d, e, f) constitute the late recovery phases in time order. The six panels show the evolution of the low-altitude electron count rates during the storm event. Filled data points are the measured electron count rates and the open data points show the simulation results that are the best fits to the data. Since the EHI count rates are very low during this event, close to the background count level, uncertainties due to Poisson counting statistics, which are significant for the low fluxes, could be significant in the EHI rate data. Therefore for this event, we don't include the EHI count rates in the model simulation.

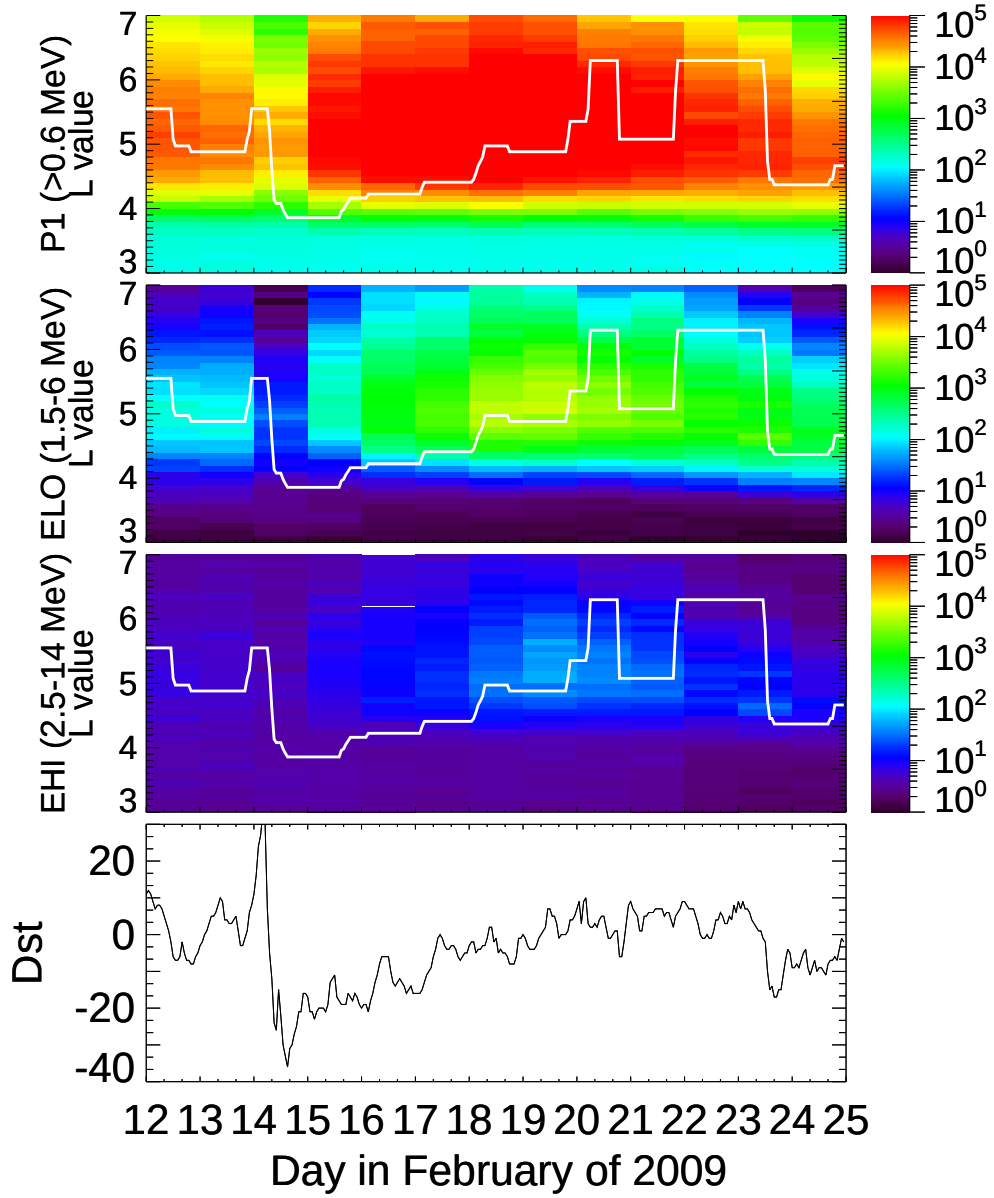

Figure 4.3: The top three panels show the electron count rate variations over the 2009/02 storm from 2009/02/12 to 2009/02/25 detected by three SAMPEX/PET counters: P1, ELO, and EHI, respectively. The count rates, in units of #/6 seconds, are daily-averaged in time axis (X-axis), color-coded in logarithm (color bar on the right), and sorted in L (L bin: 0.1 in Y-axis). The superposed white curves illustrate the plasmapause locations. The bottom panel is the Dst data during this storm.

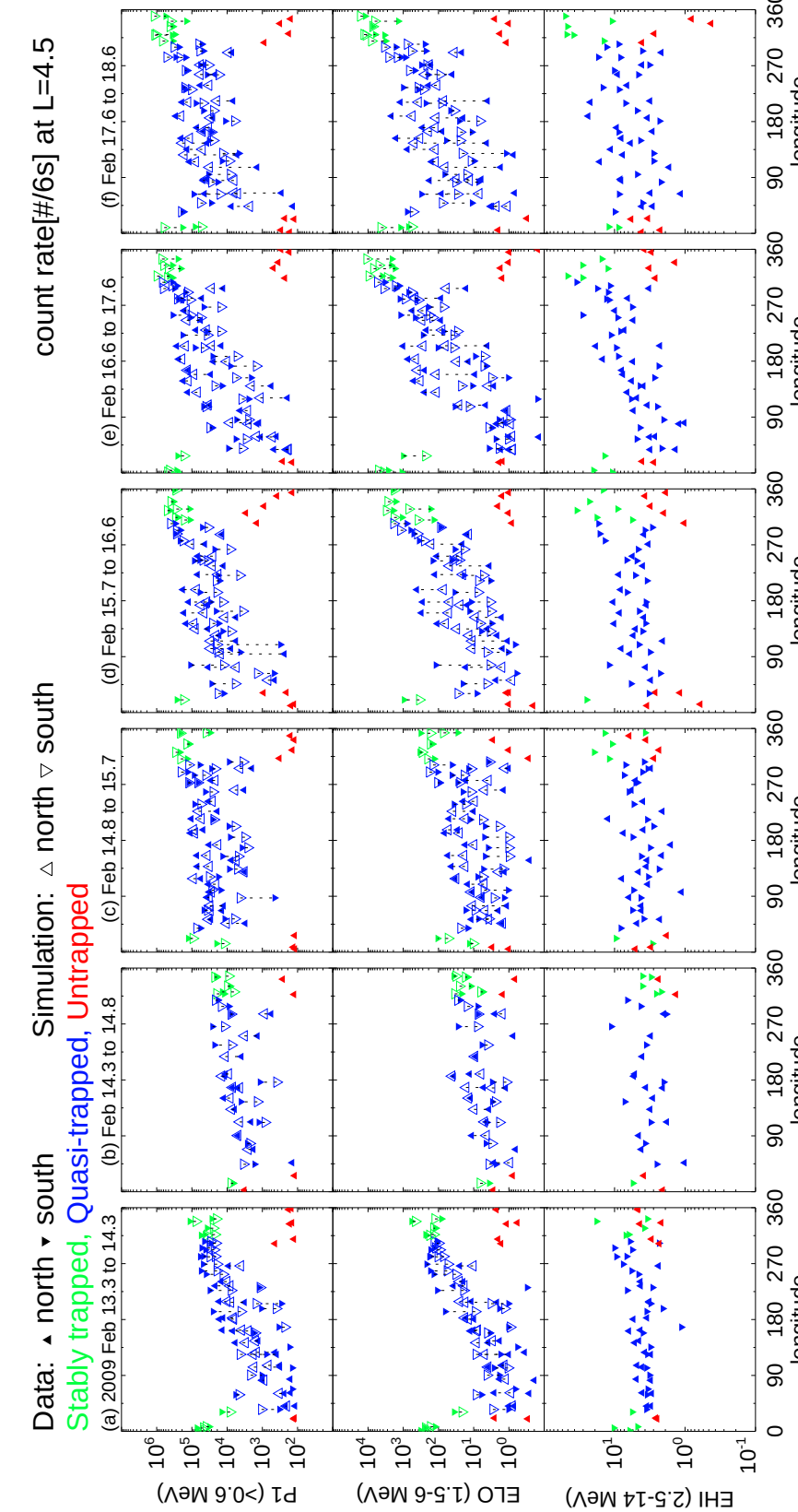

Figure 4.4: Electron count rate data (filled triangles) and model simulations (open triangles) versus geomagnetic longitude for the three rate counters at L=4.5 during (a) a quiet prestorm interval, (b) storm main phase, (c) early recovery phase and (d,e,f) late recovery phases of the 2009/02 storm. The count rate pattern (color and shape) is the same as that used in panel (b) of Figure 4.2.

During the quiet time before the storm (panel (a)), the count rates versus longitude pattern can be understood with reference to panel (b) in Figure 4.2. Three electron populations are identified: stably trapped electrons near the SAA longitudes (green downward triangles); untrapped electrons in the same longitude range but with lowest count rates (red upward triangles); and the DLC electrons in the middle (in blue). The low count rates in the DLC increase eastward with longitude because of the azimuthal drift, which indicates that the DLC is only filled in gradually by pitch angle diffusion with the drift, hence suggesting a relatively low pitch angle diffusion rate during this interval. I don't need to turn on the source to fit this data set reasonably well. Note that since our model assumes that the BLC is empty, which is a good assumption here considering the BLC data (red points) are near background, the data points within the BLC cannot be simulated.

In panel (b), the storm main phase, we notice that the stably trapped population near 0^o and 360^o longitude (green triangles) decrease significantly, which is a result of the fast electron losses into the Earth's atmosphere, suggesting enhanced pitch angle diffusion. The decrease is more significant for higher energy channels (ELO), indicating faster pitch angle diffusion for higher energy electrons. So the energy dependence index α should be negative in Eq. 4.2. The quasi-trapped population in the DLC from ~45^o to 315^o longitudes (blue triangles) also decreases during the storm main phase, but less significantly compared with the stably trapped population. Furthermore, the DLC electrons are almost at the same count rate level as the stably trapped electrons and are relatively flatly distributed over the longitude. These distributions indicate that the DLC is fully filled by pitch angle diffusion from the trapped electrons and the diffusion coefficient is required to increase significantly to produce such fast diffusion. No source is required to fit these data reasonably well.

During the early recovery phase (panel (c)), the trapped electron count rates (green triangles) almost recover to the pre-storm levels. This increase continues during the late recovery phase

(panels (d-f)), leading to the trapped count rates much higher than the pre-storm values, which requires a continuous active source during the recovery phase (panels (c-f)). On the other hand, the pitch angle diffusion rate returns to a lower value during the recovery phase, based on the decreased DLC electron count rates and the reappearance of the evident eastward increase of the DLC content over longitude.

Model fit results. The descriptions above for each interval of the February 2009 storm tell us how the model parameters are adjusted to fit the data during each interval and the simulation-data comparisons in Figure 4.4 illustrate the quality of the fits. Based on the best-fit simulations, we can obtain the optimum parameter set for each interval, and then infer the source and loss rates at L=4.5 for the storm event, as shown in the second column of Figure 4.5, together with results for other Ls in the other columns. The first row illustrates the variations of the model trapped electron intensity, j_0 (at 90^o equatorial pitch angle), versus time at six different energies: 0.5, 0.71, 1.0, 1.41, 2.0, 2.83 MeV, shown in different colors. The black curve in the background is the Dst index for this storm. The second row shows the equatorial source rate $S_0\widetilde{E}^{-\nu}$ for each energy channel. And the bottom row compares the derived electron lifetime in days and the electron replenish-time (model equatorial intensity/source rate) in days, from which we can tell which one of the two processes, loss or source, is faster. The lifetime is calculated from the parameterized pitch angle diffusion rate using Eq. 4.5. Here I discuss the fitting results for all four L regions together. But since there are very little dynamics at L=3.5 and the count rates there are very low, as illustrated in the color spectrum plot of February 2009 storm (Figure 4.3), the fitting results at the first column for L=3.5 could involve bigger errors and are not included here in the discussion.

For L=4.5 to L=6.5, we notice that the trapped electron flux, j_0, decreases during the storm main phase, more significantly for higher energies, and starts increasing at the early recovery phase,

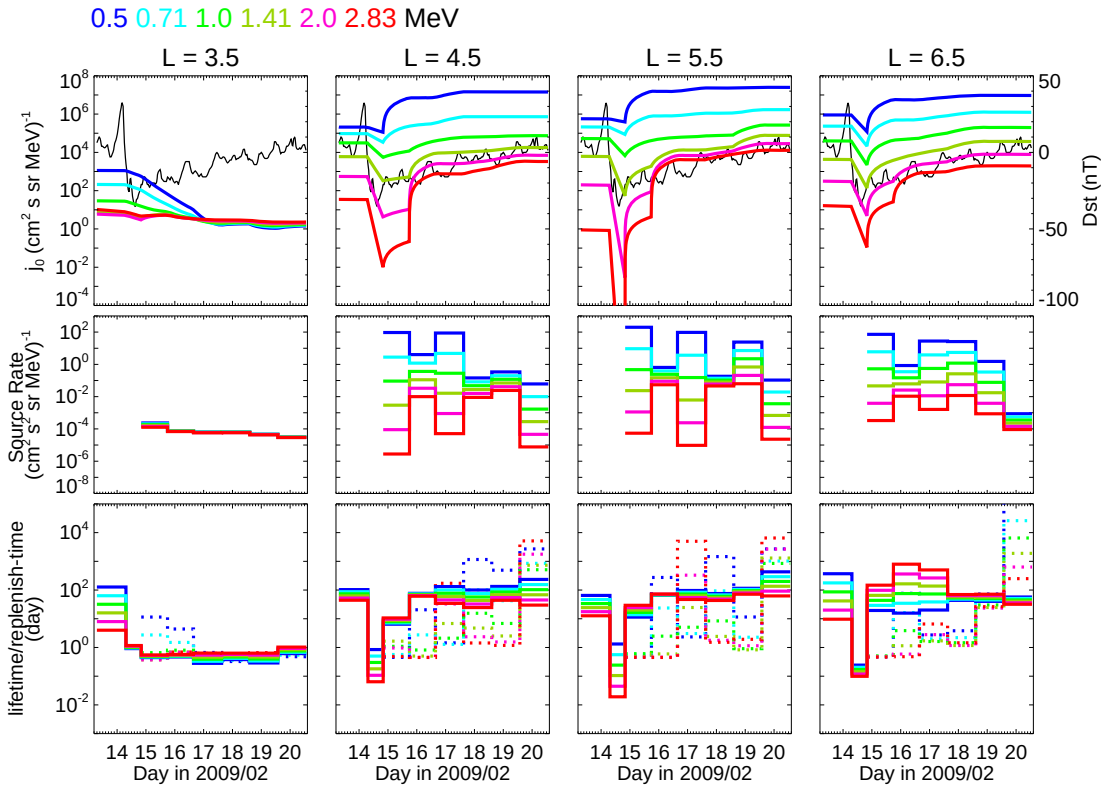

Figure 4.5: Model results from the optimum model fits to the data for the 2009/02 storm at various L locations over a range of electron energies represented in different colors (color bar on top). One column is for one L. The first row shows the equatorial intensities with the Dst profiles in the background (black curves); the second is the equatorial source rates and the bottom row compares the derived electron lifetimes (solid lines) and the electron replenish-times (dotted lines).

when the source is needed in the model. For all the three L, the increase of j_0 in the early recovery phase is more rapid for the lower energies (0.5 and 0.71 MeV), with j_0 reaching and then growing above the prestorm values within one day after the start of the recovery phase. However, j_0 at higher energies exhibits a two-boost increase during the recovery phase, a gradual raise at the early recovery phase and a more rapid one at the second time interval of the recovery phase, resulting in j_0 also higher than the prestorm values but in the late recovery phase. The trapped fluxes for all L and energies become relatively steady during the late recovery phase even though the source rates are variable, as shown in the second row of Figure 4.5.

Since we are most interested in the loss rates, we need to look at the solid lines in the third row in more detail. For the typical quiet time before the storm, the electron lifetime is above 10 days for all energies at L=4.5-6.5, with energy dependence index, α in $D_{xx} \propto E^{-\alpha}$, being negative, and the absolute value of α bigger at larger L. The loss rate becomes significantly faster during the storm main phase, with α still being negative. For the lower energies the fastest loss occurs at L=6.5, but for energies >2 MeV, the fastest loss is at L=5.5, on the scale of hours. This indicates that the radiation belt can almost be depleted within the main phase interval (~half a day), estimated by the equation $f = f_0 e^{-t/\tau} = f_0 e^{-12hour/1hour} \approx 0$, consistent with the depletion of j_0 for 2.83 MeV at L=5.5. At the early recovery phase, the loss rates quickly return to low values, but the sign of the energy dependence index flips compared with the prestorm index. For L=4.5, the loss rates are still faster than the quiet time, but for L=5.5 and 6.5, they almost return to the prestorm levels. In the late recovery phase, the energy dependence changes back for L=4.5 and 5.5 (α returns to negative), but for L=6.5, α remains positive during the entire recovery phase.

Here I would like to clarify two concepts before moving on to the next event: the electron lifetime and the electron precipitation rate. The former is directly related to the pitch angle diffusion

rate, D_{xx}, as shown in Eq. 4.5; while the latter depends on both D_{xx} and the available trapped intensity. For example, by comparing the trapped and DLC fluxes (green and blue triangles) in Panels (b) and (d) of Figure 4.4, we see that even though D_{xx} is much higher (or electron lifetime is much shorter) during the storm main phase of February 2009 storm, the precipitation level during the recovery phase in panel (d) could be comparable to or even higher than that in the main phase.

4.4.2 March 2008 Event: A Moderate Storm

For the second storm, which occurred in March 2008, the variations are basically the same, since both storms are not big storms during solar minimum. Figure 4.6 provides an overview of the electron count rate variations during this storm event, in the same format as Figure 4.3. Here I don't show the data-simulation plot for this storm, which is similar to Figure 4.4 for February 2009 storm. Only the model fitting results are illustrated in Figure 4.7, in the same format as Figure 4.5. In the trapped intensity plot, we also see the two-boost increase of j_0 for higher energies. But compared with the results of February 2009 storm, for high energies the trapped flux doesn't return to the prestorm level after the recovery phase. One thing to notice is that the energy spectrum of j_0 after the storm becomes much softer than the prestorm spectrum, mainly from the softer energy spectrum in the source rate. Similar to the February 2009 storm, source is only required to be on during the storm recovery phase for this event at all L regions. For the loss rates, the energy dependence index α is also negative during the storm main phase over all L regions but it is generally negative for the other storm phases as well, even for L=6.5, which is different from the February 2009 storm. Lifetimes can also be as short as hours during the main phase at higher energies (>1MeV) over broad L regions. After the early recovery phase, the loss rate at L=4.5 returns to the quiet time level but for L=5.5 and 6.5, the loss rates remain elevated.

4.4.3 September 2002 Event: An Intense Storm

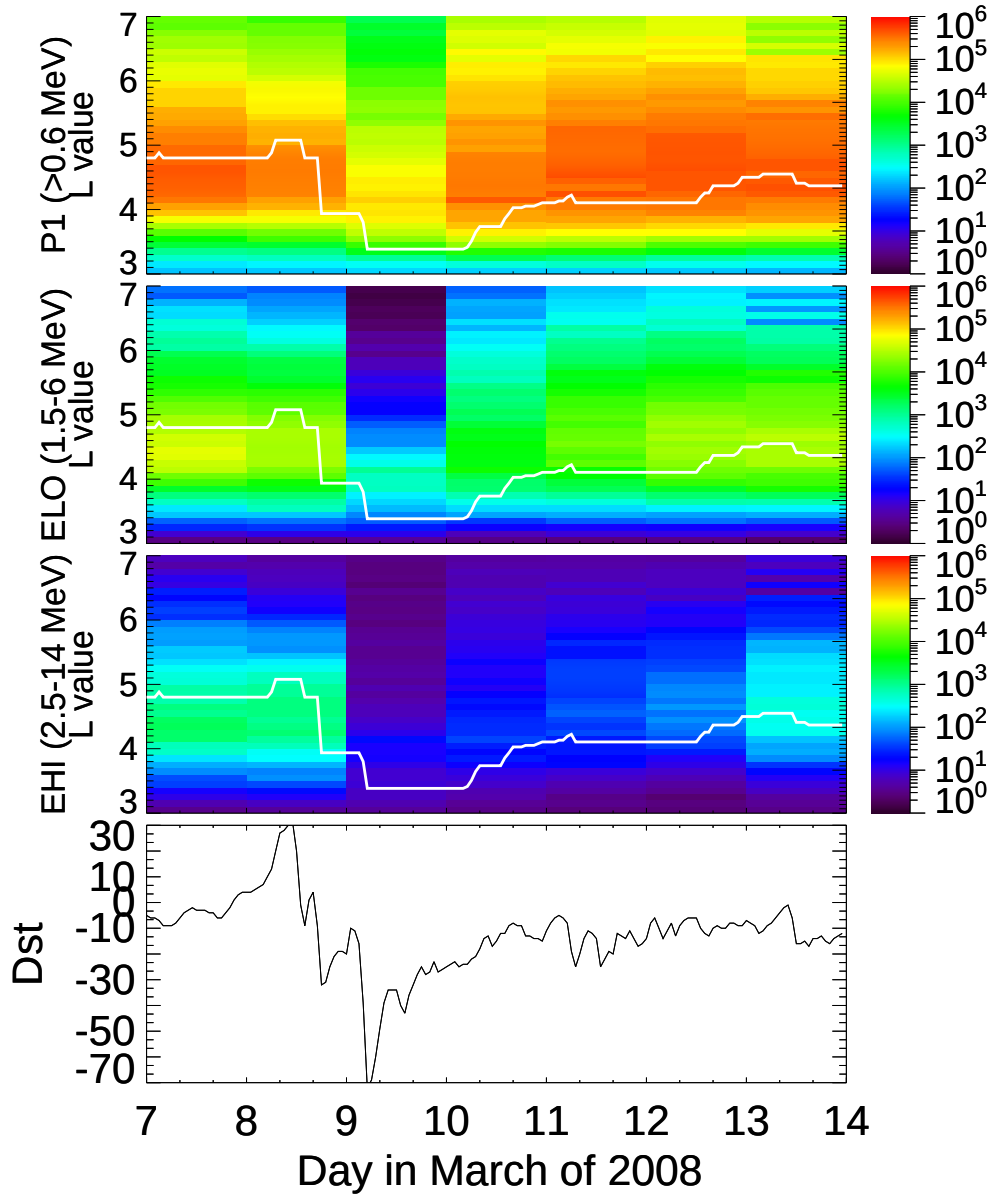

Figure 4.6: Electron count rate variations and Dst profile over the 2008/03 storm. The configuration is the same with Figure 4.3.

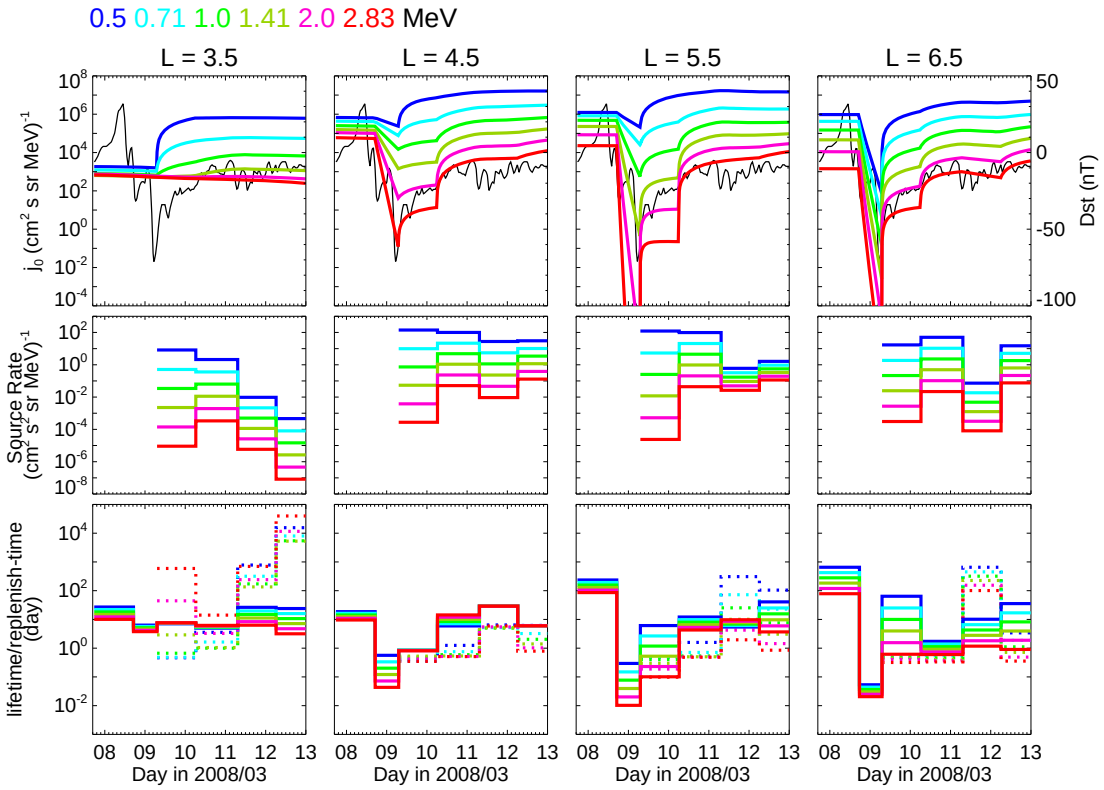

Figure 4.7: Model results for the 2008/03 storm at different L, with the same configuration in Figure 4.5.

The September 2002 storm is quite different, considering it is a much more intense storm right after the solar maximum. From Figure 4.8 we find that now L=6.5 is the place that has little dynamics and lower count rates, since the peak rate location is around L=4. Notice that the L ranges in Figure 4.8 are extended to L=2-7, from L=3-7 in Figure 4.3 and 4.6 for the other two storms. The entire outer radiation belt is compressed during solar max and the plasmasphere is also displaced inward, as illustrated by the white plasmapause location curves. For this event, EHI counts are included in the model simulation since they are much higher. The model fitting results are shown in Figure 4.9. At small L, the decrease of j_0 during the storm main phase is still more significant at higher energies, most obvious at L=4.5, and for some of the high energies, j_0 doesn't recover to the prestorm level after the storm. Source is needed from the early recovery phase to best simulate the data. However, for higher L regions (L=5.5-6.5), there is little energy dependence in the loss rates over the whole storm and a source population is not required until the second recovery interval. The trapped fluxes generally don't recover after the storm at high L, even for low energy fluxes. The softening of the flux energy spectrum is most evident at L=3.5. For this storm, the lifetime of the prestorm interval is less than 10 days but longer than 1 day for almost all energy electrons, and with positive energy dependence index, both of which are different from the other two storms in solar minimum. However, much the same as the first two storms, the loss is the fastest during the storm main phase and with a negative α (faster loss at higher energies) over wide L regions. In the late recovery phase, the loss rate returns to typical prestorm levels but the sign of α remains negative at L=3.5 and 4.5 (the peak flux locations). Another distinct feature about this storm is during the main phase at L=4.5, the lifetime at higher energies can be less than 10^{-3} day (~minute). This loss is so fast that the weak diffusion assumption breaks down. Then the current Drift-Diffusion model is not accurate in determining the lifetime. This will be discussed in the next section. But for this event the DLC electron count rate data from ELO do show an abrupt drop by >2 orders of magnitude within tens of minutes from the end of the 1st interval to the start of the

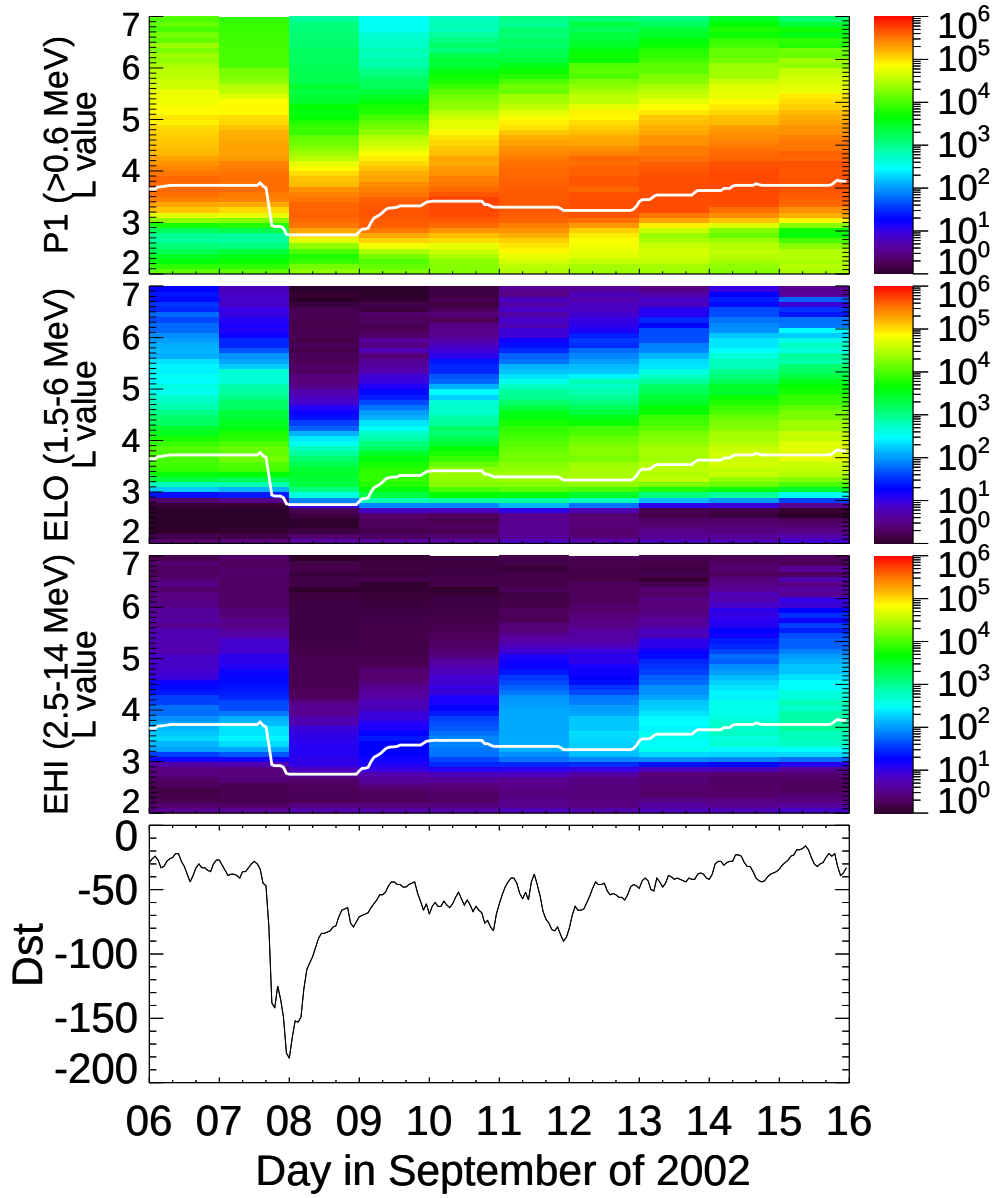

Figure 4.8: Electron count rate variations and Dst profile over the 2002/09 storm. The configuration is the same with Figures 4.3 and 4.6, but with the L ranges for the Y-axes in the top three panels broadened to L=2-7.

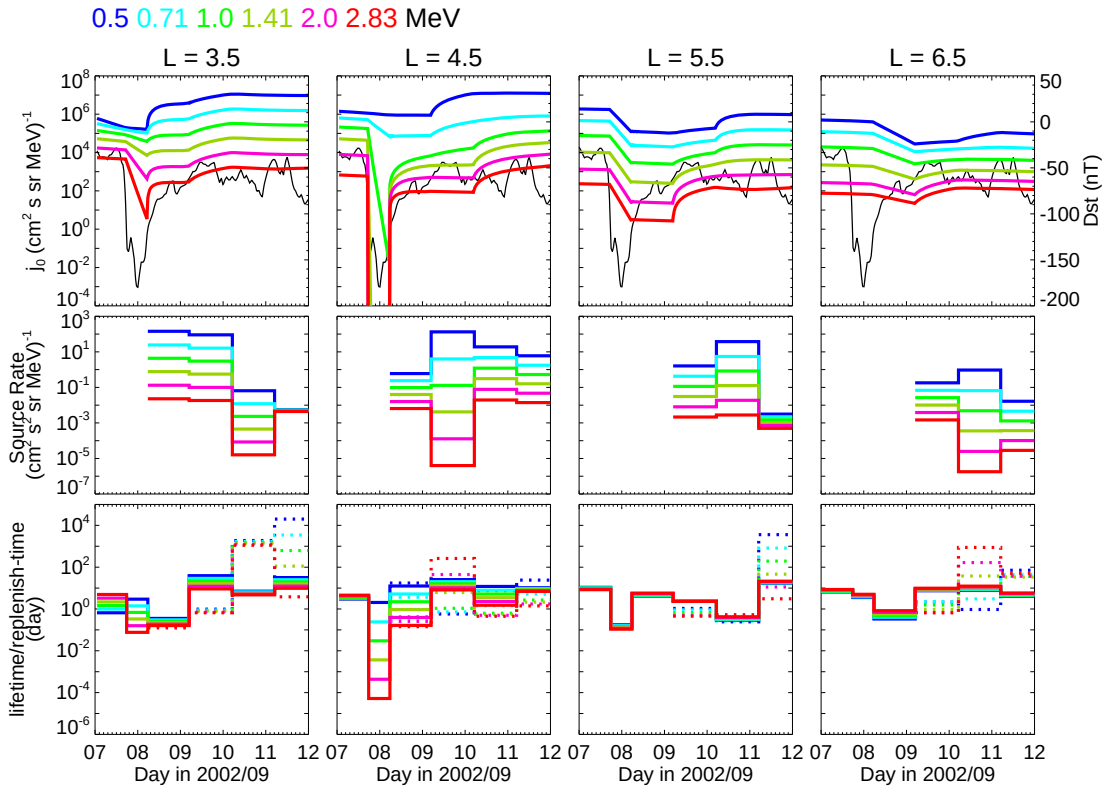

Figure 4.9: Model results for the 2002/09 storm at different L. The configuration is the same with Figures 4.5 and 4.7.

main phase interval, indicating the electron lifetimes for the high energy electrons are on the order of minutes and proving our model still provides a realistic estimate of the loss rate.

4.5 Discussion

4.5.1 Common Feature: Fast Losses for All Energy Electrons with Faster Losses at Higher Energies During Storm Main Phases

In the event study we have simulated three different types of storms, with minimum Dst around -40 nT, -70 nT and -180 nT, respectively. All the simulation results from the best fits of the three storms at four different L locations suggest some common features: that the loss of energetic electrons is always the fastest during the storm main phase and with more efficient loss at higher energies; the corresponding lifetimes for the high energies can be as short as hours for the small and moderate storms and minutes for the intense storm; and the fast losses (with timescales shorter or on the order of an hour) occur over wide L regions around the peak electron flux location, L=4.5-6.5 for the February 2009 and March 2008 storms, and L=3.5-5.5 for the September 2002 storm. As introduced, the Drift-Diffusion model can also resolve certain local time variations of the electron loss rate based on the local time coverage of SAMPEX's orbit. Based on the fitting results of D_{dawn} and D_{dusk} for three storms, very little local time dependence was observed for the fast losses during the storm main phases, except for at L=5.5 in February 2009 storm, which will be discussed in detail later.

Therefore, fast precipitation losses of energetic radiation belt electrons are confirmed during the storm main phases, with higher energy electrons lost faster, over wide range of L regions, over the SAMPEX-covered local times, no matter what the magnitude of the geomagnetic storm was. What are the possible loss mechanisms for these fast losses? Electromagnetic ion cyclotron (EMIC) waves were suggested as capable of providing rapid loss of relativistic electrons on timescale of

hours during storms [Meredith et al., 2003a; Albert, 2003], with similar energy dependence in the pitch angle diffusion rates under the assumed EMIC waves and plasma properties [Summers et al., 2007]. But they are believed to be preferentially excited along the duskside of the plasmasphere and in the regions of plumes [e.g., Erlandson and Ukhorskiy, 2001; Summers and Thorne, 2003], which is not sufficient to explain the fast losses over wide L regions and local times in some of our results. However, the fast electron precipitation during the storm main phase indicates that some intense wave activity much be present to account for the fast pitch angle diffusion of electrons. Therefore, the underlying electron loss mechanism so far can only be understood as some quick scattering processes, which functions preferably on higher energy electrons. The specific wave mode that causes the loss deserves further study and observational proof, which could also be a comprehensive effect from the gyroresonant wave-particle interactions with various magnetospheric wave modes.

Strong diffusion. The electron lifetimes at L=4.5 during the main phase of the most intense storm, the September 2002 storm, are on the order of minutes for high energy electrons. Should they be classified as strong diffusions? Under strong diffusion, the pitch angle distribution of electrons is isotropic and the assumption that BLC is relatively empty in the Drift-Diffusion model will be violated. So we check the strong diffusion limits for the same energy ranges of the results in Figure 4.9. The calculated electron lifetimes with respect to the strong diffusion rates for 0.5 MeV to 2.83 MeV electrons at L=4.5 are all on the order of 10^{-3} day [page 77-80 in Schulz and Lanzerotti, 1974]. Therefore, according to the results shown in Figure 4.9, the losses of 2.0 MeV and 2.83 MeV electrons at L=4.5 in the September 2002 storm main phase are within the strong diffusion range and they break the weak diffusion assumption in the model. These are also consistent with the count rate versus longitude plot at L=4.5 during this time period (not shown here), where the trapped and DLC rates seem to decrease down to the level of the BLC rates. Under this situation, the current Drift-Diffusion model cannot accurately determine the electron loss rates, but only provide an

approximation. Since strong diffusion only happens in extreme cases, perhaps only for very intense storms, for electrons in a certain range of energies, and at limited time and locations, our model is still valid for the other cases and is generally applicable. It would be another project to improve the model for the strong diffusion case.

4.5.2 Other Features of Electron Lifetimes

After discussing the loss rates during the storm main phases, we look into others features of the losses over all the storm phases in the three events. The first is about the energy dependence in the electron lifetimes, which has been discussed for the storm main phases. During the prestorm intervals, the energy dependence index, α, is consistently negative for the two non-major storms during solar minimum (higher energy electrons lost faster) with lifetimes generally greater than 10 days (see Figures 4.5 and 4.7). However, for the intense storm the sign of α is positive at the peak electron flux location in the quiet interval before the storm (first column in Figure 4.9), but with lifetimes within the range of 1 to 10 days, shorter than the other two less intense storms. In some intervals of the storm recovery phases, when the electron lifetimes are still shorter than the prestorm levels, the sign of the energy dependence index basically remains the same with the storm main phases (being negative). This makes sense if the same loss mechanism is still active during those periods. However, when the electron lifetimes increase back to the prestorm values in the recovery phases, indicating slow loss processes for all energy electrons considered here, the sign of energy dependence could turn out to be reversed compared to the quiet interval before the storm (e.g., L=3.5 in the September 2002 storm and L=5.5 in February 2009 storm). Therefore, based on our results, we can conclude that the energy dependence in the electron lifetimes can vary with storms, with time during a storm, and with locations.

Another property to look into is the local time dependence of the electron loss rate. As I mentioned, for the February 2009 storm, a significant dawn/dusk asymmetry of the pitch angle

diffusion rates occurs during the storm main phase at L=5.5, with diffusion at dawn ~2000 times faster than that at dusk. To illustrate the strong LT dependence, the electron count rate data and three different model simulations for that time period (DOY 45.3-45.8 of 2009) at L=5.5 are shown in Figure 4.10, with the pattern similar to Figure 4.4. Panels (a)-(c) illustrate the same count rate data (filled triangles) but different simulation results (open triangles). The number indices are similar to those in panel (b) of Figure 4.2, which number the 33 crossings at L=5.5 within this half a day in chronological order, but with the dawnside crossings in red indices and the duskside crossings in black, so that we can clearly distinguish the dawnside and duskside measurements. By looking at the data (filled triangles), we notice the dawnside crossings (with red indices, basically on the right-hand side of each panel) generally have high count rates, which are almost on the same level with the trapped electron rates (green triangles), indicating a very fast pitch angle diffusion rate at dawn; while the duskside rates (with black indices, on the left-hand side) are very low, suggesting a slow diffusion there. Therefore, to simulate the count rates within this interval requires a strong dawn/dusk asymmetry.

Our model, with separate D_{dawn} and D_{dusk} values, is capable of resolving the LT dependence in D_{xx}. Panel (a) shows the best fit results from our model, simulating the entire count rate versus longitude distribution and the separation of the dawn/dusk count rates reasonably well, with $D_{dawn} = 10^{-6.022}\ \mathrm{sec}^{-1}$, $D_{dusk} = 10^{-9.399}\ \mathrm{sec}^{-1}$ and the model performance index K^2=0.23. So D_{dawn} / D_{dusk}=2382, with diffusion at dawn much faster than at dusk. To further support our results, we performed some test runs for this time interval without LT asymmetry. D_{dawn} is forced to be equal to D_{dusk}, with the case when PA diffusion at dawn and dusk are both fast in panel (b) ($D_{dawn} = D_{dusk} = 10^{-6.022}\ \mathrm{sec}^{-1}$) and the case with diffusion both slow in panel (c) ($D_{dawn} = D_{dusk} = 10^{-9.399}\ \mathrm{sec}^{-1}$). Compared with the results in panel (a), for the panel (b) case the

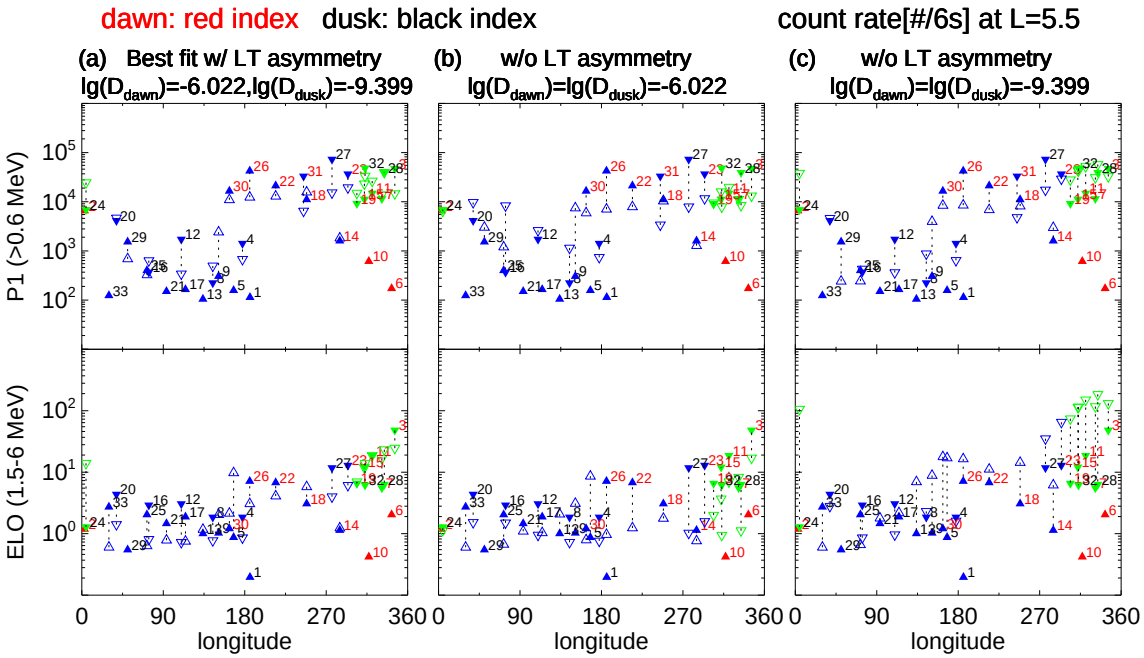

Figure 4.10: Electron count rate data (filled triangles) and three model simulations (open triangles) for counters P1 and ELO at L=5.5 during the storm main phase of 2009/02 storm. The pattern is similar to Figure 4.4 except for the number indices, which number the 33 crossings at L=5.5 within this half a day in chronological order, with the crossings in dawn in red indices and the crossings in dusk in black. Panel (a) shows the best-fit simulation from the model with dawn/dusk asymmetry ($\lg(D_{dawn})$=-6.022 and $\lg(D_{dusk})$=-9.399), compared with the simulations without dawn/dusk asymmetry, $\lg(D_{dawn})=\lg(D_{dusk})$=-6.022 in panel (b) and $\lg(D_{dawn})=\lg(D_{dusk})$=-9.399 in panel (c).

duskside count rates are generally over-reproduced by the model; while the dawnside count rate data are under-reproduced due to the insufficient simulation of the trapped electrons (green triangles). The K^2 for this case is ~0.37. However, for the case with slow diffusion at both dawn and dusk (panel (c)), the trapped electrons are greatly over-estimated and the entire count rate distribution is poorly simulated (K^2=0.53). Therefore, strong dawn/dusk asymmetry in D_{xx} is definitely necessary to model this interval.

Furthermore, by investigating the specific LT coverage of the SAMPEX crossings during this time period, we find that the observed fast pitch angle diffusion (with electron lifetimes on the order of hours) mainly occurs at ~08 hour LT. Even though we cannot rule out possible fast diffusion at other LT regions not covered by SAMPEX for this case, based on the distinct D_{dawn} and D_{dusk} values for the model results shown in panel (a) of Figure 4.10, it is confirmed that pitch angle diffusion, on average, is much faster at dawn than at dusk during the main phase of this storm at L=5.5.

Strong dawn/dusk asymmetry in the pitch angle diffusion rate is also found for the September 2002 storm (the most intense storm). But it appears in the early recovery phase (the first day in the recovery phase) and at L=3.5 (peak flux location), with dusk side 100 times faster than dawn. One thing to note is that during this early recovery phase, the electron lifetime is still short (~0.1 day, comparable to the lifetimes during main phase). For March 2008 storm, considerable dawn/dusk asymmetry shows up also during the early recovery phase (when the lifetime is also shorter than the quiet prestorm level, but in this case not comparable to the main phase values, but ≥10 times longer), and over a wide L range (L=4.5 to L=6.5), with dawn faster than dusk by 10~100 times. Those are the most significant local time variances of electron loss rates from our results, yet with very little local time dependence observed at other locations or during other storm phases.

The above are the primary characteristics of the electron lifetimes inferred from our model results. These features must be related to the changes in the scattering mechanisms, the wave spectra, and the plasma properties, the detailed analysis of which is yet beyond the scope of this paper. But the merit of our model is that using SAMPEX observation we can provide quantitative results on these detailed properties of the electron loss rates, which will lay the basis for the specific wave-loss mechanism studies.

4.5.3 Source Mechanisms

As I introduced, the estimated source rate from our model is comprehensive, including both radial diffusion and local heating. Can we separate them? For radial diffusion, the peak of electron phase space density (PSD) is at the outer boundary (higher L region) and the PSD gradient is positive throughout. So the electrons diffuse inward from the outer boundary and get energized. On the other hand, for in situ acceleration, there is an internal peak for PSD and the electrons can diffuse both inward and outward. For the estimated source rate, to quantitatively determine the relative contributions from radial diffusion and from local acceleration needs a more complicated model that explicitly includes the radial diffusion term, which will turn the 2D model to 3D.

Since here we have run the 2D model for a range of L values, is it possible to at least qualitatively disentangle radial diffusion from local heating by investigating the evolution of source rates at different L regions? This is still not easy considering the time length of each data interval, mostly daily during the recovery phase. Since within a day the MeV electrons can drift many times around the earth, if radial diffusion occurs, it is possible to see sources in all L for that interval; on the other hand, if local heating is active at some L region, within a day it can also diffuse to other L regions. Therefore, generally speaking, the variation timescale of the source rate in the current model is not enough to resolve the different evolutions of radial diffusion and internal heating. This is the case for the results of February 2009 and March 2008 storms. However, for September 2002

storm with results shown in Figure 4.9, we notice that during the early recovery phase (1st day in the recovery phase), the source is active only locally in L=3.5 and 4.5 but not in L=5.5 and 6.5. But later in the recovery phase, the active source appears at all L regions. Therefore, it is possible that during the early recovery phase local heating occurs at around L=3.5-4.5, and meanwhile, radial diffusion is too slow to transport electrons to other L regions. Later on, if the source rate at higher L (L=5.5-6.5) is due to outward diffusion from the internal source at L=3.5-4.5 or due to inward diffusion from some other external sources is still uncertain.

4.5.4 Parameter Sensitivity

We can investigate the parameter sensitivity of our model by calculating the change in the model metric K^2 (defined in Eq. 4.4) in response to a given fractional change (here as ±20%) in each of the free parameters (D_{dawn}, D_{dusk} and α in the diffusion term (Eq. 4.2), and S_0 and ν in the source term (Eq. 4.3)). The February 2009 event run at L=4.5 (Figure 4.4) is selected for the sensitivity study. We find that when pitch angle diffusion is strong the model is very sensitive to the diffusion-related parameters. For example, during the main phase of February 2009 storm (panel (b) in Figure 4.4), K^2 could change by ~10% with respect to the 20% change in D_{dawn}, and $D_{dawn/dusk}$ turns out to be more sensitive than the energy-dependence index α. However, when pitch angle diffusion is slow and the source term becomes more significant during the storm recovery phase (panels (c)-(f) in Figure 4.4), the model is more sensitive to the source term-related parameters and much less sensitive to the parameters in the diffusion term. For example, the values of K^2 can change by >20% for a 20% change in ν, the energy-dependence index in the source function, but varies only within 1% for the same fractional changes in all the diffusion-term parameters.

4.5.5 Model Limitations and Error Sources

Now I discuss the model limitations and some possible sources of error involved in the model and the simulation results. First, our model uses some simplified assumptions, such as the uniform exponential energy dependence in D_{xx} (Eq. 4.2) and S (Eq. 4.3) and the fixed power index 30 on x in D_{xx}. Although these parameterized forms of D_{xx} and S could differ from the estimations in quasi-linear wave studies [e.g., Li et al., 2007], which are also accompanied with uncertainties, the good performance of our model both in this paper and in Selesnick [2006] indicates that the forms of D_{xx} and S used in the model are generally reasonable. Second, as previously discussed, when the loss of the electrons is so fast that it approaches the strong diffusion limit, the current model is not accurate in determining the specific electron loss rates.

At high electron energies. Large uncertainties of the model results at high energies may occur when the electron count rate data from detector ELO and EHI are significantly low (close to the data background levels) and the energy dependence in D_{xx} represented by Eq. 4.2 is relatively strong (specifically, with $\alpha < -2$ from model experiments). Among all the model results shown in the chapter there are two such cases: the main phase results at L=5.5 for February 2009 storm and at L=4.5 for September 2002 storm. Under this situation, the energy-dependence index α is primarily determined by the low-energy data (or responses of PET detectors at low-energy range). Then the very low fluxes and short electron lifetimes at high energies are not well-constrained by the data, but directly derived from the uniform exponential energy dependence in Eq. 4.2. In other words, the limitation from the energy dependence form in D_{xx} leads to model inaccuracy at high energies. Therefore, for the two cases mentioned above there are uncertainties in the model results at high energy levels: specifically, in Figure 4.5 the much lower trapped flux j_0 and much shorter electron lifetimes of E≥2 MeV electrons at L=5.5 than at other L during the main phase of February 2009 storm; and similarly in Figure 4.9 the very low j_0 and short lifetimes at L=4.5 at E≥1.41

MeV during the September 2002 storm main phase. The lower threshold of the less-constrained model energy range for each case (e.g., 2 MeV for the first case and 1.41 MeV for the second) is determined by a sensitivity study (changing the model flux at the highest energy to zero to see if the simulated data change; if not, try the second highest energy, etc.). Thus for the second case, if the errors in the high energy lifetimes are truly significant, the strong diffusion scenario discussed at the end of subsection 4.5.1 may never occur.

At high L regions. Additional attention must be paid to the estimated loss rates for high L shell regions, where loss mechanisms other than pitch angle diffusion, such as magnetopause shadowing and outward radial diffusion, can be significant. In this case, the estimated loss rate would not be accurate but only provides an approximation of the overall loss. As to the quantitative estimate of the other two loss mechanisms a more complicated model that explicitly includes radial diffusion terms is needed. Another problem at high L lies in the L value calculation. The L values used in this study are obtained from the SAMPEX data, which are calculated based on the IGRF model. But during geomagnetically active times, such as the September 2002 storm, the external field from magnetospheric currents can be important, bringing errors into the L calculation. For these reasons we have compared the L values directly from the data and those calculated using the Tsyganenko 2001 storm model (T01S) parameterized by solar wind and geomagnetic indices, which is considered reasonably accurate at low altitude. The comparison shows that inside L=6 the IGRF L values from the data are quantitatively comparable to the T01S L values. Deviations are more obvious beyond L=6. But since during intense storms, the region inside L=6 is considered the more active region for electron precipitation where the electron count rate data are higher and show more dynamics, using the L values from the IGRF model is still fine for our main results.

Based on the limitation discussed above, it would be interesting to examine the loss rate results for L=5.5 and 6.5 in the September 2002 storm, which are generally energy-independent. We

calculate the last closed drift shell during this intense storm and find it could be as low as L^* =5.3 for electrons with 90° equatorial PA during the storm main phase (L^* here is Roederer L [Roederer, 1970] calculated using Tsyganenko 2001 storm model). So could it be magnetopause shadowing that caused the energy-independent losses at L=5.5 and 6.5 during the storm main and early recovery phases? The speculation is not supported by the fact that there is no sudden depletion of the trapped electron flux (j_0) at L=5.5 and 6.5 during the storm main phase (the first row of Figure 4.9). Considering the errors in L values discussed above and that the last closed drift shell is PA-dependent (the data we modeled are centered around DLC), L=5.5 and 6.5 in our model could still be closed drift shells even though the last closed drift shell for equatorially mirroring electrons is at L^*=5.3. So the loss mechanism at L=5.5 and 6.5 other than pitch angle scattering is more likely to be outward radial diffusion rather than direct magnetopause shadowing. And again, due to the errors in L calculation for high L regions and the fact that the count rates there are very low with more statistical errors, the results for September 2002 storm at L=5.5 and 6.5 could have more uncertainties.

At high equatorial pitch angles. The model works to simulate the whole pitch angle distribution although the data constraints from SAMPEX only cover low equatorial PA range around the loss cone angles. To constrain the model results at high equatorial PA, high-altitude data covering larger equatorial PA could be used, as carried out in Selesnick et al. [2003]. We agree it would be a plus for this work if our model results are also compared against observations at higher altitude. But it is not performed here since the focus in this work is the electron loss rate, for which using the low-altitude data from SAMPEX is adequate. This is because the SAMPEX data already well-cover the BLC, DLC and some trapped-electron PA, and based on previous simulation work we know that if the PA distribution reaches an equilibrium shape the electron loss rate is primarily controlled by the minimum PA diffusion rate [Albert and Shprits, 2009], near the edge of the loss

cone in our model. Therefore, even without constraints on model results with high equatorial PA, the estimated electron loss rates from our model are still reliable. However, the quantified electron source rates will have fewer uncertainties for the PA ranges covered by SAMPEX, and more uncertainties at higher equatorial PA close to 90^{o}.

Adiabatic corrections. In this work we don't perform the adiabatic corrections on the model results. It was shown previously [Selesnick, 2006] that for low-altitude electron data, the most significant adiabatic effects are the changes in mirror point altitudes and the associated energy changes during intense storms. The adiabatic intensity change observed by SAMPEX due to the rise of the mirror points can be quickly compensated by even moderate pitch angle diffusion. And by investigating if the DLC is empty we can easily determine whether such diffusion has occurred.

Selesnick [2006] proved that the adiabatic effects were small for low-altitude electrons based on the model results for two intense storms, although only for small L=3.5. But we find he didn't include the drift shell expansion when estimating the adiabatic effects, even for equatorially mirroring electrons (private communication). We know that DLC electrons are not affected by adiabatic processes since they are lost within one drift period, faster than the adiabatic timescales (~hrs for MeV electrons in outer radiation belt). In the main phases of our storm events, the quasi-trapped electron intensities in the DLC are generally higher than the BLC electrons and they are flatly distributed over longitudes, indicating that non-adiabatic processes are dominant for these events. However, based on calculations that will be discussed in the next chapter, we find that even though the adiabatic rise of mirror points can be quickly compensated by even moderate pitch angle diffusion, the adiabatic effects alone can be significant for low-altitude electrons and combined with the non-adiabatic pitch angle diffusion, the adiabatic change of electron pitch angle distributions can cause increased electron precipitation without changing the pitch angle diffusion rate. Therefore, even though we believe pitch angle diffusion is dominant over adiabatic effects for the studied

events, including adiabatic corrections in our model is still necessary, to improve the model fit to the data and the quantification of the pitch angle diffusion rate. This is one of our future works.

Resolved lifetime variations. Another limitation of the current model is that it cannot resolve the variations of the electron loss rates on timescales shorter than 12 hours, which is constrained by the length of time required for SAMPEX data to reach full longitude coverage. This is currently the best we can get out of the available data. Even though the model parameter values vary rapidly between intervals, the changes of model intensities are still gradual (as seen in e.g. first row of Figure 4.9), as it takes time for the model to respond to the new set of parameters. Additionally, due to the nature of electron lifetime (only defined for an equilibrium state as discussed in Section 4.3), the estimated electron lifetime merely represents an average loss over each modeled period (1/2 day to a day), which indicates the possibility that sometime during that interval the instantaneous electron loss rate can be actually higher, e.g., faster than hours for February 2009 storm main phase.

In order to apply estimated lifetimes to the Fokker-Planck model discussed in Chapter 3, the model needs to be improved to resolve faster lifetime variations than every half a day, since the electron loss rate can change much faster [Lorentzen et al., 2001; Shprits et al., 2009]. We first try to simulate the electron lifetimes every two hours instead of every day or half a day. The model results are shown in Figure 4.11 for the prestorm (Feb 13.3-14.3) and main phase (Feb 14.3-14.8) of the February 2009 storm at L=4.5 and for 1MeV electrons. The lifetimes every two hours are shown as red points, with the horizontal bar of each point indicating the time range of each fit and vertical bar in red indicating the error bar associated with each lifetime. The dashed lines are the old lifetime results as in Figure 4.5, a constant value for the day before the storm and another constant value for the storm main phase. We notice that the two-hour lifetimes do show more variations and for some two-hour intervals (e.g., the 13^{th} and 18^{th} interval), a source is required to reasonably fit the data within that interval, which was not needed in the old day and half-a-day runs. Since there are much

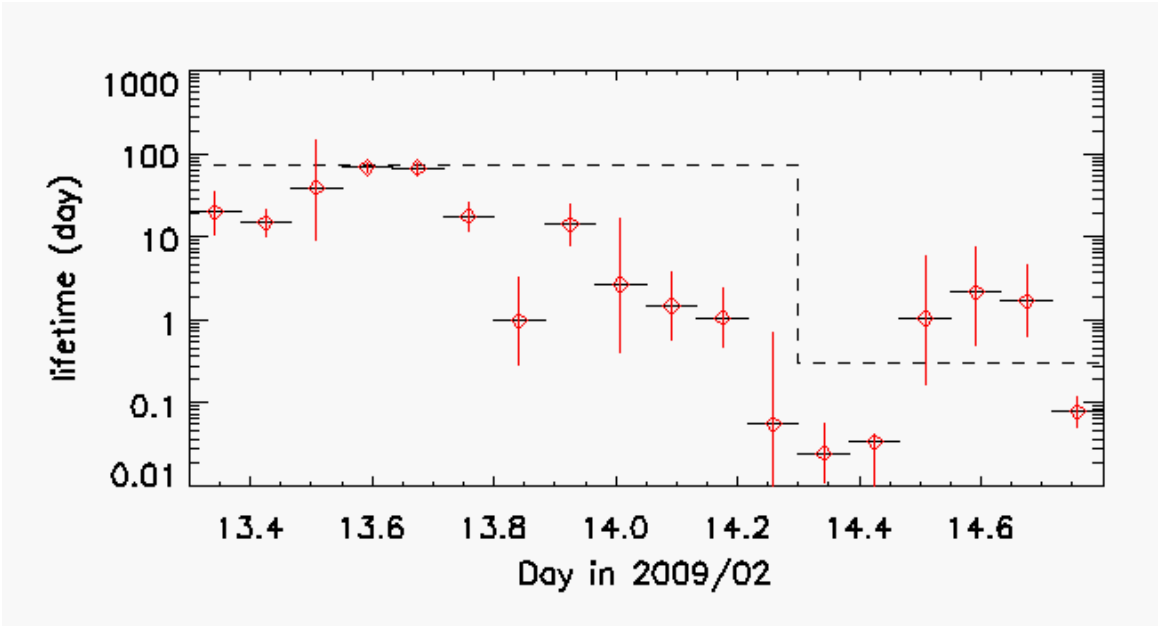

Figure 4.11: Electron lifetime results every two hours (red points) for the prestorm and main phase of the February 2009 storm at L=4.5 and for 1MeV electrons, with the horizontal bar of each point indicating the time range of each fit and the vertical bar in red indicating the error bar associated with each lifetime. The dashed lines are old lifetime results from Figure 4.5.

fewer data points to fit within each two-hour interval (4 to 6 points from each counter), data constraints are much weaker resulting in bigger error bars with the modeled lifetimes as shown by the red bars, sometimes covering a order of magnitude. We find the error bars can be very different from interval to interval due to different levels of data constraints. Therefore, to improve the resolved variations from model, there is always a compromise between the level of variations we want to resolve and the parameter uncertainties we can accept.

To compensate for the insufficient data constraints available from SAMPEX for each two-hour interval, we try to assume a correlation of electron lifetime between two consecutive two-hour intervals and make use of the prior information from the previous interval. We know the lifetimes can change quickly with time and ideally there should be no time correlations. But since the SAMPEX data cannot resolve fast changes, this is still worth-trying. After several trial runs we find that the estimated lifetime results can be very different depending on how the prior information and the fits are handled (for details see Appendix B). This is possibly due to the non-linearity of the system, and it indicates that this approach is not very promising.

Therefore, if we want to fundamentally improve the lifetime variations the model can resolve, also with small uncertainties, more and faster data coverage is required. For example, we can use data from a cluster of Low-Earth-Orbit (LEO) satellites covering different longitudes at the same time instead of only from SAMPEX. In that way, the measured electron data can reach full longitude coverage much faster than in half a day. One possibility is to use the relativistic electron measurements from existing NOAA Polar Orbiting Environmental Satellites (POES), which are in Sun-synchronous orbits at ~800-850 km altitudes. Simultaneous data are now available from at least four POES spacecrafts, NOAA 15, 16, 17, and 18, with their orbit distribution shown in Figure 4.12 panel (a) [Horne et al., 2009]. But proton contamination needs to be carefully removed for clean relativistic electron data [Lam et al., 2010]. Another proposed mission concept that is extremely

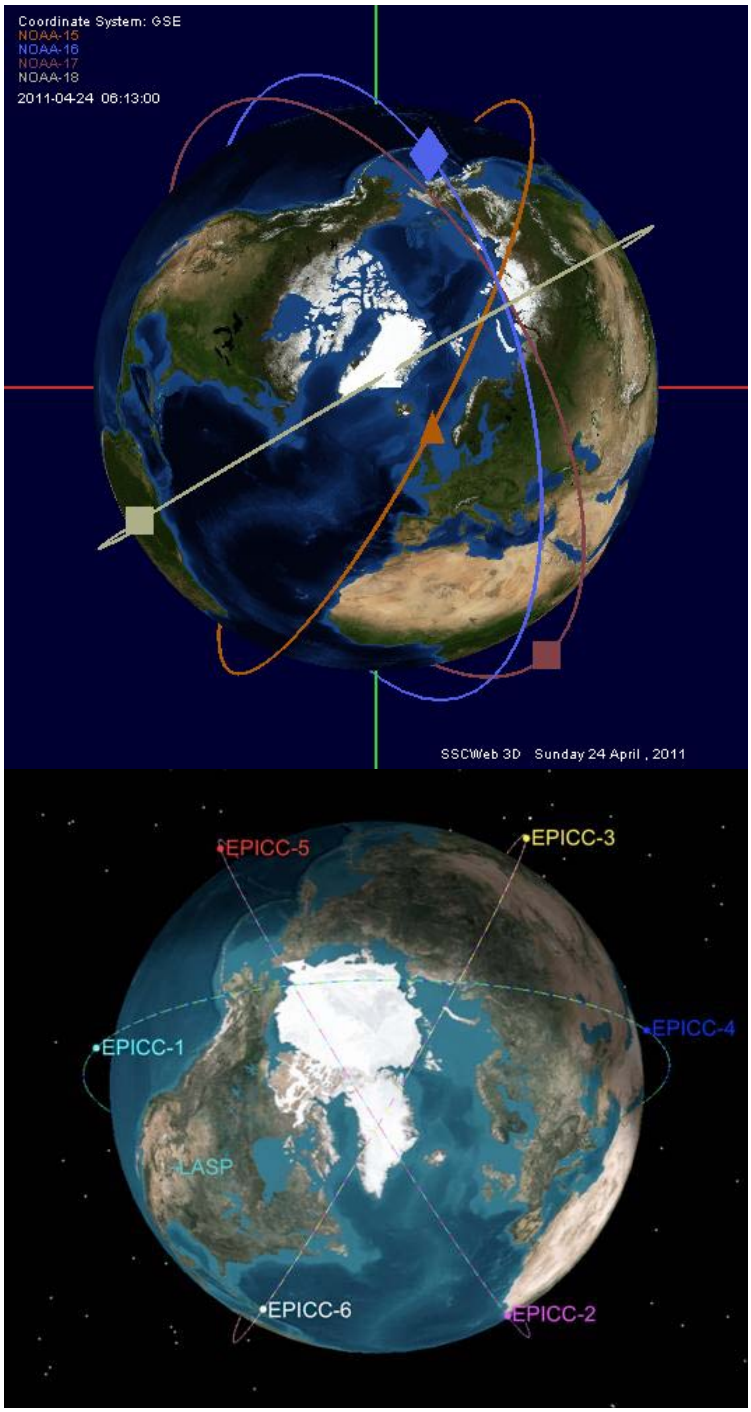

Figure 4.12: Panel (a) is the orbit configuration of four NOAA/POES satellites, named NOAA 15 (orange), 16 (blue), 17 (red), and 18 (white), provided by TIPSOD (Tool for Interactive plotting, sonification, and 3D Orbit Display). Panel (b) is Satellite Tool Kit model showing orbit configuration for mission concept of Energetic Particles from a highly Inclined Constellation (EPhIC), consisting of 9 LEO satellites in three different polar orbits. Along each orbit, the three spacecraft are each separated by 120°. Note spacecraft 7-9 are behind the Earth (courtesy of Drew Turner).

useful is called Energetic Particles from a highly Inclined Constellation (EPhIC), which includes nine Relativistic Electron and Proton Telescope integrated little experiment (REPTile) on three LEOs, separated by 120° in longitude of their ascending nodes, with three REPTiles uniformly distributed on each LEO, as shown in Figure 4.12 panel (b) [Li et al., 2010]. This mission is proposed in a white paper titled "Energetic Particles from a highly Inclined Constellation (EPhIC)" submitted to the National Research Council (NRC) for the 2010 "decadal survey" in solar and space physics (heliophysics), which I am a co-author of. The three LEOs separated by 120° in longitude (4 hr in local time) ensure full longitude coverage every 4 hours, instead of half a day from a single orbit. In addition, with three REPTile instruments per orbit on three different LEOs, EPhIC will measure outer belt electrons 36 times in one orbital period, ~1.5 hr, or about 576 times in a day. Therefore, the multiple-point measurements will be very useful to better determine the rates and the spatial and temporal variations of the precipitation loss of the outer radiation belt electrons.

4.5.6 Merits of Our Method for Electron Lifetime Quantification

As discussed in the beginning of this paper, the uncertainties and difficulties in the theoretical precipitation loss studies have guided researchers to use the empirical forms of electron loss rates (e.g., depending on the geomagnetic indices), which are inconsistent and can differ by an order of magnitude. Our method, directly comparing the Drift-Diffusion model results with the low-altitude electron data, is capable of providing more reliable results on the quantification of electron loss rate, as well as its temporal and spatial variations, as shown in Figures 4.5, 4.7 and 4.9. The results from this work can be applied to e.g., particle tracing codes, radial diffusion codes, and comprehensive radiation belt dynamics models.

It is also interesting to compare the results of the electron loss rates from our model approach to results from the theoretical quasi-linear wave study approach. Summers et al. [2007] performed a comprehensive study of the theoretical quasi-linear pitch angle diffusion rates of the outer zone

radiation belt electrons, due to the scattering by chorus, plasmaspheric hiss, and EMIC waves, separately and in combination. They made certain assumptions on the wave and plasma properties and then the bounce-averaged pitch angle diffusion coefficients and corresponding electron loss timescales were evaluated. They found that the precipitation loss timescales of electrons due to resonant pitch angle diffusion by each of the wave modes, chorus, hiss, and EMIC waves, can be one day or less, and are also energy and L dependent.

Specifically, the results on the electron precipitation by plasmaspheric hiss showed that during low geomagnetic activity times and for electrons with energy exceeding 500 keV, the loss timescales over the range $3 \leq L \leq 5$ are between 1 to 10 days, with higher energy electrons lost slightly slower. This is generally consistent with our electron lifetime results during the quiet interval before the September 2002 storm for electrons with similar energy range and at similar L locations (see Figure 4.9). Summers et al. [2007] also suggested that the electron loss timescales due to EMIC wave scattering, over the energy range 0.9-5 MeV and at L=3-5, are on the order of hours, decreasing as L gets larger, and with faster loss at higher energies. We also see the similar features in our main phase electron lifetimes at L=3.5 and L=4.5 for September 2002 storm and at L=4.5 for the other two storms.

As described above, we can always try to match our model results to the theoretical wave study results aiming at revealing the primary wave mode that causes the electron loss. However, without comprehensive observational data on the spectral properties of these waves and on the other assumed factors in the theoretical study listed above, the theoretical quasi-linear wave approach is not able to accurately determine the electron loss rate and its variations, and those observations are beyond our current capabilities. On the other hand, our model approach combined with the low-altitude electron data can directly quantify the simultaneous electron loss rates, not requiring detailed information on the above factors, which is another advantage of our method. Therefore, it

will be useful to turn the other way around and refer to the quantitative electron loss rate results from our model approach in the theoretical wave-loss studies.

4.6 Summary and Conclusions

In this chapter, the rates and the spatial and temporal variations of electron precipitation loss to the atmosphere in the Earth's radiation belt were studied. Since the electron bounce loss cone opens up at low altitude, the low-altitude electron measurements are the most useful in determining the electron precipitation loss rate into the atmosphere, for which we used the SAMPEX/PET electron count rate data. A Drift-Diffusion model was adapted from previous work to simulate the low-altitude electron distribution observed by SAMPEX as a delicate balance of azimuthal drift, pitch angle diffusion, and possible concurrent sources. After pursuing the best fit of the modeled electron rates to the data within each time interval (one day or half a day), the optimum sets of parameter values were obtained, based on which the magnitudes and variations of the electron lifetime can be quantitatively determined.

Three magnetic storms that fall into different categories of storm magnitude were selected for detailed study, including a small storm and a moderate storm within the current deep solar minimum and an intense storm right after the last solar maximum. The loss rates for electrons with energy from ~0.5 to 3 MeV were estimated at L regions from L=3.5 to L=6.5 over different phases of the three individual storm events. One common feature of the electron lifetimes was discovered based on our model results, that during the storm main phases of all the three events, fast precipitation losses of energetic radiation belt electrons, as short as hours, persistently occur over a wide range of L regions and over all the local times covered by SAMPEX, and with faster loss for higher energy electrons. The underlying electron loss mechanisms remain an open question, but the results strongly indicate that there must be some quick scattering processes, functioning preferably on higher energy electrons. Some other properties of the electron loss rates were also investigated in

this chapter. Model results over different phases of the three individual events and at various L locations suggest that the energy dependence in the electron lifetimes differs for different storms, and could be time-dependent and L-dependent. And significant dawn/dusk asymmetry in the electron loss rate can show up during the storm main phase or recovery phase in different storms, with the pitch angle diffusion rate at dawn faster than at dusk or vice versa, but primarily around the peak electron flux locations.

The method used in this chapter, combining the low-altitude observations with the Drift-Diffusion model, is capable of providing direct quantification of the electron loss rate, which is a required step towards developing comprehensive models for the radiation belt electron dynamics, and is capable of determining the spatial and temporal variations of the electron precipitation loss into the atmosphere, useful for the theoretical wave-particle interaction studies towards revealing the underlying loss mechanisms. Applying electron measurements from a cluster of Low-Earth-Orbit satellites instead of using data only from SAMPEX, the model will be able to resolve electron loss rate variations faster than every half a day.

Chapter 5

Modeling Adiabatic Electron Loss: Adiabatic Effects on Radiation Belt Electrons at Low Altitude

This chapter is based on the paper titled *"Adiabatic Effects on Radiation Belt Electrons at Low Altitude"* by Tu, W. and X. Li, in press in *J. Geophys. Res.* in 2011.

5.1 Introduction

Outer radiation belt MeV electron fluxes vary greatly during geomagnetic storms [e.g., Baker and Kanekal, 2008; Tu et al., 2009]. They are observed to decrease during storm main phases and increase in storm recovery phases [e.g., Reeves et al., 2003; Tu et al., 2010]. The causes of these variations can be classified into adiabatic and non-adiabatic processes [e.g., Li and Temerin, 2001b; Friedel et al., 2002; Millan et al., 2007; and references therein]. Non-adiabatic processes cause irreversible electron variations by breaking at least one of the three adiabatic invariants [e.g., Li et al., 1997; Tu et al., 2009]; while adiabatic processes cause reversible variations [Li et al., 1997; Kim and Chan, 1997; Selesnick and Kanekal, 2009]. The classification is quite clear, but since the observed changes are a mixed result of both processes, distinguishing between them by looking at the data alone is difficult. This warrants a quantitative analysis of pure adiabatic variations, which will help to determine the real (or non-adiabatic) losses in the radiation belt system.

The topic of adiabatic variations of radiation belt electrons is not new [e.g., McIlwain 1966, 1996]. Based on the resemblance of the temporal profile of energetic electron fluxes to the Dst profile, Li et al. [1997] introduced the term 'Dst effect' to describe the adiabatic effects on energetic electrons due to changes in the magnetic field from the storm time ring current. Kim and Chan [1997] showed that adiabatic effects cause flux decreases of more than an order of magnitude for 1

MeV and 2 MeV electrons mirroring at the equator when Dst reaches -100 nT. Here, however, we focus on (smaller pitch angle) electrons mirroring at low altitudes.

Electron intensity variations measured by SAMPEX, a satellite in a low-altitude, polar orbit (~600 km, 82°) [Baker et al., 1993], also seem to correlate well with Dst, as shown in Figure 5.1. The top three panels in Figure 5.1 panel (a) show the daily-averaged electron count rates (color-coded) observed by SAMPEX/PET from three different counters (P1, ELO and EHI) [Cook et al., 1993]. In each panel, the x-axis is time during the March 2008 storm and the y-axis is L (the radial distance of the magnetic field line in the equatorial plane under the dipole field approximation). The electron count rate drops significantly during the storm main phase and recovers as Dst recovers. Figure 5.1 panel (a) leads to our first question: are these storm-time variations adiabatic responses to geomagnetic field variations? We expand the daily-averaged data in more detail to look at variations at fixed L in Figure 5.1 panel (b). The first panel contains data from a day before the storm, the middle panel shows half a day during the storm main phase and the last panel is in the early recovery phase. Within each panel, the data points are organized in geomagnetic longitude to distinguish them as trapped, drift loss cone, and bounce loss cone electrons. For a more detailed description of these data, refer to Figure 4.2 in Chapter 4. Figure 5.1 panel (b) shows that the trapped electron count rates (green points) at L=4.5 drop by almost an order of magnitude during the storm main phase. The second question we would like to address is: quantitatively, how much of the main phase intensity drop is due to the adiabatic effects?

5.2 Adiabatic Effects at Low Altitudes

The three adiabatic invariants are $\mu = p_{\perp}^2 / 2m_0 B$ (the first invariant), $J = \oint p_{\parallel} ds$ (the second invariant, more often we use the derived quantity $K = J / 2\sqrt{2m_0 \mu}$), and $\Phi = \oint \vec{B} d\vec{A}$ (the third invariant, on which Roederer L is defined as $L^* = 2\pi M / (\Phi R_E)$, where M is Earth's

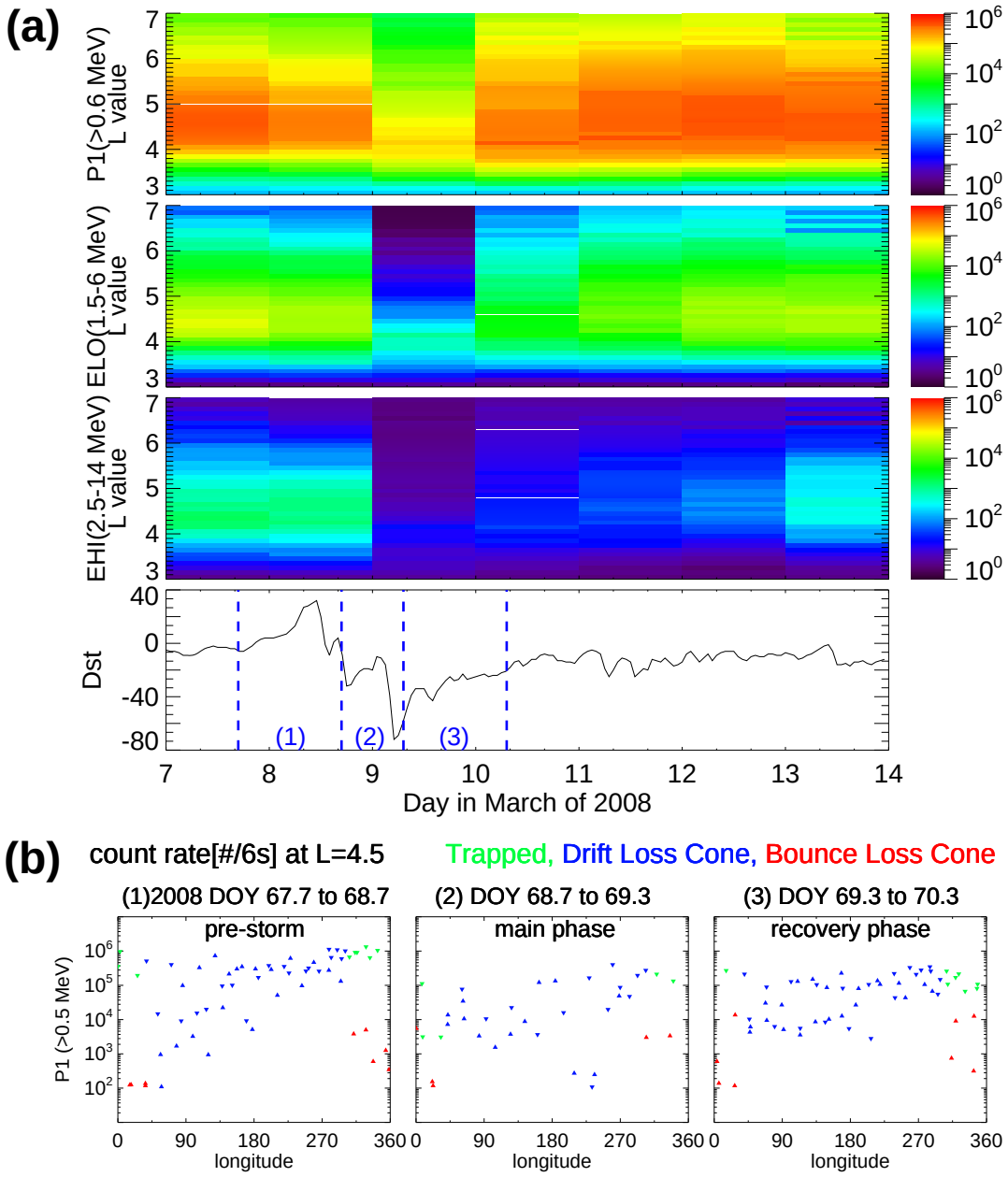

Figure 5.1: Panel (a) show the electron count rate during the March 2008 storm detected by three SAMPEX/PET counters: P1, ELO and EHI, respectively. It is the same figure as shown in Figure 4.6. Panel (b) shows the electron count rate data at L=4.5 from the P1 counter during (1) a quiet pre-storm interval, (2) storm main phase, (3) early recovery phase of the March 2008 storm. The three intervals are marked in the Dst profile above.

magnetic moment) [Roederer 1970]. Here we are interested in fully adiabatic processes in which all three adiabatic invariants are conserved.

There are three adiabatic effects on electrons mirroring at low altitude, each related to the conservation of one adiabatic invariant [Selesnick, 2006]. First, as a storm develops the ring current builds up and decreases the magnetic field in the inner magnetosphere. To conserve the third adiabatic invariant drift shells expand radially. As illustrated by Figure 5.2 panel (a), the projection of the drift shell at L^*=4.5 expands from the black field line at Dst = 0 nT to the red field line at Dst = -72 nT (minimum Dst of the March 2008 storm). Second, due to the stretching of the field line, to conserve the second adiabatic invariant K, the electron mirror point rises in altitude (from point P_1 to P_2). The field lines and mirror point locations in Figure 5.2 are calculated using the modified dipole model, which will be introduced in Section 5.3. Third, the rise of the mirror point implies a reduction of the magnetic field at the mirror point and thus a reduction in the electron energy due to the conservation of μ, which changes the measured electron flux for a given energy. The electrons mirroring at low altitudes have small equatorial pitch angles (for example, for Dst =0 nT and L^*=4.5, electrons mirroring at 600 km have an equatorial pitch angle of ~ 5.1°).

Among the three adiabatic effects described above, the rise of the mirror point in altitude is unique for low altitude observations. In Figure 5.2 panel (a), the rise of the mirror point appears small since it is on the scale of the entire field line. For greater detail I zoom into the boxed region of Figure 5.2 panel (a) in panel (b), where the rise of the mirror point from P_1 to P_2 is more evident. The blue boundary is the Earth's surface and the blue curve, 100 km above the Earth's surface, is defined as the bounce loss cone boundary, below which energetic electrons are considered lost into the atmosphere [Kennel, 1969; Blake et al., 2001]. As shown in Figure 5.2 panel (b), if all the electrons originally mirroring below P_1 (the grey region) during quiet time, t1, mirror above P_1 (the red region) at storm time, t2, a satellite at the same altitude with P_1 would see zero flux at t2. This

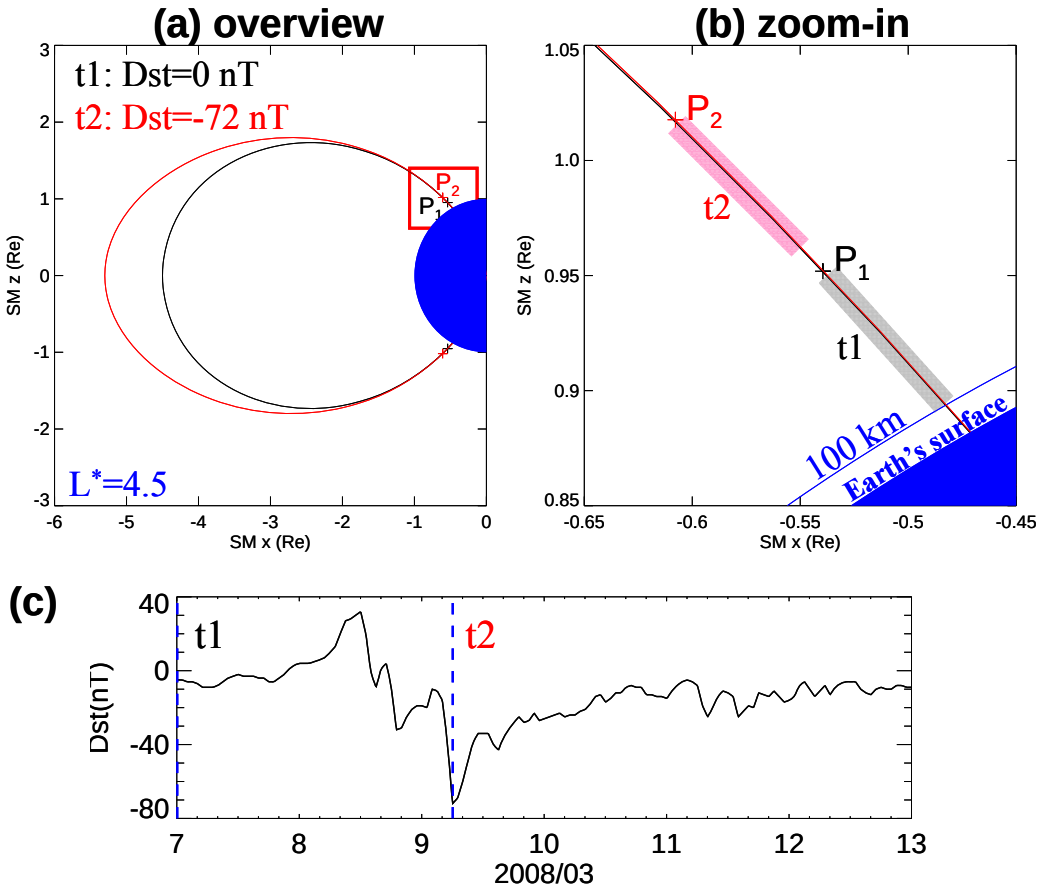

Figure 5.2: Panel (a) illustrates the expansion of the drift shell and the rise of the mirror point for L^*=4.5 during the storm main phase. The rise of the mirror point from P_1 to P_2 (boxed region in panel (a)) is zoomed-in in panel (b). The two shaded regions represent the same electron population at two times, t1 and t2, as marked in the Dst profile in panel (c) (t1 overlaps the vertical axis on left).

case represents a very significant adiabatic flux change at low altitudes. We quantitatively evaluate the rise of the mirror point for a real storm in the following section.

5.3 Quantification of the Rise of the Mirror Point in Altitude

Here we calculate the rise in altitude of the mirror point during the March 2008 storm shown in Figure 5.1. The problem is: given a mirror point P_1 at 600 km and L^*=4.5 before the storm (t1 in Figure 5.2 panel (c)), find a new mirror point P_2 at the minimum Dst (t2 in Figure 5.2 panel (c)), conserving all three adiabatic invariants. For the L^* and K calculation, a global magnetic field model is needed.

For the analysis in this and the following sections we choose the modified dipole model introduced in Selesnick and Kanekal [2009]. It combines the Earth's dipole field with a uniform southward magnetic field whose magnitude equals the Dst index. Figure 5.3 compares the pure dipole model (solid curves) with the modified dipole model (dashed curves). The dashed field lines for Dst = -72 nT are stretched, representing the effects of the ring current. Using this model, L^* can be calculated because it is an analytic function of r_{eq} (radial distance at the equator) and Dst (Equation 10 in Selesnick and Kanekal [2009]).

Based on the modified dipole model, we find that in order to conserve L^* and K, electrons originally mirroring at 600 km at L^*=4.5 (P_1 at time t1) mirror at 1181 km at Dst minimum (P_2 at t2) and, additionally, that the quiet-time 100 km mirror point rises to 637 km. Therefore, all the electrons initially mirroring between 100 km and 600 km rise to between 637 km and 1181 km, indicating that a satellite at the same altitude as P_1 (600 km, ~ SAMPEX's altitude) would see no flux during the March 2008 storm at Dst minimum, if only considering adiabatic processes.

5.4 Adiabatic Changes of Electron Flux at Low Altitude

5.4.1 Problem and Method

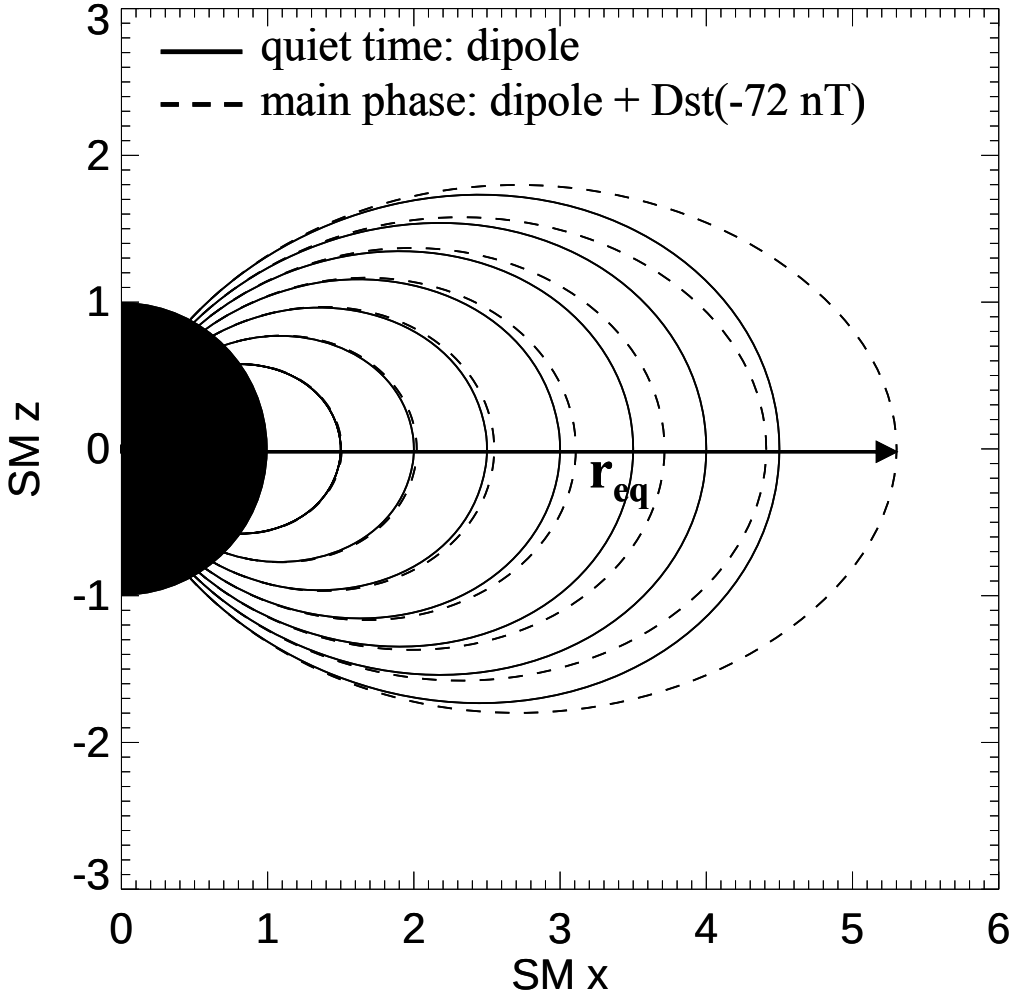

Figure 5.3: Comparison between the field lines of the dipole model (solid curves) and those of the modified dipole model with Dst = -72 nT (dashed curves).

The three adiabatic effects work together to change the electron flux at low altitudes. Here for the March 2008 storm, we calculate the adiabatic flux variations of electrons mirroring at a fixed altitude and L^* (600 km, ~ SAMPEX's altitude, and L^*=4.5), so that the results can be compared with observations from SAMPEX shown in Figure 5.1 panel (b). L^*=4.5 is chosen because it is the peak flux location during this storm (Figure 5.1 panel (a)). We look at electrons with a fixed energy. We estimate flux j_2 at 600 km and L^*=4.5 for electrons with energy E_2=1MeV at different times during the storm (total 144 points with 1 hr resolution), as indicated on the top of Figure 5.4 panel (a). Note throughout this section, terms with subscript '1' indicate they are at fixed quiet time t1 (marked in Figure 5.2 panel (c)); while terms with subscript '2' corresponds to time t2, times within the storm starting from t1.

The calculation method for j_2 at time t2 is described as follows, corresponding to each step of the calculation procedure shown in Figure 5.4 panel (a).

Step 1: Find r_{eq2}. To conserve L^*=4.5, $r_{eq1,}$ the radial distance of the field line at the equator at quiet time t1 (dipole field), is 4.5 Re (marked in Figure 5.4 panel (b)). At time t2, given the Dst value, r_{eq2} can be calculated (Equation 10 in Selesnick and Kanekal [2009]).

Step 2: Calculate quantities at t2. We trace the field line from the equatorial point at r_{eq2} to obtain the entire field line at L^*=4.5 at t2 (the red curve in Figure 5.4 panel (b)). Since we look at a fixed mirror point at 600 km at t2, on the red field line we can find the location of P_2, and calculate the equatorial pitch angle of electrons mirroring at P_2 as α_{eq2}, the local magnetic field strength at P_2 as B_{m2}, and the corresponding K value (2nd adiabatic invariant).

Step 3: Calculate mapped quantities at quiet time t1. Now we have α_{eq2} and E_2 (fixed as 1 MeV), we cannot directly calculate j_2 because the energy spectrum and pitch angle distribution of

(a) Goal: $j_2(E_2 = 1\text{MeV}, 600\text{km}, L^* = 4.5)$

1. $L^* = 4.5 \xrightarrow{\text{Dst at t2}} r_{eq2}$

2. $r_{eq2} \xrightarrow{\text{mirror at 600km}} \text{P}_2 \text{ location}, \alpha_{eq2}, B_{m2}, K$

3. $\begin{cases} r_{eq1} \xrightarrow{\text{conserve K}} \text{P}_1 \text{ location}, \alpha_{eq1}, B_{m1} \\ (E_2, B_{m1}, B_{m2}) \xrightarrow{\text{conserve } \mu} E_1 \end{cases}$

4. $(E_1, \alpha_{eq1}) \xrightarrow{\text{assumed quiet time } j_1(E,\alpha_{eq})} j_1(E_1, \alpha_{eq1}, r_{eq1})$

$$j_2(E_2, \alpha_{eq2}, r_{eq2}) = j_1(E_1, \alpha_{eq1}, r_{eq1}) \times (B_{m2} / B_{m1})$$

(b)

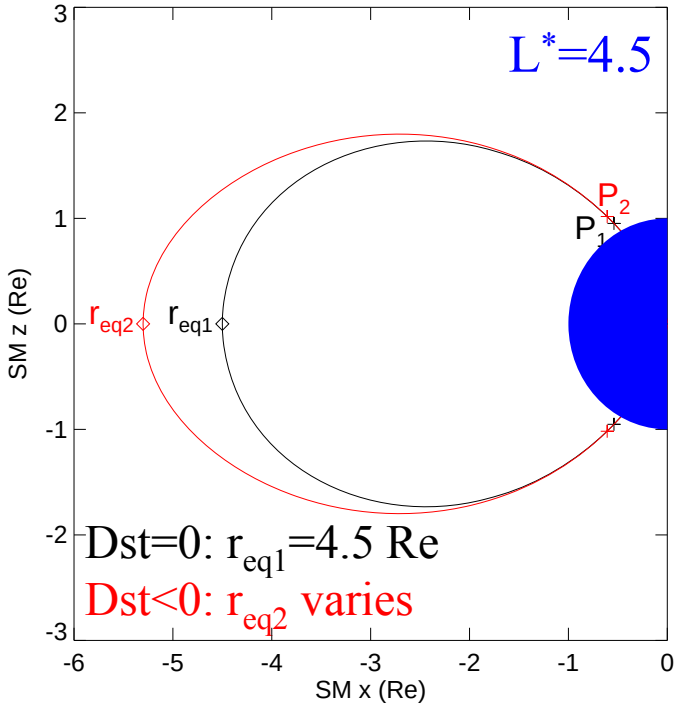

Figure 5.4: The calculation procedure for the adiabatic flux change at a single time step during the storm, including four steps, with auxiliary figure illustrations shown in panel (b).

j_2 varies with time. Therefore, we need to consistently map the j_2 state back to the quiet time state, whose flux distribution is used as a fixed reference and is assumed to be:

$$j_1(E,\alpha) = \begin{cases} j0 \times E^{-3} \times \sin^2 \alpha & \text{mirror point above 100 km} \\ 0 & \text{mirror point below 100 km} \end{cases} \quad (5.1)$$

The electron energy spectrum normally follows a power law with index = 3 [Burin des Roziers and Li, 2006] and the pitch angle distribution is assumed 90 degree peaked with power index = 2 on a sine function [Gannon et al., 2007]. We use $j0 = 6.5 \times 10^5$ (#/cm^2 sr s MeV) (E in Equation 5.1 is normalized by 1 MeV) to make the j_1 distribution consistent with the observed quiet time spectrum from the SAMPEX PET/PHA data [Tu et al., 2010]. On the other hand, when the electrons are within the bounce loss cone the flux is zero.

In the mapping, to conserve the K value obtained in step 2, we find the mapped, quiet time mirror point (P_1 in Figure 5.4 panel (b)), and acquire the magnetic field at P_1 (B_{m1}) and the equatorial pitch angle of electrons mirroring at P_1 (α_{eq1}). To find point P_1, we trace the field line from the equatorial point at r_{eq1} and iterate the calculation of K until it is equal to the K value of P_2 from step 2. Using conservation of μ, the mapped quiet time electron energy, E_1, can be calculated:

$$E_1 = -mc^2 + \sqrt{(mc^2)^2 + \frac{B_{m1}}{B_{m2}}(E_2^2 + 2mc^2 E_2)} \quad (5.2)$$

Step 4: Calculate fluxes. Using E_1, α_{eq1}, and Equation 5.1, the mapped quiet time electron flux j_1 can be calculated. Then based on Liouville's theorem, j_2 is calculated from j_1 using the derived equation [Schulz and Lanzerotti, 1974; Kim et al., 2010]:

$$j_2(E_2, \alpha_{eq2}, r_{eq2}) = j_1(E_1, \alpha_{eq1}, r_{eq1}) \times (B_{m2} / B_{m1}) \quad (5.3)$$

5.4.2 Results: Two Cases of Adiabatic Flux Change at Different Altitudes

We repeat the above procedure for each hour of the storm and obtain j_2 at 600 km and L^*=4.5 for one MeV electrons from March 7th to March 13th. The results are shown in Figure 5.5 panel (a). The top five panels show intermediate results for calculating j_2, showing variations of r_{eq2} (from step 1 in subsection 5.4.1), altitude of the mapped mirror point P_1 at quiet time (from step 3), mapped equatorial pitch angle α_{eq1}, energy E_1 (both from step 3), and mapped electron flux j_1 at quiet time (from step 4), respectively. The resulting j_2 variation is shown in panel (a6), with the Dst profile in the bottom panel. The variations of all the plotted quantities correlate well with the Dst profile. The drop of α_{eq1} and the increase of E_1 both contribute to the decrease of j_1. Near Dst minimum, we find two null j_1 points (circled in red), which correspond to the two points in panel a2 (also circled) showing that the mapped mirror point at quiet time is below 100 km. Therefore, for the resulting j_2 variations, we find that the flux decreases as Dst drops, and disappears at minimum Dst.

We perform the same calculation for a slightly higher altitude, 700 km. The results are shown in Figure 5.5 panel (b) in the same format as in Figure 5.5 panel (a). In this case, the altitude of the mapped mirror point at quiet time reaches a minimum of 158 km at Dst minimum (panel (b2)), still above the 100 km atmosphere boundary. So the flux, j_2, does not disappear, but decreases by a factor of 2.67 at Dst minimum (panel (b6)). This is the second case of the electron flux drop at low altitude due to the adiabatic effects during the storm main phase. These two cases are discussed further in subsection 5.5.1.

5.4.3 Energy Dependence of the Adiabatic Flux Change

Performing the same calculation for eight logarithmically spaced energies from 0.5 to 5.66 MeV, we find that the electron flux decreases at all energies (Figure 5.6 panel (a)). As shown in Figure 5.6 panel (b), the decrease factors at Dst = -72 nT range from 2.4 to 2.8 for electrons with energies from 0.5 to 5.66 MeV at L^*=4.5 and 700 km altitude. The decrease factor, which is

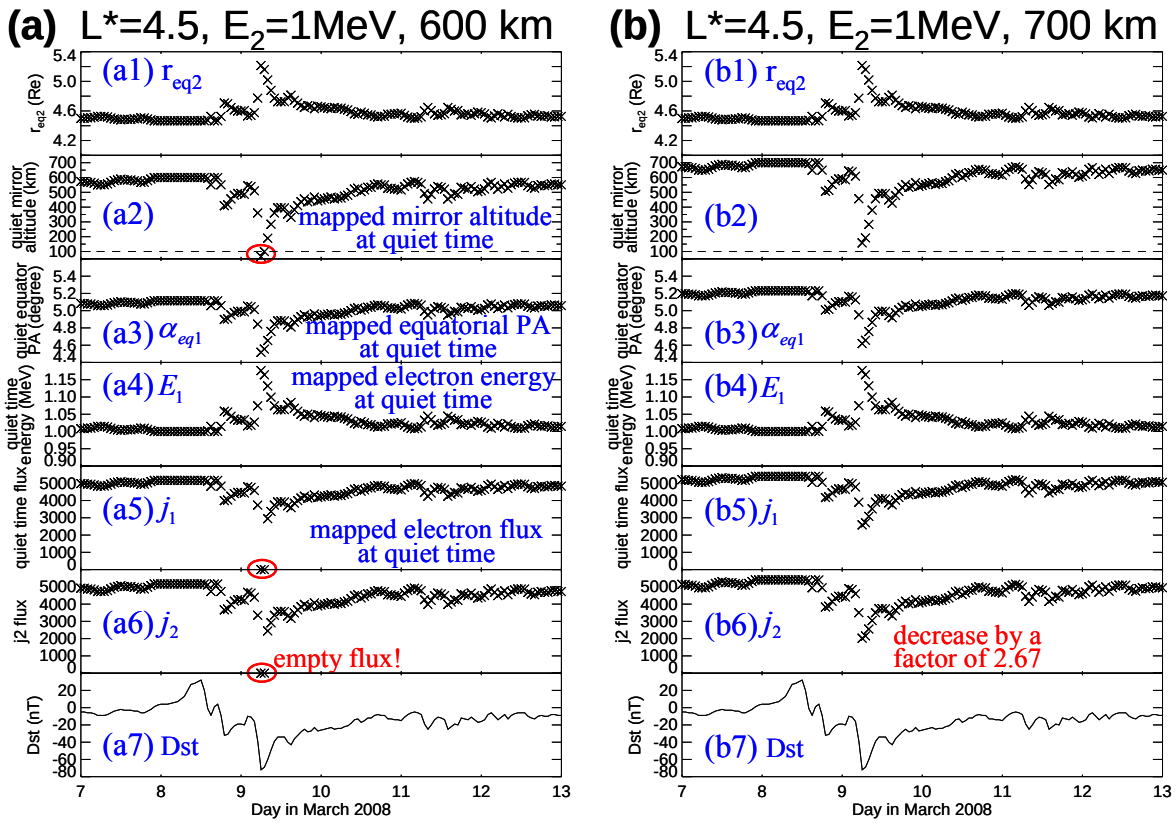

Figure 5.5: Calculation results for the adiabatic flux variations (j_2) at low altitude (600 km in panel (a) and 700 km in panel (b)) and L^*=4.5 for electrons with energy E_2=1MeV over the entire 2008/03 storm. In each column, the top five panels are intermediate results for j_2 calculation, showing r_{eq2}, the mapped quiet-time P_1 altitude, α_{eq1}, energy E_1 and j_1, respectively. The resulting j_2 (in unit of $(\#/\mathrm{cm}^2\ \mathrm{sr\ s\ MeV})$) variations are shown in the sixth panel, with the Dst profile in the bottom panel.

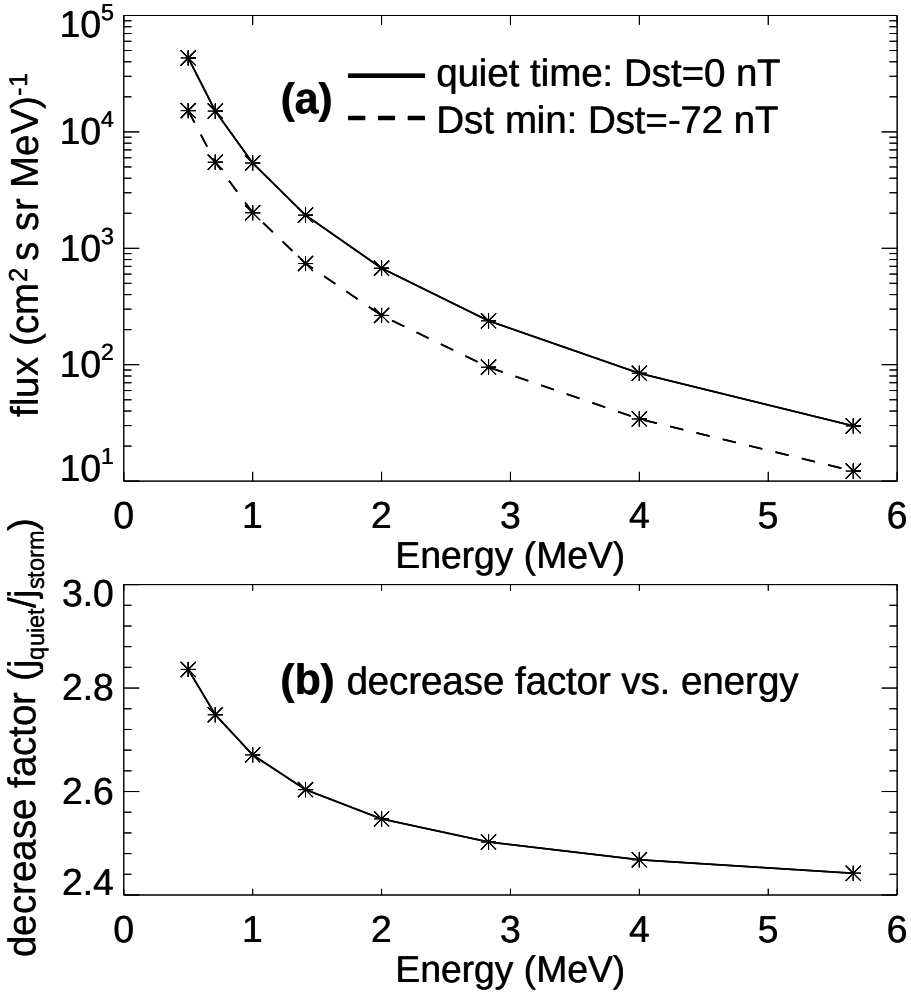

Figure 5.6: Panel (a) compares the energy spectrum of the quiet time electron flux at L^*=4.5 and 700 km (solid line) with the calculated new energy spectrum at Dst = -72 nT (dashed line). Panel (b) shows the decrease factors at Dst = -72 nT versus electron energies for electrons at L^*=4.5 and 700 km altitude.

proportional to $(E_2/ E_1)^{-3}$ from Equation 5.1 and 5.3, is slightly larger for lower energy electrons, since Equation 5.2 shows that E_1/ E_2 decreases as E_2 increases, causing a lower decrease factor, or less of a decrease in flux, for higher electron energies.

5.5 Discussion

5.5.1 Altitude-Dependent Adiabatic Flux Change During Storm Time

The storm-time adiabatic flux variations at a fixed low altitude are calculated to demonstrate two cases. The first case occurs when electrons originally mirroring below the investigated altitude and above the atmospheric boundary at quiet time all rise to mirror above that altitude during the storm, causing a complete dropout of the measured flux. The second case occurs when the storm-time rise of the 100 km mirror point is well below the investigated altitude, causing a fractional reduction of the flux. Separating the two cases is the maximum altitude the quiet time 100 km mirror point rises to, defined as 'cutoff altitude', which is 637 km for the March 2008 storm. Thus, the magnitude of the adiabatic flux drop at low altitude is altitude-dependent. Furthermore, since the value of the 'cutoff altitude' is storm-dependent (for bigger storms the mirror point rises higher because the magnetic field is further stretched), we conclude that the adiabatic flux change at a fixed low altitude during storm time is both altitude and storm dependent.

In the second case, the decrease factor at Dst = -72 nT is only 2.4-2.8 for relativistic electrons at L^*=4.5 and 700 km altitude. After performing a similar calculation for equatorially mirroring electrons, we find that at Dst = -72 nT, the flux of 1 MeV electrons mirroring at the equator decreases by a factor of 15 (as shown in Figure 5.7 panel (b)) due to adiabatic effects, a lot more than the decrease at the low altitude in the second case. This larger decrease factor is because during storms the relative magnetic field strength decrease (B_{m2}/ B_{m1}) at low altitudes is much smaller than that near equator. This results in a smaller adiabatic decrease of the electron energy from Equation

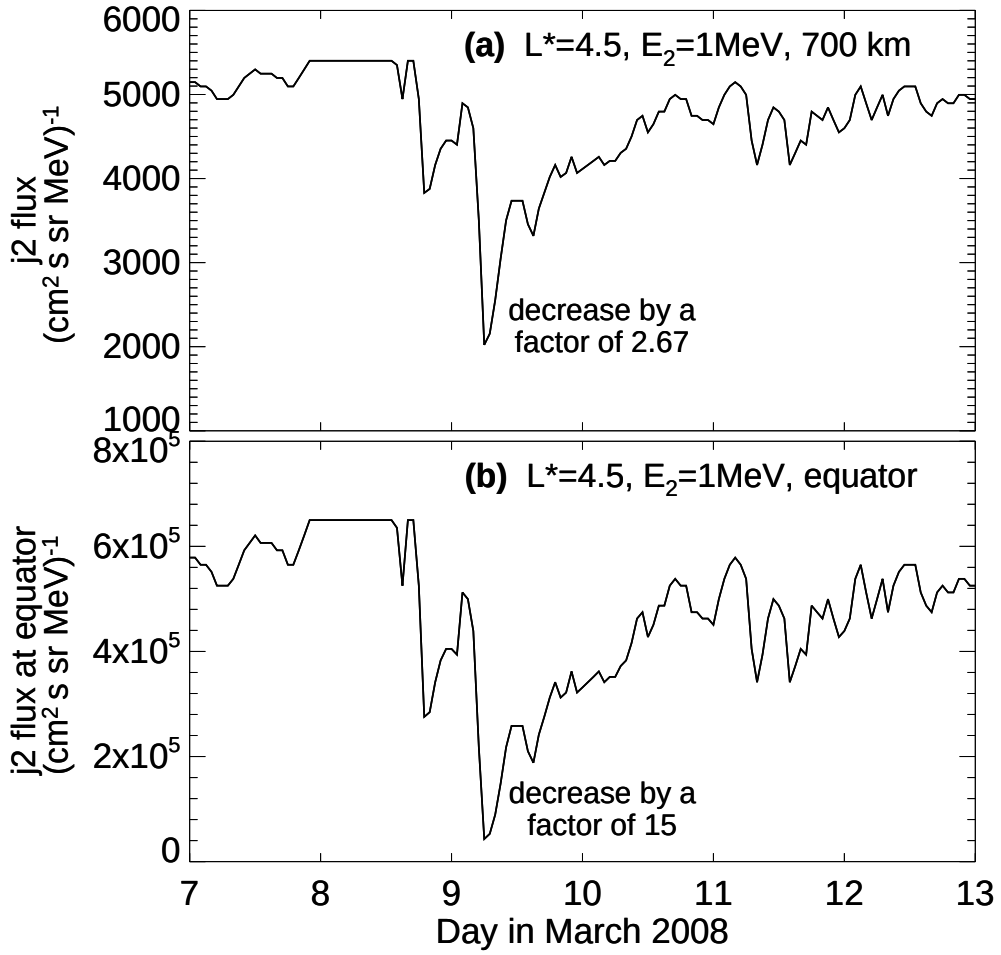

Figure 5.7: Calculation results for the adiabatic flux variations (j_2) at L^*=4.5 for E_2=1MeV electrons over the entire 2008/03 storm, with results for electrons mirroring at 700 km shown in panel (a) (same results as in the sixth panel of Figure 5.5b) and for electrons mirroring at the equator shown in panel (b).

5.2 as well as a smaller multiplication factor in Equation 5.3, thus a smaller adiabatic flux drop at low altitudes. Even though both the energy decrease and pitch angle shift contribute to the decrease in flux of electrons mirroring at low altitudes, these effects are much smaller compared to the effect of the more significant energy decrease at the equator on the flux drop of equatorially mirroring electrons. Kanekal et al. [2001] found remarkable coherence of outer zone electrons by the strong correlation coefficients between electron fluxes measured at different altitudes. We also calculate the correlation coefficient between the two time series shown in Figure 5.7, which are both adiabatic flux variations (j_2) at L^*=4.5 for E_2=1MeV electrons over the entire 2008/03 storm, one for electrons mirroring at 700 km shown in Figure 5.7 panel (a), and the other for electrons mirroring at the equator in Figure 5.7 panel (b). The correlation coefficient is as high as 0.987, indicating the flux variations at low altitude and at the equator due to the adiabatic effects are also remarkably coherent, even though the relative decrease factors of the electron flux are quite different. The quantitative difference of the adiabatic flux variations at different altitudes was not so obvious until our calculations performed in this study.

5.5.2 Adiabatic Effects plus Non-Adiabatic Pitch Angle Diffusion

The two cases above include only purely adiabatic responses. It is useful though to discuss how adiabatic and non-adiabatic processes, such as pitch angle diffusion, work together to affect the electron flux at low altitudes. In the first case previously described, electrons at 600 km disappear: in Figure 5.2 panel (b) when all electrons move above P_1 at time t2, a null in the pitch angle distribution is created for electrons mirroring above 100 km and below 637 km (the lower end of the red region). Under moderate pitch angle diffusion, this void in the pitch angle distribution can be filled quickly. For example, at t2 the mirror point at 637 km corresponds to an equatorial pitch angle of 3.23°, while the mirror point at 100 km corresponds to an equatorial pitch angle of 2.85°; assuming a pitch angle diffusion rate D_{xx}, as defined by Schulz and Lanzerotti [1974], equal to

10^{-9}/s (corresponding to electron e-folding lifetime ~ 100 days [Tu et al., 2010]) filling the void in the pitch angle distribution takes only several minutes. Then the electron flux would not drop to zero but instead by a factor similar to that seen in the second case. However, since the pitch angle diffusion rate, caused by resonance with a variety of plasma waves, depends on the spectral and latitudinal distribution of the wave power, the ratio of the plasma frequency to electron gyrofrequency (f_{pe}/f_{ce}), the distribution of wave normal angles, and the electron energies etc., the D_{xx} for MeV energy electrons at low altitude can at times be much slower than 10^{-9}/s [Li et al., 2007; Horne et al., 2009]. For example, based on the results shown in Figure 2 of Li et al. [2007] we know that D_{xx} from chorus waves for 1 MeV electrons at equatorial pitch angles near 3.23° can be less than 10^{-12}/s. For $D_{xx} = 10^{-12}$/s, filling the zero fluxes at the low altitudes now takes about a day, while adiabatic processes act on timescales on the order of hours or shorter. Therefore, the null fluxes at the low altitudes created by adiabatic effects can persist for very slow pitch angle diffusion.

From previous calculations and discussions, we understand that the different levels of adiabatic flux drops at different equatorial pitch angles change the electron pitch angle distribution as a magnetic storm develops, as illustrated in the leftmost diagram of Figure 5.8 with larger drop at the equator from the adiabatic effects than at low altitudes. Simultaneously, non-adiabatic pitch angle diffusion also evolves the pitch angle distribution from an arbitrary initial distribution to an equilibrium state, which is the lowest-order eigenmode of the bounce-averaged pitch angle diffusion operator [Shprits et al., 2006b; Albert and Shprits, 2009]. The derivation for this process can also be found in Appendix A (pitch angle diffusion equation in Eq. A.2 and derivation results in Eqs. A.7 and A.8). The equilibrium state decays steadily in time with the decay rate represented by the corresponding eigenvalue of the lowest-order eigenmode that is independent of the electron pitch angle. Higher-order eigenmodes may be included in the initial phase of the evolution, but they decay much faster [Selesnick et al., 2003] . Note all the initial pitch angle distributions in the three

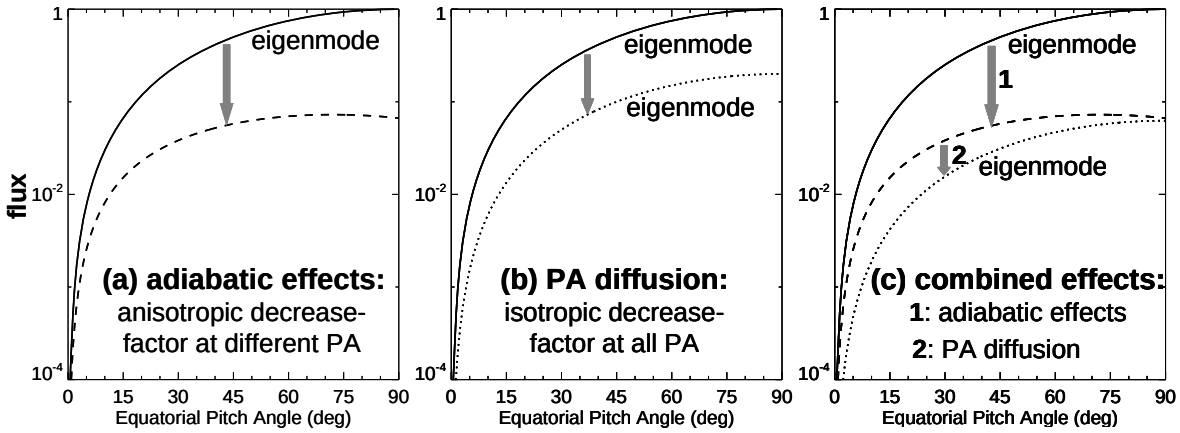

Figure 5.8: Diagrams showing the variations of the electron pitch angle distribution, under (a) dominant adiabatic effects, (b) dominant pitch angle diffusion, and (c) adiabatic effects plus pitch angle diffusion.

diagrams of Figure 5.8 are assumed as the equilibrium eigenmode-shape reached after sustained pitch angle diffusion. Therefore, after reaching the equilibrium eigenmode, pitch angle diffusion keeps an isotropic decrease factor for all the electron pitch angles, as shown in the middle diagram of Figure 5.8.

Adiabatic processes and pitch angle diffusion may occur simultaneously, but at different timescales. As illustrated in the rightmost diagram of Figure 5.8, after reaching the equilibrium eigenmode by pitch angle diffusion, adiabatic effects bring the distribution to the dashed curve (step 1 in the diagram), same as in the leftmost diagram with different decrease factors at different pitch angles. The dashed curve then serves as an initial distribution for the pitch angle diffusion. Therefore, if the pitch angle diffusion rate remains roughly constant throughout the storm, pitch angle diffusion tends to restore the pitch angle distribution to the same eigenmode shape (step 2 in the diagram).The time required to relax the initial distribution (the dashed curve) to the equilibrium eigenmode (the dotted curve), named the 'relaxation time', depends on the strength of the pitch

angle diffusion rate and how far the initial distribution is from the lowest-order eigenmode. For the case where the relaxation timescale is on the same order as the adiabatic change timescale or shorter, pitch angle diffusion can isotropize the relative flux reduction at the equator and at low altitudes (illustrated by step 1 plus step 2 in the rightmost diagram or by the middle diagram with pitch angle diffusion more dominant than the adiabatic effects). Furthermore, since the adiabatic effects continuously reshape the pitch angle distribution away from the lowest-order eigenmode, during the pitch angle diffusion, higher-order eigenmodes will be consistently excited, which decay faster in time and will cause increased electron precipitation without changing the pitch angle diffusion rate. To quantify the additional precipitation from the adiabatic change in the electron pitch angle distribution requires detailed modeling, which will be conducted in future work. On the other hand, if the relaxation timescale is much slower than the adiabatic change timescale, which is possible during weak pitch angle diffusion, the anisotropic adiabatic flux changes at different pitch angles will remain during the storm time and the pitch angle distribution will barely return to the eigenmode (close to the case in the leftmost diagram of Figure 5.8 with adiabatic effects more dominant than pitch angle diffusion).

5.5.3 Comparison with SAMPEX Data

It is useful to compare the adiabatic flux drops from the two cases (drop to zero or by a small factor as discussed in subsection 5.5.1) to observed data to answer the two questions raised at the end of the Section 5.1, or equivalently, to what degree adiabatic changes can account for flux variations observed by SAMPEX during storms. Notice that our calculation results are for electrons locally mirroring at 600 and 700 km, while SAMPEX is actually in a ~550×675 km orbit with a wide detector opening angle [Cook et al., 1993]. Thus the integral flux measured by SAMPEX is a weighted average of electrons mirroring at and below SAMPEX (a range of mirror point altitudes), able to cover electrons in either of these two cases discussed previously or both of them. For

example, if all the electrons detected by SAMPEX mirror at altitudes belonging to the second case, all above the 'cutoff altitude', SAMPEX would see a fractional flux drop; in contrast, if the electrons detected by SAMPEX partly or entirely fall into the 'null flux' case, the measured integral flux would drop more. Realistic simulation of the adiabatic integral flux change detected by SAMPEX requires integration over a range of pitch angles and energies covered by the detector based on its angular and energy responses, as well as implementing SAMPEX's orbit in a realistic magnetic field model, which is much more complicated than the calculations performed in Section 5.4 for locally mirroring electrons.

The SAMPEX data in Figure 5.1 panel (b) indicates that the trapped electron count rates (green points) at L=4.5 decrease by almost an order of magnitude during the storm main phase. This demonstrates that the second case discussed in subsection 5.5.1 is not the main form of adiabatic effects during this storm, since it can only account for a small fraction of the observed flux drop, a factor of 2.4-2.8 for relativistic electrons. Then is it non-adiabatic processes that play a leading role in the storm-time flux drop? Or is it due to some other forms of adiabatic flux change at SAMPEX, e.g., a weighted combination of the first and the second cases as discussed above? Adiabatic effects have little influence on the flux of the drift loss cone electrons, since they will be lost within one electron drift period, which is much faster than the adiabatic changes. Data show that during the storm main phase the trapped electrons decrease more significantly than the drift loss cone electrons (blue points), meanwhile the drift loss cone electrons exhibit a flatter distribution over longitude compared with the pre-storm interval. These are all indicators of enhanced pitch angle diffusion [Tu et al., 2010]. Therefore, even though we cannot answer exactly how much of the observed trapped electron flux drop during the storm main phase is from the adiabatic effects due to the difficulties described above, we can still conclude that the observed storm-time flux variations at SAMPEX are not purely adiabatic responses, and non-adiabatic processes are dominant in this event.

In Section 5.4 we analyzed the adiabatic flux change for electrons mirroring at a fixed altitude (~ SAMPEX's altitude) and fixed L^*=4.5, rather than at a fixed point in space. This differs from the analysis performed in Kim and Chan [1997] for a fixed point at geosynchronous altitude, which is at different L^* for different times within the storm due to the adiabatic expansion of the drift shell. For example, for a fixed equatorial point at r_{eq1} in Figure 5.4 panel (b) (4.5 Re), its L^* changes from 4.5 at quiet time to L^*=4.06 at Dst = -72 nT calculated using the modified dipole model. Therefore, since the fixed point maps to different L^* shells at quiet times, to estimate the storm-time adiabatic effects for a fixed point at the equator requires further consideration of the radial dependence of the quiet time electron flux in addition to the energy and pitch angle dependences [Kim and Chan, 1997]. However, for a fixed point at low altitude, the change of L^* during a storm is much less than that at equator, due to the fact that most of the drift shell expansion occurs at high altitude (or lower latitude), as seen in Figure 5.2 panel (a), where the black and red field lines almost co-locate at P_1 altitude (more evident in Figure 5.2 panel (b)). More quantitatively the L^* of a fixed point at P_1 at 600 km initially with L^*=4.5 at quiet time, decreases to 4.49 at Dst = -72 nT, almost negligible compared to the L^* change at the equator. Taking this into account, our conclusions from looking at electrons mirroring at a fixed altitude and fixed L^* are expected to be similar to those at a fixed point in space at low altitude.

5.5.4 Uncertainties in the Quantitative Results

As a final point, I discuss the possible uncertainties of our quantitative results. First, for the quiet time flux distribution in Equation 5.1, we chose 3 as the power law index for the energy dependence and 2 as the power index for the sine-form pitch angle dependence. The choice of these two numbers affects the calculated decrease factors in subsection 5.4.2. For example, the pitch angle distribution $\sin^2\alpha$ is obtained from Gannon et al. [2007] by fitting to quiet-time CRRES data near the equator, which is actually not capable of resolving the pitch angle distribution at low

altitudes near the loss cone that is relevant to our study. Thus, the lack of a clear picture of the pitch angle distribution near the loss cone could introduce uncertainties to our calculation results. Specifically, the results show that when the power index for the pitch angle dependence changes from 2 to 5, the range of the decrease factors shown in Figure 5.6 panel (b) changes from 2.4-2.8 to 3.5-4.1, but the qualitative conclusions in the paper remain unaffected. Similarly, moving the atmospheric boundary from 100 km to a different altitude, e.g., 80 km or 120 km, would change the value of the 'cutoff altitude', but again the overall conclusions remain valid.

The quantitative results for these adiabatic flux decrease factors and the value of the 'cutoff altitude' depend on the magnetic field model used in the calculation. In this work we use the modified dipole model due to its simplicity. It is useful to compare the results from the simplified model with a more realistic model. A similar calculation on the rise of the mirror point in altitude as in Section 5.3 is performed using the Tsyganenko 2001 storm-time field model (T01S) [Tsyganenko, 2002a, 2002b]. We look at electron mirror points in the midnight plane, southern hemisphere, and find that the 600 km mirror point rises to 1356 km at Dst minimum, and the 100 km mirror point rises to 851 km, implying a null flux at 600 km at Dst minimum. The calculated rise of the mirror point in altitude using the T01S model is larger than that using the modified dipole model by ~ 200 km. This can be understood by looking at the solar wind dynamic pressure data during the storm main phase (not shown here), which remains high and further stretches the magnetic field on the nightside. This effect is not included in the simplified field model, which primarily captures the global ring current effects. However, the modified dipole model still provides reasonable results, generally comparable to those using T01S model.

5.5.5 Future Applications

As discussed before, the variations in observed data are due to a combination of both adiabatic and non-adiabatic effects and to simulate the observed electron variations a physical

model must include both adiabatic and non-adiabatic processes. However, currently most models simulating electron losses do not include adiabatic losses. For example, the Tu et al. [2010] model (or the loss model discussed in Chapter 4) represents the low-altitude electron distribution as a balance of pitch-angle diffusion, azimuthal drift and possible sources, and is used to quantify the electron lifetimes from the estimated loss rate D_{xx} by fitting the model results to SAMPEX data. However, adiabatic losses are not explicitly included in the model, which can be improved by applying the adiabatic analysis performed here. Specifically, we can include the adiabatic corrections at each simulation time step, updating the modeled phase space densities as a function of energy and equatorial pitch angle with the adiabatically corrected ones. By including adiabatic corrections, the model fit to the data can be improved and the pitch angle diffusion rate can be more accurately determined.

5.6 Conclusions

The work presented here is the first quantitative study of the storm-time adiabatic effects on radiation belt electrons at low altitudes. The adiabatic effects on low-altitude electrons during the storm main phase include the expansion of the drift shell, the rise of electron mirror point in altitude and the shift in the energy spectrum of the electron flux. We found that even for the moderate storm of March 2008, the rise of the mirror point is sufficient to cause a complete disappearance of the electron flux at SAMPEX's altitude.

Calculations of adiabatic flux changes at a fixed low altitude suggest two cases, well-separated by a 'cutoff altitude' defined as the highest altitude the mirror point, originally located at 100 km (the sharp atmospheric bounce loss cone boundary) during quiet time, rises to for a given storm. Due to adiabatic effects, a satellite below the 'cutoff altitude' sees no flux for some time during the storm main phase, because electrons originally mirroring below the satellite and above the atmospheric boundary at quiet times now all move to mirror above the satellite. The

second case is for a satellite at low altitude located well above the 'cutoff altitude', which sees a fractional flux drop of locally mirroring electrons during the storm. The drop is less than that seen in equatorially mirroring electrons. These two cases suggest that the adiabatic flux change at a fixed low altitude during storms is both altitude and storm dependent and it is not simply analogous to that for equatorially mirroring electrons.

However, generally the flux variations at low altitudes depend on the relative timescales of adiabatic processes and non-adiabatic processes, such as pitch angle diffusion. Even though moderate pitch angle diffusion can quickly fill the 'null flux' case, under certain circumstances the pitch angle diffusion for relativistic electrons can be very slow during storms and the zero flux at the low altitudes created by adiabatic effects can persist. Pitch angle diffusion also tends to relax the pitch angle distribution to the lowest-order eigenmode of the bounce-averaged pitch angle diffusion operator. If the relaxation timescale is shorter or on the same order of the adiabatic processes, pitch angle diffusion would isotropize the relative flux reduction at the equator and at low altitudes. Furthermore, the adiabatic change in the electron pitch angle distribution can result in increased electron precipitation by exciting higher-order eigenmodes of pitch angle diffusion without changing the pitch angle diffusion rate. By comparing the calculated adiabatic flux change with data for the March 2008 storm and by further investigating the variations of the drift loss cone electron flux, we found that even though adiabatic processes contribute to the decrease of the trapped electron flux observed in the main phase, non-adiabatic processes are still dominant for this particular event. For future applications the adiabatic analysis performed here can be used to improve loss models of outer radiation belt electrons [e.g., Tu et al. 2010].

Chapter 6

Quantification of the Radial Diffusion Rate by MHD Simulation

For the work presented in this chapter, we collaborated with Dr. Scot Elkington in LASP, who ran the LFM MHD simulation for our event and performed the low-pass filter on the LFM fields.

6.1 Introduction

The physical picture of radial diffusion was introduced in subsection 2.4.2 of Chapter 2, together with discussions about radial diffusion rate or radial diffusion coefficient, D_{LL}. Theoretically, D_{LL} is defined as $D_{LL} = \frac{<(\Delta L)^2>}{2t}$, representing the change of L for a large number of particles over a long time scale t, with $t \gg 2\pi / \omega_d$, where ω_d is the particle drift frequency [Schultz and Lanzerotti, 1974]]. The particle radial diffusion rates due to stochastic electric and magnetic field perturbations were first derived by Fäthammar [1965]. That derivation is for nonrelativistic particles in a dipole field, and only includes single mode magnetic fluctuations (m=1, m is mode number which will be introduced later), and assumes some relation between the magnetic and induced electric fields. Fei et al. [2006] generalized the electric and magnetic diffusion coefficients to include relativistic electrons and multiple mode numbers of magnetic fluctuations. Their derivations are for an asymmetric magnetic field, and they found that symmetric resonance modes generally dominate the radial diffusion. In Appendix C, using a treatment similar to Fei et al. [2006], I re-derive the electric and magnetic diffusion coefficients of relativistic electrons at the equator in a symmetric dipole field. The derived results are consistent with those in Fei et al. [2006] and Fäthammar [1965] (for details please see Appendix C), as:

$$\begin{cases} D_{LL}^{E} = \dfrac{L^6}{8R_E^2 B_E^2} \sum_m P_m^E(m\omega_d) \\ D_{LL}^{B} = \dfrac{\mu^2 L^4}{8e^2 {R_E}^4 {B_E}^2 \gamma^2} \sum_m m^2 P_m^B(m\omega_d) \end{cases} \tag{6.1}$$

where D_{LL}^{E} is electric diffusion coefficient due to the perturbations of electric field and D_{LL}^{B} is magnetic diffusion coefficients due to magnetic field perturbations, μ is the first adiabatic invariant, e is the electron charge, R_E is the Earth radius, B_E is equatorial magnetic field strength at the surface of the Earth, γ is the Lorentz relativistic factor, $P_m^E(m\omega_d)$ and $P_m^B(m\omega_d)$ are the power spectral densities of the electric and magnetic field, respectively, at frequency m-times the drift frequency, ω_d, and m is the azimuthal mode number of the fluctuations (basically indicating how many wave peaks can be seen in the azimuthal direction). Thus the total diffusion coefficient is the sum of the electric and magnetic diffusion coefficients, as:

$$D_{LL}^{total} = D_{LL}^{E} + D_{LL}^{B}. \tag{6.2}$$

From Eq. 6.1 we understand the radial diffusion rate is related to the power spectral density of the stochastic fluctuating fields at the electron drift frequency and its harmonics, which is in Pc5 range of ULF waves (2-7 mHz [Kivelson and Russell, 1995]) for relativistic electrons in the outer radiation belt. However, it is not easy to determine the global power spectral density and mode structure of ULF waves in the magnetosphere. For example, in order to determine the mode structure of waves at a given frequency up to mode m, generally 2m azimuthal measurements are required. Normally, there is insufficient satellite coverage at a given L shell to properly evaluate the power spectral density of ULF waves as a function of m. Due to these difficulties, previous analyses have assumed that the power is all in the m=1 mode [e.g., Brautigam et al., 2005]. Various forms of empirical diffusion coefficients have been used, which are inconsistent and can differ significantly

in magnitude [e.g., Brautigam and Albert, 2000; Li et al., 2001a]. Here we take the empirical D_{LL}^{Kp} from Brautigam and Albert [2000] as an example, which is a function of the Kp index:

$$D_{LL} = 10^{(0.506Kp-9.325)} L^{10} \tag{6.3}$$

This empirical D_{LL} was adopted for our work in Chapter 3 (where it was written as $D_{LL}(Kp)$) to simulate the radial diffusion rate but with a free parameter to adjust its strength (Eq. 3.2).

Based on the derivation results in Eq. 6.1, we find the empirical D_{LL} forms not realistic. For example, D_{LL} should be a function of the first adiabatic invariant, μ. Explicitly, D_{LL}^{B} in Eq. 6.1 has a μ-dependence factor μ^2. Implicitly, higher μ values indicate higher electron energies in different L regions and since higher-energy electrons have faster drift frequencies, where the power spectrum of magnetic and electric field fluctuations is weaker, the power spectral density terms in Eq. 6.1 are decreasing functions of μ. Additionally, the L dependence in Eq. 6.1 is not always equal to L^{10} as in D_{LL}^{Kp} (Eq. 6.3). It includes the explicit L^6 and L^4 shown in Eq. 6.1, and implicit L dependence in γ and the wave power spectral densities (whose L-dependence changes with time). Therefore, the empirical form of D_{LL}^{Kp}, without a dependence on μ and with fixed L dependence (L^{10}), may not be realistic.

Therefore, in order to better quantify the contribution of radial diffusion which is included in our model described in Chapter 3, physical radial diffusion coefficients as represented in Eq. 6.1 are needed. Due to the difficulties in calculating D_{LL} based only on data as discussed above, global MHD simulations are used here. MHD simulation can provide the mode structure and the power spectrum of the magnetic and electric field fluctuations in the inner magnetosphere for a specific storm event (described in Section 6.2), which are then applied to Eq. 6.1 for the calculation of D_{LL} (Section 6.3). The calculated D_{LL} is more realistic than the empirical D_{LL}^{Kp} used in Chapter 3 and

can be directly applied to the Fokker-Planck model used there. Finally, due to the known limitations of the MHD code, the MHD fields need to be further validated by field measurements from real satellites (Section 6.4). This is the outline of our work performed in this chapter.

6.2 MHD Simulation

A moderate geomagnetic storm event in March 2008 is selected for calculating the radial diffusion coefficient. The storm has already been studied in Chapter 4 and 5 for quantifying non-adiabatic and adiabatic loss rates. Solar wind conditions during this event are shown in the upper four panels of Figure 6.1, with the lower two panels showing the Dst and AE indices. The event is a CIR storm driven by a high speed solar wind, with multiple Dst dips in the storm main phase and a prolonged storm recovery phase. The AE index is high during the storm main phase and recovery phase.

We simulate this storm event using the Lyon-Fedder-Mobarry (LFM) MHD code. The LFM code is one of the major three-dimensional MHD codes used to simulate Earth's magnetospheric dynamics [Lyon et al., 2004]. It solves ideal MHD equations which use upstream solar wind data as inputs. The LFM MHD code has been popular in studies of outer radiation belt dynamics [e.g., Elkington et al., 2002, 2004; Fei et al., 2006; Huang et al., 2010a, 2010b]. Figure 6.2 shows three snapshots of electric and magnetic field results from LFM MHD simulations during the event, at the times marked by the three red lines in Figure 6.1, that shows the related solar wind and geomagnetic conditions. The results are on the Solar Magnetic (SM) equator, with the color in each panel representing the value of azimuthal electric field, E_φ, negative (clockwise) being bluish and positive (counterclockwise) being reddish. The black contours are the contours of compressional magnetic fields, B_z, which is the dominant magnetic field component at the SM equator. Panel (a) is a quiet time before the storm (time marked by the leftmost red line in Figure 6.1), and there is no

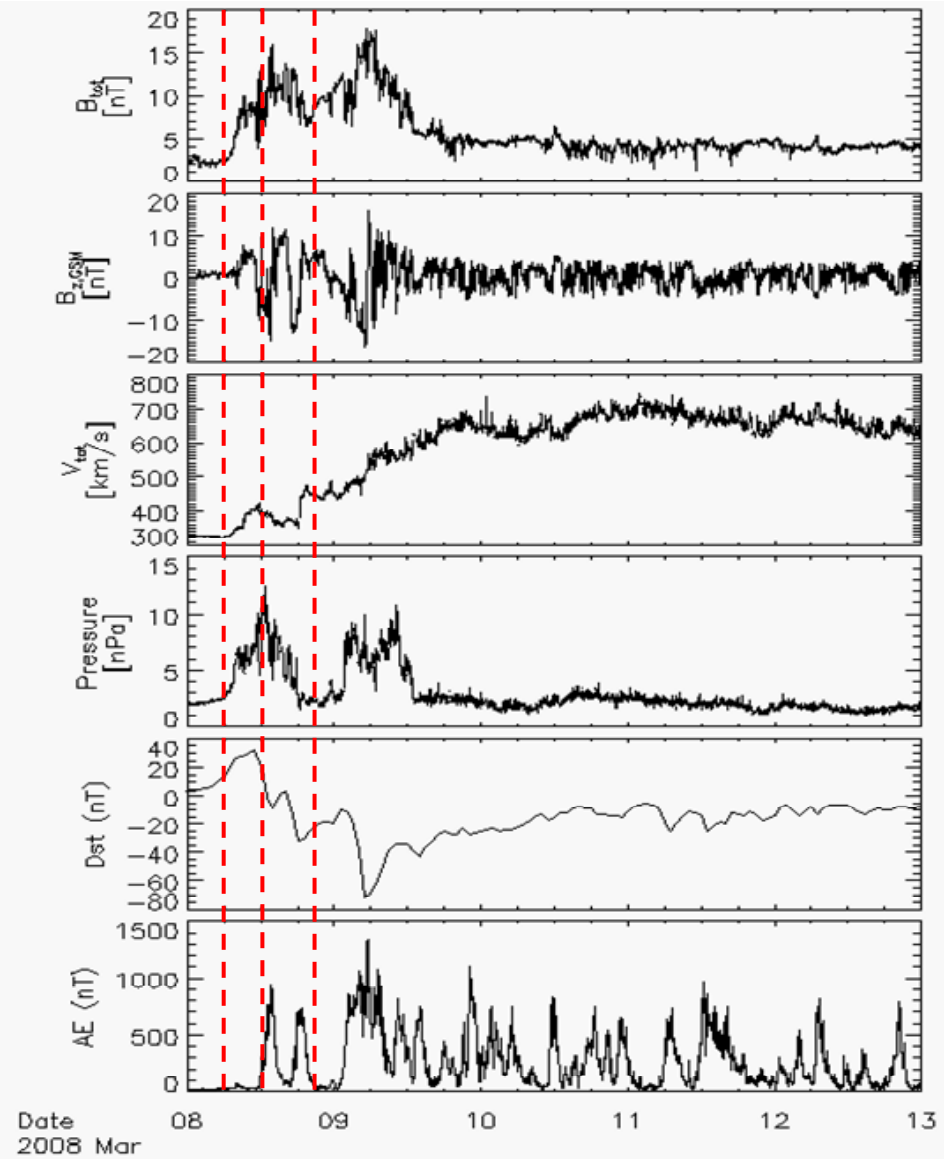

Figure 6.1: OMNI solar wind conditions during the March 2008 storm, including the total Interplanetary Magnetic Field (IMF), IMF B_z, bulk flow velocity and dynamic pressure, with geomagnetic indices, Dst and AE, shown at the bottom two panels (from CDAWeb, see http://omniweb.gsfc.nasa.gov/).

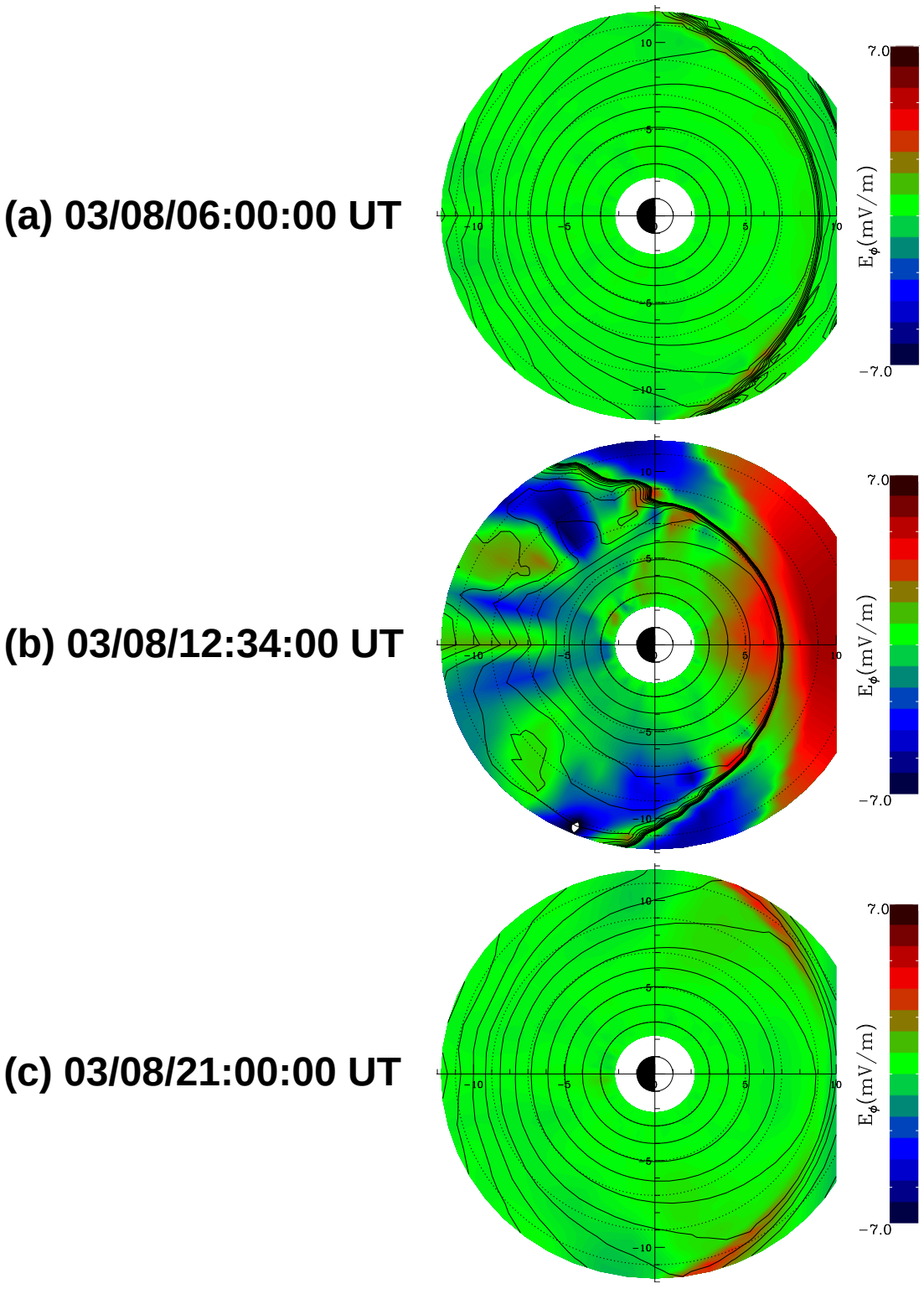

Figure 6.2: Three snapshots of the electric and magnetic field results on the SM equator from LFM/MHD simulations during the March 2008 event, corresponding to the times marked as three red lines in Figure 6.1. Color represents the value of E_φ and black contours are contours of B_z.

strong E_φ inside the magnetosphere (mostly green-colored). At the storm commencement (the middle red line in Figure 6.1), there is a solar wind pressure peak and IMF B_z turns southward. Correspondingly, panel (b) shows positive E_φ in the upwind direction, and the magnetopause (defined as the last contour of B) is significantly compressed compared to the quiet time position (e.g., in panel (a)). Vortical features are found near the flank region, possibly due to Kelvin-Helmholtz Instability (KHI) at the magnetospheric boundary [e.g., Hasegawa et al., 2004]. In the tail there is strong dawn-dusk electric field (negative being clockwise). Later at 2100UT on March 8th after the first small dip in Dst (the rightmost red line in Figure 6.1), the solar wind dynamic pressure drops down and the IMF B_z returns to northward. We notice that in panel (c) the magnetopause expands back and there is only some positive E_φ at the boundary region. Overall, the three snapshots indicate that the LFM field configurations respond reasonably to the changes in the solar wind conditions during this event.

One thing that needs to be mentioned is that the LFM field results shown in Figure 6.2 have been post-processed using a low-pass filter. The original LFM outputs are taken every minute as the instantaneous fields, but contain a type of artificial wave in the electric field. After applying a low-pass filter to the LFM outputs, the artificial waves are successfully removed. For details please see Appendix D.

6.3 Radial Diffusion Rate Calculation

With the global electric and magnetic field results from LFM, we can calculate the inputs needed for the D_{LL} calculation in Eq. 6.1, which are the power spectral densities of magnetic and electric fields at frequency $m\omega_d$, $P_m^B(m\omega_d)$ and $P_m^E(m\omega_d)$, for different mode numbers. Here we focus on electrons mirroring at the equator, for which the derivation of Eq. 6.1 is valid. Thus we

only take the LFM field outputs on the SM equator as shown in Figure 6.2. First, in order to resolve the azimuthal mode structure of the LFM fields at the equator, at a given L shell an FFT series expansion is performed on the azimuthal angle, φ, to calculate the wave component in each m mode, as shown in the equations:

$$\begin{aligned} E_{\varphi}(r,\varphi,t) &= E_{\varphi,0}(r,\varphi) + \sum_{m} E_{\varphi,m}(r,t)\cos m\varphi \\ B_{z}(r,\varphi,t) &= B_{z,0}(r,\varphi) + \sum_{m} B_{z,m}(r,t)\cos m\varphi \end{aligned} \tag{6.4}$$

Then, for each wave component at mode m, $E_{\varphi,m}(r,t)$ and $B_{z,m}(r,t)$, a second FFT is taken in the time domain to calculate the power spectral density $P_m^B(m\omega_d)$ and $P_m^E(m\omega_d)$, which are direct inputs for D_{LL} calculation. The resolution of the LFM output is 1 min and the time window of the FFT calculation is 2 hrs, thus resulting in a frequency range of the spectrum from 0.14 mHz to 8.3 mHz with a frequency resolution of 0.14 mHz, with the Pc5 wave range well covered.

Some calculated mode spectrum results of the LFM fields are illustrated in Figures 6.3 and 6.4. Figure 6.3 shows the mode spectrum of B_z at the SM equator at L=6.6 for the first two days of the storm, March 8th-9th. In panel (a) the color represents the integrated B_z power summed over all the frequencies in the frequency range, distributed over time (Y-axis) and mode number (X-axis). The results show that during these two days the power at m=1 is always dominant, but sometimes the contributions from power at m>1 are also significant (e.g., around 1200UT on March 8th and 0400UT on March 9th). This demonstrates that the assumption made in previous studies that the wave power all comes from the m=1 mode [e.g., Brautigam et al., 2005] is not appropriate, and using the global MHD simulation to acquire the mode structure of the ULF waves is important. To better understand the changes in the B_z mode spectrum with time, the results in panel (a) are shown in a different manner in the upper two plots in panel (b). The corresponding variations of the solar wind dynamic pressure and AE and Dst indices are also shown in the lower plots. In panel (b)

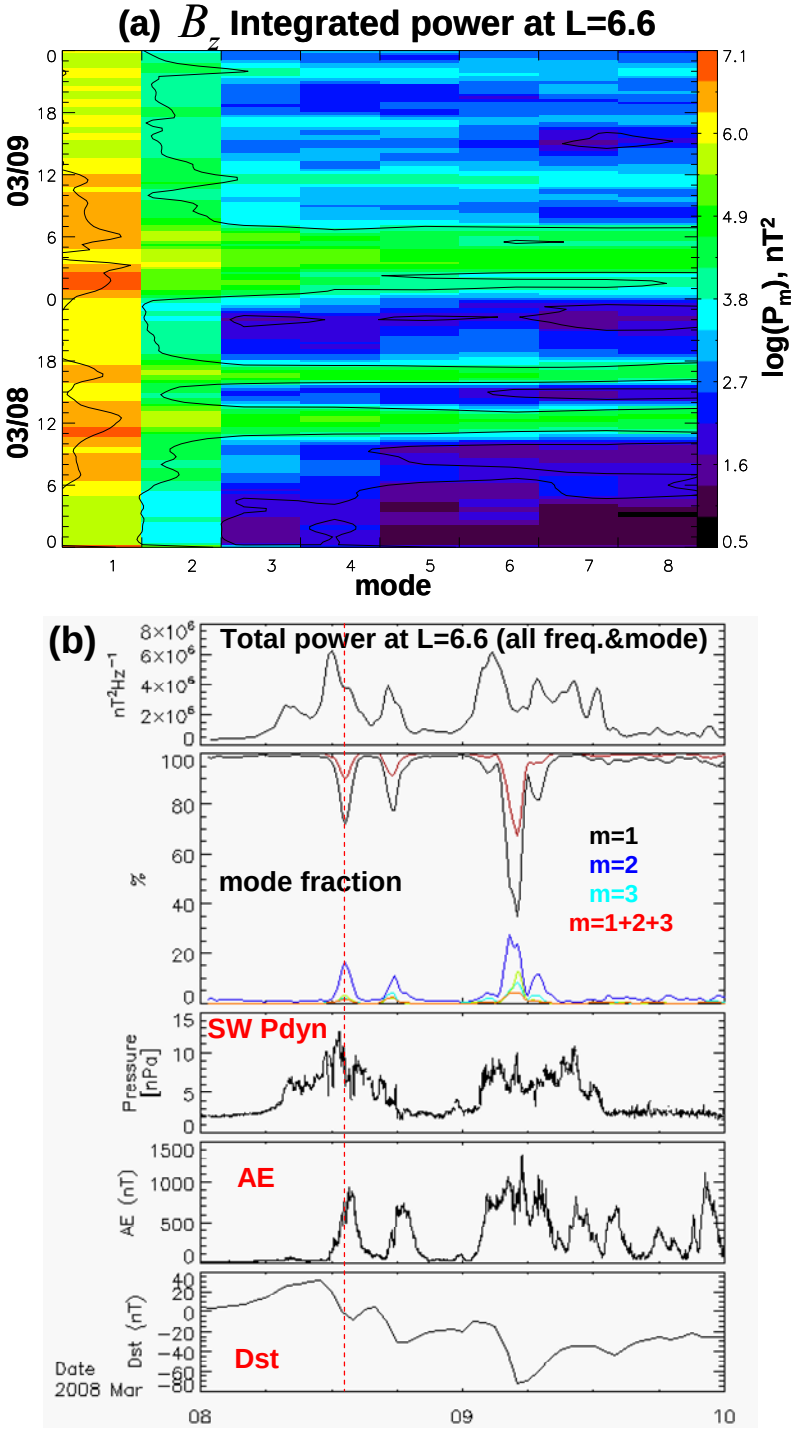

Figure 6.3: (a) Integrated LFM B_z power (color-coded) on the SM equator at L=6.6 over March 8th-9th, 2008 (Y-axis) and mode number (X-axis). (b) Time variations of total B_z power at L=6.6, mode fractions, solar wind dynamic pressure, AE, and Dst over March 8th-9th, respectively.

the X-axis is time and the top plot illustrates the time variations of total B_z power at L=6.6, summed over not only all the frequencies but also over all the mode numbers. The total power variations suggest a close correlation with the changes of solar wind dynamic pressure, with a generally higher power when solar wind dynamic pressure is high. Some modulations in AE are also evident (e.g., around 1800UT on March 8th the second strong peak in AE). The second plot shows the fractions of LFM power at different mode numbers with respect to the total power shown in the top plot. The black curve represents the fraction of power at m=1, blue curve is for m=2, cyan curve for m=3, etc., and the red curve on top is the summed fraction of power over m=1, 2, 3. Again, even though the power at m=1 is always dominant during these two days, we find the power at m>1 generally increases when the AE index is high (e.g., around 1300UT on March 8th marked by the dashed vertical line in panel (b)). The mode fraction from m=1 power is less than 50% of the total power around 0500UT on March 9th, indicating that assuming power all comes from m=1 at that time will underestimate the total power by a factor of two. Overall, the mode spectrum results of LFM B_z suggest that the total B_z power, mostly from the m=1 mode, is generally related to the solar wind dynamic pressure variations, while m>1 power is mostly related to nightside geomagnetic activity (represented by high AE index).

The same mode spectrum analysis is performed for LFM E_φ fields as illustrated in Figure 6.4. Similar to the B_z mode spectrum, the E_φ power at m=1 for these two days always has the highest mode fraction (second plot in panel (b)). The difference is for E_φ the m=1 power is not as dominant as that for B_z, and the power spreads over a wider range of mode numbers. The total E_φ power at L=6.6 is also correlated with solar wind dynamic pressure and the AE index. When solar wind dynamic pressure increases, total power goes up. In addition, when the total power increases we find two clear features of mode fraction (second plot): first, the mode fraction for m=1

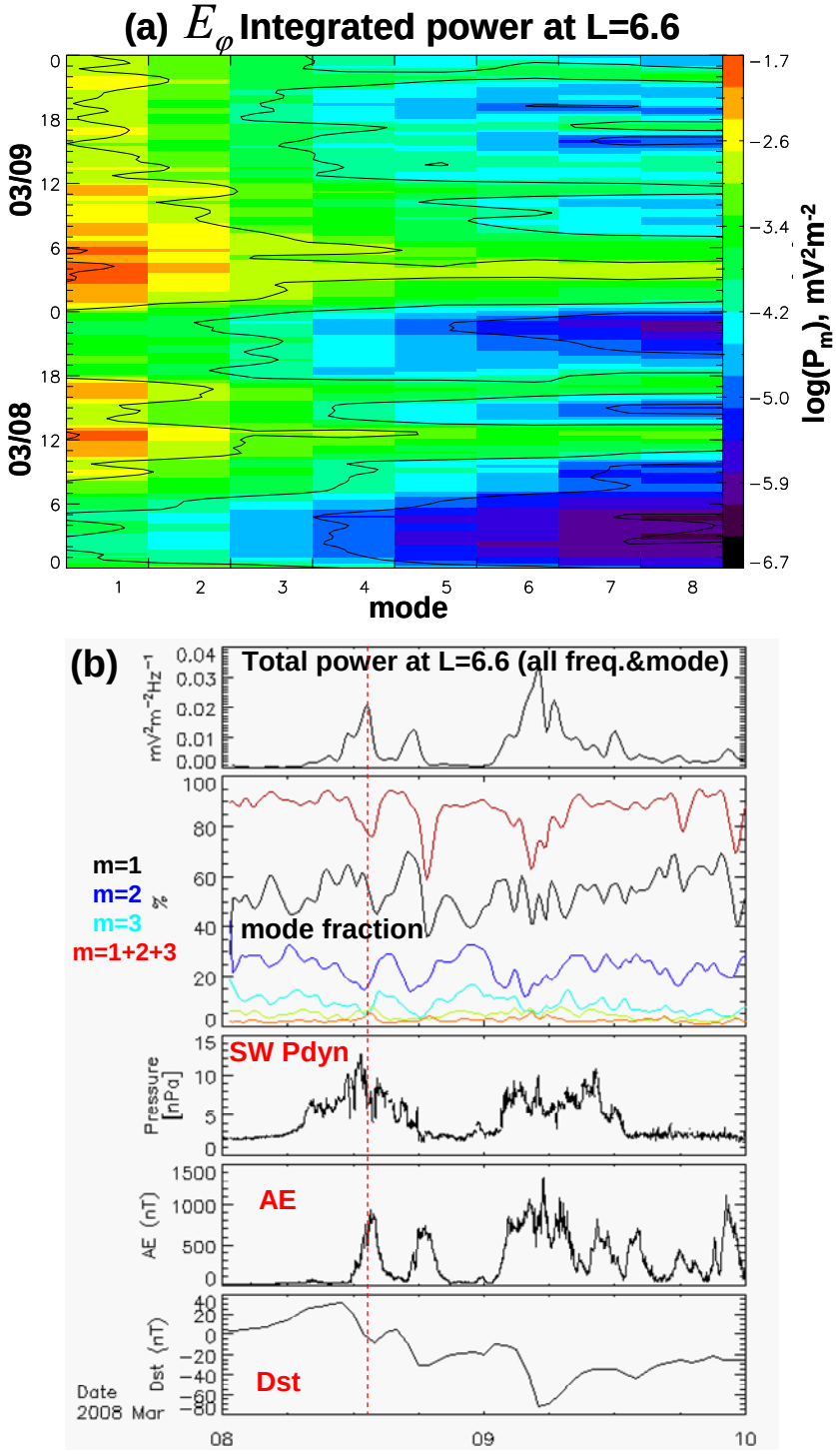

Figure 6.4: Mode spectrum results for LFM E_φ, with the same configuration as in Figure 6.3.

generally increases or remains the same (black curve), indicating the increasing power at m=1; second, the summed mode fraction over m=1, 2, 3 decreases (note an anti-correlation with the change of total power, red curve in second plot versus the black curve in the top plot). These indicate the increased fraction of power at m>3 and decreased power fractions at m=2 and 3 since the m=1 fraction normally increases or remains unchanged. The increase of power fractions at m>3 is found to be generally correlated with the increase of the AE index. For example, at the time marked by the dashed vertical line in panel (b), the total power reaches a peak value when the AE index increases to a peak. Meanwhile, the summed mode fraction over m=1, 2, 3 drops to a local minimum, as well as the fractions at m=2 and 3, while the fractions at m>3 modes reach local maximums and the m=1 fraction is also around a peak. This explains why the AE modulation of the total power is evident in the top plot of panel (b).

The above results are the mode spectrum analysis for the integrated electric and magnetic field power over all the frequencies, while the direct inputs needed for the D_{LL} calculation are the power spectral densities of magnetic and electric fields at the resonance frequencies, $P_m^B(m\omega_d)$ and $P_m^E(m\omega_d)$. Figure 6.5 shows magnetic power spectral densities, $P_m^B(m\omega_d)$, for azimuthal modes m=1, 2, 3, respectively in panel (a), and $P_m^E(m\omega_d)$ for m=1, 2, 3 in panel (b), as functions of L (Y-axis) and time (X-axis, starting from 0600UT on March 8th). There are some common features in the magnetic and electric power spectral densities. Firstly, there is more power when solar wind dynamic pressure is high and/or the AE index is enhanced, and there is more power in the lower modes. These features are consistent with the mode spectrum results discussed previously. Second, there is more power at higher L regions. In contrast, the magnetic power spectral density also has some different features compared with the electric power spectral density. For example, the magnetic power spectral density has steeper L dependence, and it decreases faster than the electric power as the mode number increases. But note that in Eq. 6.1 the magnetic radial diffusion

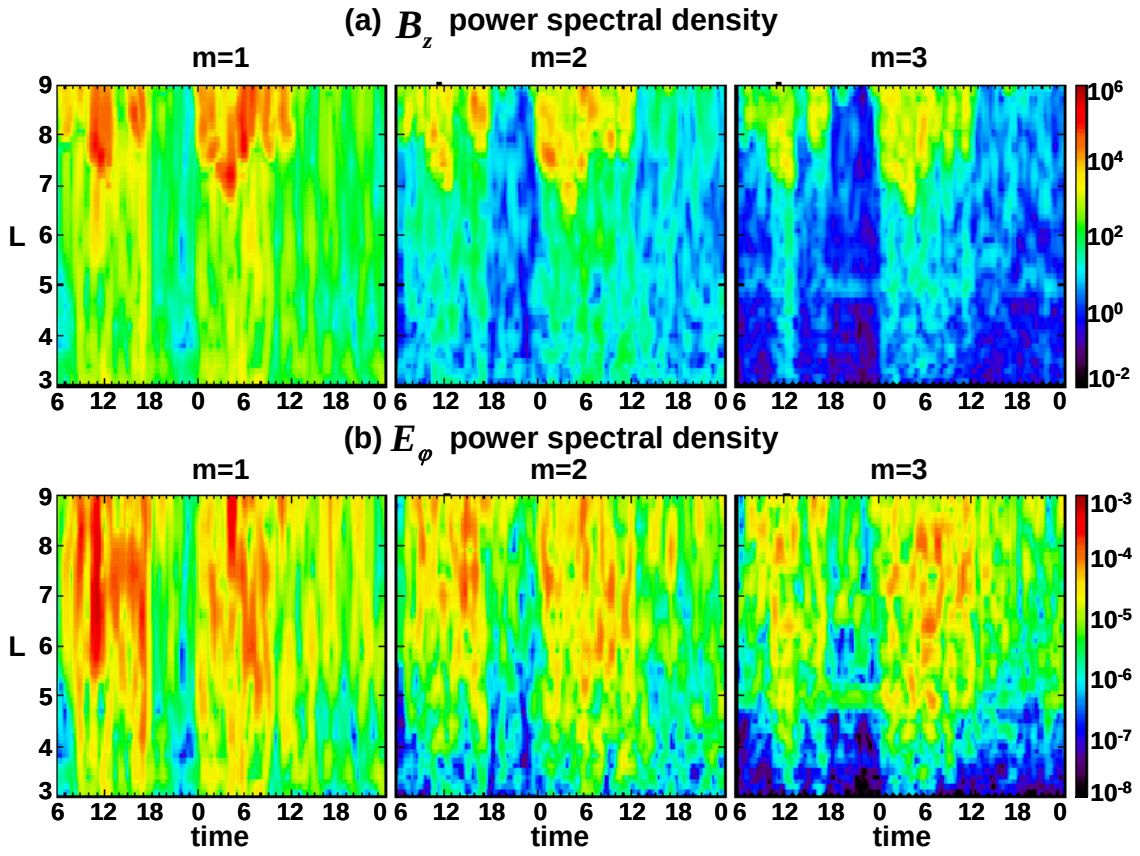

Figure 6.5: Power spectral densities (color-coded) of magnetic and electric fields at the resonance frequencies, $P_m^B(m\omega_d)$ (panel (a) in unit of nT^2/Hz) and $P_m^E(m\omega_d)$ (panel (b) in unit of $(V/m)^2/Hz$) for mode number m=1, 2, 3, distributed over L (Y-axis) and time (X-axis, labels are UT hours, starting from 0600UT on March 8th).

coefficient, D_{LL}^{B}, contains a factor of m^2 which enhances the contributions from high-mode magnetic power.

With calculated power spectral densities, the diffusion coefficients can be calculated based on Eq. 6.1 as a function of the first adiabatic invariant, μ, L, and time. All the $P_m^B(m\omega_d)$ and $P_m^E(m\omega_d)$ at different azimuthal mode numbers, but with $m\omega_d$ within the resolved frequency range, are included in the summations in Eq. 6.1. The calculated diffusion coefficients for μ=2083 MeV/G are shown in Figure 6.6, with D_{LL}^{B} of Eq. 6.1 in the upper left panel, D_{LL}^{E} in the upper right panel, and total diffusion coefficient D_{LL}^{total} in the lower left panel. Consistent with the features of the power spectral densities shown in Figure 6.5 discussed in the previous paragraph, the diffusion coefficients are generally higher during the period when solar wind dynamic pressure and/or AE index is high and the diffusion is faster at higher L shells. The electric diffusion coefficient D_{LL}^{E} is much smaller than the magnetic diffusion coefficient D_{LL}^{B}, thus D_{LL}^{total} is mostly contributed by D_{LL}^{B}. Now, the physically calculated diffusion coefficient D_{LL}^{total} is ready to be used as input into diffusion models, such as the Fokker-Planck model discussed in Chapter 3.

It is worthwhile to compare our calculated diffusion coefficients with the empirical D_{LL}^{Kp} as expressed in Eq. 6.3. The values of D_{LL}^{Kp} for the same time period starting from 0600UT on March 8th are shown in the lower right panel of Figure 6.6 (with 3-hour resolution since the Kp index is available every three hours). The comparison between the calculated D_{LL}^{total} and D_{LL}^{Kp} suggests that the empirical D_{LL}^{Kp} generally underestimates the diffusion coefficient, with worse performance at higher L regions and during the first high D_{LL}^{total} period (between 0600UT and 1800UT on March 8th) during the storm commencement and early main phase. This is clearly shown in panel (a)

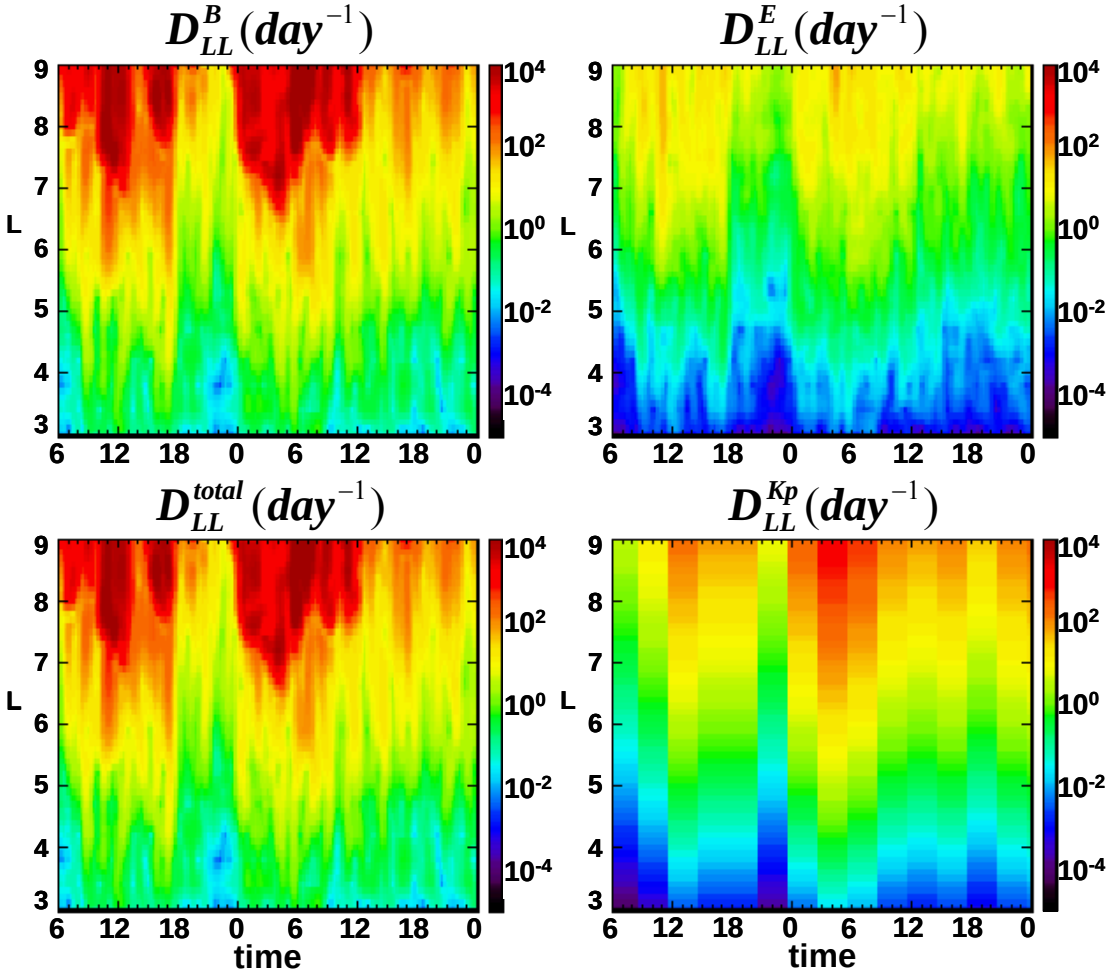

Figure 6.6: Calculated diffusion coefficients (color-coded in unit of day^{-1}) for $\mu = 2083$ MeV/G distributed over time (UT hours, starting from 0600UT on March 8th) and L, including D_{LL}^{B} (upper left), D_{LL}^{E} (upper right), $D_{LL}^{total} = D_{LL}^{B} + D_{LL}^{E}$ (lower left), and empirical D_{LL}^{Kp} (lower right).

of Figure 6.7, which shows the comparison between the calculated D_{LL}^{total} and D_{LL}^{Kp} at fixed L=6.6 during the same time period as in Figure 6.6. The black solid curve is for μ=2083 MeV/G (same as in Figure 6.6), and the variations of D_{LL}^{Kp} are plotted as the dotted line. It is clear that D_{LL}^{Kp} generally underestimates D_{LL}^{total} and sometimes it is even two orders of magnitude smaller.

Furthermore, empirical D_{LL}^{Kp} does not include the dependence on the first adiabatic invariant, μ, but the physical D_{LL}^{total} does. In panel (a), the calculated D_{LL}^{total} for μ=1000 MeV/G and 4000 MeV/G are also plotted in blue and red curves, respectively. Comparing the D_{LL}^{total} results at different μ values, it is found that they normally do not scale by the factor of μ^2 as in Eq. 6.1. As discussed at the end of Section 6.1, the power spectral density terms may be decreasing functions of μ that degrade the μ^2 dependence. In spite of that, sometimes the D_{LL}^{total} for μ=1000 MeV/G and 4000 MeV/G can still differ by an order of magnitude (e.g., at the time a little past 1800UT on March 8th). Additionally, since D_{LL}^{Kp} assumes a fixed L dependence as L^{10}, it is useful to compare that with the L dependence of the calculated D_{LL}^{total}. In panel (b) of Figure 6.7, the variations of D_{LL}^{total} for μ=2083 MeV/G at three selected times during the storm event versus L are plotted as solid curves, compared with the L dependence of D_{LL}^{Kp} at the same times plotted as dashed curves. X and Y axes are both logarithmic, and the three time (vertical) cuts in the D_{LL}^{total} panel of Figure 6.6 are taken at 0600 UT on March 8th (pre-storm, blue curves), 0500 UT on March 9th (main phase, black curves), and 2200 UT on March 9th (recovery phase, red curves). Due to the fixed L^{10}-dependence, D_{LL}^{Kp} curves are always straight and parallel to each other. However, the D_{LL}^{total} versus L curves calculated from the LFM fields are not straight and their shapes change with time. Again, at the pre-storm time (the blue solid and dashed curves), it is evident that D_{LL}^{Kp} is

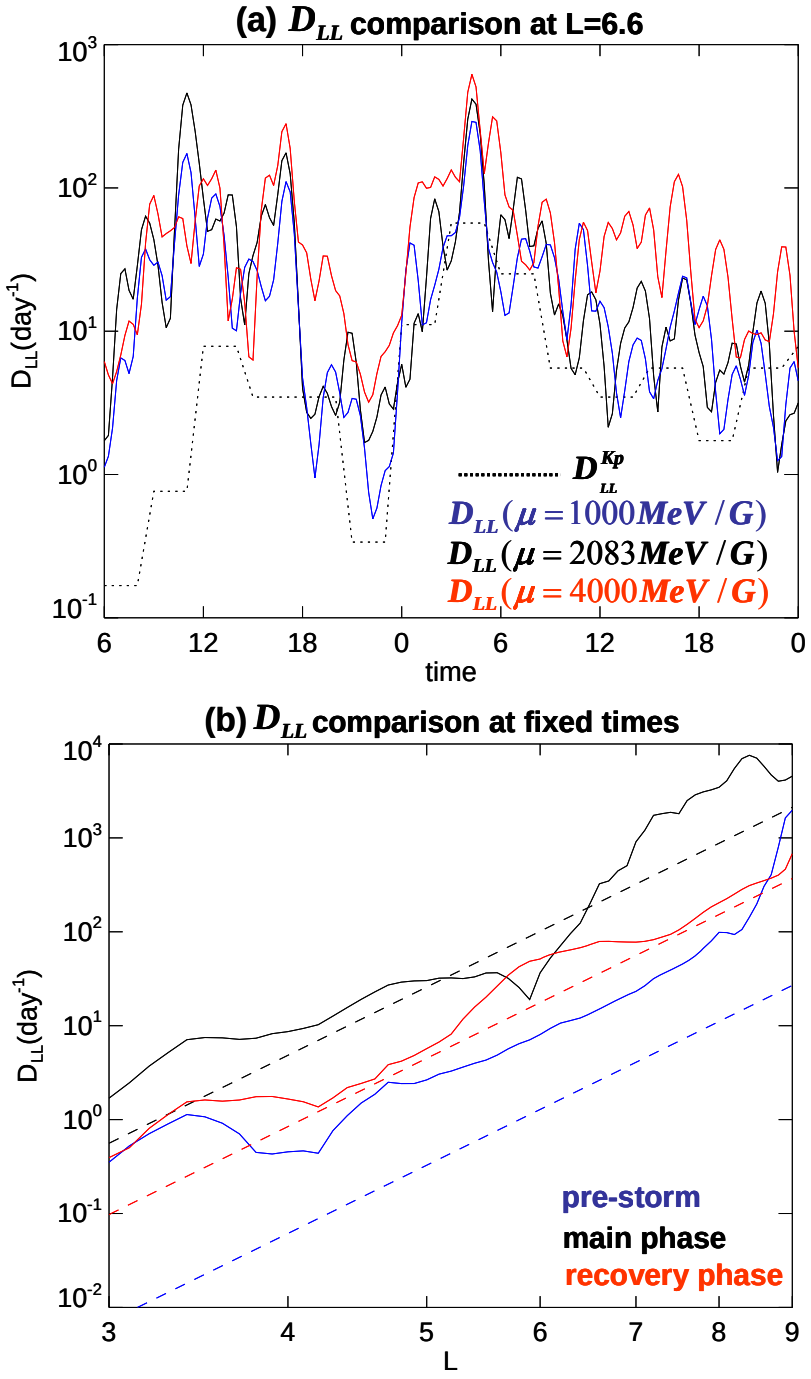

Figure 6.7: (a) Comparison between D_{LL}^{total} (solid curves) and D_{LL}^{Kp} (dotted curve) at fixed L=6.6 during the same time period as in Figure 6.6, with D_{LL}^{total} for different μ values shown in different colors; (b) Comparison between D_{LL}^{total} (solid curves) and D_{LL}^{Kp} (dashed curves) at three selected times during the storm event as a function of L. X and Y axes are both logarithmic.

much smaller than D_{LL}^{total} over all the L regions. Therefore, due to the complex and sometimes strong dependence of D_{LL}^{total} on μ, and the non-uniform L dependence of D_{LL}^{total}, and the fact that D_{LL}^{Kp} is much smaller than D_{LL}^{total} calculated from the LFM fields, the formula of D_{LL}^{Kp} is not realistic. This further suggests the necessity of achieving a more realistic diffusion coefficient, such as D_{LL}^{total} here.

6.4 MHD Field Validation

The previous sections suggest that using the global fields from LFM MHD simulations, we can determine physical radial diffusion rates that are more realistic than the empirical ones. However, the LFM MHD simulation has its own limitations that are related to the Pc5 wave fields. For example, the ring current is insufficiently represented in the LFM code, causing under-stretched LFM magnetic fields on the nightside during storm time [Huang et al., 2006] and the lack of high-mode number Pc5 waves induced by ring current instabilities [Hudson et al., 2004]. In addition, the lack of cold plasma in the inner magnetosphere in LFM will lead to a higher Alfven velocity, thus contributing to errors in the field line resonance (FLR) frequencies [Claudepierre et al., 2010]. More importantly, since the LFM MHD simulation is a global model developed to describe the large-scale configurations and variations, the small-scaled features, such as substorm dipolarization, and their exact timing, size, and locations may not be well-captured by LFM. Due to these limitations of the LFM MHD code, it is necessary to validate the LFM field results using magnetic and electric field measurements from satellites, such as the magnetic field data from the NOAA geosynchronous satellites, GOES, and both the electric and magnetic field data measured by the Time History of Events and Macroscale Interactions During Substorms (THEMIS) mission.

GOES satellites continuously provide magnetic field observations at geosynchronous orbit from multiple longitude positions at the same time. Panel (a) of Figure 6.8 shows the comparison of

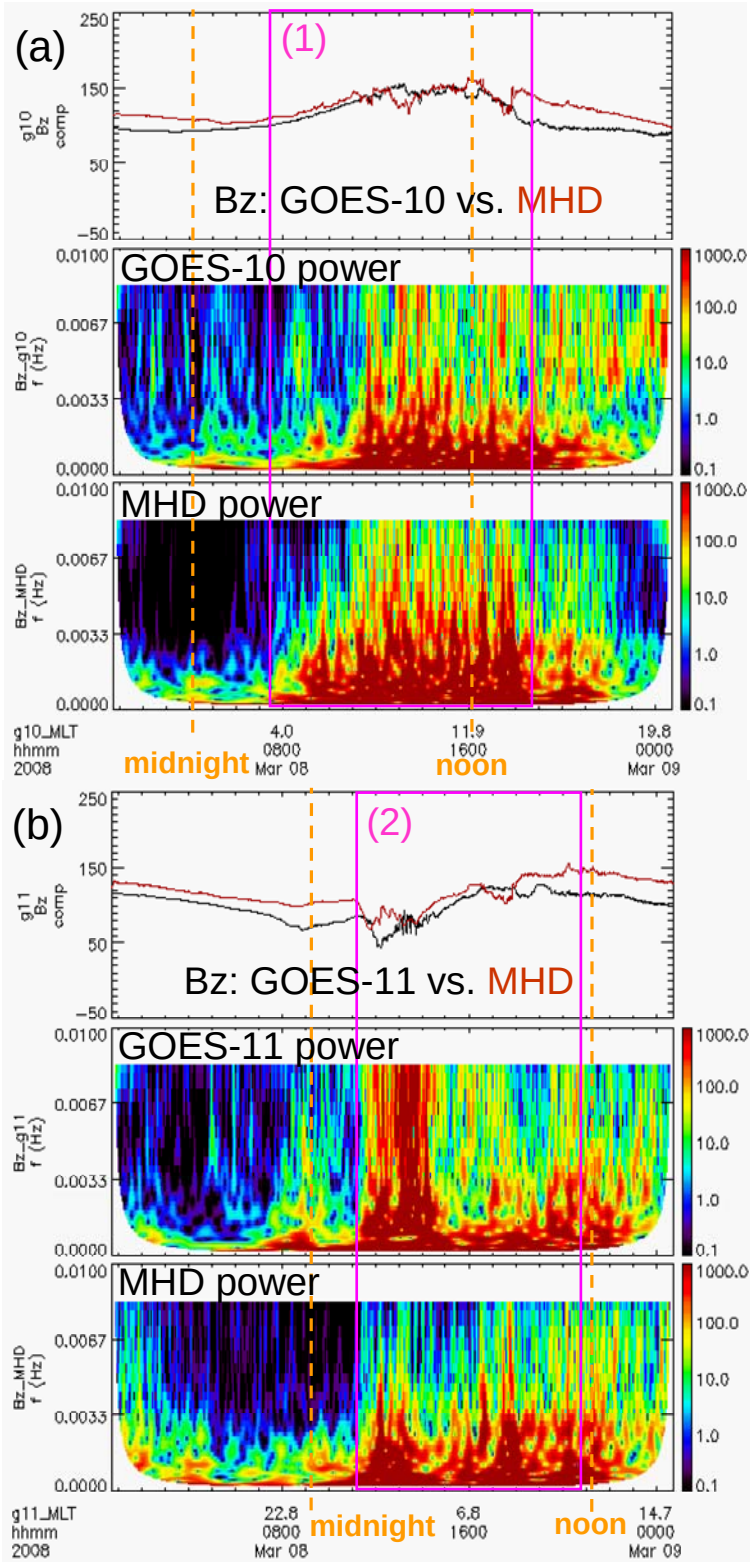

Figure 6.8: B_z comparison between LFM MHD fields and GOES field data, (a) GOES-10 and (b) GOES-11, during March 8th, including field comparison (top plots) and power spectrum comparison (middle and bottom plots).

the magnetic B_z component in SM coordinates between field data from the GOES-10 satellite and LFM fields during the day of March 8th. The black curve in the top plot is the B_z data from GOES-10, with the known, strong diurnal variations (peak around noon at the right orange vertical line). The corresponding power spectrum of the observed GOES-10 B_z data is calculated using a wavelet analysis with a Morlet wavelet [Morlet et al., 1982] and it is shown in the middle plot of panel (a). The color represents the value of power spectral density, X-axis is time, and Y-axis is frequency. The corresponding LFM B_z fields at GOES-10's orbit are shown in the red curve of the top panel. Since the LFM field outputs are only taken at the SM equator, here we assume GOES-10 is at the SM equator and find its positions in LFM domain according to its radial and azimuthal locations. This assumption may introduce some uncertainty to our field comparisons. Similarly, the power spectrum of the LFM B_z fields is shown in the bottom plot of panel (a) to compare with the GOES-10 spectrum. The solar wind and geomagnetic conditions during March 8th are shown in the left panel of Figure 6.9. By comparing with the solar wind conditions, we find that during the same period when the solar wind dynamic pressure is high (the boxed period marked with (1) in Figure 6.9), GOES-10 observes high B_z wave power on the dayside (the same period as in Figure 6.9 is also boxed in purple with mark (1) in Figure 6.8). The scale of the enhanced power region is very large, almost covering half of GOES-10's orbit. Comparing with the LFM B_z power, we find the increased power on the dayside related to the high solar wind dynamic pressure is well-reproduced by the MHD simulation, including the timing, the scale, and the magnitude.

Panel (b) of Figure 6.8 illustrates the B_z comparison for the same day (March 8th), but between field measurements from another GOES satellite, GOES-11, and LFM fields. By comparing the GOES-11 power in panel (b) with the solar wind and geomagnetic conditions in the

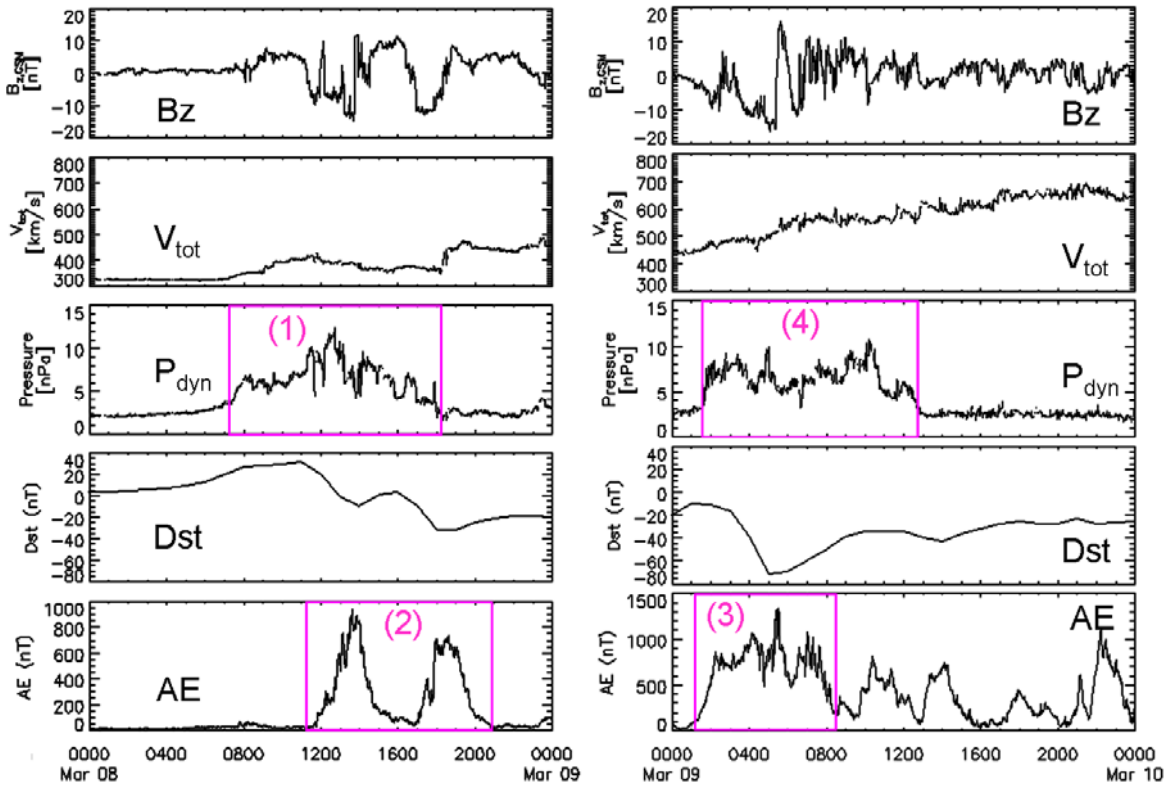

Figure 6.9: Solar wind and geomagnetic conditions during March 8th (left) and March 9th (right). The purple box marked with (1) is the same period with the purple box in Figure 6.8 marked with (1). The same applies for boxes (2), (3), but for box (3) please see Figure 6.10.

left panel of Figure 6.9, it is noticed that increased power is observed by GOES-11 when AE index is high (during the same time period both marked as box (2) in Figures 6.8 and 6.9). GOES-11 was near the nightside during this period (midnight crossing is marked by the orange vertical line on the left). We note the increased power on the nightside related to high AE activity and it has small temporal and spatial scales compared to the dayside power shown in panel (a). The LFM code also generates comparable Pc5 power during the high AE period, except for the high frequency part of the observed GOES-11 power, which is related to the highly wiggly wave packet illustrated in the GOES-11 B_z data (black curve in the top plot). The cause of this wave packet needs to be studied in more detail in the future. But it is still appropriate to conclude that the LFM MHD simulation also fairly well reproduces the Pc5 wave power on the nightside related to AE activity on March 8th.

Figure 6.10 shows similar B_z comparison but for the second day of the storm, March 9th, with the corresponding solar wind and geomagnetic conditions shown in the right panel of Figure 6.9. Panel (a) shows the comparison between GOES-10 and LFM B_z fields. Again, GOES-10 observes high Pc5 wave power during high AE period on the nightside (boxed as (3) in panel (a) and in Figure 6.9). But for this period the power is greatly underestimated by LFM. GOES-11 was in the dusk to midnight sector during the same high AE period (see box (3) in Figure 6.10 panel (b)). The observed high power by GOES-11 is also under-reproduced by LFM. One possible reason for the insufficient power from LFM could be related to its 'unstable' performance. For example, LFM may be able to reasonably reproduce the wave power during the first substorm event right after the launch of the code (high AE period on March 8th), but not perform well for the subsequent substorm event. Or the second high AE period may represent a type of substorm event that is different from the first period, which contributes to the different performance of the LFM code. Another possibility is that the LFM code does capture the strong nightside B_z disturbance, but at a slightly different location. It is so localized that we missed it when we looked at the same radial and

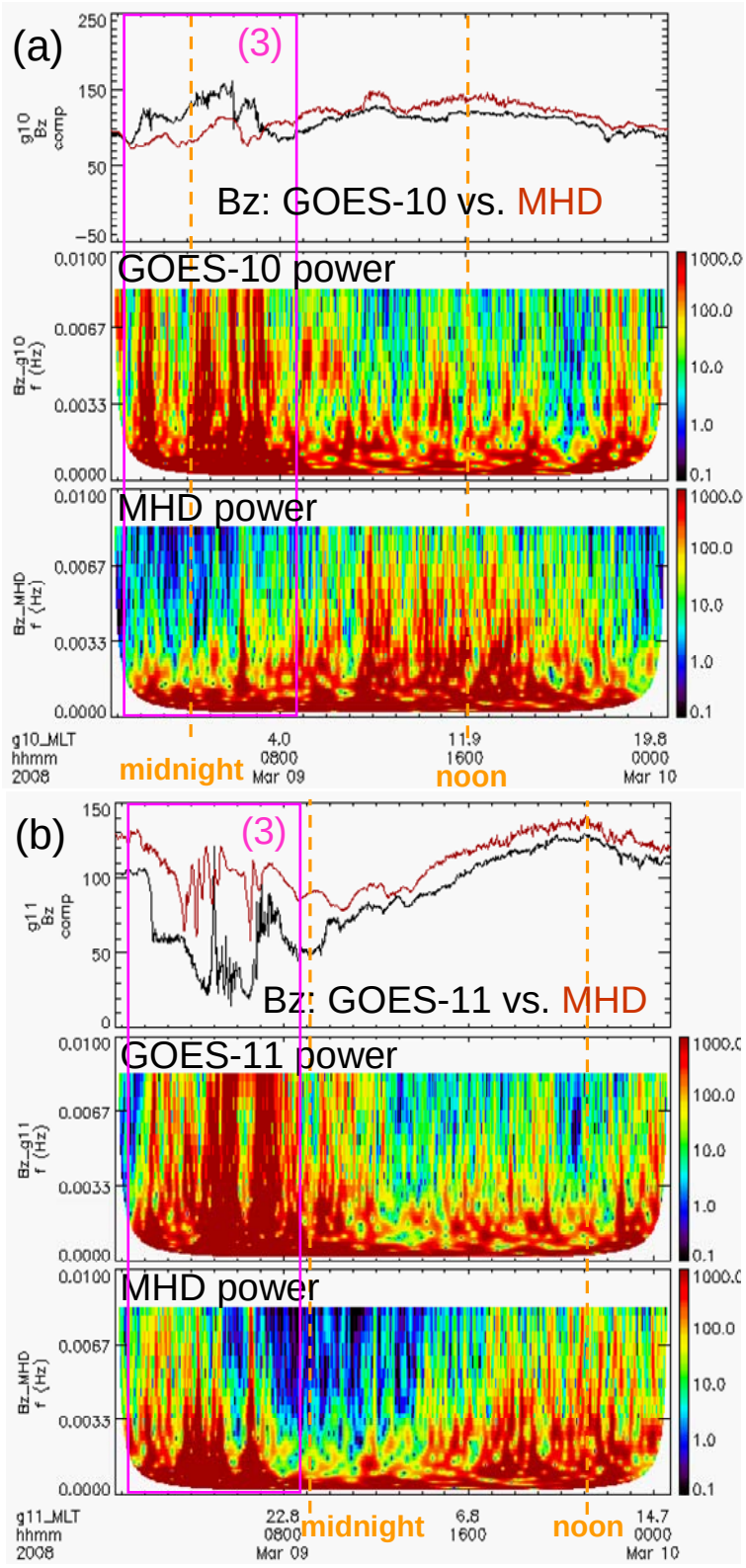

Figure 6.10: B_z comparison between LFM MHD fields and GOES field data during March 9th, with the same configuration as in Figure 6.8.

longitude location as GOES-10 and assumed GOES-10 was on SM equator. To investigate this possibility, global field configurations on the SM equator and off the equator during this period need to be carefully inspected. High solar wind dynamic pressure was also observed on March 9th (the box marked with (4) in Figure 6.9), which may have caused some high Pc5 power on the dayside as did the high pressure on March 8th. Unfortunately, no GOES satellite was near the dayside during that time period.

Based on the preliminary B_z comparison results between GOES field measurements and the fields generated by LFM, we find that Pc5 wave power generated by solar wind dynamic pressure variations is primarily on the dayside, and it is generally well-reproduced by the LFM fields. However, Pc5 waves related to the high AE periods are located on the nightside, and they are small-scale variations. In our comparison, LFM reasonably well reproduces the Pc5 wave power during the first high AE period on the nightside but underestimates the power during the second high AE period on March 9th. As discussed, the insufficient power from LFM could be due to that we are not looking in the right location. However, if it is true that LFM underestimates the Pc5 wave power during that time, some normalization of the LFM power needs to be performed. For example, the mode structure results of B_z shown in Figure 6.3 suggest that the power on the nightside mostly contribute to the power at m>1. One possible normalization method is that during the time when the Pc5 power on the nightside related to the high AE activity is underestimated in LFM, the LFM Pc5 power at m>1 can be normalized by the observed GOES power, while keeping the power at m=1 unchanged. This would lead to even more power at high mode numbers during this time.

Another useful data source for LFM field validation is from the THEMIS mission, which consists of five microsatellites traversing the magnetosphere near the equatorial plane, providing both electric and magnetic field measurements [Angelopoulos, 2008]. The validation by THEMIS

field data is complementary to the validation work with the GOES data, because THEMIS has both high-quality magnetic and electric field data. The electric field data is needed for validation of the LFM electric field results and more accurate estimation of D_{LL}^{E}. Furthermore, THEMIS data has a wider L coverage compared to geosynchronous satellites. Since the validation of LFM electric field has never been done before, we need to be very careful about where and what aspects of the electric field data should be compared and how the validation work should be performed. For example, we only care about the electric field variations in the Pc5 range, rather than the total field strength that may be dominated by the static co-rotational electric field in the inner magnetosphere, which is absent in the LFM code used here. One thing to notice is that from the calculated diffusion coefficients discussed in Section 6.3, we found that the total diffusion coefficient mostly comes from the magnetic part, D_{LL}^{B}, with a much less significant contribution from D_{LL}^{E}. Therefore, as long as the LFM electric field power is not different from the real value by orders of magnitude, the validation of the LFM electric field is not as critical as that for magnetic field. More detailed validation work based on GOES and THEMIS data and appropriate normalization of the LFM fields will be done in the future.

6.5 Discussion and Summary

To achieve more realistic quantification of the radial diffusion rate for electrons in the outer radiation belt, physical electron radial diffusion coefficients due to resonance with stochastic electric and magnetic field perturbations have been derived in this work. The radial diffusion coefficient derived in a dipole field is a function of the power spectral densities of the stochastic fluctuating fields at the electron drift frequency and its harmonics, and a function of the value of the first adiabatic invariant, the L shell value, and time. Due to difficulties in calculating the diffusion coefficient from measured field data only, global LFM MHD simulations were used, to provide the

mode structure and power spectrum of the magnetic and electric field fluctuations in the inner magnetosphere for a CIR storm event in March 2008.

The MHD simulation results demonstrated that the LFM field configurations respond reasonably to the variations of the upstream solar wind conditions during the March 2008 storm. Mode spectrum analyses were performed on these fields to study the mode structure of the integrated field power summed over all the frequencies in the Pc5 range. We found some common features of the integrated magnetic and electric field power at L=6.6: (1) The total power variations of the LFM fields are closely related to the changes of solar wind dynamic pressure, with a generally high power when solar wind dynamic pressure increases; (2) The total power is also modulated by AE activity, with some increase of the total power clearly related to the high AE index; (3) The power at m=1 always has the highest fraction of the total power, indicating that the increase of solar wind dynamic pressure mostly contributes to the Pc5 wave power at low mode numbers; (4) Sometimes, the contributions to the total power from modes with m>1 are also significant, with increasing fraction of high-mode power when the AE index is high (enhanced nightside geomagnetic activity). In contrast, the analysis results also show some different features of the integrated magnetic and electric field power at L=6.6. For example, even though the m=1 power always has the highest fraction in both electric and magnetic powers, the E_φ power spreads over a wider range of mode numbers. In addition, during high AE periods, the fractions of B_z power at m>1 all increase, while the fractions of E_φ power show clear increases only at m>3. The power spectral densities of magnetic and electric fields at the resonance frequencies further show that there is more power at higher L regions, and the magnetic power spectral density has a steeper L dependence than the electric power spectral density, and it decreases faster than the electric power as the mode number increases.

Using the calculated power spectral densities of magnetic and electric fields at the resonance frequencies from LFM fields, the diffusion coefficients were calculated using theoretically derived equations. The results show that the total diffusion coefficient is mostly dominated by the magnetic part of the diffusion coefficients, with much smaller contributions from the electric part. The diffusion coefficients are generally higher when solar wind dynamic pressure and/or the AE index are high and the diffusion is faster at higher L shells. The calculated diffusion coefficients exhibit a complex and sometimes strong dependence on the first adiabatic invariant, and a non-uniform L-dependence, which are not captured in the empirical diffusion coefficient D_{LL}^{Kp} used in Chapter 3. Quantitatively, we found D_{LL}^{Kp} generally underestimated the diffusion coefficients calculated from the LFM fields during our storm event.

We have performed some preliminary validation work for the LFM MHD fields. By comparisons with GOES magnetic field measurements, we found the LFM code reasonably well-reproduced the Pc5 wave power generated by solar wind dynamic pressure variations and by nightside geomagnetic activity. More detailed validation work is required and planned to be done in the future.

As a final remark, the physical diffusion coefficient quantified in our study is much more realistic than the empirical one based on the Kp index. Even though the LFM MHD fields have several limitations and the validation work is not trivial, using MHD fields validated by observations is still the best way to obtain the global ULF wave spectra and mode structure. In this way, the physical radial diffusion rate can be quantified as a function of L, the first adiabatic invariant or electron energies, and time. This can be then directly used by radial diffusion models, such as the Fokker-Planck model in Chapter 3, to better simulate the radial diffusion process in the outer radiation belt.

Chapter 7

Conclusion

7.1 Summary and Conclusions

The primary goal of this work is to quantify the relative contribution of radial diffusion, wave heating, and loss to the enhancement and decay of the radiation belt electrons, which is one of the central questions in radiation belt research. The question cannot be resolved by data analysis alone since the observed radiation belt variation is a combination of these processes acting simultaneously, and for quantitative studies physical models are needed. This establishes the spirit of this thesis, in which we opened up multiple fronts of modeling the various competing processes acting on the outer radiation belt electrons, together and individually.

In Chapter 3, an empirical Fokker-Planck model that incorporates all the factors of radial diffusion, internal heating, and loss was developed to test the relative importance and timing of these processes against data. By simulating the observed electron phase space density variations during the second half of year 2002, the model reproduced the average variations of radiation belt electrons but with over-prediction and under-prediction at different times, suggesting that the same set of parameters cannot be applied to all storms within that half year. Detailed simulation results for four individual storms indicated that three storms could be reproduced either by radial diffusion only with losses or by internal heating only with losses, but including both led to the best results; while the other storm clearly required significant local heating during the storm recovery phase. Therefore, we conclude that the required magnitudes of radial diffusion and internal heating for the enhancement of energetic electrons in the outer radiation belt vary from storm to storm, and after

further analysis of the model results we suggest that internal heating generally contributes more to the enhancements of relativistic electrons at L=4 than radial diffusion.

However, the results from Chapter 3 contain uncertainties, since the radial diffusion, source, and loss terms in the Fokker-Planck model are empirical functions of geomagnetic indices, though with some free parameters to be tuned against data. Uncertainties from these empirical terms lead to uncertainties in our conclusions about the relative contributions of individual acceleration and loss mechanisms to the variations of outer radiation belt electrons. For example, without a realistic loss rate, we cannot accurately include the source needed to compensate the loss and reproduce the observed electron enhancement. Therefore, our goal is to first achieve more realistic quantification of the loss and radial diffusion rates using independent modeling approaches, which fixes two of the three empirical terms, and then incorporate them into the Fokker-Planck model to determine the local heating rate with less uncertainty. This is the motivation of our work in Chapters 4, 5, and 6.

Precipitation loss into the atmosphere is the dominant non-adiabatic loss mechanism for electrons in the heart of the outer radiation belt. This loss is not well understood due to the lack of adequate observation of the waves and a clear picture of the pitch angle distribution of electrons near the loss cone. In Chapter 4, we applied a Drift-Diffusion model to quantify the rate as well as the spatial and temporal variations of electron precipitation loss in the outer radiation belt. The model includes the effects of azimuthal drift and pitch angle diffusion to simulate the low-altitude electron distribution observed by SAMPEX. Model results for three individual storms (a small storm, a moderate storm, and an intense storm) show that fast precipitation losses of relativistic electrons, on the time scale of hours, persistently occur in the storm main phase and with more efficient losses for higher-energy electrons over wide range of L values. These results indicate that there must be some quick scattering processes, functioning preferably on higher energy electrons during the storm main phase. We also found that the energy dependence in the electron loss rate

differs for different storms, which could be time- and L-dependent, and significant dawn-dusk asymmetry in the loss rate can occur during the storm main phase or recovery phase.

After quantifying the non-adiabatic electron loss, a quantitative study of the storm-time adiabatic loss of radiation belt electrons was presented in Chapter 5, which for the first time focused primarily on electrons mirroring at low altitude. During the main phase of a geomagnetic storm the adiabatic effects on low-altitude electrons include the expansion of the drift shell, the rise of the mirror point in altitude that is unique for electrons mirroring off-equator, and a shift in the energy spectrum. Calculations of the adiabatic flux change at low altitudes using a modified dipole model demonstrated that the storm-time adiabatic effects on electron flux are both altitude and storm dependent. The rise of the electron mirror points can lead to a null flux region at low altitudes. A satellite in the null flux region sees zero flux during the storm time due solely to adiabatic effects, which can persist when the non-adiabatic pitch angle diffusion is very slow. A low-altitude satellite above the null flux region will see a fractional flux drop due to the adiabatic effects. For example, for the March 2008 geomagnetic storm with minimum Dst of -72 nT, there would be a factor of 2.4-2.8 decrease in the flux of relativistic electrons mirroring at 700 km and L*=4.5, compared to a decrease of a factor of ~15 for equatorially mirroring electrons due to adiabatic effects.

After focusing on the electron loss rate in Chapter 4 and 5, in Chapter 6 the physical electron radial diffusion rate due to resonance with stochastic electric and magnetic field perturbations was derived and calculated. Due to the difficulties of specifying power spectral density and global mode structure of the Ultra-Low-Frequency (ULF) waves from real data, global magnetic and electric fields from the LFM MHD simulation were used. The calculation results showed that the total diffusion rate is dominated by the contribution from magnetic field perturbations, and much less from the electric field perturbations. The diffusion rates are generally higher when solar wind dynamic pressure is high or nightside geomagnetic activity is strong and the diffusion is faster at

higher L regions. The calculated diffusion coefficient was shown to be more realistic than the empirical diffusion coefficient, D_{LL}^{Kp}, used in Chapter 3. It has a complex and sometimes strong dependence on the first adiabatic invariant and a non-uniform L-dependence, which are features not captured by D_{LL}^{Kp}. Quantitatively, we found D_{LL}^{Kp} generally underestimates the diffusion coefficients calculated from the LFM fields during our storm event. Due to the limitations of the LFM MHD code, the LFM fields need to be validated by field measurements form real satellites, such as the magnetic field data from GOES and both the magnetic and electric field data from THEMIS. This validation work is still very preliminary, but exhibits high promise.

Individually, the studies presented in this thesis all achieved significant results. More importantly, they tie together to form a promising framework for obtaining quantitative understanding of the relative importance of radial diffusion, wave heating, and loss to the dynamics of radiation belt electrons. First, the Drift-Diffusion model combined with the low-altitude observations is capable of providing direct quantification of the electron precipitation loss rate into the atmosphere, as well as its spatial and temporal variations. Second, our study on the adiabatic electron loss is the first quantitative analysis combining both observation and modeling for adiabatic effects on the variation of outer radiation electrons at low altitude. Adiabatic effects can be implemented in the loss models of outer radiation belt electrons to more accurately quantify the non-adiabatic loss. Moreover, the physically calculated diffusion coefficient as a function of L, the first adiabatic invariant or electron energies, and time, is more realistic than empirically derived ones. Finally, our comprehensive Fokker-Planck model including radial diffusion, internal heating, and loss is able to take the above results as inputs and determine the internal heating rate from data, eventually resolving the relative importance and timing of all these processes. These studies open up opportunities for various future projects and are closely related to the RBSP mission as discussed below.

7.2 Future Work

Some future work along the line of this thesis include improving individual models as well as incorporating all the models together to form a comprehensive modelling framework to simulate the outer radiation belt electron dynamics and to quantify the relative contribution from radial diffusion, wave heating, and loss processes.

First, the Drift-Diffusion model introduced in Chapter 4 to quantify the precipitation loss of radiation belt electrons can be improved to resolve faster electron lifetime variations. As discussed in subsection 4.5.5 of Chapter 4, constrained by the length of time required for SAMPEX data to reach full longitude coverage, the current model cannot resolve the variations of electron loss rate on timescales shorter than 12 hours. However, higher-resolution electron lifetimes are required as inputs for the Fokker-Planck model introduced in Chapter 3, since the electron loss rate can change much faster than 12 hours. One straightforward solution is to rely on more and faster data coverage at low altitude, such as data from a cluster of LEO satellites covering different longitudes at the same time. In subsection 4.5.5, we proposed one existing data source, the NOAA POES multi-satellite electron measurements, and another proposed constellation mission, EPhIC. The idea is straightforward, while realizing it is not easy. For example, if we want to use POES data together with SAMPEX data in the Drift-Diffusion model, first we need better knowledge of the POES electron detector and its response functions, as well as a clear understanding of the proton contamination issue in the relativistic electron data and how to remove it appropriately. In addition, cross-satellite calibration is needed between POES and SAMPEX electron data before implementing both data sets into our model.

Second, since the observed electron flux variations, such as SAMPEX electron data, are a combination of both adiabatic and non-adiabatic effects, it is more realistic to incorporate the adiabatic effects analyzed in Chapter 5 into the Drift-Diffusion model in Chapter 4 to investigate

how that would affect the resolved electron precipitation loss rate, and how the model fit to SAMPEX data can be improved, even though a generally good data fit is already achieved by using only the Drift-Diffusion model. This can be realized by including the adiabatic corrections at each simulation time step of the Drift-Diffusion model, updating the modeled phase space densities as a function of energy and equatorial pitch angle with the adiabatically corrected ones. In addition, in subsection 5.5.2 of Chapter 5 we proposed that the resulting adiabatic change in the electron pitch angle distribution can cause increased electron precipitation without changing the pitch angle diffusion rate, by exciting higher-order eigenmodes of the bounce-averaged pitch angle diffusion. This additional precipitation can be tested and quantified by combining the adiabatic variations in the Drift-Diffusion model which includes the effect of pitch angle diffusion.

Third, more detailed validation work of the LFM MHD fields against real field measurements needs to be done. In Section 6.4 of Chapter 6, some preliminary validation of the LFM fields using the GOES magnetic field data was performed. Further validation work includes more extensive investigation of the LFM fields when comparing with the data from a certain satellite instead of only looking at the SM equator and at the exact satellite locations, validating the LFM fields with THEMIS electric and magnetic fields which cover a wider L range, and some appropriate normalization on the LFM field power. This validation of LFM fields requires collaborations between our group and colleagues who are actively developing the LFM code. This is a challenging but promising task.

Finally, the well-quantified loss rate and radial diffusion rate of outer radiation belt electrons from the models above will be used as inputs to the comprehensive Fokker-Planck model described in Chapter 3. By simulating the observed electron phase space density variations and with more realistic electron lifetime and radial diffusion coefficient, the model can determine the local heating rate of radiation belt electrons with less uncertainty. Then we will have a comprehensive modeling

framework that is able to simulate the outer radiation belt dynamics well and quantify the relative contribution of radial diffusion, wave heating, and loss processes. This modeling approach can be applied to a variety of geomagnetic storms covering different phases of solar cycles or different solar wind conditions, to investigate what aspects of the solar wind are primarily responsible for electron enhancement and decay in the outer radiation belt.

7.3 Relation with NASA/RBSP Mission

The Radiation Belt Storm Probes (RBSP) Mission, part of NASA's Living With a Star (LWS) program, is scheduled to be launched in 2012. It will orbit the Earth and sample the radiation belt with an orbital inclination $\leq 18^0$, perigee altitude of ~500 kilometers and apogee altitude of ~30,600 kilometers. With two launched spacecraft taking identical measurements and following the same path, the NASA/RBSP mission will provide accurate particle, magnetic and electric field and wave measurements that change in both space and time. The mission's main science objectives include: discover which processes, singly or in combination, accelerate and transport radiation belt electrons and ions and under what conditions; understand and quantify the loss of radiation belt electrons and determine the balance between competing acceleration and loss processes; and understand how the radiation belts change in the context of geomagnetic storms. These objectives are well aligned with the goal of this thesis.

On one hand, the mission will provide accurate particle and field measurements, which can serve as the database for our models and quantify our understanding. First, the well-resolved electron flux data (both in energy and pitch angle) from RBSP will have wide L coverage and include electrons at high altitude well outside the loss cone. These data will enrich the database for our model, such as the PSD data for the Fokker-Planck model which is currently not continuous over L (see panel (a) of Figure 3.1), and provides further data constraints for the loss model at high pitch angles (Chapter 4). Second, more accurate field and wave data from RBSP can help us to

better quantify the loss and acceleration rates and to understand the underlying mechanisms. For example, with RBSP wave data more realistic pitch angle diffusion coefficients can be calculated based on quasi-linear theories, which can then be used to replace the assumed diffusion coefficient in Eq. 4.2. Furthermore, the quantified electron loss rates in Chapter 4 can be compared against the wave measurements to address the possible electron loss mechanisms. In addition, the measured Pc5 wave measurements by RBSP can be used to validate the ULF waves from LFM MHD fields for quantifying radial diffusion (Chapter 6).

On the other hand, our work helps the RBSP mission to achieve full science closure. Firstly, since the observed variation of radiation belt electron flux is a delicate balance of energization, transport, and loss, conclusive results about the relative contribution from individual processes cannot be achieved by data analysis alone. Physics-based modeling efforts are required for quantitative understanding, like the projects performed in this thesis. Secondly, in Chapter 4 we discussed using SAMPEX data to estimate the loss rate of radiation belt electrons. With an angular resolution ~10 degrees near the equatorial plane, the RBSP measurements cannot resolve the electron pitch angle distribution near and inside loss cone. Therefore, SAMPEX still has the best data to address the precipitation loss and it is likely that SAMPEX will still be operating after RBSP's launch (currently, SAMPEX is operated by Aerospace Corporation and data have been continuously collected). Therefore, our work will help the mission to ensure full science closure by obtaining a better understanding of the precipitation loss.

7.4 Lessons Learned

While working on the various projects included in this thesis work, I have learned several lessons described below. I end my thesis with the lessons learned in order to help me learn from the past and to share some useful experience with the readers.

First, lessons learned in literature reading. When stepping into a new field of study, literature reading always comes first. But, I sometimes found myself in two types of bad situations. The first is getting lost in literature searching. For example, I read about a new concept in a paper with some references therein. After digging into those references I found further referred papers that need to be read but without finding the fundamental explanation of that concept. Then I dug even deeper but ended with more than ten papers in hand and finding myself lost and distracted. Another bad state is getting too ambitious in learning new concepts or theories. For example, in a long review book I found various types of concepts and related theories are listed and discussed. Wanting to understand them all at one time, I made up my mind to read one chapter per week and to finish the book in one month. But normally what happened in the end was either quitting in the middle or superficially finishing the whole book with little really learned. The above two methods of literature reading are very inefficient. After years of experience, I realized that motivation is very important in literature reading. Either motivated by your own research project or some interesting results heard from a meeting or the discussions (even arguments) with your colleagues will greatly improve your efficiency in literature reading and the learning of new concepts or theories. Also, learning some skills of extensive reading is very helpful. Finally, keeping track of the newly published papers in your field is as important as reading review papers or books, which can keep you updated on other colleagues' projects and inspire or directly contribute to your own research. It can be approached by signing up for the E-alert of relevant journals and visiting their websites on a weekly basis.

Second, lessons learned in the modeling work and coding experience, which include two parts, working on other colleagues' code and writing my own code. When working on a code written by others, I learned the following lessons: 1. Do not start reading from line to line. Try to learn the algorithm used in the code first (ask the code writer or find out by yourself), and then divide the entire code (usually as long as hundreds of lines) into several blocks according to their functionalities. Then read from block to block. 2. Always save the original code and make sure the

original code runs fine in your computer and the original results can be reproduced. 3. Keep records of all the changes you made in the code. After implementing one changed step, if the code works as you want, save the code in a separate file where you can return. While writing your own code, similar tips from the above may also apply, e.g., starting with generating a code algorithm and building several big blocks first, and saving code to a separate file whenever a step of functionality is realized. Another important tip is to make as many comments in the code as possible, indicating the function of each line or block. You will find them extremely helpful when the code is revisited a long time after it is written. In addition, pay attention to the numerically bad results from the code rather than ignoring them, since they may represent some weakness of your algorithm, such as a numerical instability that may be related to the grid resolution, etc.

There are also some miscellaneous lessons I learned during my research work. It is very important to communicate with your colleagues about your research and theirs, which can broaden your mind and inspire your work. Meetings or conferences are the best chance for you to talk to people. Second, whenever there is a chance for you to give a talk, take it. Whenever you give a talk, make it good. Third, take good notes of the details during your work as well as random ideas. Fourth, if time allows, type all your derivations in a computer instead of keeping them on a piece of paper with your scratchy handwritings. This can help organize the logical flow and make it easier for others and yourself to read later. Finally, be cautious about the uncertainties in both data and model during your research. For example, from Chapter 4, I am aware of the uncertainties in SAMPEX data, and in Chapter 6, I learned about the limitations and artificial waves in the LFM MHD simulation. When a quantitative analysis is performed, error bars need to be calculated along the way due to the uncertainties from data and in the model. This is something overlooked in my previous work and more attention will be paid to it in the future.

Bibliography

Abel, B., and R. M. Thorne (1998), Electron scattering loss in Earth's inner magnetosphere 1. Dominant physical processes, *J. Geophys. Res.*, *103*(A2), 2385-2396.

Albert, J. M. (2003), Evaluation of quasi-linear diffusion coefficients for EMIC waves in a multispecies plasma, *J. Geophys. Res.*, *108*(A6), 1249, doi:10.1029/2002JA009792.

Albert, J. M., and Y. Y. Shprits (2009), Estimates of lifetimes against pitch angle diffusion, *J. Atmos. Sol. Terr. Phys.*, *71*, 1647-1652, doi:10.1016/j.jastp.2008.07.004.

Angelopoulos, V. (2008), The THEMIS Mission, *Space Sci. Rev.*, doi:10.1007/s11214-008-9336-1.

Baker, D. N., R. L. McPherron, T. E. Cayton, and R. W. Kebesadel (1990), Linear Prediction Filter Analysis of Relativistic Electron Properties at 6.6 R_E , *J. Geophys. Res.*, *95*(A9), 15,133-15,140.

Baker, D. N., G. M. Mason, O. Figueroa, G. Colon, J. Watzin, and R. Aleman (1993), An overview of the SAMPEX mission, IEEE Trans. Geosc. Elec., 31, 531, 1993.

Baker, D. N., J. H. Allen, S. G. Kanekal, and G. D. Reeves (1998a), Disturbed space environment may have been related to pager satellite failure, *Eos Trans. AGU*, *79*(40), 477.

Baker, D.N., et al. (1998b), Coronal mass ejections, magnetic clouds, and relativistic magnetospheric electron events: ISTP, *J. Geophys. Res.*, 103, 17,279-17,291.

Baker, D.N., et al. (1998c), A strong CME-related magnetic cloud interaction with the Earth's magnetosphere: ISTP observations of rapid relativistic electron acceleration on May 15, 1997, *Geophys. Res. Lett., 25*, 2975-2978.

Baker, D. N., and S. Kanekal (2008), Solar cycle changes, geomagnetic variations, and energetic particle properties in the inner magnetosphere, *J. Atmos. Sol. Terr. Phys., 70*(2-4), 195-206, doi:10.1016/j.jastp.2007.08.031.

Barker, A. B., X. Li, and R. S. Selesnick (2005), Modeling the radiation belt electrons with radial diffusion driven by the solar wind, *Space Weather*, Vol. 3, No. 10, S1000310.1029/2004SW000118.

Blake, J. B., W. A. Kolasinski, R. W. Fillius, and E. G. Mullen (1992), Injection of electrons and protons with energies of tens of MeV into L <3 on March 24, 1991, *Geophys. Res. Lett., 19*, 821, 1992.

Blake, J., U. Inan, M. Walt, T. Bell, J. Bortnik, D. Chenette, and H. Christian (2001), Lightning-induced energetic electron flux enhancements in the drift loss cone, *J. Geophys. Res., 106*(A12), 29733-29744.

Brautigam, D. H., and J. M. Albert (2000), Radial diffusion analysis of outer radiation belt electrons during the 9 October 1990 magnetic storm, *J. Geophys. Res., 105*, 291.

Brautigam, D. H., G. P. Ginet, J. M. Albert, J. R. Wygant, D. E. Rowland, A. Ling, and J. Bass (2005), CRRES electric field power spectra and radial diffusion coefficients, *J. Geophys. Res., 110*, A02214, doi:10.1029/2004JA010612.

Burin des Roziers, E. and X. Li (2006), Specification of >2 MeV geosynchronous electrons based on solar wind measurements, *Space Weather*, 4, S06007, doi:10.1029/2005SW000177.

Chen, Y., R. H. W. Friedel, and G. D. Reeves (2006), Phase space density distributions of energetic electrons in the outer radiation belt during two Geospace Environment Modeling Inner Magnetosphere/Storms selected storms, *J. Geophys. Res., 111*, A11S04, doi:10.1029/2006JA011703.

Chen, Y., G. D. Reeves and R. H. W. Friedel (2007), The Energization of Relativistic Electrons in the Outer Van Allen Radiation Belt, *Nature Physics*, *3*(9, doi:10.1038/nphys655), 614-617.

Claudepierre, S. G., M. K. Hudson, W. Lotko, J. G. Lyon, and R. E. Denton (2010), Solar wind driving of magnetospheric ULF waves: Field line resonances driven by dynamic pressure fluctuations, *J. Geophys. Res., 115*, A11202, doi:10.1029/2010JA015399.

Cook, W. R., et al. (1993), PET: A Proton/Electron Telescope for studies of magnetospheric, solar, and galactic particles, IEEE Trans. Geosc. Remote Sens., 31, 565-571.

Elkington, S. R., M. K. Hudson, and A. A. Chan (1999), Acceleration of relativistic electrons via drift-resonant interaction with toroidal-mode Pc-5 ULF oscillation. *Geophysical Research Letters 26*, 3273-3276.

Elkington, S.R., M.K. Hudson, M.J. Wiltberger, and J.G. Lyon (2002), MHD/particle simulations of radiation belt dynamics, *J. Atmos. Sol. Terr. Phys., 64*, 607-615, doi:10.1016/S1364-6826(02)00018-4.

Elkington, S.R., M.K. Hudson, and A.A. Chan (2003), Resonant acceleration and diffusion of outer zone electrons in an asymmetric geomagnetic field, *J. Geophys. Res., 108*(A3), 1116, doi:10.1029/2001JA009202.

Elkington, S.R., M. Wiltberger, A.A. Chan, and D.N. Baker (2004), Physical models of the geospace radiation environment, *J. Atmos. Sol. Terr. Phys., 66,* 1371-1387, doi:10.1016/j.jastp.2004.03.023.

Engebretson M. J., et al. (2008), Pc1-Pc2 waves and energetic particle precipitation during and after magnetic storms: Superposed epoch analysis and case studies, *J. Geophys. Res., 113*, A01211, doi:10.1029/2007JA012362.

Erlandson, R. E., and A. J. Ukhorskiy (2001), Observations of electromagnetic ion cyclotron waves during geomagnetic storms: Wave occurrence and pitch angle scattering, *J. Geophys. Res.*, *106*(A3), 3883-3895.

Fäthammar, C. G. (1965), Effects of time-dependent electric fields on geomagnetically trapped radiation, *J. Geophys. Res., 70,* 2503.

Fei, Y., A. A. Chan, S. R. Elkington, and M. J. Wiltberger (2006), Radial diffusion and MHD-particle simulations of relativistic electron transport by ULF waves in the September 1998 storm, *J. Geophys. Res.* 111, A12209, doi:10.1029/2005JA011211.

Fennell, J. F., H. C. Koons, J. L. Roeder, and J. B. Blake (2001), Spacecraft charging: Observations and relationship to satellite anomalies, in Proceedings of 7th Spacecraft Charging Technology Conference, Eur. Space Agency Spec. Publ., ESA SP-476, p. 279.

Fok, M.-C., R. B. Horne, N. P. Meredith, and S. A. Glauert (2008), Radiation Belt Environment model: Application to space weather nowcasting, *J. Geophys. Res., 113,* A03S08, doi:10.1029/2007JA012558.

Fraser, B. J., and T. S. Nguyen (2001), Is the plasmapause a preferred source region of electromagnetic ion cyclotron waves in the magnetosphere?, *J. Atmos. Terr. Phys., 63*, 1225, 2001.

Friedel, R. H. W., G. D. Reeves, and T. Obara (2002), Relativistic electron dynamics in the inner magnetosphere - a review, J. Atmos. *Sol. Terr. Phys.*, 64, 265-282.

Gannon, J. L., X. Li, and D. Heynderickx (2007), Pitch angle distribution analysis of radiation belt electrons based on Combined Release and Radiation Effects Satellite Medium Electrons A data, *J. Geophys. Res.*, 112, A05212, doi:10.1029/2005JA011565.

Gonzalez, W. D., Tsurutani, B. T, and Clua de Gonzalez, A. L. (1999), Interplanetary origin of geomagnetic storms, *Space Sci. Rev.*, 88, 529.

Gosling, J. T., S. J. Bame, D. J. McComas, and J. L. Phillips (1990), Coronal mass ejections and large geomagnetic storms, *Geophys. Res. Lett.,* 17(7), 901-904.

Gosling, J., D. McComas, J. Phillips, and S. Bame (1991), Geomagnetic Activity Associated with Earth Passage of Interplanetary Shock Disturbances and Coronal Mass Ejections, *J. Geophys. Res.,* 96(A5), 7831-7839.

Green, J. C., and M. G. Kivelson (2004), Relativistic electrons in the outer radiation belt: Differentiating between acceleration mechanisms, *J. Geophys. Res., 109*, A03213, doi:10.1029/2003JA010153.

Gustafsson, G., N. E. Papitashvili, and V. O. Papitashvili (1992), A Revised Corrected Geomagnetic Coordinate System for Epochs 1985 and 1990, *J. Atmos. Terr. Phys.*, 54, 1609-1631.

Hasegawa, H., et al. (2004), Transport of solar wind into Earth's magnetosphere through rolled-up Kelvin-Helmholtz vortices, *Nature*, *430*, 755.

Hayakawa, M., and Sazhin, S.S. (1992), Mid-latitude and plasmaspheric hiss: a review. Planetary and Space Science 40, 1325-1338.

Hilmer, R., G. Ginet, and T. Cayton (2000), Enhancement of equatorial energetic electron fluxes near L = 4.2 as a result of high speed solar wind streams, *J. Geophys. Res., 105*, 23,311-23,322.

Horne, R. B., and R. M. Thorne (1998), Potential waves for relativistic electron scattering and stochastic acceleration during magnetic storms, *Geophys. Res. Lett., 25*, 3011, 1998.

Horne, R. B., et al. (2005a), Wave acceleration of electrons in the Van Allen radiation belts, *Nature,* 437, 227.

Horne, R. B., R. M. Thorne, S. A. Glauert, J. M. Albert, N. P. Meredith, and R. R. Anderson (2005b), Timescale for radiation belt electron acceleration by whistler mode chorus waves, *J. Geophys. Res., 110*, A03225, doi:10.1029/2004JA010811.

Horne, R. B., R. M. Thorne, S. A. Glauert, N. P. Meredith, D. Pokhotelov, and O. Santolík (2007), Electron acceleration in the Van Allen radiation belts by fast magnetosonic waves, *Geophys. Res. Lett.*, *34*, L17107, doi:10.1029/2007GL030267.

Horne, R. B., M. M. Lam, and J. C. Green (2009), Energetic electron precipitation from the outer radiation belt during geomagnetic storms, *Geophys. Res. Lett., 36,* L19104, doi:10.1029/2009GL040236.

Huang, C.−L., H. E. Spence, J. G. Lyon, F. R. Toffoletto, H. J. Singer, and S. Sazykin (2006), Storm−time configuration of the inner magnetosphere: Lyon−Fedder−Mobarry MHD code, Tsyganenko model, and GOES observations, *J. Geophys. Res.*, 111 , A11S16, doi:10.1029/2006JA011626.

Huang, C.−L., H. E. Spence, H. J. Singer, and W. J. Hughes (2010a), Modeling radiation belt radial diffusion in ULF wave fields: 1. Quantifying ULF wave power at geosynchronous orbit in observations and in global MHD model, *J. Geophys. Res.*, 115, A06215, doi:10.1029/2009JA014917.

Huang, C.−L., H. E. Spence, M. K. Hudson, and S. R. Elkington (2010b), Modeling radiation belt radial diffusion in ULF wave fields: 2. Estimating rates of radial diffusion using combined MHD and particle codes, *J. Geophys. Res.*, 115, A06216, doi:10.1029/2009JA014918.

Hudson, M. K., A. D. Kotelnikov, X. Li, I. Roth, M. Temerin, J. Wygant, J. B. Blake, and M. S. Gussenhoven (1995), Simulation of proton radiation belt formation during the March 24, 1991 SSC, *Geophys. Res. Lett., 22*, 291, 1995.

Hudson, M.K., Elkington, S.R., Lyon, J.G., Goodrich, C.C., and Rosenberg, T.J. (1999), Simulation of radiation belt dynamics driven by solar wind variations. In: Burch, J.L., Carovillano, R.L., Antiochos, S.K. (Eds.), Sun-Earth Plasma Connections, Geophys. Monograph. Series, Vol. 109. AGU, Washington, DC, pp. 171-182.

Hudson, M.K., S.R. Elkington, J.G. Lyons and C.C. Goodrich (2000), Increase in relativistic electron flux in the inner magnetosphere: ULF wave mode structure. *Advances in Space Research 25*, 2327-2337.

Hudson, M., R. Denton, M. Lessard, E. Miftakhova, and R. Anderson (2004), A study of Pc-5ULF oscillations, *Ann. Geophys., 22*, 289.

Iles, R. H. A., A. N. Fazakerley, A. D. Johnstone, N. P. Meredith, and P. Bühler (2002), The relativistic electron response in the outer radiation belt during magnetic storms, *Ann. Geophys.*, 20, 957-965.

Iles, R. H. A., N. P. Meredith, A. N. Fazakerley, and R. B. Horne (2006), Phase space density analysis of the outer radiation belt energetic electron dynamics, *J. Geophys. Res.*, *111*, A03204, doi:10.1029/2005JA011206.

Imhof, W., H. Voss, J. Mobilia, D. Datlowe, E. Gaines, J. McGlennon, and U. Inan (1992), Relativistic electron microbursts, *J. Geophys. Res.*, *97*, 13,829-13,837.

Jordanova, V. K., C. J. Farrugia, R. M. Thorne, G. V. Khazanov, G. D. Reeves, and M. F. Thomsen (2001a), Modeling ring current proton precipitation by electromagnetic ion cyclotron waves during the May 14–16, 1997 storm, *J. Geophys. Res.*, *106*, 7-22.

Jordanova, V. K., R. M. Thorne, C. J. Farrugia, Y. Dotan, J. F. Fennell, M. F. Thomsen, G. D. Reeves, and D. J. McComas (2001b), Ring current dynamics during the 13–18 July 2000 storm period. Solar Physics 204, 361-375.

Kanekal, S., D. Baker, and J. Blake (2001), Multisatellite measurements of relativistic electrons: Global coherence, *J. Geophys. Res., 106*(A12), 29721-29732.

Kennel, C.F., and Petschek, H.E. (1966), Limit on stably trapped particle fluxes, *J. Geophys. Res.* 71, 1.

Kennel, C. F. (1969), Consequences of a magnetospheric plasma, *Rev. Geophys.*, 7(1, 2), 379-419.

Kim, H.-J., and A. A. Chan (1997), Fully adiabatic changes in storm time relativistic electron fluxes, *J. Geophys. Res., 102*,22,107-22,116, doi:10.1029/97JA01814.

Kim, K. C., D.−Y. Lee, H.−J. Kim, E. S. Lee, and C. R. Choi (2010), Numerical estimates of drift loss and Dst effect for outer radiation belt relativistic electrons with arbitrary pitch angle, *J. Geophys. Res., 115,* A03208, doi:10.1029/2009JA014523.

Kivelson, M. G., and C. T. Russell (Eds.), *Introduction to Space Physics*, Cambridge Univ. Press, New York, 1995.

Koller, J., Y. Chen, G. D. Reeves, R. H. W. Friedel, T. E. Cayton, and J. A. Vrugt (2007), Identifying the radiation belt source region by data assimilation, *J. Geophys. Res., 112,* A06244, doi:10.1029/2006JA012196.

Kondrashov, D., Y. Shprits, M. Ghil, and R. Thorne (2007), A Kalman filter technique to estimate relativistic electron lifetimes in the outer radiation belt, *J. Geophys. Res., 112*, A10227, doi:10.1029/2007JA012583.

Lam, M. M., R. B. Horne, N. P. Meredith, S. A. Glauert, T. Moffat-Griffin, and J. C. Green (2010), Origin of energetic electron precipitation >30 keV into the atmosphere, *J. Geophys. Res., 115*, A00F08, doi:10.1029/2009JA014619.

Li, W., Y. Y. Shprits, and R. M. Thorne (2007), Dynamic evolution of energetic outer zone electrons due to wave-particle interactions during storms, *J. Geophys. Res., 112*, A10220, doi:10.1029/2007JA012368.

Li, X., I. Roth, M. Temerin, J. R. Wygant, M. K. Hudson, and J. B. Blake (1993), Simulation of the prompt energization and transport of radiation particles during the March 23, 1991 SSC, *Geophys. Res. Lett., 20*, 2423, 1993.

Li, X., D. Baker, M. Temerin, T. Cayton, E. Reeves, R. Christensen, J. Blake, M. Looper, R. Nakamura, and S. Kanekal (1997), Multisatellite observations of the outer zone electron variation during the November 3–4, 1993, magnetic storm, *J. Geophys. Res.*, *102*(A7), 14,123-14,140.

Li, X., D. Baker, M. Teremin, T. Cayton, G. Reeves, R. Selesnick, J. Blake, G. Lu, S. Kanekal, and H. Singer (1999), Rapid enchancements of relativistic electrons deep in the magnetosphere during the May 15, 1997, magnetic storm, *J. Geophys. Res.*, *104*(A3), 4467-4476.

Li, X., M. Temerin, D. N. Baker, and G. D. Reeves (2001a), Quantitative prediction of radiation belt electrons at geostationary orbit based on solar wind measurements, *Geophys. Res. Lett.*, *28*(9), 1887-1890.

Li, X., and M. A. Temerin (2001b), The electron radiation belt, *Space Sci. Rev.*, 95, 569.

Li, X. (2004), Variations of 0.7–6.0 MeV electrons at geosynchronous orbit as a function of solar wind, *Space Weather*, 2, S03006, doi:10.1029/2003SW000017.

Li, X., D. N. Baker, M. Temerin, G. D. Reeves, R. Friedel, and C. Shen (2005), Energetic electrons, 50 keV-6 MeV, at geosynchronous orbit: their responses to solar wind variations, *Space Weather*, 3, S04001, doi:10.1029/2004SW000105.

Li, X., D. N. Baker, T. P. O'Brien, L. Xie, and Q. G. Zong (2006), Correlation between the inner edge of outer radiation belt electrons and the innermost plasmapause location, *Geophys. Res. Lett.,* 33, L14107, doi:10.1029/2006GL026294.

Li, X., Drew Turner, Weichao Tu, and Cora Randall (2010), Energetic Particles from a highly Inclined Constellation (EPhIC), white paper submitted to the National Research Council (NRC) for the 2010 "decadal survey" in solar and space physics (heliophysics), available at: http://www8.nationalacademies.org/SSBSurvey/DetailFileDisplay.aspx?id=627&parm_type=HDS.

Lorentzen, K., J. Blake, U. Inan, and J. Bortnik (2001), Observations of relativistic electron microbursts in association with VLF chorus, *J. Geophys. Res.*, 106, 6017-6027.

Loto'aniu, T. M., H. J. Singer, C. L. Waters, V. Angelopoulos, I. R. Mann, S. R. Elkington, and J. W. Bonnell (2010), Relativistic electron loss due to ultralow frequency waves and enhanced outward radial diffusion, *J. Geophys. Res.,* 115, A12245, doi:10.1029/2010JA015755.

Lyon, J. G., J. A. Fedder, and C. M. Mobarry (2004), The Lyon-Fedder-Mobarry (LFM) global MHD magnetospheric simulation code, *J. Atmos. Solar Terr. Phys.*, *66*(15), 1333, doi:10.1016/j.jastp.2004.03.020.

Lyons, L., R. Thorne, and C. Kennel (1972), Pitch-angle diffusion of radiation belt electrons within the plasmasphere, *J. Geophys. Res.*, 77, 3455.

Lyons, L.R., and Thorne, R.M. (1973), Equilibrium structure of radiation belt electrons, *J. Geophys. Res.*, 78, 2142.

Mabry, D.J., S.J. Hansel, and J.B. Blake (1993), The SAMPEX data Processing Unit (DPU), IEEE Trans. Geosci. and Remote Sens., 1993. 31: p. 572-574.

McIlwain, C. E. (1961), Coordinates for mapping the distribution of magnetically trapped particles, *J. Geophys. Res., 66*(11), 3681-3691.

McIlwain, C. E. (1966), Ring current effects on trapped particles, *J. Geophys. Res., 71*, 3623-3628.

McIlwain, C. E. (1996), Processes acting upon outer zone electrons, In Radiation Belts: Models and Standards, Geophys. Monogr. Set., vol. 97, pp. 15-26, edited by J. F. Lemaire, D. Heynderickx, and D. N. Baker, AGU, Washington, D.C..

Meredith, N. P., R. B. Horne, and R. R. Anderson (2001), Substorm dependence of chorus amplitudes: implications for the acceleration of electrons to relativistic energies, *J. Geophys. Res.*, 106, 13165-13178.

Meredith, N. P., R. B. Horne, R. H. A. Iles, R. M. Thorne, D. Heynderikx, and R. R. Anderson (2002), Outer zone relativistic electron acceleration associated with substorm-enhanced whistler mode chorus, *J. Geophys. Res., 107*(A7), 1144, doi:10.1029/2001JA900146.

N. P. Meredith, R. M. Thorne, R. B. Horne, D. Summers, B. J. Fraser, and R. R. Anderson (2003a), Statistical analysis of relativistic electron energies for cyclotron resonance with EMIC waves observed on CRRES, *J. Geophys. Res.*, *108*(A6), 1250, doi:10.1029/2002JA009700.

Meredith, N. P., M. Cain, R. B. Horne, R. M. Thorne, D. Summers, and R. R. Anderson (2003b), Evidence for chorus-driven electron acceleration to relativistic energies from a survey of geomagnetically disturbed periods, *J. Geophys. Res.*, 108, A61248.

Meredith, N. P., R. B. Horne, R. M. Thorne, and R. R. Anderson (2003c), Favored regions for chorus-driven electron acceleration to relativistic energies in the Earth's outer radiation belt, *Geophys. Res. Lett., 30*(16), 1871, doi:10.1029/2003GL017698.

Meredith, N. P., R. B. Horne, R. M. Thorne, D. Summers, and R. R. Anderson (2004), Substorm dependence of plasmaspheric hiss, *J. Geophys. Res.*, *109*, A06209, doi:10.1029/2004JA010387.

Meredith, N. P., R. B. Horne, S. A. Glauert, R. M. Thorne, D. Summers, J. M. Albert, and R. R. Anderson (2006), Energetic outer zone electron loss timescales during low geomagnetic activity, *J. Geophys. Res.*, *111*, A05212, doi:10.1029/2005JA011516.

Meredith, N. P., R. B. Horne, S. A. Glauert, and R. R. Anderson (2007), Slot region electron loss timescales due to plasmaspheric hiss and lightning-generated whistlers, *J. Geophys. Res.*, *112*, A08214, doi:10.1029/2007JA012413.

Mewaldt, R. A. et al. (2005), Proton, helium, and electron spectra during the large solar particle events of October–November 2003, *J. Geophys. Res.*, 110, A09S18, doi:10.1029/2005JA011038.

McIlwain, C. E. (1961), Coordinates for Mapping the Distribution of Magnetically Trapped Particles, *J. Geophys. Res., 66*, pp. 3681-3691.

Millan, R. M. and R. M. Thorne (2007), Review of radiation belt relativistic electron loss, *J. Atmos. Sol. Terr. Phys., 69,* 363-377.

Morlet, J., G. Arens, E. Fourgeau, and D. Giard (1982), Wave propagation and sampling theory, *Geophysics*, 47, 203, doi:10.1190/1.1441328.

Nakamura, R., K. Kamei, Y. Kamide, D. Baker, J. Blake, and M. Looper (1998), SAMPEX observations of storm-associated electron flux variations in the outer radiation belt, *J. Geophys. Res., 103*(A11), 26261-26269.

Northrop, T. G. (1968), The adiabatic motion of charged particles. Interscience Publishers, New York.

O'Brien, T. P., and M. B. Moldwin (2003), Empirical plasmapause models from magnetic indices, *Geophys. Res. Lett.*, *30*(4), 1152, doi:10.1029/2002GL016007.

O'Brien, T. P., M. D. Looper, and J. B. Blake (2004), Quantification of relativistic electron microburst losses during the GEM storms, *Geophys. Res. Lett.*, *31*, L04802, doi:10.1029/2003GL018621.

Paulikas, C. A. and Blake, J. B. (1979), Effects of the Solar Wind on Magnetospheric Dynamics: Energetic Electrons at the Synchronous Orbit, *Quantitative Modeling of Magnetospheric Processes* 21, Geophys. Monograph Series.

Reeves, G. D., R. H. W. Friedel, R. D. Belian, M. M. Meier, M. G. Henderson, T. Onsager, H. J. Singer, D. N. Baker, X. Li, and J. B. Blake (1998), The relativistic electron response at geosynchronous orbit during the January 1997 magnetic storm, *J. Geophys. Res.*, *103*(A8), 17,559-17,570.

Reeves, G. D., K. L. McAdams, R. H. W. Friedel, and T. P. O'Brien (2003), Acceleration and loss of relativistic electrons during geomagnetic storms, *Geophys. Res. Lett.*, 30, 36-1-36-4.

Roederer, J. G. (1970), Dynamics of Geomagnetically Trapped Radiation, Springer, New York.

Rostoker, G., S. Skone, and D. N. Baker (1998), On the origin of relativistic electrons in the magnetosphere associated with some geomagnetic storms, *Geophys. Res. Lett., 25*(19), 3701-3704.

Schulz, M., and L. Lanzerotti (1974), Particle Diffusion in the Radiation Belts, Springer, New York.

Selesnick, R. S., and J. B. Blake (1997), Dynamics of the Outer Radiation Belt, *Geophys. Res. Lett.*, *24*(11), 1347-1350.

Selesnick, R. S., and J. B. Blake (2000), On the source location of radiation belt relativistic electrons, *J. Geophys. Res.*, *105*(A2), 2607-2624.

Selesnick, R. S., J. B. Blake, and R. A. Mewaldt (2003), Atmospheric losses of radiation belt electrons , *J. Geophys. Res.*, *108*, 1468, doi:10.1029/2003JA010160.

Selesnick, R. S., M. D. Looper, and J. M. Albert (2004), Low-altitude distribution of radiation belt electrons, *J. Geophys. Res., 109*, A11209, doi:10.1029/2004JA010611.

Selesnick, R. S. (2006), Source and loss rates of radiation belt relativistic electrons during magnetic storms, *J. Geophys. Res.*, *111*, A04210, doi:10.1029/2005JA011473.

Selesnick, R. S. and S. G. Kanekal (2009), Variability of the total radiation belt electron content, *J. Geophys. Res.*, 114, A02203, doi:10.1029/2008JA013432.

Shprits, Y. Y., and R. M. Thorne (2004), Time dependent radial diffusion modeling of relativistic electrons with realistic loss rates, *Geophys. Res. Lett.*, *31*, L08805, doi:10.1029/2004GL019591.

Shprits, Y. Y., R. M. Thorne, G. D. Reeves, R. Friedel (2005), Radial diffusion modeling with empirical lifetimes: Comparison with CRRES observations, *Ann. Geophys.*, 23, 1467-1471.

Shprits, Y. Y., R. M. Thorne, R. Friedel, G. D. Reeves, J. Fennell, D. N. Baker, and S. G. Kanekal (2006a), Outward radial diffusion driven by losses at magnetopause, *J. Geophys. Res.*, *111*, A11214, doi:10.1029/2006JA011657.

Shprits, Y. Y., W. Li, and R. M. Thorne (2006b), Controlling effect of the pitch angle scattering rates near the edge of the loss cone on electron lifetimes, *J. Geophys. Res., 111*, A12206, doi:10.1029/2006JA011758.

Shprits, Y. Y., N. P. Meredith, and R. M. Thorne (2007), Parameterization of radiation belt electron loss timescales due to interactions with chorus waves, *Geophys. Res. Lett.*, *34*, L11110, doi:10.1029/2006GL029050.

Shprits, Y. Y., L. Chen, and R. M. Thorne (2009), Simulations of pitch angle scattering of relativistic electrons with MLT-dependent diffusion coefficients, *J. Geophys. Res., 114*, A03219, doi:10.1029/2008JA013695.

Subbotin, D. A. and Y. Y. Shprits (2009), Three-dimensional modeling of the radiation belts using the Versatile Electron Radiation Belt (VERB) code, *Space Weather*, 7, S10001, doi:10.1029/2008SW000452.

Subbotin, D., Y. Shprits, and B. Ni (2010), Three-dimensional VERB radiation belt simulations including mixed diffusion, *J. Geophys. Res., 115*, A03205, doi:10.1029/2009JA015070.

Summers, D., R. M. Thorne, and F. L. Xiao (1998), Relativistic theory of wave-particle resonant diffusion with application to electron acceleration in the magnetosphere, *J. Geophys. Res.*, *103*(A9), 20,487-20, 500.

Summers, D., and R. M. Thorne (2003), Relativistic electron pitch-angle scattering by electromagnetic ion cyclotron waves during geomagnetic storms, *J. Geophys. Res.*, *108*(A4), 1143, doi:10.1029/2002JA009489.

Summers, D., B. Ni, and N. P. Meredith (2007), Timescales for radiation belt electron acceleration and loss due to resonant wave-particle interactions: 2. Evaluation for VLF chorus, ELF hiss, and electromagnetic ion cyclotron waves, *J. Geophys. Res., 112*, A04207, doi:10.1029/2006JA011993.

Tarantola, Albert (2005), *Inverse Problem Theory and Methods for Model Parameter Estimation*, Society for Industrial and Applied Mathematics. ISBN 0-89871-572-5.

Taylor, M. G. G. T., R. H. W. Friedel, G. D. Reeves, M. W. Dunlop, T. A. Fritz, P. W. Daly, and A. Balogh (2004), Multisatellite measurements of electron phase space density gradients in the Earth's inner and outer magnetosphere, *J. Geophys. Res.*, *109*, A05220, doi:10.1029/2003JA010294.

Temerin, M., I. Roth, M. K. Hudson, and J. R. Wygant (1994), 'New Paradigm for the Transport and Energization of Radiation Belt Particles', *AGU, Eos*, 538.

Thorne, R. M., and C. F. Kennel (1971), Relativistic Electron Precipitation during Magnetic Storm Main Phase, *J. Geophys. Res.*, *76*(19), 4446-4453.

Thorne, R. M., T. P. O'Brien, Y. Y. Shprits, D. Summers, and R. B. Horne (2005), Timescale for MeV electron microburst loss during geomagnetic storms, *J. Geophys. Res.*, *110*, A09202, doi:10.1029/2004JA010882.

Tsyganenko, N. A. (2002a), A model of the near magnetosphere with a dawn-dusk asymmetry: 1. Mathematical structure, *J. Geophys. Res., 107*(A8), 1179, doi:10.1029/2001JA000219.

Tsyganenko, N. A. (2002b), A model of the near magnetosphere with a dawn-dusk asymmetry: 2. Parameterization and fitting to observations, *J. Geophys. Res., 107*(A8), 1176, doi:10.1029/2001JA000220.

Tu, W., X. Li, Y. Chen, G. D. Reeves, and M. Temerin (2009), Storm-dependent radiation belt electron dynamics, *J. Geophys. Res.*, 114, A02217, doi:10.1029/2008JA013480.

Tu, W., R. Selesnick, X. Li, and M. Looper (2010), Quantification of the precipitation loss of radiation belt electrons observed by SAMPEX, *J. Geophys. Res.*, 115, A07210, doi:10.1029/2009JA014949.

Turner, Drew, and Xinlin Li (2008), Quantitative forecast of relativistic electron flux at geosynchronous orbit based on low-energy electron flux, *Space Weather,* Vol. 6, S05005, doi:10.1029/2007SW000354.

Ukhorskiy, A. Y., K. Takahashi, B. J. Anderson, and H. Korth (2005), Impact of toroidal ULF waves on the outer radiation belt electrons, *J. Geophys. Res.*, *110*, A10202, doi:10.1029/2005JA011017.

Vampola, A. L., and A. Korth (1992), Electron drift echoes in the inner magnetosphere, *Geophys. Res. Lett.*, 19, 625, 1992.

Varotsou, A., D. Boscher, S. Bourdarie, R. B. Horne, S. A. Glauert, and N. P. Meredith (2005), Simulation of the outer radiation belt electrons near geosynchronous orbit including both radial diffusion and resonant interaction with Whistler-mode chorus waves, *Geophys. Res. Lett., 32*, L19106, doi:10.1029/2005GL023282.

Walt, M. (1966), Loss rates of trapped electrons by atmospheric collisions, in Radiation Trapped in the Earth's Magnetic Field, edited by B. M. McCormac, p. 37, D. Reidel, Norwell, Mass.

Appendix A

Derivation of Electron Lifetime from Pitch Angle Diffusion Rate

Based on the best-fit parameters, we can determine the longitude averaged pitch angle diffusion coefficient:

$$\overline{D} = (D_{dawn} + D_{dusk})\widetilde{E}^{-\mu} / 2 \tag{A.1}$$

Then the drift-averaged pitch angle diffusion equation can be written as:

$$\frac{\partial f}{\partial t} = \frac{\omega_b}{x}\frac{\partial}{\partial x}(\frac{x}{\omega_b} D_{xx} \frac{\partial f}{\partial x}) \tag{A.2}$$

Note f here is different from the f in Eq. 4.1 since in Eq. A.2 $\partial f / \partial t$ is only the decay of the bounce-averaged electron distribution function from pitch angle diffusion, which needs to be looked into separately for electron lifetimes; while the change of f in Eq. 4.1 is due to azimuthal drift, diffusion and concurrent sources. After plugging in the longitude averaged pitch angle diffusion rate $D_{xx} = \overline{D}\dfrac{1}{10^{-4} + x^{\sigma}}$ (from Eq. 4.2), Eq. A.2 becomes:

$$\frac{\partial f}{\partial(\overline{D}t)} = \frac{\omega_b}{x}\frac{\partial}{\partial x}(\frac{x}{\omega_b}\frac{1}{10^{-4} + x^{\sigma}}\frac{\partial f}{\partial x}) \tag{A.3}$$

Then we separate variables in Eq. A.3 by defining $f = \mathrm{T}(t)\mathrm{X}(x)$. Eq. A.3 now turns into

$$\frac{d\mathrm{T} / d(\overline{D}t)}{\mathrm{T}} = \frac{\dfrac{\omega_b}{x}\dfrac{d}{dx}(\dfrac{x}{\omega_b}\dfrac{1}{10^{-4} + x^{\sigma}}\dfrac{d\mathrm{X}}{dx})}{\mathrm{X}} \equiv -\lambda \tag{A.4}$$

in which the constant value for both sides of Eq. A.4 is defined as $-\lambda$, independent of both t and x. Solving the equation related to time, we get $\mathrm{T}(t) = Ae^{-\lambda\overline{D}t}$ and

$f = \mathrm{T}(t)\mathrm{X}(x) = \mathrm{X}(x)Ae^{-\lambda \overline{D} t} \propto e^{-t/\tau}$, where τ is the electron lifetime, or the e-folding lifetime of f. Then τ could be defined as

$$\tau = 1/(\lambda \overline{D}) \tag{A.5}$$

In order to obtain the value λ, we need solve the x-related part of the equation Eq. A.4:

$$-\frac{\omega_b}{x}\frac{d}{dx}\left(\frac{x}{\omega_b}\frac{1}{10^{-4}+x^{\sigma}}\frac{d\mathrm{X}}{dx}\right) = \lambda \mathrm{X}(x) \tag{A.6}$$

which is an eigenequation, after solving for which we can get several sets of eigenvalue and its corresponding eigenfunction: $\lambda_n, \overline{g}_n(x)$. And the final general solution for f is:

$$f = \sum_{\mathrm{n}=1}^{\infty} \mathrm{a}_{\mathrm{n}} \overline{g}_n(x) e^{-t/\tau_n}, \tau_n = 1/(\lambda_n \overline{D}) \tag{A.7}$$

Since the eigenvalues λ_n increases rapidly with n, the solution f quickly evolves to a electron distribution that decays at a rate given by λ_1, the lowest order eigenvalue of Eq. A.6. Therefore, the electron lifetime can be finally represented as

$$\tau = 1/(\lambda_1 \overline{D}) \tag{A.8}$$

Appendix B

Additional Results of Resolving Faster Electron Lifetime Variations

At the end of subsection 4.5.5, I discussed the necessity of resolving faster electron lifetime variations from the loss model, instead of only updating the estimated lifetimes every half a day. I showed the results of directly forcing the model to simulate the electron loss rate every two hours and discussed that due to the insufficient data constraints within each two-hour interval, the modeled loss rates have very big error bars.

In order to compensate for the inadequate data constraints for each two-hour interval and make the solution well-defined in all cases, we assume some time correlation of electron loss rates between two consecutive intervals and use the prior information from the last interval to further constrain the loss rate in the current interval. In the loss model, for parameter tuning of each interval the Quasi-Newton method is applied [Tarantola, 2005]. The prior information for each interval include prior parameter vector $\vec{m}_{prior}$ and the prior covariance matrix associated with $\vec{m}_{prior}$, C_M. After iterations for each interval i, we achieve an optimum parameters set $\vec{m}_i$ and its covariance matrix $\widetilde{C}_{M,i}$, from whose diagonal elements we can calculate the error bar for each parameter. How to use $\vec{m}_{i-1}$ and $\widetilde{C}_{M,i-1}$ of interval $i-1$ to define the prior information $\vec{m}_{prior}$ and C_M for interval i deserves careful consideration.

Some correlation between intervals is assumed, but we know ideally there should be no time correlations of electron loss rate every two hours since it may change with time. We find a compromise by making the correlation decay with time, in that the prior information for interval i

are defined as: $\vec{m}_{prior} = \vec{m}_{i-1}$, $C_M = \widetilde{C}_{M,i} \times A$, where the A is called the decay factor. $A = \infty$ indicates no correlation between intervals, which is the case for the old long-interval runs. The decay means that earlier information will be lost. If the lifetime changes quickly between intervals and the two-hour interval has enough data to reflect this change, then the data should override the prior constraint and we will see the full change in parameters. On the other hand, if the data are insufficient then the estimated lifetime would still be partly constrained by the prior information, so we should see a gradual change over a few intervals. The decay factor, A, need to be tuned to achieve this.

Using this method, 18 two-hour intervals within the prestorm and main phase of the February 2009 storm at L=4.5 are tested, like the results shown in Figure 4.11 but now with assumed time correlation between intervals. Since in the old day and half-a-day runs, no source is needed to fit the data reasonably well, we first try to simulate these 18 intervals without any source. After running with different decay factor values between 1.2 and 5.0, we find an optimal value with A=3.8, which provides the 'best' fit to data for all the intervals as well as smaller error bars compared with those in Figure 4.11. The lifetime results with A=3.8 and for 1MeV electrons are shown in panel (a) of Figure B.1. The 'best' fit to data is only the best among all the decay factors, but on average not as good as the fit from the old day and half-a-day runs. The old runs basically provide the best averaged parameter for that day or half a day which guarantee generally good fit for all the points within that long interval. However, two-hour runs tend to achieve the best fit for each short interval, thus a lot of times with better fits compared to those from the long-interval runs, but occasionally with fits even worse than the long-interval runs when the optimal parameter set for the previous interval from the best fit differ a lot from the long-interval parameters and then give bad prior constraints to the current interval. In addition, we find source is required for the last two-hour interval to achieve a reasonably good fit to data. This brings out the source issue. In the old runs, for

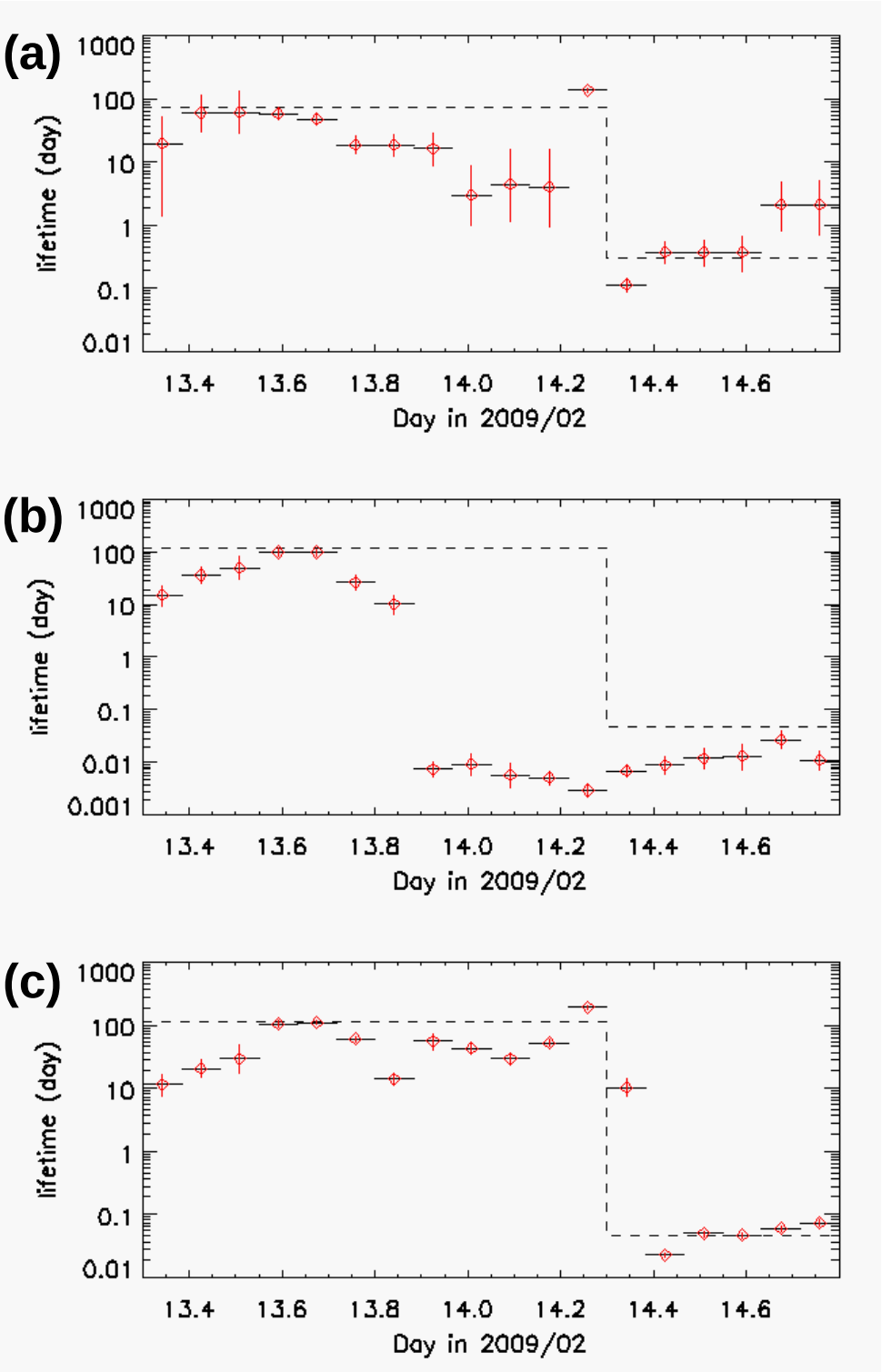

Figure B.1: Electron lifetime results every two hours for the prestorm and main phase of the February 2009 storm at L=4.5 and for 1MeV electrons. Same format with Figure 4.11, but with assumed time correlations between intervals and (a) without source, (b) with tunable source, and (c) fixed source for each interval.

each day or half a day interval, the prior information are manually given, so it is fine to turn on or off the source for different intervals. Now for the two-hour runs, prior information is automatically passed from previous interval to this interval, it is not very consistent to manually turn on the source from certain interval. For consistency as well as better fits to data, we try to include the source term from the beginning (the first two-hour interval).

In order to use the corresponding long-interval run results as reference, we rerun the long-interval runs for the prestorm and main phase intervals, but this time with tunable source on. The optimal source values for both intervals are very small and the new lifetimes for the two intervals are shown as the dashed line in panel (b) and (c) of Figure B.1. For the two-hour runs, I first add tunable source to all the intervals and again try to find the optimal decay factor between intervals. The best A value is equal to 3.5 and the new lifetime results are shown in panel (b) of Figure B.1. For this run, I achieve a consistent good fit to data as well as very small lifetime error bars, but the estimated the source rates are unrealistically higher than the long-interval ones, resulting in unrealistically faster losses, as shown in panel (b) (note the change of scale in Y-axis). This is because adding tunable source means adding two more parameters in the model, the solution is even worse-defined considering the still weak data constraints. Then a possible solution is to fix the sources according to the values from the long-interval runs and no more parameters will be added. The best decay factor is also found as equal to 4.5, while for interval 13 where the source value is manually changed, the prior covariance matrix is set to $C_M = I$. The lifetime results are shown in panel (c). In this run, the model performs well in providing good fit to data as well as small lifetime error bars, except for that few data points are still not as well fitted as by the long-interval runs. This run seems to be the best choice for now.

However, while thinking of the justification for all the assumptions made in the previous run, for testing I tried another run also with fixed sources but with the prior covariance matrix $C_M = I$

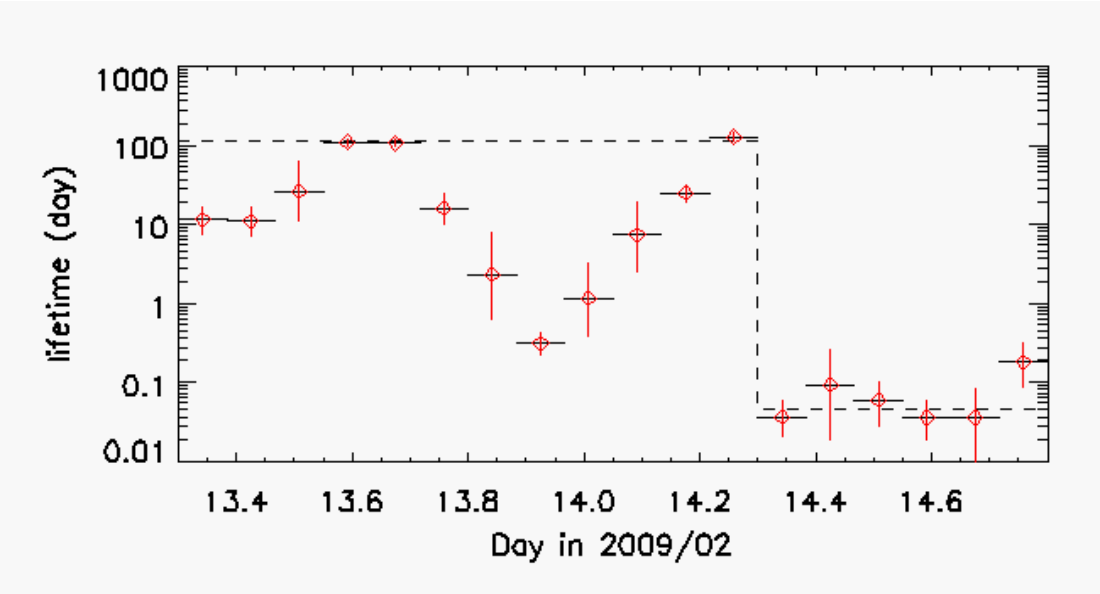

Figure B.2: Same format with Figure 4.11, but assuming prior covariance matrix $C_M = I$ and fixed source for all intervals.

for all the intervals. The results are shown in Figure B.2, with generally bigger error bars compared to those in panel (c) of Figure B.1, which is expected since C_M is bigger, but more importantly, we achieve very different lifetime variations from interval 6 to 10 (centered around Feb. 13.9). This brings further concern on the results we achieved.

Therefore, we decide that the method of assuming time correlation of lifetimes between intervals and using the prior information to provide extra constraints for the parameter is not very convincing and reliable. First, among all the trail runs only by manually fix the source can we achieve reasonably good results. How to justify this assumption and should we fix or tune the sources for later intervals? Second, it is not straightforward to justify the uniform decay factor used between all intervals, since the correlations between different intervals can be very different. Even though it works to provide good fit to data, reasonable estimation of parameters with small error bars, how do we know it is the only way or the true way? Third, all the results prove that the lifetime results can be very different depending on how the prior information is defined and how the

fit is controlled. This is fundamentally due to the insufficient constraints from the data and the variations are from the non-linearity of the system. Thus, in order to fundamentally improve the lifetime variations the model can resolve, more and faster data coverage is required as discussed in subsection 4.5.5.

Appendix C

Derivation of Radial Diffusion Coefficient

C.1 Introduction

Radial Diffusion Coefficient, D_{LL}, is defined as [Fäthammar, 1965]:

$$D_{LL} = \frac{< (L - L_0)^2 >}{2t} = \frac{1}{2t}\int_0^t \frac{d < (L - L_0)^2 >}{d\tau} d\tau \qquad \text{(C.1)}$$

The symbol $\langle\ \rangle$ denotes the expectation value of the quantity inside the symbol on a large time scale: $t >> 2\pi/\Omega$, where L_0 is the initial L value and Ω is particle's drift frequency. Therefore, the key step to calculate radial diffusion coefficient is to obtain $\frac{dL}{dt}$.

C.2 Background Field

The background field is assumed as a dipole magnetic field: $B = \frac{B_E R_E{}^3}{r^3}$ (C.2)

where r is radial distance from the center of the Earth, R_E is the Earth radii, B_E is equatorial magnetic field strength at the surface of the Earth. Fei et al. [2006] included dipole field plus a day-night asymmetry term as their background field, but found the symmetric radial diffusion coefficients (or the ones not related to the day-night asymmetry) are mostly dominant. Therefore, here I only consider dipole background fields for simplicity.

The quantity L used here is defined as the average radial distance (in R_E) of a particle drift orbit: $L^3 = \frac{B_E}{B}$. In dipole field this definition of L is consistent with Roederer's definition of L, which is $L^* = -\frac{2\pi B_E R_E^2}{\phi}$ [Roederer, 1970]. For dipole background field,

$$\phi = \int_{LR_E}^{\infty}\int_0^{2\pi} \frac{B_E {R_E}^3}{r^3} r dr d\varphi = -\frac{2\pi B_E {R_E}^3}{LR_E} = -\frac{2\pi B_E {R_E}^2}{L}$$
$$\Rightarrow L^* \approx L$$

Combing our definition of L and Eq. (C.2), we have:

$$\frac{B_E}{L^3} = \frac{B_E {R_E}^3}{r^3} \Rightarrow r = LR_E, \frac{dr}{dL} = R_E \tag{C.3}$$

C.3 Small Disturbances of Electric and Magnetic Fields

Radial diffusion is caused by disturbances in electric and magnetic fields. Since this derivation is for particles on magnetic equator, here I limit the discussion to field disturbances that allow the particles to remain in the equatorial plane. More specifically, I assume the electric field disturbance, E, is parallel to the equatorial plane, and the magnetic field disturbance, δB, is perpendicular to the plane. Note here E is the disturbance on total electric field, including both of convective electric field and of inductive electric field. Furthermore, here I only consider small disturbances in electric and magnetic fields. The magnetic disturbance satisfies:

$$\left|\delta B / B_d\right| \le \varepsilon << 1 \tag{C.4}$$

where $B_d = B_E / L^3$. A measure of the strength of the electric disturbance is given by the quantity:

$$Q = \left|E / r\Omega B_d\right| \tag{C.5}$$

where Q satisfies the condition:

$$\left|\Omega\int_{t_0}^{t_0+1/\Omega} Q dt\right| \le \eta << 1 \qquad \text{(C.6)}$$

C.4 Derive $\frac{dL}{dt}$

Since $r = LR_E$, in order to calculate $\frac{dL}{dt}$, I can first calculate $\frac{dr}{dt}$. From Fäthammar [1965] we have $\frac{dr}{dt} = -\frac{E_\varphi}{B} + \frac{\mu}{eB}\frac{1}{r}\frac{\partial B}{\partial \varphi}$, where μ is the orbital magnetic moment of the charged particle given by $\mu = m w_\perp^{\ 2} / 2B$, where $w_\perp$ is the spiraling velocity. Now $B = \frac{B_E R_E^{\ 3}}{r^3} + \delta B$, then $\frac{dr}{dt}$ can be represented as:

$$\frac{dr}{dt} = -\frac{1}{B_d + \delta B}(E_\varphi - \frac{\mu}{er}\frac{\partial \delta B}{\partial \varphi}) = B_d^{\ -1}(1 + \frac{\delta B}{B_d})^{-1}(-E_\varphi + \frac{\mu}{er}\frac{\partial \delta B}{\partial \varphi})$$
$$= (1 + \frac{\delta B}{B_d})^{-1}(-\frac{E_\varphi}{B_d} + \frac{\mu}{er}\frac{\partial \delta B / \partial \varphi}{B_d})$$

With the first order approximation of δB, we have:

$$\frac{dr}{dt} = (1 - \frac{\delta B}{B_d})(-\frac{E_\varphi}{B_d} + \frac{\mu}{er}\frac{\partial \delta B / \partial \varphi}{B_d}) = -\frac{E_\varphi}{B_d} + \frac{\mu}{er}\frac{\partial \delta B / \partial \varphi}{B_d} \qquad \text{(C.7)}$$

Then,

$$\frac{dL}{dt} = \frac{dL}{dr}\cdot\frac{dr}{dt} = \frac{1}{R_E}\frac{L^3}{B_E}(-E_\varphi + \frac{\mu}{er}\frac{\partial \delta B}{\partial \varphi})$$
$$= \frac{L^3}{R_E B_E}(-E_\varphi) + \frac{L^3}{R_E B_E}\frac{\mu}{er}\frac{\partial \delta B}{\partial \varphi} = -\frac{L^3}{R_E B_E}E_\varphi + \frac{\mu L^2}{e R_E^{\ 2} B_E}\frac{\partial \delta B}{\partial \varphi}$$

Finally, under the relativistic condition, we have:

$$\frac{dL}{dt} = -\frac{L^3}{R_E B_E}E_\varphi + \frac{\mu L^2}{e R_E^{\ 2} B_E \gamma}\frac{\partial \delta B}{\partial \varphi} \qquad \text{(C.8)}$$

where γ is the Lorentz factor.

C.5 Derive Radial Diffusion Coefficient

I define $\frac{dL}{dt} = -\frac{L^3}{R_E B_E} E_\varphi + \frac{\mu L^2}{e {R_E}^2 B_E \gamma} \frac{\partial \delta B}{\partial \varphi} = u^E(t) + u^B(t)$, where:

$u^E(t) = -\frac{L^3}{R_E B_E} E_\varphi = A E_\varphi$, only related to the electric field disturbance E_φ

where $A = -\frac{L^3}{R_E B_E}$

$u^B(t) = \frac{\mu L^2}{e {R_E}^2 B_E \gamma} \frac{\partial \delta B}{\partial \varphi} = C \frac{\partial \delta B}{\partial \varphi}$, only related to the magnetic field disturbance δB

where $C = \frac{\mu L^2}{e {R_E}^2 B_E \gamma}$

$\Rightarrow L = \int_0^t [u^E(t) + u^B(t)] dt + L_0$, then

$$\begin{aligned}
&\frac{d<(L-L_0)^2>}{dt} = <\frac{d}{dt}(L-L_0)^2> = 2<(L-L_0)\frac{d(L-L_0)}{dt}> \\
&= 2<\int_0^t [u^E(\varepsilon) + u^B(\varepsilon)] d\varepsilon \cdot [u^E(t) + u^B(t)]> \\
&= 2<\int_0^t u^E(t) u^E(\varepsilon) d\varepsilon + \int_0^t u^E(t) u^B(\varepsilon) d\varepsilon + \int_0^t u^B(t) u^E(\varepsilon) d\varepsilon + \int_0^t u^B(t) u^B(\varepsilon) d\varepsilon> \\
&= 2\{\int_0^t <u^E(t) u^E(\varepsilon)> d\varepsilon + \int_0^t <u^E(t) u^B(\varepsilon)> d\varepsilon + \int_0^t <u^B(t) u^E(\varepsilon)> d\varepsilon + \int_0^t <u^B(t) u^B(\varepsilon)> d\varepsilon\}
\end{aligned} \tag{C.9}$$

The above terms could be divided into three groups:

Group 1: Only related to electric disturbance E_φ: $\int_0^t <u^E(t) u^E(\varepsilon)> d\varepsilon$

Group 2: Only related to magnetic disturbance δB: $\int_0^t <u^B(t) u^B(\varepsilon)> d\varepsilon$

Group 3: E-B Mixed terms: $\int_0^t <u^E(t) u^B(\varepsilon)> d\varepsilon$, $\int_0^t <u^B(t) u^E(\varepsilon)> d\varepsilon$

C.5.1 Analyze Group 3

Let's first analyze the first term in Group 3: $\int_0^t < u^E(t)u^B(\varepsilon) > d\varepsilon$, with $u^E(t) = AE_\varphi$ and $u^B(t) = C\frac{\partial \delta B}{\partial \varphi}$. E_φ is comprised of two parts: the disturbance in the convection electric fields, E_{con}, and the perturbation in the induced electric field associated with the magnetic disturbance δB, E_{ind}. Therefore, $E_\varphi = E_{con} + E_{ind}$, then,

$$< u^E(t)u^B(\varepsilon) >=< AE_\varphi(t) \times C\frac{\partial \delta B}{\partial \varphi}(\varepsilon) >= AC < (E_{con}(t) + E_{ind}(t))\frac{\partial \delta B}{\partial \varphi}(\varepsilon) >$$

$$= AC[< E_{con}(t)\frac{\partial \delta B}{\partial \varphi}(\varepsilon) > + < E_{ind}(t)\frac{\partial \delta B}{\partial \varphi}(\varepsilon) >]$$

If we assume that the disturbance in the convection electric fields is independent of the magnetic field perturbation, thus $< E_{con}(t)\frac{\partial \delta B}{\partial \varphi}(\varepsilon) >=< E_{con}(t) >< \frac{\partial \delta B}{\partial \varphi}(\varepsilon) >$. If we further assume the field perturbations, E_{con} and δB, are stochastic processes that are individually and jointly stationary and ergodic. Then $< E_{con}(t) >=< \frac{\partial \delta B}{\partial \varphi}(t) >= 0 \Rightarrow < E_{con}(t)\frac{\partial \delta B}{\partial \varphi}(\varepsilon) >= 0$.

Then we consider the induced electric field. Based on Faraday's law, we know that $\oint \vec{E}_{ind} \bullet d\vec{l} = -\int \frac{\partial \vec{B}}{\partial t} \bullet d\vec{a}$. Then E_{ind} is correlated with $\frac{\partial \delta B}{\partial \varphi}$ and $< E_{ind}(t)\frac{\partial \delta B}{\partial \varphi}(\varepsilon) >\neq 0$. However, the induced electric field is not easily derivable from the time-dependent magnetic field, unless frozen-field condition of plasma is assumed and detailed field line tracing is performed [Fäthammar, 1965]. Due to its complexity, here I ignore the contribution of mixed E-B term, $< E_{ind}(t)\frac{\partial \delta B}{\partial \varphi}(\varepsilon) >$, from the induced electric field and magnetic field disturbance, to the total radial diffusion coefficient, which may introduce uncertainty to the final D_{LL} derived here.

The above derivations and statements are similarly valid for the second term in Group 3.

C.5.2 Analyze Group 1: $\int_0^t < u^E(t)u^E(\varepsilon) > d\varepsilon$

Set $\varepsilon = t - \tau$, then,

$$\int_0^t < u^E(t)u^E(\varepsilon) > d\varepsilon = \int_t^0 < u^E(t)u^E(t-\tau) > (-d\tau) = \int_0^t < u^E(t)u^E(t-\tau) > d\tau \qquad \text{(C.10)}$$

and $u^E(t) = -\dfrac{L^3}{R_E B_E} E_\varphi = AE_\varphi$.

According to Fäthammar [1965], the solution of the equations of motion to zero order approximation are:

$$\begin{cases} r = r_0 = cons \tan t \\ \varphi = \Omega_0 t + \alpha \end{cases} \qquad \text{(C.11)}$$

where φ is the azimuthal angle (zero at noon), Ω_0 is the drift frequency of particles, and α is the initial angle position. Because series $\sum_{n=0}^{\infty} \cos(n\varphi + \gamma_n(r_0,t))$ is a complete set, $E_\varphi(r_0,\varphi,t)$ can be written in the form $E_\varphi(r_0,\varphi,t) = \sum_{n=0}^{\infty} E_{\varphi n}(r_0,t)\cos(n\varphi + \gamma_n(r_0,t))$. In practice it can be approximated by a finite sum:

$$E_\varphi(r_0,\varphi,t) \approx \sum_{m=0}^{N} E_m(r_0,t)\cos(m\varphi + \gamma_m(r_0,t)) \qquad \text{(C.12)}$$

where I rewrite the angular term as :

$$m\varphi + \gamma_m(r_0,t) = m(\Omega_0 t + \alpha) + \gamma_m(r_0,t) = m\Omega_0 t + m\alpha + \gamma_m(r_0,t) \equiv m\Omega_0 t + \phi_m$$

in which $\phi_m \equiv m\alpha + \gamma_m(r_0,t)$.

I assume that there is only time variation in the amplitudes $E_m(r_0,t)$ and not in the direction angles $\gamma_m(r_0,t)$. Therefore ϕ_m is a constant. Thus:

$$< u^E(t)u^E(t-\tau) >= A^2 < \sum_m E_m(r_0,t)\cos(m\Omega_0 t+\phi_m)\sum_n E_n(r_0,t-\tau)\cos(n\Omega_0 t-n\Omega_0\tau+\phi_n) >$$
$$= A^2\sum_{m,n} < E_m(t)E_n(t-\tau)\cos(m\Omega_0 t+\phi_m)\cos(n\Omega_0 t-n\Omega_0\tau+\phi_n) >$$
$$= A^2\sum_{m,n} < E_m(t)E_n(t-\tau) > \cos(m\Omega_0 t+\varphi_m)\cos(n\Omega_0 t-n\Omega_0\tau+\varphi_n)$$

Since E_n is both individually and jointly stochastic functions, the quantities $< E_m(t)E_n(t-\tau) >$ are independent of time and equal to $< E_m(t)E_n(t+\tau) >$ both when $m=n$ and when $m\neq n$.

Using the trigonometric identity, $\cos(a-b)=\cos a\cos b+\sin a\sin b$, we have:

$$< u^E(t)u^E(t-\tau) >= A^2\sum_{m,n} < E_m(t)E_n(t+\tau) > \{\cos(m\Omega_0 t+\phi_m)\cos(n\Omega_0 t+\phi_n)\cos(n\Omega_0\tau)$$
$$+\cos(m\Omega_0 t+\phi_m)\sin(n\Omega_0 t+\phi_n)\sin(n\Omega_0\tau)\}$$

Separating the sums where $m=n$ from $m\neq n$, we have:

$$< u^E(t)u^E(t-\tau) >= A^2\sum_m < E_m(t)E_m(t+\tau) > \cos^2(m\Omega_0 t+\phi_m)\cos(m\Omega_0\tau)$$
$$+A^2\sum_m < E_m(t)E_m(t+\tau) > \cos(m\Omega_0 t+\phi_m)\sin(m\Omega_0 t+\phi_m)\sin(m\Omega_0\tau)$$
$$+A^2\sum_{\substack{m,n\\ m\neq n}} < E_m(t)E_n(t+\tau) > \cos(n\Omega_0 t+\phi_n)\cos(m\Omega_0 t+\phi_m)\cos(m\Omega_0\tau)$$
$$+A^2\sum_{m,n} < E_m(t)E_n(t+\tau) > \cos(n\Omega_0 t+\phi_n)\sin(m\Omega_0 t+\phi_m)\sin(m\Omega_0\tau)$$

Assume now that the definite integrals:

$$I_{mn1}=\int_0^\infty < E_m(t)E_n(t+\tau) > \cos(m\Omega_0\tau)d\tau$$
$$I_{mn2}=\int_0^\infty < E_m(t)E_n(t+\tau) > \sin(m\Omega_0\tau)d\tau \qquad \text{(C.13)}$$

exist in the sense that the indefinite integrals:

$$\int_0^t < E_m(t)E_n(t+\tau) > \cos(m\Omega_0\tau)d\tau \text{ and } \int_0^t < E_m(t)E_n(t+\tau) > \sin(m\Omega_0\tau)d\tau$$

are approximately independent of t when it exceeds a certain finite value t_1. (The integrands are independent of t.) Then, when $t >> t_1$,

$$2\int_0^t < u^E(t)u^E(t-\tau) > d\tau = 2A^2\{\sum_m \cos^2(m\Omega_0 t+\phi_m)I_{mm1} + \sum_m \cos(m\Omega_0 t+\phi_m)\sin(m\Omega_0 t+\phi_m)I_{mm2}$$
$$+ \sum_{\substack{m,n \\ m\neq n}} \cos(n\Omega_0 t+\phi_n)\cos(m\Omega_0 t+\phi_m)I_{mn1} + \sum_{m,n} \cos(n\Omega_0 t+\phi_n)\sin(m\Omega_0 t+\phi_m)I_{mn2}\}$$

From Eq. C.1, I define the radial diffusion coefficient due to the term in Group 1 as D_{LL}^E:

$$D_{LL}^E = \frac{1}{2t}\int_0^t \{2\int_0^t < u^E(t)u^E(t-\tau) > d\tau\}dt$$
$$= \frac{A^2}{t}\{\sum_m \int_0^t \cos^2(m\Omega_0 t+\phi_m)I_{mm1}dt + \sum_m \int_0^t \cos(m\Omega_0 t+\phi_m)\sin(m\Omega_0 t+\phi_m)I_{mm2}dt$$
$$+ \sum_{\substack{m,n \\ m\neq n}} \int_0^t \cos(n\Omega_0 t+\phi_n)\cos(m\Omega_0 t+\phi_m)I_{mn1}dt + \sum_{m,n} \int_0^t \cos(n\Omega_0 t+\phi_n)\sin(m\Omega_0 t+\phi_m)I_{mn2}dt\}$$

Since:

$$\int_0^t \cos^2(m\Omega_0 t+\phi_m)dt = \frac{1}{2}\int_0^t [\cos 2(m\Omega_0 t+\phi_m)+1]dt = \frac{1}{2}t + \frac{1}{2m\Omega_0}[\sin 2(m\Omega_0 t+\phi_m) - \sin 2\phi_m]$$

and since the sine terms are bounded by 1, I can replace those terms with $O(1)$. This is Big-O notation, which indicates that the term in parentheses is an upper bound for the term it replaces, thus, $\int_0^t \cos^2(m\Omega_0 t+\phi_m)dt = \frac{1}{2}t + \frac{O(1)}{\Omega_0}$. For the same reason:

$$\int_0^t \cos(m\Omega_0 t+\phi_m)\sin(m\Omega_0 t+\phi_m)dt = \frac{O(1)}{\Omega_0}$$
$$\int_0^t \cos(n\Omega_0 t+\phi_n)\cos(m\Omega_0 t+\phi_m)dt = \frac{O(1)}{\Omega_0} \quad (2\cos a\cos b = \cos(a-b)+\cos(a+b))$$
$$\int_0^t \cos(n\Omega_0 t+\phi_n)\sin(m\Omega_0 t+\phi_m)dt = \frac{O(1)}{\Omega_0}$$

Therefore,

$$D_{LL}^{E} = \frac{A^2}{t}\{\sum_m I_{mm1}(\frac{1}{2}t + \frac{O(1)}{\Omega_0}) + \sum_m I_{mm2}\frac{O(1)}{\Omega_0} + \sum_{\substack{m,n \\ m\neq n}} I_{mn1}\frac{O(1)}{\Omega_0} + \sum_{m,n} I_{mn2}\frac{O(1)}{\Omega_0}\}$$

$$= \frac{A^2}{2}\sum_m I_{mm1} + \frac{A^2}{t}\{\sum_m I_{mm1}\frac{O(1)}{\Omega_0} + \sum_m I_{mm2}\frac{O(1)}{\Omega_0} + \sum_{\substack{m,n \\ m\neq n}} I_{mn1}\frac{O(1)}{\Omega_0} + \sum_{m,n} I_{mn2}\frac{O(1)}{\Omega_0}\}$$

Now I would like to show that all but the first one of the terms in the above equation are negligible. I begin by only considering times such that $t >> 1/\Omega_0$, which means that the term I_{mm1} will dominate over the terms of order $I_{mm1}/\Omega_0, I_{mm2}/\Omega_0, I_{mn1}/\Omega_0, I_{mn2}/\Omega_0$ provided I_{mm1} does not vanish. Then I can write

$$D_{LL}^{E} = \frac{A^2}{2}\sum_m I_{mm1} = \frac{A^2}{2}\sum_m \int_0^\infty < E_m(t)E_m(t+\tau) > \cos(m\Omega_0\tau)d\tau$$

$$= \frac{1}{2}(\frac{L^3}{R_E B_E})^2 \sum_m \int_0^\infty < E_m(t)E_m(t+\tau) > \cos(m\Omega_0\tau)d\tau \qquad \text{(C.14)}$$

$$= \frac{L^6}{2R_E{}^2 B_E{}^2}\sum_m \int_0^\infty < E_m(t)E_m(t+\tau) > \cos(m\Omega_0\tau)d\tau$$

Now, since the electric power spectral density:

$$P_m^E(m\Omega_0) = P_m^E(\omega) = 4\int_0^\infty < E_m(t)E_m(t+\tau) > \cos(\omega\tau)d\tau$$

then I finally get:

$$D_{LL}^{E} = \frac{L^6}{8R_E^2 B_E^2}\sum_m P_m^E(m\Omega_0) \qquad \text{(C.15)}$$

C.5.3 Analyze Group 2: $\int_0^t < u^B(t)u^B(\varepsilon) > d\varepsilon$

Again, $\int_0^t < u^B(t)u^B(\varepsilon) > d\varepsilon = \int_0^t < u^B(t)u^B(t-\tau) > d\tau$, and $u^B(t) = C\frac{\partial \delta B}{\partial \varphi}$, where

$$C = \frac{\mu L^2}{eR_E{}^2 B_E \gamma}.$$

The same as in electric disturbance case: $\delta B(r_0,\varphi,t)=\sum_m B_m(r_0,t)\cos(m\varphi+\gamma_m(r_0,t))$

$$\Rightarrow u_1^B(t)=-C\sum_m mB_m(r_0,t)\sin(m\Omega_0 t+\phi_m)$$

Similarly,

$$< u^B(t)u^B(t-\tau) >= C^2 < \sum_m mB_m(r_0,t)\sin(m\Omega_0 t+\phi_m)\sum_n nB_n(r_0,t-\tau)\sin(n\Omega_0 t-n\Omega_0\tau+\phi_n) >$$
$$= C^2\sum_{m,n} mn < B_m(t)B_n(t-\tau)\sin(m\Omega_0 t+\phi_m)\sin(n\Omega_0 t-n\Omega_0\tau+\phi_n) >$$
$$= C^2\sum_{m,n} mn < B_m(t)B_n(t-\tau) > \sin(m\Omega_0 t+\phi_m)\sin(n\Omega_0 t-n\Omega_0\tau+\phi_n)$$
$$= C^2\sum_{m,n} mn < B_m(t)B_n(t-\tau) > \{\sin(m\Omega_0 t+\phi_m)\sin(n\Omega_0 t+\phi_n)\cos(n\Omega_0\tau)$$
$$+\sin(m\Omega_0 t+\phi_m)\cos(n\Omega_0 t+\phi_n)\sin(n\Omega_0\tau)\}$$

Similar to the analysis of Group 1, only part of the $m=n$ term will contribute the diffusion coefficient:

$$\Rightarrow < u^B(t)u^B(t-\tau) >= C^2\sum_m m^2 < B_m(t)B_m(t+\tau) > \sin^2(m\Omega_0 t+\phi_m)\cos(m\Omega_0\tau)$$
$$= \frac{C^2}{2}\sum_m m^2 < B_m(t)B_m(t+\tau) > \cos(m\Omega_0\tau)[1-\cos 2(m\Omega_0 t+\phi_m)]$$

$$\Rightarrow D_{LL}^B=\frac{1}{2t}\int_0^t\{2\int_0^t < u_1^B(t)u_1^B(t-\tau) > d\tau\}dt$$
$$= \frac{1}{t}\frac{C^2}{2}t\sum_m m^2\int_0^\infty < B_m(t)B_m(t+\tau) > \cos(m\Omega_0\tau)d\tau$$
$$= \frac{C^2}{8}\sum_m m^2 P_m^B(m\Omega_0)=\frac{1}{8}\left(\frac{\mu L^2}{eR_E{}^2B_E\gamma}\right)^2\sum_m m^2P_m^B(m\Omega_0)$$

$$\Rightarrow D_{LL}^B=\frac{\mu^2L^4}{8e^2R_E{}^4B_E{}^2\gamma^2}\sum_m m^2P_m^B(m\Omega_0) \qquad \text{(C.16)}$$

where the magnetic power spectral density:

$$P_m^B(m\Omega_0)=P_m^B(\omega)=4\int_0^\infty < B_m(t)B_m(t+\tau) >\cos(\omega\tau)d\tau$$

C.6 The results

To sum, the derived electric and magnetic radial diffusion coefficients are:

$$\begin{cases} D_{LL}^{E} = \dfrac{L^6}{8R_E^2 B_E^2}\sum_m P_m^E(m\Omega_0) \\ D_{LL}^{B} = \dfrac{\mu^2 L^4}{8e^2 {R_E}^4 {B_E}^2 \gamma^2}\sum_m m^2 P_m^B(m\Omega_0) \end{cases} \tag{C.17}$$

where L is Roederer L, R_E is earth radii, $B_E \approx 0.3\ Gauss$ is the equatorial magnetic field on the Earth's surface, μ is the first adiabatic invariant, e is the electron charge, γ is the Lorentz relativistic factor, $P_m^E(m\Omega_0)$ is the power spectral density of the total electric field at frequency $m\Omega_0$, $P_m^B(m\Omega_0)$ is the power spectral density of the magnetic field at frequency $m\Omega_0$, Ω_0 is the is the particle drift frequency and m is the mode number.

The total diffusion coefficient is: $$D_{LL} = D_{LL}^{E} + D_{LL}^{B} \tag{C.18}$$

Appendix D

Artificial Wave in LFM MHD Simulation and Successful Low-Pass Filter

At the end of Section 6.2 the issue of the artificial waves in LFM field results was identified. Examples of these waves are illustrated in the left panels of Figure D.1. They are launched from the bow shock and propagate radially inward. It was recently discovered that these waves are an unintended consequence from the shock-capturing algorithm in the LFM code, which is a numerical algorithm that allows solution in regions of especially steep gradients. These artificial waves have characteristic frequency ~ 120 mHz in the version of LFM used in our work, though their frequency does depend on the grid resolution in LFM (private communication with Scot Elkington in LASP). However, even though the original LFM outputs have much higher time resolutions, for our work the output is only taken in a cadence of every minute to save computer disk space, thus resulting a Nyquist frequency (the highest frequency wave the output fields can resolve) equal to 8.3 mHz, which is in the Pc5 wave range and sufficient for our study. Therefore, the frequency of the artificial waves is far above the output Nyquist frequency and they cannot be distinctively resolved in the output spectrum. But it doesn't mean the artificial waves would not affect our output results. In fact, the wave power of the artificial waves is aliased into our Pc5 frequency range, causing the artificial waves shown in the left panels of Figure D.1, as well as in the left panel of Figure D.2. In Figure D.2 the color represents the power spectral density of E_φ for m=1 and at L=6.6, as a function of frequency (X-axis, in unit of f_0=0.14 mHz) and time (Y-axis). The abnormal high power at high frequencies in the power spectrum is also aliased from the artificial wave at much higher frequency.

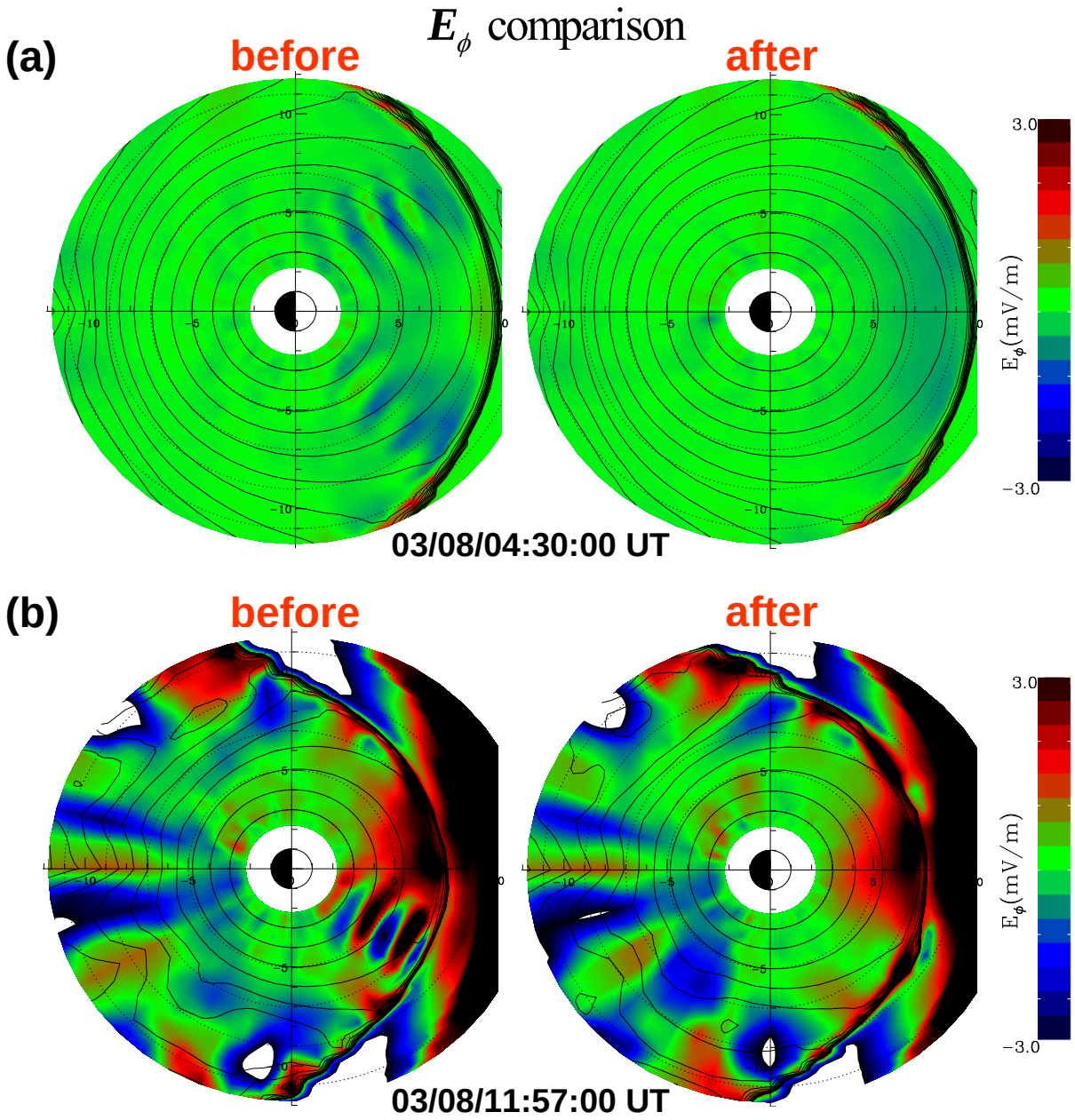

Figure D.1: E_φ results from LFM MHD simulations before (left) and after (right) the low-pass filter, showing comparisons at (a) 0430UT and (b) 1157UT on March 8th, 2008. For each panel, the format is the same with Figure 6.2.

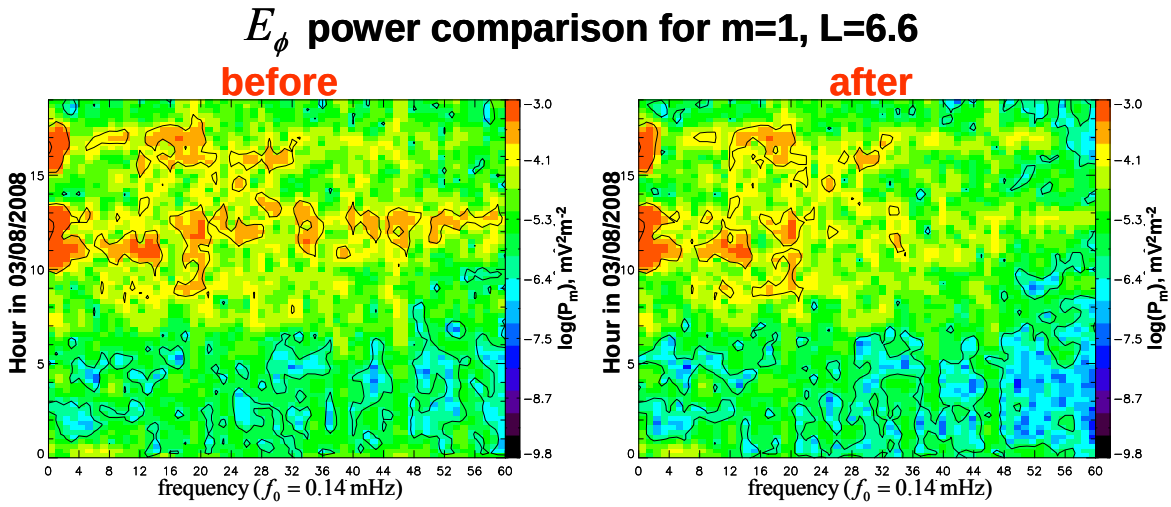

Figure D.2: Comparison of E_φ power spectrum before and after the low-pass filter. The logarithm of E_φ power spectral density for m=1 and at L=6.6 is color-coded, with frequencies in unit of f_0=0.14 mHz shown in the X-axis and time in unit of hour in March 8th, 2008 in Y-axis.

After recognizing the artificial waves and their aliasing effects on our outcomes, we need to eliminate these aliasing waves. For this purpose, we apply a low-pass filter in the time domain on a pointwise basis to the original LFM outputs (with much higher time resolution) when taking the output fields every minute. Specifically, rather than taking the instantaneous field values from LFM every minute, the accumulated and filtered values in the form $\langle q \rangle_N = \frac{\sum_{i=1}^{N} q_i dt_i}{\sum_{i=1}^{N} dt_i}$ are taken every minute, where q_i is the instantaneous higher-resolution LFM output (with resolution dt_i as low as 0.3 sec) within the one minute cadence and N is the number of q_i within each minute. After applying the low-pass filter, we achieve new LFM fields shown in the right panels in Figures D.1 and D.2. Comparing the E_φ distributions before and after the filter (Figure D.1), we find the low-pass filter successfully removes the artificial waves, while leaving the waves associated with the Kelvin-Helmholtz instability, magnetopause movement, etc., virtually untouched. Figure D.2 shows that the artificial high-frequency power in the E_φ spectrum is also efficiently removed.